WESTFÄLISCHE
WILHELMS-UNIVERSITÄT
MÜNSTER

Bastian Bathen

Jet Measurements and Reconstruction Biases in Proton–Proton and Pb–Pb Collisions with ALICE at the LHC

-2012-

Experimentelle Physik

Jet Measurements and Reconstruction Biases in Proton–Proton and Pb–Pb Collisions with ALICE at the LHC

Inaugural-Dissertation
zur Erlangung des Doktorgrades
der Naturwissenschaften im Fachbereich Physik
der Mathematisch-Naturwissenschaftlichen Fakultät
der Westfälischen Wilhelms-Universität Münster

vorgelegt von
Bastian Bathen
aus Münster

-2012-

Dekan: Prof. Dr. T. Kuhn
Erster Gutachter: Prof. Dr. J. P. Wessels
Zweiter Gutachter: Prof. Dr. M. Klasen

Tag der Disputation: 24.08.2012
Tag der Promotion: 24.08.2012

Contents

Chapter 1

Introduction

The aim of the ALICE experiment is the study of the quark-gluon plasma (QGP). It has been predicted in the 1970s as a possible new state of the fundamental constituents of strongly coupled matter: the quarks and gluons. As objects carrying color charges, quarks and gluons are prevented by the strong force from existing as free particles. In normal nuclear matter, they are confined in color-neutral objects, so-called hadronic matter, such as protons and neutrons. A phase transition from normal nuclear matter to the QGP is expected at a temperature above $T_c \approx 2 \cdot 10^{12}$ K [KL03], which is about 10^5 times the temperature in the center of the sun [YHM08]. At low temperatures, a formation of the QGP is expected if the baryon number density reaches several times the density of normal nuclear matter, $\rho_{\mathrm{nm}} = 0.16\,\mathrm{fm}^{-3}$ [YHM08]. In the new phase, the quarks and gluons can travel distances which exceed the dimension of a nucleon.

The conditions for the formation of a QGP at high temperature probably existed in the early universe up to 10 µs after the Big Bang [YHM08]. Later, with an expanded and cooler universe, the quarks and gluons formed protons, neutrons, and other hadrons. The QGP at high baryon densities may today be realized in the center of neutron stars. The only possibility to study the QGP under laboratory conditions are ultra-relativistic heavy-ion collisions. In these processes, sufficiently high energy densities are expected.

The possible generation of a QGP in accelerator experiments has to be inferred from the color neutral objects measured in the detectors. First evidence for a produced hot and dense matter has been seen in the 1990s in the heavy-ion program at the Super Proton Synchrotron (SPS) at CERN in Geneva. Stronger evidences for the QGP were found at the beginning of this century at the Relativistic Heavy-Ion Collider (RHIC) in Brookhaven, USA. Since 2010, the investigation of the QGP is continued with the Large Hadron Collider (LHC) at CERN. From the SPS over RHIC to the LHC, the collision energy increased by more than two orders of magnitude, which is expected to result in a higher initial temperature and energy density of the system, with a longer life-time of the QGP.

One of the most convincing pieces of evidence for the QGP at RHIC was a suppressed yield of single hadrons with high transverse momentum (p_t) in heavy-ion collisions, compared to the expectations from proton-proton (pp) collisions. In general, high p_t hadrons originate from hard-scattered quarks or gluons, also called partons. The scattered partons evolve in a parton shower and finally freeze-out to a spray of hadrons—a so-called jet—due to the color confinement. In the presence of a QGP, the partons traverse it before the hadronisation. In that case, they strongly interact with the hot and dense medium. This interaction is expected to cause an energy loss of the partons corresponding to a modification of the fragmentation process, which can result in a suppressed yield of produced high p_t particles. This is known as *jet quenching*. For a more detailed study of the QGP and its impact on the partonic fragmentation process, a full jet reconstruction and a measurement of the jet structure is the ultimate goal. With the larger collision energy at the LHC, it is possible for the first time to reconstruct jets with a rate large enough for these studies.

The analyses presented in this work are based on jet reconstruction in pp and lead-lead (Pb–Pb) collisions measured in the ALICE experiment (A Large Ion Collider Experiment), one of the four large experiments at the LHC. ALICE is dedicated to measure heavy-ion collisions and the signatures of a potentially produced QGP. The measurements of pp collisions are used as a baseline for fragmentation in vacuum.

The jet-related analyses in this thesis are divided into three aspects. Prior to the analyses, some theoretical background information (Chapter 2) and a description of the ALICE experiment and the LHC is given (Chapter 3). This also includes an introduction to the analysis framework which was used for this work. In Chapter 4, the characteristics of the jet reconstruction in ALICE are discussed, followed by the first part of the analysis in Chapter 5. The latter comprises a first measurement of the momentum distribution in jets with ALICE. The study is based on pp collisions with a collision energy of $\sqrt{s} = 7$ TeV. It demonstrates the capabilities of the experiment with a jet measurement which is an essential reference for a medium-modified jet fragmentation. Moreover, Monte-Carlo simulations of jet fragmentation are verified with real data for the new energy regime.

The LHC provides a much higher quantity of pp collisions to the experiments than can be recorded and analyzed. Also most of the collisions are not of interest for the study of rare events. Therefore, an efficient trigger which selects events with potentially interesting signals is required. One of those interesting signals are hard-scattered partons which appear in the final state as jets. Faster detectors can provide information about the event before slower detectors are read-out. This reduces the overall dead-time of the experiment. The Transition Radiation Detector (TRD) of ALICE is built to provide Level-1 (L1) trigger decisions based on online-reconstructed high-p_t tracks (jets) and identified electrons (heavy flavor decays, e. g. from J/ψ's). The feasibility of a jet trigger with the TRD is discussed in Chapter 6, the second part of the analysis. The main focus is on the introduced bias on the triggered jets, especially concerning their fragmentation pattern.

In the final jet analysis aspect of this thesis (Chapter 7), the focus is shifted from pp to Pb–Pb collisions at the LHC. The jet reconstruction in heavy-ion collisions is strongly affected by soft background from the underlying event. For an appropriate correction and interpretation of the jet observables, it is essential to understand the influence of the background and its fluctuations on the reconstructed jets. For this purpose, well-defined probes were embedded into measured heavy-ion data, and their reconstruction was studied in the presence of a bulk of soft background.

Chapter 2

Theoretical Basics

2.1 Standard Model of Particle Physics

The Standard Model (SM) of particle physics describes the fundamental components of matter and the interactions between them. In this chapter a brief overview is presented. More details can be found in standard books such as [Per00]. The SM was developed in the last century with most progress in the 60s and 70s. Since the mid-1970s all matter is considered to consist of six *leptons* and six *quarks*. Those point-like particles are *fermions* with spin $\frac{1}{2}$. They interact via four fundamental forces: the strong force, the weak force, the electromagnetic force, and gravity. The focus of this chapter is on the strong force, since it causes the relevant coupling of the quark-gluon plasma (QGP).

2.1.1 Fundamental Fermions

As a spin $\frac{1}{2}$ particle, a fundamental fermion obeys the Fermi-Dirac statistics. The fundamental fermions are grouped into three families of two leptons and two quarks. In each family the two particle charges differ by one unit of e. Three leptons carry negative elementary electric charge ($-e$) and differ only by mass: the electron e, the muon μ, and the tauon τ (Table 2.1a). Only the electron as the lightest charged lepton is stable. Muon and tauon decay via weak interaction. The other three leptons are *neutrinos* (ν) with no charge and a mass close to zero. Each neutrino is assigned the *flavor* of a charged lepton according to their family: electron neutrino ν_e, muon neutrino ν_μ, and tauon neutrino ν_τ. Neutrinos interact only weakly with very low cross-section. Therefore it took more than 20 years from the initial postulation of the electron

Table 2.1: Leptons and Quarks. Masses are taken from [Nak+10]. Note that for the light quarks (u, d, s) the bare current masses are listed.

(a) Leptons.

	charge q	mass m
e	-1e	0.511 keV/c^2
ν_e	0e	< 2 eV/c^2
μ	-1e	105.7 MeV/c^2
ν_μ	0e	< 0.19 MeV/c^2
τ	-1e	1.776 GeV/c^2
ν_τ	0e	< 18.2 MeV/c^2

(b) Quarks.

	charge q	mass m
u	$+2e/3$	~ 2.5 MeV/c^2
d	$-1e/3$	~ 5.0 MeV/c^2
c	$+2e/3$	~ 1.3 GeV/c^2
s	$-1e/3$	~ 100 MeV/c^2
t	$+2e/3$	~ 173 GeV/c^2
b	$-1e/3$	~ 4.2 GeV/c^2

neutrino by Pauli in 1930 [Bro78] to its discovery by Cowan and Reines [RC53; RC56].

The six quarks are called up (u), down (d), strange (s), charmed (c), bottom (b), and top (t). Each family consists of one quark with fractional charge $+\frac{2}{3}e$ and another with fractional charge $-\frac{1}{3}e$ (see Table 2.1b). In addition to the electric charge, quarks carry a so-called *color charge*. Three types of color charge exist: *blue* (b), *green* (g), and *red* (r). Via the color charge, the quarks are subject to the strong interaction. The concept of quarks as constituents of hadronic particles has first been used by Gell-Mann and Zweig in 1964 to explain the multiplet structure of baryons and mesons which have been observed in collision experiments [Gel64; Zwe64]. This was the basis for the theoretical description of the strong force.

Contrary to leptons, quarks cannot exist as free particles. Besides under some extreme conditions which will be discussed in Section 2.2, quarks are always in a bound state like the proton (uud) or neutron (ddu). More about this so-called *confinement* of the quarks is discussed later in context of the strong interaction.

For each fermion exists also an anti-particle with the same properties but opposite additive quantum numbers, e. g. the positron (e^+) as anti-particle of the electron (e^-) or the anti-electron-neutrino ($\overline{\nu_e}$) as anti-particle of the electron neutrino (ν_e). Accordingly, there also exist anti-particles from the bound states of quarks, like the anti-proton $\overline{p}$, with corresponding anti-quarks carrying anti-color ($\overline{b}$,$\overline{g}$, or $\overline{r}$).

Table 2.2: Fundamental forces. The relative magnitude is for protons just in contact [Per00].

force	mediator	rel. magnitude
strong	gluon	1
electromagnetic	photon	10^{-2}
weak	$W^{\pm}, Z^0$	10^{-7}
gravity	graviton	10^{-39}

2.1.2 Interactions and Gauge Bosons

Next the four fundamental interactions are discussed. Expect for Gravitation, for all interactions a relativistic Quantum Field Theory (QFT) has been formulated. In those QFTs the interactions are described by individual *gauge bosons* as mediators of the forces. Bosons are particles of integral spin which obey the Bose-Einstein statistics. A list of the individual mediators of the forces is given in Table 2.2.

Electromagnetic Interaction

The processes of the electromagnetic interaction are described by the QFT called quantum electrodynamics (QED). It is the first developed QFT and serves as prototype for other QFTs. The electromagnetic interaction occurs between all particles which carry electric charge. It is responsible for the formation of atoms and molecules. The gauge group of QED is U(1) with the photon as an exchange boson which itself is electrically neutral and massless. It does not exchange charge; the interaction has only an attractive or repulsive effect. The strength of the coupling of the photon at an elementary charged particle is in QFT specified by the coupling constant [Per00]

$$\alpha = \frac{e^2}{4\pi\hbar c} \approx \frac{1}{137}, \tag{2.1}$$

where e is the electric charge, $\hbar$ the Planck constant, and c the speed of light. Actually, the effective coupling depends on the momentum exchange Q^2 via the photon or the distance of the interaction $r \propto 1/Q$, respectively. The reason for this is a screening of the bare electric charge by virtual e^+e^- pairs. The coupling constant α only represents the coupling for a fixed momentum exchange $Q^2 = \mu^2$. The effective *running* coupling $\alpha_{\mathrm{em}}(Q^2)$ increases with increasing momentum transfer Q^2 or shorter distance r, respectively, since the bare electric charge is less shielded. The running coupling parameter can be written as [Per00]:

$$\alpha_{\mathrm{em}}(Q^2) = \frac{\alpha(\mu^2)}{1 - \frac{1}{\pi}\alpha(\mu^2)\ln\left(\frac{Q^2}{\mu^2}\right)}. \tag{2.2}$$

μ is the renormalization point at which the coupling $\alpha_{\mathrm{em}}(Q^2, \mu^2)$ is compared.

In classical description the electromagnetic interaction between elementary charges is given by the Coulomb potential:

$$V_{\mathrm{em}}(r) = -\frac{\alpha}{r}. \tag{2.3}$$

Strong Interaction

The QFT of the strong interaction is quantum chromodynamics (QCD). It was formulated by Gell-Mann, Fritzsch, and Leutwyler in 1972 [FG72; FGL73]. Instead of interaction between electric charge the strong force appears between all particles which carry color charge, namely quarks and gluons. Color neutral objects are obtained by combining the quarks in *baryons* (a state of three quarks, like protons and neutrons) or *mesons* (a state of a quark and an anti-quark, like pions[1]). All particles composed of quarks are called *hadrons*. The colors of the constituent quarks always neutralize each other, like e. g. (rgb) in baryons or $(r\bar{r})$ in mesons.

Ordinary nuclear matter is build up of only up and down quarks. Other types of matter composed of heavier quarks are only produced in high energy reactions, e. g. at accelerators or caused by cosmic rays. The strong interaction is also responsible for the binding of protons and neutrons in nuclei. However, this is only evoked by a residual strong force mediated by pion exchange [MS01].

The coupling strength of the strong force is given by [Per00]:

$$\alpha_{\mathrm{s}} = \frac{g_s^2}{4\pi\hbar c} \approx \mathcal{O}(1), \tag{2.4}$$

where g_s is the color charge of the quarks. Via comparison of the lifetime in electromagnetic and strong baryonic decays, the strong coupling can be

---

[1] $|\pi^+\rangle = |\mathrm{u}\overline{\mathrm{d}}\rangle$, $|\pi^-\rangle = |\mathrm{d}\overline{\mathrm{u}}\rangle$, $|\pi^0\rangle = \frac{1}{\sqrt{2}}\left(|\mathrm{u}\overline{\mathrm{d}}\rangle + |\mathrm{d}\overline{\mathrm{u}}\rangle\right)$

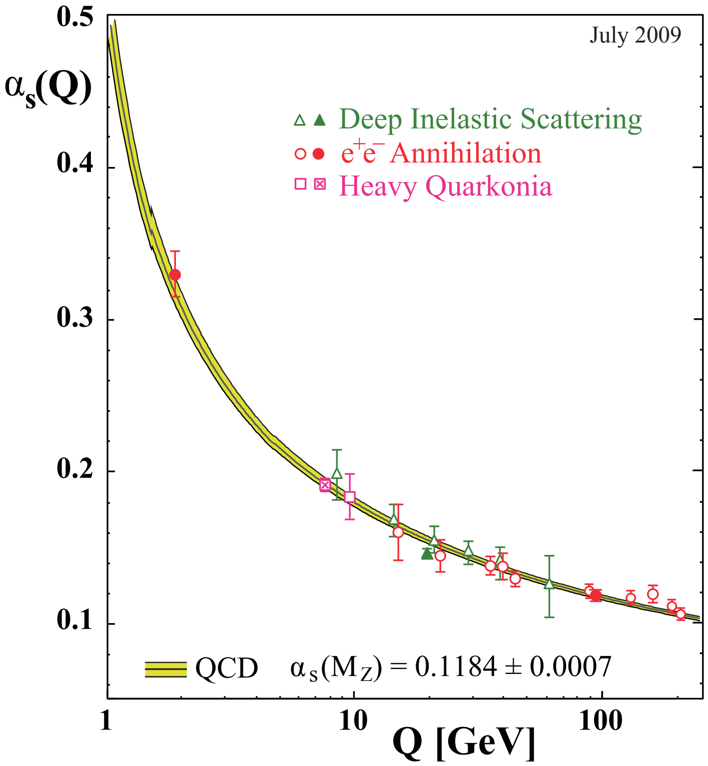

Figure 2.1: Strong coupling α_s as a function of the respective energy scale Q [Bet09].

roughly estimated to be about 100 times larger than the electromagnetic coupling [Per00]. However, this is only a crude estimate with decay energies of $Q \approx 100 - 200$ MeV.

The interaction of color charges is mediated by *gluons*, and the gauge group of QCD is the non-Abelian SU(3) with eight different gluons. As the mediator of the electromagnetic force, gluons are massless and electrically neutral. In addition, the gluons themselves carry a combination of color–anti-color. With three available colors, eight color–anti-color combinations[2] are possible and gluon states exist, respectively. As theory with gauge group SU(3) QCD is also called Yang-Mills theory, since a gauge theory based on special unity groups, SU(n), was first discussed by Yang and Mills [BW09]. The ultimate consequence of color charged gluons is that they interact among each other.

---

[2] $3^2 - 1 = 8$, as dimension of the SU(3). The colorless singlet $1/\sqrt{3}(r\bar{r} + b\bar{b} + g\bar{g})$ does not exist in SU(3).

This feature of the mediators is an essential difference in QCD compared to QED and is of fundamental relevance for the special character of the strong force.

Furthermore, the self-interaction leads to a disproportionate increase ($\alpha_\mathrm{s} > 1$) of the coupling for long distances r and small momentum exchange Q^2, respectively, while it becomes small ($\alpha_\mathrm{s} < 1$) for short distances and large momentum exchange. This phenomenon at short distances is called *asymptotic freedom*. The evolution of the strong coupling, α_s, as a function of the respective energy scale Q is shown in Figure 2.1. In general, the dependence of the strong coupling with the momentum exchange or distance is not only inverse to the electromagnetic coupling, the change is also more pronounced. However, α_s is always larger than α_em in all measured reactions so far.

The strong coupling is perturbatively calculable if $\alpha_\mathrm{s} \ll 1$, which is fulfilled for large momentum transfers considerable above the so-called QCD scale $\Lambda_\mathrm{QCD} \approx 200\,\mathrm{MeV}$. This was first solved by Gross, Wilczek and Politzer in 1973 [GW73; Pol73]. On that condition the running coupling is in leading order (LO) [BW09]:

$$\alpha_\mathrm{s}(Q^2) = \frac{12\pi}{(33-2N_f)\ln(Q^2/\Lambda^2_\mathrm{QCD})}, \qquad Q^2 \gg \Lambda^2_\mathrm{QCD}, \tag{2.5}$$

where N_f is the number of relevant quark flavors. This approximation becomes inaccurate for low Q^2 ($\approx Q_0^2 = 1\,\mathrm{GeV} > \Lambda^2_{QCD}$), where the strong coupling is not calculable anymore. Therefore no fundamental description of the color confinement exists. A phenomenological explanation shall be given with the QCD potential.

Contrary to the Coulomb potential of the electromagnetic force, the QCD potential does not simply evolve with $1/r$. It is rather described by [Per00]:

$$V_\mathrm{s} = -\frac{4}{3}\frac{\alpha_\mathrm{s}}{r} + kr, \tag{2.6}$$

where k is $0.85\,\mathrm{GeV\,fm^{-1}}$. At large distances r, the second term becomes dominant. Then the coupling energy between two quarks increases by 0.85 GeV per fermi. This derives from multiple gluon loops at larger distances due to the self-interaction, which can be imagined as a strong string between the quarks. This string grows with increasing distances and stores the energy which is necessary to depart the quarks. At some point, before the quarks could be separated, the energy is large enough to produce a new quark–anti-quark pair.

It is not possible to educe a free quark, they are confined in the color-neutral hadronic state.

Weak Interaction

The weak interaction affects all leptons and quarks, but its force is much weaker in comparison to electromagnetic or strong force. Therefore it is mostly relevant in reactions which are forbidden for other interactions. For example, the strong eigenstates of the quarks are mixed with respect to the weak interaction. Consequently, weakly interacting quarks can change their flavor, which is forbidden in strong interactions. Another unique characteristic is the coupling to neutrinos which do not interact via electromagnetic or strong force. Well known examples of particle decays caused by weak interaction are the nuclear β decay and the decays of the pion and the muon.

The weak interaction is described via the exchange of weak currents. It is distinguished between charged-current, which causes a change of the electric charges, and neutral-current with no exchange of electric charge. Accordingly, there are two charged gauge bosons ($W^{\pm}$, 80.4 GeV/c^2) and one neutral gauge boson (Z^0, 91.2 GeV/c^2) as mediators of the weak interaction. Due to the large masses of the gauge bosons the weak force has only a short range.

A formulation as QFT exists with the Weinberg-Salam-Glashow model. In the 1960s Weinberg, Salam and Glashow developed an unification of the electromagnetic interaction and the weak interaction to the electroweak interaction with gauge group SU(2)×U(1) [Gla61; Wei67; Sal80]. In their model the electroweak interaction with the four gauge bosons (photon, Z^0, $W^{\pm}$) is spontaneously broken at low energies ($Q^2 \lesssim 10^4\,\mathrm{GeV}^2$) [Per00].

Gravitational Interaction

Gravity is on small scales in the dimension of nuclei by far the weakest of all forces (Table 2.2). It has a long range, though, and becomes dominant on a cosmological scale. The mediator of the gravity couples to the mass. It is supposed to be the graviton, but it was neither detected yet nor does a fully formulated QFT of gravity exist. On scales which are relevant for high energy particles physics, the gravitational interaction can be neglected.

2.1.3 Beyond the Standard Model

The SM of particle physics has been tested with great success by experimental data over the last 40 years in most aspects. Nevertheless, there are some open questions and contradictions. For example, the SM does not comprehend a description of the gravitational interactions.

One of the most essential open questions of the SM is the existence of the Higgs boson. It is predicted and indispensable for the SM to explain the high masses of the $W^{\pm}$ and Z^0 bosons. The search for the Higgs is currently the main objective of the ATLAS and CMS experiments at the Large Hadron Collider (LHC). The most recent results hint to a Higgs around 125 GeV [ATL12; Cha+12a]. The confirmation or exclusion of the Higgs boson is expected at the latest after analysis of the full LHC 2012 data.

A widely discussed possible extension of the SM is the existence of supersymmetric (SUSY) partners for all existing particles [Per00]. This explicitly means that to each fermion a bosonic partner exists and vice versa. For example a *squark* $\tilde{\mathrm{q}}$ with spin 0 would exist, and a *photino* $\tilde{\gamma}$ with spin $\frac{1}{2}$ [Per00]. Actually, some SUSY particles are expected to have masses within the scope of the LHC. Up to now no possible SUSY particles have been found thus far.

2.2 Quark-Gluon Plasma

The topic of research of the ALICE experiment and motivation of this thesis is the quark-gluon plasma (QGP). It was predicted as a new state of quarks and gluons at extremely high energy density just after the formulation of QCD [CP75b; CP75a; BW09]. The name was established by Shuryak in 1978 [Shu78]. As discussed before, colored particles in nature are confined into color-neutral hadrons. Nevertheless, quarks and gluons can be considered as relevant degrees of freedom at sufficiently high temperature and/or high baryon density. This comes along with a phase transition from the hadronic to a quark-gluon phase which is the QGP, see Figure 2.2. Then the quarks and gluons cover path-lengths larger than the scale of a proton. The properties of QCD allow to infer the existence of such a phase transition, but it can as perturbation theory never describe the phase transition since this is intrinsically non-perturbative [YHM08].

This issue can be solved within a formulation of QCD that is discretized on a space-time lattice. The so-called lattice QCD approach [Wil74] predicts

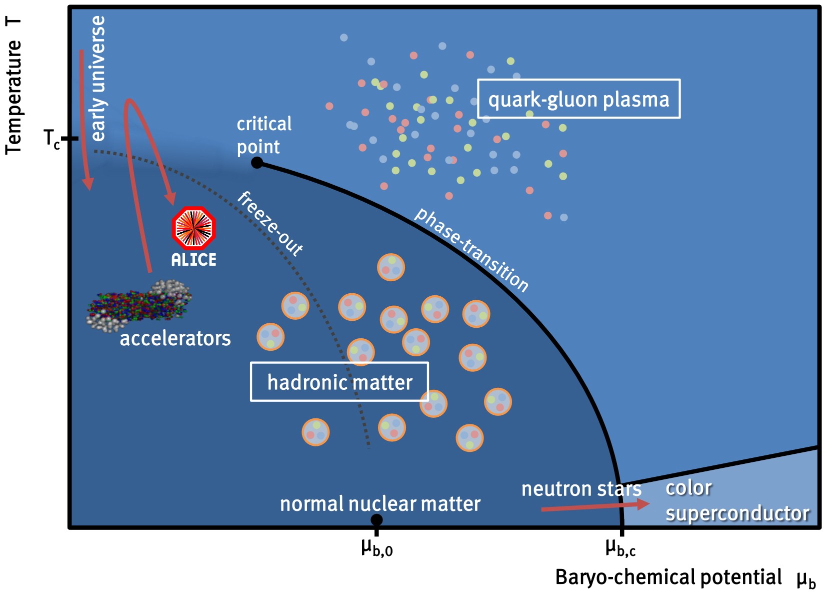

Figure 2.2: Sketch of a phase diagram of strongly interacting matter as function of temperature T and baryo-chemical potential μ_b. Shown is a first order transition between the hadronic matter and QGP up to a critical point. At lower μ_b a cross-over is supposed. How the phases are truly separated is part of present research, see e. g. [Phi11].

a transition from the hadron phase to the quark-gluon phase at an energy density of about $\epsilon_c = 1\,\mathrm{GeV/fm^3}$ [KL03]. In Figure 2.3, for a baryo-chemical potential of $\mu_b = 0$, a clear increase of the degrees-of-freedom is apparent in a transition region at $T \approx 150\,\mathrm{MeV}$ [Bor+10]. Corresponding energy densities are assumed to have existed in the early universe up to about 10 µs after the Big Bang [YHM08]. In the present universe, such energy densities are still expected in terms of high baryon density in the center of compact stars, like neutron stars. On earth it is supposed to be reached in the form of high temperature in collisions of ultra-relativistic, heavy nuclei. This is also shown in Figure 2.2, a corresponding schematical phase diagram as a function of temperature T and baryo-chemical potential μ_b with phase transition from hadronic matter to the QGP. The phase transition is predicted to be of first order up to a critical point. At lower μ_b a cross-over is expected [Aok+06]. Furthermore, for extremely high baryon density as can be reached in neutron stars, another

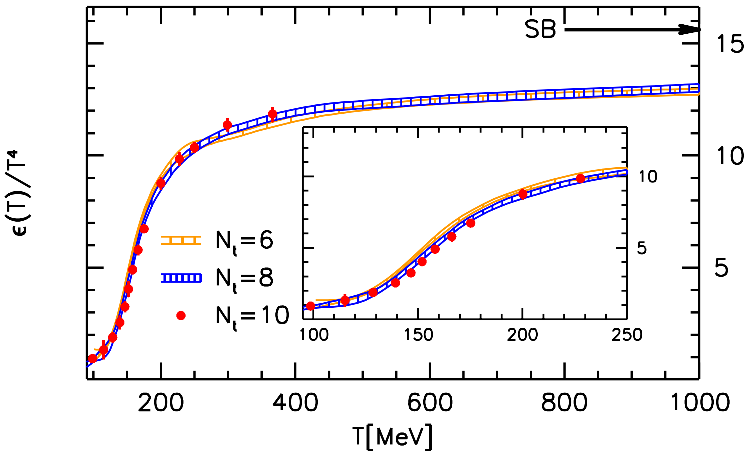

Figure 2.3: The energy density normalized by T^4 as function of temperature from lattice QCD calculations ($\mu_b = 0$). It is calculated for two light (up and down) and one heavier (strange) degenerated quark flavors ($n_f = 2+1$), for different resolutions of the lattice, noted by N_t. The Stefan-Boltzmann limit (SB) is indicated by an arrow. Taken from [Bor+10].

color superconducting state [Bar77; BW09] is possible. The exact view of this phase diagram is still speculative and topic of present experimental [STA10] and theoretical [Phi11] research.

Large heavy-ion accelerators allow the preparation of heavy-ion collisions in an experimental accessible environment. First evidence of a QGP was seen at the Super Proton Synchrotron (SPS) at the CERN in 1990s [HJ00]. Currently the QGP is studied at the Relativistic Heavy-Ion Collider (RHIC) at the Brookhaven National Laboratory (BNL) [Ars+05; Bac+05; Ada+05; Adc+05] and at the LHC at CERN [Aam+10b; Aam+10d; Cha+11a; Aad+10]. Experiments measure only color-neutral products of such collisions, due to the color confinement. Unfortunately, there is no explicit signature of the QGP. Only multiple different indications enrich the evidence of the production of a hot and dense phase with deconfined quarks and gluons. As an example, some of the signatures for a QGP which are discussed in [YHM08] are listed:

- Enhanced production of strangeness and charm.
- Increase of an elliptic flow (v_2).
- Modification of the properties of heavy mesons.

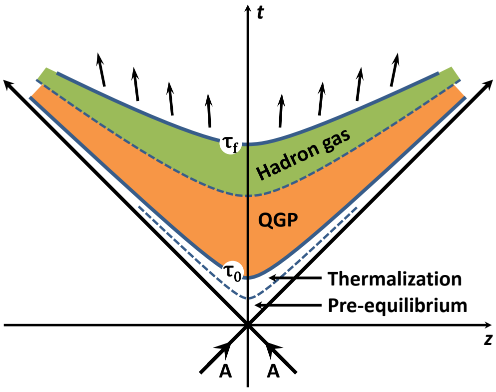

Figure 2.4: Longitudinal evolution of a heavy-ion (AA) collision in a space-time diagram. The angle bisector illustrate the colliding nuclei and their spectators (non-colliding nucleons). In between the matter evolves a pre-equilibrium and thermalization stage ($\tau < \tau_0$), the hydrodynamical evolution with the QGP ($\tau_0 < \tau < \tau_\mathrm{f}$), and the post-equilibrium stage ($\tau_\mathrm{f} < \tau$) after freeze-out of hadrons. Adapted from [YHM08].

- Enhancement of thermal and dileptons.
- Suppression of high p_t hadrons.

Figure 2.4 illustrates in a space-time diagram the evolution of the matter after a heavy-ion collision with the formation of a QGP. The evolution can be classified in three stages with transitions at proper time τ [YHM08]:

$0 < \tau < \tau_0$	pre-equilibrium stage and thermalization
$\tau_0 < \tau < \tau_\mathrm{f}$	hydrodynamical evolution and freeze-out
$\tau_\mathrm{f} < \tau$	freeze-out and post-equilibrium

The evolution of the matter directly after a collision is theoretically difficult to describe. At this point it shall be taken as a non-equilibrium, highly excited and virtual stage. First, real quarks and gluons come into being after the time of de-excitation τ_de. The time-scale can only roughly be given with $1\,\mathrm{fm}/c \approx 1/\Lambda_\mathrm{QCD}$ or much less [YHM08]. It varies with the momentum of the particles, since it is Lorentz dilated in the center-of-mass frame. The emerging partons start to interact and form a thermally equilibrated plasma, the QGP, at time $\tau = \tau_0$. This equilibrated stage is still expected to be reached within less than $1\,\mathrm{fm}/c$ [YHM08].

The QGP is a continuously expanding system, whose evolution can be described by relativistic hydrodynamics. With expansion it cools down and undergoes a phase transition at critical temperature T_c into the hadronic phase. For the time being the hadronic phase is still in local thermal equilibrium and inelastic interactions take place. Next, the produced hadronic particles are defined when the inelastic interactions stop. This is the chemical freeze-out. At thermal freeze-out, $\tau = \tau_\mathrm{f}$, the hadrons leave the equilibrium state, i. e. their free path length exceeds the system size. At this point, the shapes of the measured momentum spectra of the hadrons are also defined.

In a system where no QGP is formed, the partons from the thermalization directly freeze-out into an equilibrated hadron phase. Therefore a comparison of the chemical and kinematical composition of measured particles from pp (with a priori no QGP) and from central heavy-ion collisions (with presumably generated QGP) allow to draw some conclusions about the QGP state. An ansatz to study objects which are known to be produced only short time after impact and preferably before the formation of an equilibrated state is discussed in the next section.

2.3 Hard Probes and Jet Quenching

A valuable tool to obtain information about the QGP are so-called *hard probes*. These are hard-scattered partons with a momentum transfer, Q^2, well above the QCD scale ($\Lambda_\mathrm{QCD} \approx 0.2\,\mathrm{GeV}$). As the perturbative limit $Q_0 = \mathscr{O}(1\,\mathrm{GeV}) > \Lambda_\mathrm{QCD}$ [dEn09] can be chosen:

$$p_\mathrm{t}^\mathrm{hard} \geq \frac{Q_0}{c} > \frac{\Lambda_\mathrm{QCD}}{c}, \tag{2.7}$$

An advantage of these probes is that their cross-section can be calculated perturbatively. Therefore, they are also well suited for verification of QCD in pp collisions and well-calibrated probes in heavy-ion collisions. Furthermore, they are produced at time τ before the potential formation of a QGP at τ_0 [dEn09]:

$$\tau \leq \frac{\hbar c}{Q_0} \approx 0.2\,\mathrm{fm}/c < \tau_0. \tag{2.8}$$

Hence, they probe the QGP in its hottest and densest state.

In the case of no formation of a QGP, as it is the case in pp collisions, the hard-scattered partons of high virtuality branch, in vacuum, in a parton shower which finally hadronizes [Wie09]. The final state appears as collimated hadrons with high p_t, which can be identified as so-called jets. In ideal case, by jet reconstruction, the properties of the parent parton can be identified from the spray of hadrons. The fragmentation function (FF) encodes the perturbative aspects of the parton branching and the non-perturbative fragmentation process.

A hard scale cannot only be given by p_t but also by the mass $m \geq Q_0/c^2$. So-called heavy quarkonia, like J/Ψ ($\mathrm{c\bar{c}}$) or Y ($\mathrm{b\bar{b}}$), also originate from hard-scattered partons, independent of their momentum. As probes they bring the same advantage as high p_t partons. Nevertheless, in this work the reconstruction of jets is discussed, where the particle identification is of no relevance.

The cross-section for the production of a hadron h in a nucleus-nucleus collision produced by a hard scattering process is given by a convolution at leading order of

1. the parton distribution functions (PDFs), $f_\mathrm{a,A}$, $f_\mathrm{b,B}$, of the partons a and b in the colliding nuclei A and B,
2. the cross-section, $\mathrm{d}\sigma^\mathrm{hard}_\mathrm{ab\to cd}$, of the hard scatter ab → cd, and
3. the fragmentation function, $\mathscr{D}_\mathrm{c\to h}$, of parton c in hadron h ,

which results in [dEn09]

$$\begin{aligned}\mathrm{d}\sigma^\mathrm{hard}_\mathrm{AB\to h} =& f_\mathrm{a,A}(x_\mathrm{a}, Q^2) \otimes f_\mathrm{b,B}(x_\mathrm{b}, Q^2) \\ &\otimes \mathrm{d}\sigma^\mathrm{hard}_\mathrm{ab\to cd}(x_\mathrm{a}, x_\mathrm{b}, Q^2) \otimes \mathscr{D}_\mathrm{c\to h}(z_\mathrm{c}, Q^2) + \mathscr{O}(1/Q^2).\end{aligned} \tag{2.9}$$

x_a and x_b are the fractional initial momentum of parton a and b in the nuclei A and B, and $z_\mathrm{c} = p_\mathrm{h}/p_\mathrm{c}$ is the momentum fraction of the hadron h relative to the momentum of parton c. The PDFs and the FF are non-perturbative. They can be obtained from experimental measurements, for example from deep inelastic scattering (DIS) in electron-proton collisions, from electron-positron or proton-proton collisions. The cross-section of hard-scattered partons can directly be calculated from perturbative QCD (pQCD).

In the presence of a QGP, the fragmentation and consequently the hadron spectrum is expected to be modified. The hard-scattered partons traverse the hot and dense medium where they undergo multiple interactions and loose energy before the hadronisation. In the final state of measured hadrons this is visible as a suppression of high p_t particles (see Section 2.3.2). This suppression is called *jet quenching* [WG92], since high p_t hadrons are considered as (leading) particles of jets. For the leading parton, the interaction with the medium results in a concrete energy loss. Whereas jet reconstruction ideally recovers this energy from surrounding particles and the jet structure allows to study the mechanism of energy loss in the QGP in more detail. Though, in reality it can also happen that the energy is distributed outside the reconstructed jet area. Then the modified fragmentation pattern causes depletion or even extinction of reconstructed jets.

Two main methods are supposed for the energy loss:

1. elastic collisions with other partons in the medium, and
2. medium-induced gluon radiation.

In 1982, J. D. Bjorken had already noted “possible extinction of high p_t jets in hadron-hadron collisions” due to elastic scattering [Bjo82]. Today it is assumed that medium-induced gluon radiation (bremsstrahlung) is the dominant process of partonic energy loss in the QGP.

2.3.1 Models of Energy Loss in QGP

A phenomenological and successful model of medium-induced partonic energy loss and consequent changes of the jet structure is the BDMPS model [Bai+97b; Bai+97a]. This model was proposed by R. Baier, Yu. L. Dokshitzer, A. H. Mueller, S. Peigné, and D. Schiff in 1996. They assume multiple soft scatterings at various scattering centers in a colored medium [dEn09]. With each interaction, the parton splits into an outgoing parton and a radiated gluon. The resulting gluon spectrum is $\omega \mathrm{d}I/\mathrm{d}\omega$, which integrates to an average energy loss of [Bai03]:

$$\Delta E = \int^{\omega_c} \frac{\omega \mathrm{d}I}{\mathrm{d}\omega} \cong \alpha_s \omega_c, \tag{2.10}$$

with the characteristic gluon energy

$$\omega_c = \frac{1}{2}\hat{q} L^2. \tag{2.11}$$

L is the traversed length and system size, respectively. The opacity of the medium for the colored parton is defined by the transport coefficient [Bai03]:

$$\hat{q} = \rho \int \mathrm{d}^2 q_\mathrm{t} q_\mathrm{t}^2 \frac{\mathrm{d}\sigma}{\mathrm{d}^2 q_\mathrm{t}}. \tag{2.12}$$

where ρ is the density of the medium and σ the cross section of the gluon-medium interaction with momentum exchange of q_t. For cold nuclear matter, the transport coefficient is very small ($\hat{q} \approx 0.05\,\mathrm{GeV}^2/\mathrm{fm}$). For a QGP with an energy density of $\epsilon \approx 50 - 100\,\mathrm{GeV/fm}^3$, as it is expected at the LHC, the transport coefficient is estimated to be as large as $\hat{q} \approx 100\,\mathrm{GeV}^2/\mathrm{fm}$ [Acc+03].

With a model by Armesto, Salgado, and Wiedemann (ASW) the probability $P_E(\varepsilon;\hat{q})$ can be calculated that a proton loses a fraction $\varepsilon = \Delta E/E$ of its energy in a medium with transport coefficient $\hat{q}$. The expected medium-modified fragmentation function is for such a medium then [dEn09]:

$$\mathscr{D}^\mathrm{med}_{\mathrm{i}\to\mathrm{h}}(z', Q^2) = P_E(\varepsilon;\hat{q}) \otimes \mathscr{D}^\mathrm{vac}_{\mathrm{i}\to\mathrm{h}}(z, Q^2). \tag{2.13}$$

The predictions from those models can be tuned to experimental measurements. Two common experimental observables to quantify the energy loss are introduced in the next two sections. The first measurement is based on the single hadron production, the second is an approach to directly measure the fragmentation pattern via jet reconstruction.

2.3.2 Nuclear Modification Factor $\mathbf{R}_\mathrm{AA}$

The nuclear modification factor R_AA measures the suppression of hadrons in heavy-ion collisions compared to proton-proton (pp) collisions. The yield of hadrons in heavy-ion collisions is scaled by the average number of binary nucleon-nucleon collisions, $\langle N_\mathrm{coll}\rangle$. It is derived from the Glauber model [Mil+07] for an impact parameter b which corresponds to the considered collision centrality. The nuclear modification factor can then be written as [Aam+11c]:

$$R_\mathrm{AA}(p_\mathrm{t}) = \frac{1}{\langle N_\mathrm{coll}\rangle} \frac{\left(1/N^\mathrm{AA}_\mathrm{evt}\right) \mathrm{d}^2 N_\mathrm{AA}/\mathrm{d}\eta \mathrm{d}p_\mathrm{t}}{\left(1/N^\mathrm{pp}_\mathrm{evt}\right) \mathrm{d}^2 N_\mathrm{pp}/\mathrm{d}\eta \mathrm{d}p_\mathrm{t}}. \tag{2.14}$$

The hadron yields are in general normalized to the pseudo-rapidity interval $\mathrm{d}\eta$. By means of the Glauber model the number of binary nucleon-nucleon

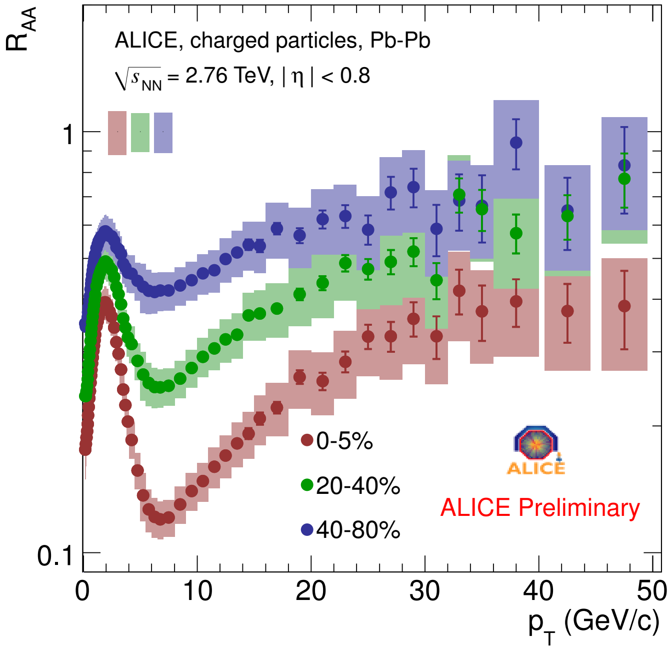

Figure 2.5: Nuclear modification factor R_{AA} for charged particles in three different centrality intervals of Pb–Pb collisions at $\sqrt{s_{\rm NN}} = 2.76\,\text{TeV}$ [App11].

---

collisions is $N_{\rm coll} = T_{\rm AA}\sigma_{\rm pp}^{\rm inel}$, whereas $T_{\rm AA}$ is the nuclear overlap function for the impact parameter b. Often directly the average overlap function, $\langle T_{\rm AA}\rangle$, is used together with the hadron cross-section in pp collisions, $\mathrm{d}\sigma_{\rm pp}^{\rm inel}/\mathrm{d}p_{\rm t}$, in place of the hadron yield.

$R_{\rm AA}$ is smaller than one at high $p_{\rm t}$ if the hadron production is suppressed, which can be interpreted as energy loss of the originating partons. In case of no modification $R_{\rm AA}$ is unity. This principle can be tested with electromagnetic probes that do not couple strongly to the QGP, like direct photons.

Recent measurements at the LHC [Aam+11c; App11; Cha+12b] show a strong suppression ($R_{\rm AA} \approx 0.12$ at $p_{\rm t} = 6-8$ GeV/c [App11]) in central lead-lead (Pb–Pb) events, see Figure 2.5. These measurements from collisions at $\sqrt{s_{\rm NN}} = 2.76\,\text{TeV}$ suggest the creation of a denser medium as it was produced in former experiments at RHIC with lower collision energies [Adl+04; Ada+03]. The harder underlying parton spectrum at the LHC also provides more details about the actual energy loss mechanisms [Ren+11]. Nevertheless, the measurement of single high-p_t hadrons has only limited sensitivity to a dense QGP [Esk+05]. Most of the measured hadrons are expected to originate from partons close to the surface of the nuclear overlap region. This is also known as *surface bias*.

A first step to overcome this is the measurement of two-particle azimuth-correlations [Aam+12b]. While the trigger particle is strongly surface biased, the away-side parton do traverse through the medium [Kle11a]. An even more conclusive picture and tomography of the QGP is expected from full jet reconstruction. Its aim is to trace the fragmented hadrons back to the parent parton. Jet reconstruction also provides some insight in the fragmentation process via the jet structure, whose measurement is discussed in the next section.

2.3.3 Jet-Structure Observables

Full jet reconstruction experimentally provides the most direct link to the hard-scattered parent parton. It is less biased by the actual fragmentation process than single hadron measurements and the medium is probed in its earliest stage. On the other side, jet reconstruction is more restricted by the soft underlying event. Besides some preliminary studies at RHIC in the last years, single-hadron and hadron-correlation measurements were the only promising approach to measure the jet quenching in experiments before the LHC-era. With LHC energies, due to the harder parton spectrum, jet reconstruction is possible in heavy-ion collisions with rates large enough for detailed studies for the first time. Details about the jet reconstruction in ALICE and the impact of the underlying event in heavy-ion collisions are discussed in Chapter 4 and Chapter 7.

Once event-by-event jet reconstruction is possible, it enables the study of the jet structure with largest sensitivity to the fragmentation process and properties of the medium. A basic observable of the jet structure is the fragmentation function, which measures the longitudinal jet pattern:

$$F(z) = \frac{1}{N_\mathrm{jet}} \frac{\mathrm{d}N}{\mathrm{d}z}, \qquad \text{where} \qquad z = \frac{p_\mathrm{t}^\mathrm{particle}}{p_\mathrm{t}^\mathrm{jet}}. \tag{2.15}$$

$F(z)$ quantifies the fractional particle p_t distribution in relation to the jet p_t. This is done in the first part of analysis in this thesis for pp collisions, which is shown in Chapter 5. Since only charged tracks are reconstructed in the presented studies, strictly speaking not the full fragmentation function is measured, in terms of $\mathscr{D}_{\mathrm{c}\to\mathrm{h}}(z_{\mathrm{c}})$ in Equation 2.9. Though the measurement is biased and the energy scale shifted, the analysis procedure and physics interpretation is the same as for the fragmentation function $\mathscr{D}$. In comparison of pp to heavy-ion collisions, $F(z)$ should demonstrates the decrease of the number of particles with high p_{t} and high z and the simultaneous increase of the number of particles with low p_{t} and low z due to the partonic energy loss.

Perturbative QCD calculations predict a depletion of particles with small z, due to angular ordering of the partonic branching process and QCD coherence [Dok+91; Dok+88; Azi+86]. On a $\ln(1/z)$ scale the hadron spectrum form a close to Gaussian shape. The maximum is based on the perturbative limit Q_0 and can be further constrained by the opening angle of the cone. A consequence is a shifted maximum towards a softer distribution with increasing jet energy. A measurement of the fragmentation pattern as function of

$$\xi = \ln\left(\frac{1}{z}\right) = \ln\left(\frac{p_{\mathrm{t}}^{\mathrm{jet}}}{p_{\mathrm{t}}^{\mathrm{track}}}\right), \tag{2.16}$$

allows a careful measurement of the branching process. The distribution was introduced and is known as *hump-backed plateau* [DFK82]. Figure 2.6 shows $\mathrm{d}N/\mathrm{d}\xi$ distributions which were measured at the OPAL and TASSO experiments together with respective theoretical predictions from the modified leading logarithmic approximation (MLLA) approach for fragmentation in vacuum and in medium.

In view of the medium-modified fragmentation pattern, the distribution of ξ is convenient because it emphasizes the soft momentum component of the jet. It is mainly sensitive to the expected enhancement of multiplicity at high ξ, as visible in Figure 2.6 [BW05]. The relation between ξ, z and fragment p_{t} for some specific jet p_{t} is given in Table 2.3.

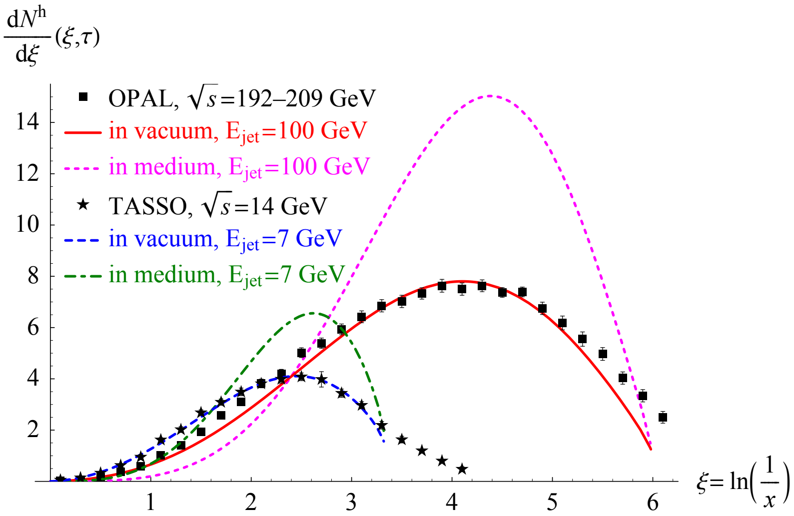

Figure 2.6: Measured jet fragmentation from the OPAL and TASSO experiments and appropriate MLLA calculations, in vacuum and in presence of a medium. Taken from [BW05].

Table 2.3: $\xi = \ln(1/z) = \ln(p_t^{jet}/p_t^{track})$.

ξ	0	1	2	3	4	5	6	7
z	1.0	0.37	0.14	0.05	0.018	0.0067	0.0025	0.0009
jet p_t (GeV/c)	track p_t (GeV/c)							
20	20.0	7.4	2.7	1.0	0.37	0.13	0.05	0.02
40	40.0	14.7	5.4	2.0	0.73	0.27	0.10	0.04
60	60.0	22.1	8.1	3.0	1.10	0.40	0.15	0.05
80	80.0	29.4	10.8	4.0	1.47	0.54	0.20	0.07
100	100.0	36.8	13.5	5.0	1.83	0.67	0.25	0.09
150	150.0	55.2	20.3	7.5	2.75	1.01	0.37	0.14
200	200.0	73.6	27.1	10.0	3.66	1.35	0.50	0.18

Chapter 3

Experimental Environment

3.1 The Accelerator: Large Hadron Collider

The ALICE experiment (described in the next section) is located at the Large Hadron Collider (LHC) [EB08] at CERN[1], Geneva. It is, together with ATLAS[2] [Aad+08], CMS[3] [Cha+08], and LHCb[4] [Alv+08], one of the four big experiments at the LHC. The LHC is the world's largest accelerator for hadrons with a circumference of 26.7 km in a tunnel between 45 m up to 170 m below the surface. It is operated with superconductive dipole magnets with up to 8.33 T at the nominal beam energy of 7 TeV. The magnets are cooled by superfluid helium to 1.9 K. The LHC is supported by various pre-accelerators, like PS (Proton Synchrotron) and SPS (Super Proton Synchrotron), see Figure 3.1.

The LHC can accelerate either protons for proton-proton (pp) collisions or stripped heavy-ions, like $^{208}\text{Pb}^{82+}$, for the heavy-ion program. The nominal peak luminosity is $10^{34}\,\text{cm}^{-2}\text{s}^{-1}$ with 2802 bunches of $1.1 \cdot 10^{11}$ protons each. For ALICE, the luminosity is limited to $10^{30}\,\text{cm}^{-2}\text{s}^{-1}$ by colliding less bunches than at the other experiments and by displacing the beams. For the heavy-ion runs, the maximum luminosity is $10^{27}\,\text{cm}^{-2}\text{s}^{-1}$ with 592 bunches of $7.0 \cdot 10^{7}$ Pb ions each.

The LHC provided the first proton-proton (pp) collisions in November 2009. First lead-lead (Pb–Pb) collisions were delivered by the LHC in November 2010. In the first two years, the LHC was running with half of the nominal beam

---

[1] European Organization for Nuclear Research

[2] A Toroidal LHC ApparatuS

[3] Compact Muon Solenoid experiment

[4] Large Hadron Collider beauty experiment

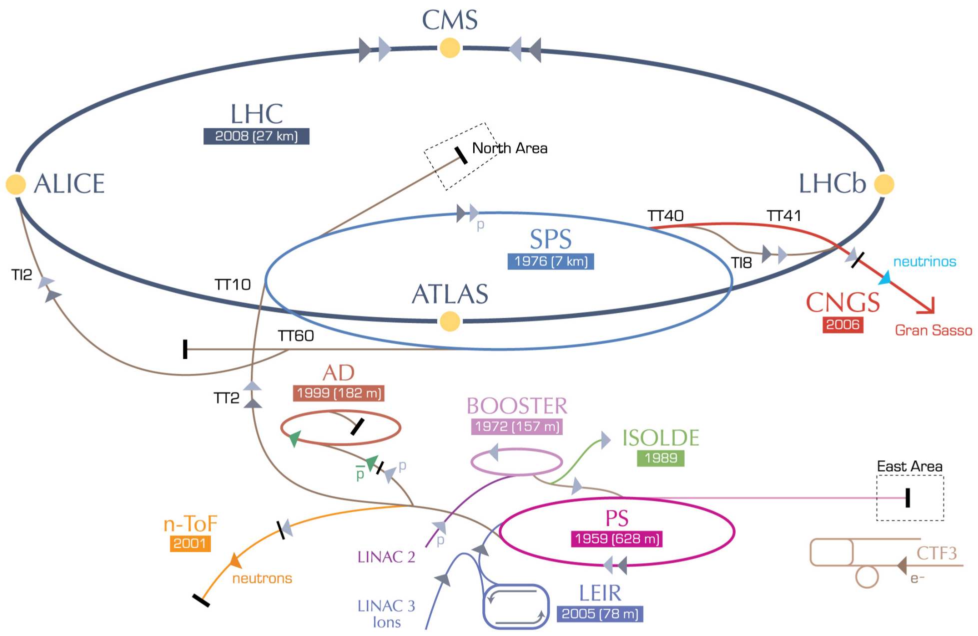

Figure 3.1: CERN's accelerator complex. SPS, PS, plus LEIR and LINAC 3 (ions) or BOOSTER and LINAC (protons) are used as pre-accelerator for the Large Hadron Collider (LHC). Image taken from [CDS].

energy, i.e. collision energy of $\sqrt{s} = 7$ TeV in pp collisions and a collision energy per nucleon-nucleon (NN) pair of $\sqrt{s_{\rm NN}} = 2.76$ TeV in Pb–Pb collisions.[5] Some data at lower energy has been taken as well, like pp collisions at injection energy $\sqrt{s} = 900$ GeV and intermediate energy $\sqrt{s} = 2.76$ TeV for comparison with Pb–Pb data. Since the beginning of the run period in 2012 the collision energy is $\sqrt{s} = 8$ TeV (pp). End of 2012 p–Pb collisions are scheduled, before a shutdown of about 1.5 years is planned for maintenance and upgrades to allow collisions with the design energy.

Analyses in this thesis use data which was taken with the ALICE experiment from first year's (2010) pp collisions at $\sqrt{s} = 7$ TeV and Pb–Pb collisions at $\sqrt{s_{\rm NN}} = 2.76$ TeV.

---

[5] $s \equiv (p_a + p_b)^2$ is one of the Mandelstam variables (s,t,u), where p_a and p_b are the four-momenta of the incoming particles a and b. Then $\sqrt{s}$ equates to the total energy in the center-of-mass frame [YHM08].

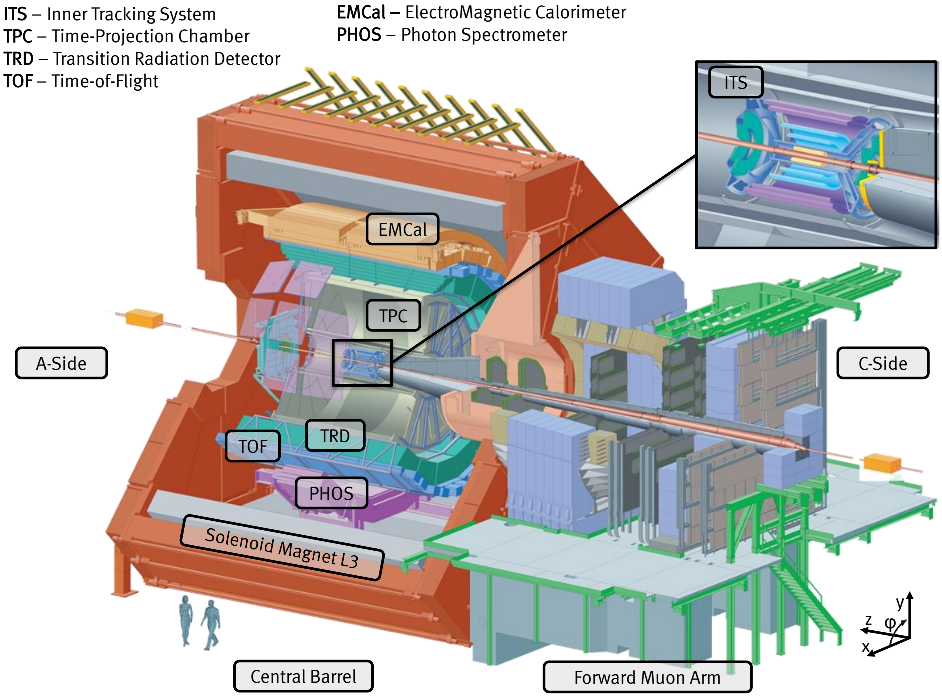

Figure 3.2: Schematic setup of ALICE. Only the largest detectors of the central barrel are labeled.

3.2 The Experiment: A Large Ion Collider Experiment

ALICE (A Large Ion Collider Experiment) [Aam+08] is the dedicated experiment for heavy-ion collisions at the LHC. It is built for good tracking capabilities of charged particles from very low transverse momentum ($p_\mathrm{t} = 150\,\mathrm{MeV}/c$) to high transverse momentum above $100\,\mathrm{GeV}/c$ with excellent particle identification in a high multiplicity environment (up to $\mathrm{d}N_\mathrm{ch}/\mathrm{d}\eta = 8\,000$) at mid-rapidity. ALICE is basically divided in the central barrel detectors and the forward muon arm, as described in the following sections.

In the local coordinate system of the experiment, the Cartesian coordinate's origin is located at the nominal bunch-crossing point in the center of the L3 magnet. The x-axis points to the center of the LHC circuit, the y-axis upwards, and the z-axis in beam direction away from the muon-arm (see Figure 3.2).

Due to the cylindrical orientation of the detectors around the beam-pipe, the azimuth angle ϕ in the (x,y) plane is often used, which is zero at the x-axis. Instead of the θ angle in (y,z) plane the usage of pseudo-rapidity [YHM08]

$$\eta = -\ln(\tan(\theta/2)) \tag{3.1}$$

is common in high-energy collision experiments. The pseudo-rapidity describes the orientation of a particle with respect to the beam axis:

$$\eta = \frac{1}{2}\ln\left(\frac{p+p_{\mathrm{L}}}{p-p_{\mathrm{L}}}\right), \tag{3.2}$$

where p is the particle's momentum and p_{L} the longitudinal component of the momentum. For particles with high transverse momentum, p_{t}, (with rest mass $m_0c \ll p_{\mathrm{t}}$) the pseudo-rapidity η is equivalent to the rapidity

$$y = \frac{1}{2}\ln\left(\frac{1+\beta}{1-\beta}\right), \tag{3.3}$$

where $\beta = v/c$.

The side of the experiment in counter-clock direction of the beam-pipe $(+z)$ is called "A-side" and in clock direction $(-z)$ "C-side". Further there is the "I-side" inwards of the LHC $(+x)$ and the "O-side" outwards of the LHC $(-x)$. As is described in the next section, some of the major detectors in the central barrel are segmented in 18 azimuth sectors. They are numbered consecutively with increasing ϕ, beginning with zero at $\phi = 0$.

3.2.1 Central Barrel Detectors

The central barrel detectors are arranged in a solenoid magnet with an inner radius of 5.93 meters. The magnet was inherited from the L3 experiment at the former LEP accelerator. The nominal magnetic flux of the L3 magnet is 0.5 T.

The main detectors of ALICE are cylindrically arranged around the beam pipe, with the bunch crossing point of both beams in the center. With full coverage in azimuth and a pseudo-rapidity range of at least $|\eta| < 0.9$ there are—from inner to outer—the Inner Tracking System (ITS), the Time Projection Chamber (TPC), the Transition Radiation Detector (TRD), and the Time-Of-Flight (TOF) detector. They are the tracking devices for charged tracks at mid-rapidity.

Other detectors with smaller acceptance are the electromagnetic calorimeter (EMCAL) ($|\eta| < 0.7$, $80° < \phi < 190°$), the photon spectrometer (PHOS) ($|\eta| < 0.12$, $220° < \phi < 320°$), the High-Momentum Particle Identification Detector (HMPID) which is a ring imaging Cherenkov detector, and other smaller detectors within the L3 magnet.

Inner Tracking System

The Inner Tracking System (ITS) [Aam+10a] is a composite of three times two layers of different silicon detectors. With a radius of 3.9 cm of the first layer, the ITS is the closest detector system to the beam pipe. The two innermost layers are Silicon Pixel Detectors (SPD), the next two layers are Silicon Drift Detectors (SDD), and the outermost two layers are Silicon Strip Detectors (SSD). The last layer has a radius of 43.0 cm. They cover at least a pseudo-rapidity range of $|\eta| < 0.9$ over the full azimuth. The innermost layer has a wider acceptance in pseudo-rapidity of $|\eta| < 1.98$.

The aim of the ITS is a good tracking resolution close to the interaction point in order to improve the track momentum resolution and a precise reconstruction of the primary vertex and secondary vertices from heavy flavor decays. In addition, the SPD works together with the VZERO detector (which is described later in this section) as minimum-bias trigger (see Section 3.5.2).

Time Projection Chamber

The Time Projection Chamber (TPC) [Alm+10] is the main tracking detector of ALICE for charged particles. The active volume has an inner radius of about 0.85 m, an outer radius of about 2.46 m, and a length along the beam direction of about 5.00 m. This results in an active volume of nearly 87 m^3, making it the world-largest time projection chamber. The TPC is filled with a $\mathrm{Ne} - \mathrm{CO}_2 - \mathrm{N}_2$ (85.7%–9.5%–4.8%) gas mixture. The volume is separated at the center of the chamber, at $\eta = 0$, by a 100 kV electrode for an axial drift field of 400 V/cm. At both end plates the chamber is read-out. These end plates are segmented in 18 (azimuth) sectors, with one inner (IROC) and one outer (OROC) readout wire chamber each. The maximum drift time is 94 µs.

For full tracking length, the TPC covers a pseudo-rapidity of $|\eta| < 0.9$. The TPC is used for tracking and particle identification via energy deposition $\mathrm{d}E/\mathrm{d}x$. It is the next detector to the beam-pipe (in radial distance) after the inner tracking system.

Transition Radiation Detector

With a distance of 2.90 meters to the beam pipe the Transition Radiation Detector (TRD) [Cor01] is the next detector after the TPC. The TRD is built up of multi-wire proportional chambers with included radiators for highly relativistic particles. The transition radiation enables the electron-pion separation at high p_t ($> 1\,\mathrm{GeV}/c$). As a multi-wire proportional detector and with an extended tracking path, the TRD improves the momentum resolution, especially for high p_t tracks. In addition, the TRD is with its short drift time of only $2\,\mu\mathrm{s}$ and highly parallel read-out a dedicated trigger detector. It can be used as high p_t hadron trigger, e.g. for jets, or electron trigger, e.g. for heavy flavor particles, like J/Ψ and others.

Since studies of the TRD as a jet trigger are presented and discussed in this work (Chapter 6), the detector and its read-out capabilities are described in more detail in Section 3.4.

Time-Of-Flight Detector

The Time-Of-Flight (TOF) detector [Del+00] measures with a resolution of about 40 ps the time of traversing charged particles in a radial distance from the beam-pipe of 3.77 meters. The start signal (collision time) is provided by the T0 detector (see below). From the measured time-of-flight, the track length and the particle's momentum the mass of the particle can be determined. This facilitates the particle identification, especially of pions, kaons and protons, in the intermediate p_t range of a few GeV/c.

TOF is the last detector in the central barrel which covers the full azimuth and the pseudo-rapidity range of $|\eta| < 0.9$. With a distance of 3.77 meters to the beam-pipe it sits behind the TRD. The outer radius is 3.99 m. Just as the TRD, also TOF consists of 18 super modules (SMs) in azimuth. They are build-up with multiple individual Multi-gap Resistive-Plate Chambers (MRPCs) over an active length of 7.41 m. The 10-gap double-stack MRPCs do not have drift regions only amplification regions. That gives from traversing, ionizing particles well peaked signals without tails, as it is otherwise common in gaseous detectors.

T0 and V0 Detector

The T0 and V0 detectors are the only detectors outside the central rapidity region that shall be mentioned here in more detail, since they are important trigger detectors and the V0 detector is used in this thesis for event plane measurements. Furthermore, the V0 is used to estimate the collisional centrality in heavy-ion collisions.

The **V0** (or VZERO) detector consists of two arrays of scintillator counters, called V0A for the array at A-side and V0C for the array at C-side of the experiment. V0A covers the pseudo-rapidity $2.8 < \eta < 5.1$ and V0C the pseudo-rapidity $-3.7 < \eta < 1.7$. Each of the two arrays is segmented in 32 individual counters, arranged in 8 azimuthal sectors and 4 radial rings.

The **T0** detector consists of two arrays of Cherenkov counters in a distance of only 72.7 cm from the nominal vertex at C-side (T0-C) and about 3.75 m at A-side (T0-A). They cover a pseudo-rapidity of $-3.28 < \eta < -2.97$ (T0-C) and $-4.61 < \eta < -4.92$ (T0-A). Both arrays are each built up of 12 photomultiplier counters coupled to a quartz radiator. The T0 detector provides a start signal (time of collision, T0) to the TOF.

T0 and V0 detector signals are used by the pre-trigger system, which provides a wake-up signal to the TRD. This is further discussed in Section 3.4.

3.2.2 Forward Detectors

Besides the central barrel detectors, a system of trigger and tracking detectors in the forward rapidity ($-4.0 < \eta < -2.5$) region also exists. They are placed behind a massive absorber and a dipole magnet outside of the L3 solenoid with the intention to detect muons. The complete arrangement is called *muon arm*. It is not further discussed in this thesis.

3.2.3 Other Detectors

In addition to the detectors mentioned in the previous sections, some smaller detectors belong to ALICE, mostly at larger pseudo-rapidity, like the Zero Degree Calorimeter (ZDC), the Photon Multiplicity Detector (PMD), the Forward Multiplicity Detector (FMD), and the ALICE Cosmic Ray Detector (ACORDE). They are of no or only little relevance for this thesis. Such as the information of some of these detectors is used for the physics event selection, which is provided by the AliRoot framework (Section 3.5). The energy deposition in the ZDC, for example, can be used as an additional measurement of the event centrality in heavy-ion collisions. The main method is with the VZERO detector.

3.3 ALICE Trigger System

The ALICE experiment is composed of 18 different detector types with different rate capabilities, data output, requirements of start signals, and aim of physics signals (e. g. rare or bulk observables). The challenge of the trigger system is to provide all detectors with start signals in case of physically interesting events and otherwise minimize the overall dead time of the detectors and the amount of recorded data on storage elements. The trigger decision logic is provided by the Central Trigger Processor (CTP) [Fab+04; Vil+07; Bha+07]. The CTP receives the trigger input and busy signal from the individual detectors via their Local Trigger Units (LTUs). It evaluates the trigger inputs and the decision is send to the LTUs of the detectors again.

The ALICE trigger system has a temporal sequence of four different trigger levels: Level-0 (L0), Level-1 (L1), Level-2 (L2), and the High-Level Trigger (HLT). This facilitates the trigger system to receive trigger inputs from different detectors and provide them with trigger decisions according to their individual capabilities, especially what concerns their read-out and busy time. The CTP has 60 inputs (L0: 24, L1: 24, L2: 12) for the trigger signals from detectors. Not all detectors have an input at each trigger level, some can provide multiple triggers. From the trigger inputs, the trigger decision is independently determined for up to 50 *trigger classes*, which are groups of detectors with a required trigger signature. Is the trigger decision positive for a trigger class, only detectors which are part of this class are read-out. Detectors can be part of more than one trigger class. That allows, for example, separate trigger setups for faster detectors with special trigger requests, e. g. the muon arm, or individual trigger for some detectors for calibration or standalone runs.

A trigger class is activated by the L0 signal. With each following trigger level the CTP receives new inputs from the trigger detectors. The detectors await a positive decision within a defined time, otherwise they abort the read-out process and are ready for the next event. A purposive trigger *accept* (L2a) or *reject* (L2r) is send by the CTP only at L2. In Table 3.1, the latencies after a collision are specified for all trigger levels within which the input from the

Table 3.1: Latencies of the trigger signals after a collision.

trigger level	at CTP	at detectors
L0	0.8 µs	1.2 µs
L1	7.3 µs	7.7 µs
L2	94 µs	–[6]

detectors is required at the CTP, and the decision of the CTP is expected at the detectors.

Only the fastest detectors can provide a trigger contribution within 0.8 µs (L0) after the collision to the CTP. This are e. g. VZERO, SPD, and TOF. The trigger set-up at this stage is quite elementary, like multiplicity or centrality trigger. Also periodical trigger on random bunch-crossings (BCs) do contribute to L0.

The time scale of the L1 trigger signals (7.3 µs [Kle11d]) already allows more complex trigger conditions with the aim to select specific signatures. These can be resonances or jets. For example, the TRD and EMCAL contribute to the L1. Based on the L1 trigger, the TPC is read-out. Hence, the collective L1 accept rate is limited by the maximum TPC read-out rate. The L1 latency time limits the sensitivity of the TPC in terms of the radial distance to the beam pipe. The drift time of the TPC of 94 µs defines the earliest time of the L2 response. At that level a past-future protection against pile-up is implemented. In case the pile-up is too large the event is rejected. This is actually the last level of the conventional hardware trigger.

The HLT is another type of trigger which runs after complete detector read-out with the data from the major detectors fully available on a computer cluster in a counting room next to the pit of the ALICE experiment. The HLT carries out an online, full event building, even though still simplified, and runs some physics analyses. Based on the results, the event will be fully or partially (region of interest (RoI)) written on tape or discarded. Also data compression is provided by the HLT. The aim of the HLT is an efficient use of storage elements; there is no improvement of the detector busy times. The maximum allowed data stream written to mass storage is 1.25 GB/s, about 10 % of the data read-out in Pb–Pb collisions at nominal luminosity.

---

[6] The L2a/L2r is generated latest 4096 nominal bunch crossings, i. e. 102.4 µs, after the L1 decision. But it is sent with low priority only and can have some delay before it arrives at the LTUs [Fab+04].

The TRD is fast enough to provide a L1 trigger signal [Kle11d]. However, it needs a wake-up signal before the L0 trigger and at a lower rate than the nominal bunch-crossing rate. Therefore the TRD has its own so-called *pre-trigger (PT)* system which is independent of the central trigger system. The wake-up signal is necessary since the TRD goes in stand-by, to minimize the heat dissipated by the read-out electronics, whenever there is no event and the TRD is not read-out. For low latency, the complete pre-trigger system is located within the solenoid magnet. It provides the TRD with a wake-up signal within 200 ns after the interaction, based on signals from TOF, VZERO, and T0 which are directly linked with the PT electronics. The maximum PT rate sent to the TRD read-out boards is 100 kHz. In the ideal case the PT replicates the L0 trigger decisions as good as possible to ensure an efficient running of the TRD.

The nominal pp beam luminosity is $\mathscr{L} = 10^{30}\,\mathrm{cm}^{-2}\mathrm{s}^{-1}$ [EB08] at the ALICE interaction point. Assuming an inelastic cross section of roughly $\sigma_{\mathrm{MB}} \approx 80\,\mathrm{mb}$ [MBD07] at nominal collision energy ($\sqrt{s} = 14\,\mathrm{TeV}$), the minimum-bias interaction rate is of the order of

$$R = \mathscr{L} \cdot \sigma_{\mathrm{MB}} \approx 80\,\mathrm{kHz}. \tag{3.4}$$

As approximation a minimum bias (L0) rate of 100 kHz, which is equal to the maximum TRD pre-trigger rate, is considered for the trigger studies in Chapter 6. That assumes a fully efficient pre-trigger, which also depends on the filling scheme of the LHC. For L1 the rate needs to be reduced to 1 kHz (maximum TPC read-out rate). Hence, at least a rejection factor of 100 is required. For an individual physics L1 trigger, like a jet trigger, the desired rejection factor is 10^4 or more, not to exhaust the whole L1 bandwidth by a single trigger input.

3.4 ALICE Transition Radiation Detector

Once it is fully installed, the Transition Radiation Detector (TRD) [Cor01] will be made up of 522 individual detector chambers. They are arranged in 18 super modules (SMs), one SM per azimuthal segment. The SMs occupy a radial position between 2.90 and 3.68 m, with an active length in beam direction of 7 meters. That gives a coverage in pseudo-rapidity of $|\eta| < 0.84$. Each SM consists of 30 chambers, in five stacks along the beam direction (z) and six layers in radial direction. Three SMs in the sectors in front of PHOS

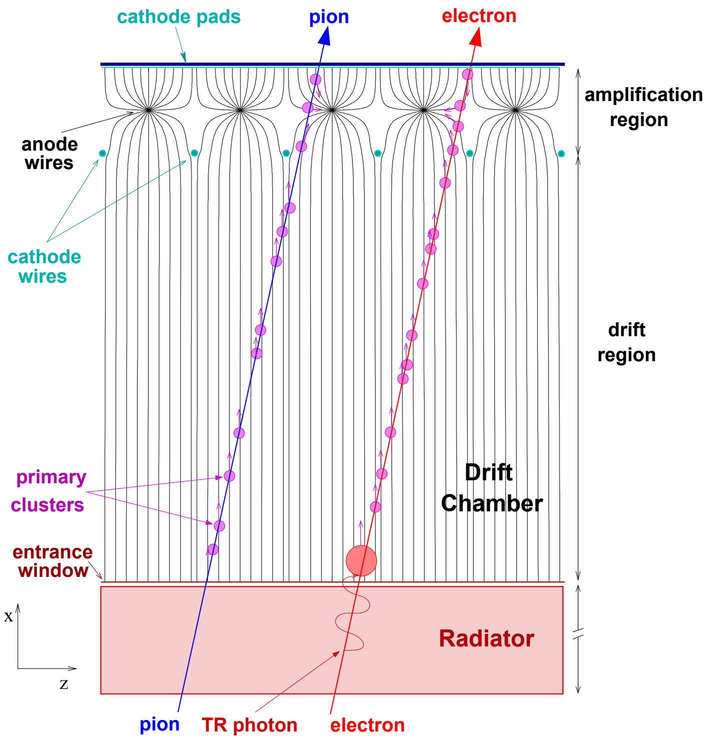

Figure 3.3: Section view of a TRD chamber with an illustration of the charge deposit of an electron and a pion. In case of the high p_t electron ($\gamma \gtrsim 1000$), in the radiator X-ray photons are produced which leads to additional charge deposit at the beginning of the drift region. Image taken from [Aam+08].

---

will leave out the stack at $\eta \approx 0$, directly in front of PHOS, in order to minimize the radiation length.

During the first LHC running period in 2010 seven SMs in sectors 00, 01, 07, 08, 09, 10, and 17 were installed. In the winter shut-down before 2011, another three SMs (sectors 11, 15, and 16) were integrated. Since beginning of 2012, three more SMs (sectors 02, 03, 06), i. e. overall 13 SMs, are available. The TRD will be completed in the long maintenance shut-down of the LHC in 2013.

The TRD chambers are basically multi-wire proportional chambers, with a 30 mm drift section and 7 mm multi-wire proportional section, and an additional radiator (see Figure 3.3). The radiator in front of the chambers is a 48 mm Rohacell/polypropylene sandwich. The chamber is closed with a 22 mm hon-

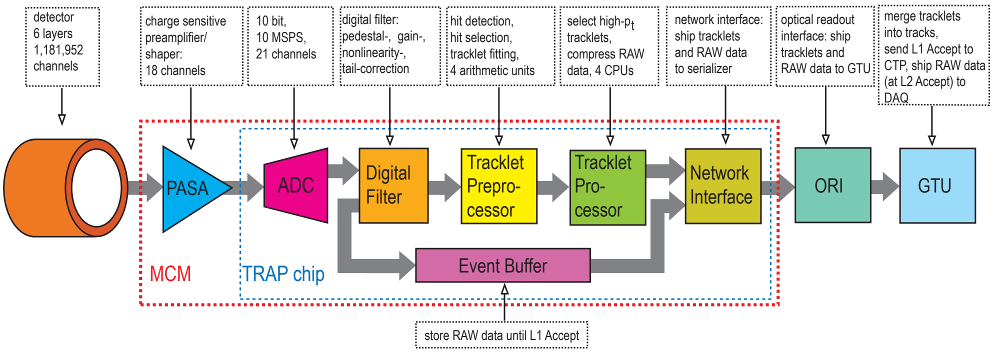

Figure 3.4: Schematic overview of the readout electronics of the TRD. Image taken from [Aam+08].

eycomb carbon-fiber sandwich, which supports the readout pads at the inner surface and the readout electronics. The TRD gas volume of 27.2 m^3 is filled with a $Xe - CO_2$ (85%–15%) gas mixture. The drift field is 0.7 kV/cm. The gas mixture is optimized for good conversion probability of the transition radiation generated by highly relativistic electrons (see Figure 3.3).

The readout electronics on top of each chamber allow fast, highly parallelized online data processing for triggering [Ang06; Kle11d]. The data flow of the TRD follows its segmentation in 18 SMs with five stacks of six chambers. Each of the 522 TRD chambers is equipped with 96 or 128 Multi Chip Modules (MCMs) depending on the type of chamber. They are connected to 12 or 16 times 144 readout pads of the chamber. In the MCMs, the signals are treated in a preamplifier shaper (PASA) and the so-called Tracklet Processor (TRAP) which form the Local Tracking Unit (LTU) of the TRD, not to be confused with the Local Trigger Unit (LTU) discussed in the previous section (see Figure 3.4). The TRAPs digitize and filter the signal. The filtered raw data is stored in an event buffer of the MCM and, in addition, in an online fitting process, tracklets are calculated. Via a network interface, the online data are sent from all TRAPs of a TRD half-chamber to an Optical Readout Interface (ORI). Two of those ORIs sit on each TRD chamber. The ORIs are linked via optical fibers to the Global Tracking Unit (GTU) of the TRD outside of the L3 magnet.

The GTU [Kir+10], again, consists of different processing units. The hierarchical structure of the GTU is shown in Figure 3.5. In logical order, the first sub-unit is the Track Matching Unit (TMU). Overall 90 TMUs exist, one per

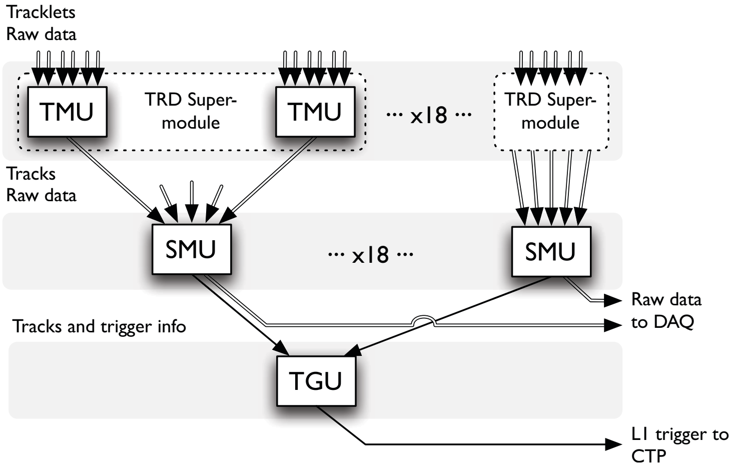

Figure 3.5: Hierarchical structure of the GTU. The first layer represents the 90 Track Matching Units (TMUs), one per TRD stack, the second layer the 18 Super Module Units (SMUs), and the third layer the Trigger Unit (TGU). Figure taken from [Kir+10].

---

stack. From the 12 ORIs of one TRD stack they receive the information from the online reconstructed tracklets, each. The six tracklets of the individual chambers are matched in the TMU to tracks of one stack. Tracklets, belonging to one track, are matched as they are projected to a virtual middle plane [Cuv09]. Projected tracklets which coincide in a defined window are considered for a track. Ignoring their curvature, a straight line fit through the tracklets is performed. The displacement a of the fit to the nominal collision point is inversely proportional to the transverse momentum of the track. The calculation of a is a possibility to estimate an equivalent to the track p_{t} within a time-scale which is available for the trigger decision. In a TMU the number of tracks and their individual parameter a is known, but not their exact position (η,ϕ). This is the substantial information of an event which is available for a jet trigger based on the TRD.

The next units which collect and concentrate the information in order to generate trigger decisions are 18 Super Module Units (SMUs). They receive all information from the TMUs (stacks) of one super module. From those the information and trigger decision is propagated to the Trigger Unit (TGU), which sends the final trigger decision from the TRD, within 6.1 µs after receiving the L0 signal, to the CTP of ALICE.

The stored raw data in the event buffers of the MCMs is sent to the ALICE data acquisition (DAQ) when a L1 accept of the CTP is received. Otherwise the buffers are cleared after the expected L1 arrival time. If no L1 was received or when the raw data is sent, the TRD goes back in stand-by mode and awaits the next pre-trigger signal. The TRD also aborts the read-out process if no L0 trigger was received.

3.5 Analysis Framework

The common analysis framework of the ALICE collaboration is AliRoot [AliOff; AliSVN]. It is based on the ROOT system [Root], a C++ object orientated framework for data analyses. AliRoot provides additional ALICE specific libraries for event simulation, data reconstruction and analysis. Several event generators, like PYTHIA and PHOJET, are available. The geometrical material and readout of all detectors can be emulated for realistic detector response. The particle transport can be done by GEANT3, GEANT4, or FLUKA via a Virtual Monte-Carlo Interface.

The analysis code in AliRoot is subdivided according to the physics working groups (PWGs) in ALICE. For the presented analyses in this thesis, this was PWG4 (PWG for high p_t and photons) up to the end of 2011. Since the beginning of 2012 the working groups were reorganized with a separated jet working group, PWG-JE. In the PWGJE (previously PWG4) folder there is only pure user analysis code and macros. Some of the important classes which have been developed for this thesis are available in this folder, e. g. `AliAnalysisTaskFragmentationFunction` and `AliAnalysisTaskJetResponseV2`. Most of the technical code for jet reconstruction can be found in the JETAN folder. Some relevant classes are e. g. `AliAnalysisTaskJetCluster` and `AliAnalysisTaskFastEmbedding`. The fast-embedding methods in `AliAnalysisTaskFastEmbedding` and some related functions in other classes, e. g. for the jet matching `GetJetMatching` in `PWG/Tools/AliAnalysisHelperJetTasks.cxx`, have been developed in context of this work. The analyses of the background fluctuations were done with AliRoot v5-02-04-AN [AliSVNa]. For the presented studies of the momentum distribution in jets and the TRD jet-trigger AliRoot v5-03-08-AN [AliSVNb] was used.

3.5.1 Data Processing

The data recorded from real events or simulated data is in general available in Event Summary Data (ESD) or Analysis Object Data (AOD) files. Both types have a tree structure in ROOT format with branches for different information, like reconstructed tracks, vertices, or in case of simulated data also Monte Carlo truth information. This is supported by additional files (e. g. `Kinematics.root` and `TrackRefs.root`). AODs contain filtered data obtained from the ESD files and are in general composed for dedicated analyses. They can also store additional information like reconstructed jets.

Even more information of the event (which is in generally not necessary for physics analysis) are stored in so-called ESD friends. They contain detector specific information which are used for calibration or debugging. This additional information is by default only stored for a subset of 3% of all events. In this thesis ESD friends are used to access the TRD stand-alone tracks for the trigger studies in Chapter 6.

ESDs (and ESD friends) are filled in the reconstruction process. This either starts from digits in case of simulated data or raw data as received from data acquisition. Digits are digitized signals. In simulation, they are obtained in several steps from generated particles and their energy deposit in the subsequent detector simulation. The estimation of digits from raw data and vice-versa is also possible. This allows an identical reconstruction of the data, independent if it is simulated or real. In the case of the tracking from digits, or raw data, so-called clusters are produced. They represent a set of adjacent signals which were presumable produced by the same particle. From those digits finally tracks are reconstructed, which are stored in an ESD file. Local tracks reconstructed from clusters of a single detector (e. g. TRD standalone or TPC only tracks) are stored as well as global tracks combined from all available detectors.

AODs are filled by analysis tasks which provide information which are relevant for various other analyses. Typical tasks are the physics selection which filter the events according to genuine collisions, background event rejection and active triggers. Or the ESD filter task which flags tracks according to different track cuts by setting a filter bit. For jet analyses, jet finder tasks also often run with the AOD production. They provide information about reconstructed jets to the AODs, if needed from different jet finders, settings, and track cuts. Individual user analyses can access the tracks with required quality cut flags or reconstructed jets from those AODs without the need to run the corresponding task again.

The information from *global tasks* (e. g. jet finder) is also available for user tasks if they run on ESDs. Therefore, the tasks run in so-called *trains* with different tasks as *wagons*. The global tasks run first and their output is filled on-the-fly into the AODs structure which the user tasks can access in memory even though the AODs are not permanently stored.

3.5.2 Event Selection

All analyzed data in this work has been taken with an online minimum-bias (MB) trigger. The trigger conditions were slightly different for pp collisions at $\sqrt{s} = 7\,\text{TeV}$ [Aam+10c] and for Pb–Pb collisions at $\sqrt{s_{\text{NN}}} = 2.76\,\text{TeV}$ [Aam+10b]. In any case, it was based on the SPD and the VZERO detectors. In pp collisions, at least one hit was required either in

- the SPD (inner layer: $|\eta| < 1.4$ or outer layer: $|\eta| < 2.0$),
- the VZERO-A ($2.8 < \eta < 5.1$), or
- the VZERO-C ($-3.7 < \eta < -1.7$).

In addition, the trigger required a coincidence with two beam pick-up counters at both sides of the interaction region which indicate the passage of proton bunches. In the Pb–Pb collisions at least two of the following three conditions were required:

- A minimum of two hits in the outer layer of the SPD,
- a signal in VZERO-A,
- a signal in VZERO-C.

The aim of the minimum-bias trigger is an efficient selection of all inelastic events in pp and hadronic events in Pb–Pb. For inelastic events in pp, the trigger efficiency is with the applied trigger $95-97\,\%$ [Gro10].

In addition, an offline event selection [Aam+11a] is applied, which is called physics selection and described in Section 3.5.1. It validates the online trigger; eventually with tuned conditions. This is of particular importance for the pilot runs, since at the beginning, the online trigger was kept as sensitive as possible

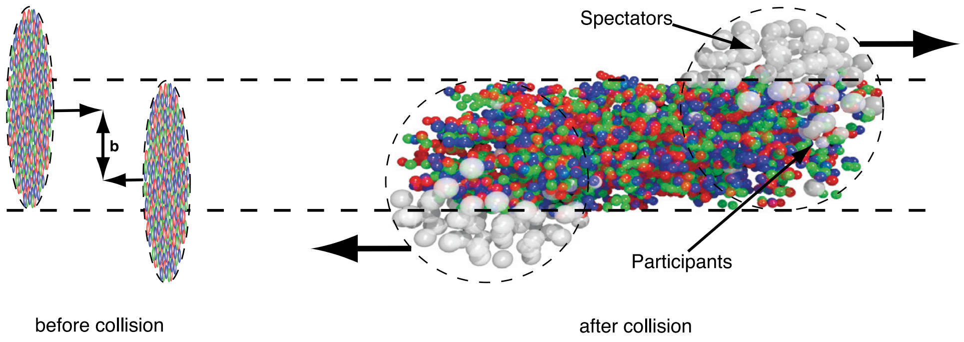

Figure 3.6: Nuclei before the collision (left) with impact parameter b and after the collision (right) with deconfined colored objects in the participant zone and spectator nucleons. Taken from [Sne11].

---

and consequently more background events were recorded. The offline selection can ensure same conditions for all runs. Furthermore, the offline event selection rejects beam-gas collisions and, in Pb–Pb, also electromagnetically induced interactions.

Besides these mainly physically motivated selections, additional requirements are often made which are supposed to ensure good experimental conditions. That, for example, also includes a pile-up rejection of the ALICE trigger system. In the analyses presented in this work, a reconstructed interaction point, so-called primary vertex, (according to the number of contributions) is required. The primary vertex has to be within $|z_{\mathrm{vtx}}| < 8\,\mathrm{cm}$, as maximum separation in beam direction from the center of the central barrel detectors. This is important for an equal tracking efficiency within the track acceptance region and avoids edge effects in jet reconstruction.

3.5.3 Collision Centrality

For the characterization of heavy-ion collisions, the centrality of the collisions is of prime importance. If the nuclei collide head-on (central) or peripheral defines the number of participant nucleons, N_{part}, in the collision and therefore determines the possible system size and energy density. The Glauber model [Mil+07] describes nuclear collisions as multiple collisions of individual nucleons. Glauber Monte-Carlo simulations provide a useful tool to estimate for a given nuclear charged density the average overlap or thickness function $\langle T_{\mathrm{AB}} \rangle$

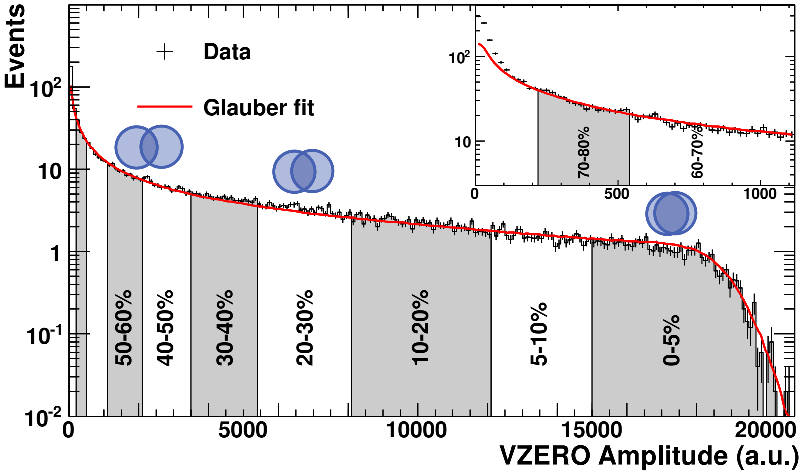

Figure 3.7: Example of a distribution of VZERO amplitudes (histogram) with a Glauber model fit (line) and the resulting centrality classes. Taken from [Aam+11a].

---

for a specified impact parameter b. The impact parameter is the distance between the centers of the two nuclei (see Figure 3.6). For head-on collisions, it is zero and approximately the sum of the radii of both nuclei for ultra-peripheral collisions. Together with an inelastic nucleon-nucleon cross-section, the thickness function defines the average number of participants, $\left\langle N_{\text{part}}\right\rangle$, and the average number of binary nucleon-nucleon collisions $\langle N_{\text{coll}}\rangle$. The second is important e. g. for the normalization of hard processes, as discussed already in context of the nuclear modification factor (Section 2.3.2).

In the experiment, the centrality is either estimated from the multiplicity in the event or an equivalent quantity which can be related to N_{part}. The collision centrality is indicated in percentiles of the total cross-section, integrating from the most central events. Furthermore, the events are divided in centrality classes. Events of centrality $0-10\,\%$ represent the $10\,\%$ most central events and centrality $80-90\,\%$ means pheripheral events of the same amount. In ALICE jet analyses, often four centrality classes are distinguished. From central to peripheral these are $0-10\,\%$, $10-30\,\%$, $30-50\,\%$, and $50-80\,\%$.

A common method in ALICE—which is also used in this work—is the estimation of the event centrality from the summed VZERO signals [Aam+11a; Toi11]. According to a Glauber model fit on its distribution, the VZERO amplitudes are related to different collision centralities; see Figure 3.7 as an example. At very low VZERO amplitudes which correspond to the most peripheral events, experimentally it is difficult to distinguish between non-diffractive events and background, like elastic interactions from electromagnetic scatterings. In addition, trigger inefficiencies occur in this region. The Glauber model does not explain the data of this part anymore, which is apparent as a deviation of fit and data. Therefore, the analysis of heavy-ion data is limited to $0-80\,\%$ centrality in this work. The effective number of $100\,\%$ events is appropriatly extrapolated according to the Glauber model.

Alternatively, it can be estimated from the energy deposit of the spectator nucleons in detectors at zero degree to the beam axis, like the ZDC in ALICE. However, at colliders with this method it is difficult to distinguish between central and very peripheral events. In very peripheral event, almost intact fragments of the colliding nuclei stay in the beam pipe. Therefore, in ALICE the ZDC is assisted by small electromagnetic calorimeters in forward rapidity (ZEM) [Aam+08]. Furthermore, the centrality can be determined from the number of TPC tracks.

3.5.4 Collective Flow

A global feature of heavy-ion collisions is the collectivity which is observed in the so-called collective flow of particles [VZ96; PV98; Aam+10d; Sne11]. The initial condition of the hot and dense system created in heavy-ion collisions is defined by the geometry of the overlap region of the colliding nuclei. An initial spatial anisotropy leads in the emerging collective system to a pressure gradient. This evolves to an anisotropic, collective flow in the final state momentum of hadrons. It is measured in the yield of particles in dependence of the azimuthal direction in form of a Fourier series [Aam+10d]:

$$E\frac{\mathrm{d}^3N}{\mathrm{d}\vec{p}^3} = \frac{1}{2\pi}\frac{\mathrm{d}^2N}{p_\mathrm{t}\mathrm{d}p_\mathrm{t}\mathrm{d}y}\left(1+\sum_{n=1}^{\infty}2v_n\cos[n(\phi-\psi_n)]\right), \tag{3.5}$$

where E is the energy, p the momentum, p_t the transverse momentum, ϕ the azimuthal angle, y the rapidity of the particle, and ψ_n is the symmetry plane angle of the harmonic of order n [Aam+11b]. A reaction plane (RP) ψ_RP is defined by the beam axis and the impact parameter. The harmonic symmetries ψ_n deviate from the reaction plane due to event-by-event fluctuations in the matter distribution of the colliding nuclei. Odd harmonics emerge only due to those fluctuations.

In this thesis, only the second and third harmonic shall be discussed since those are relevant in later analysis of soft background in heavy ion collisions (in Chapter 7). The *elliptic flow* is characterized by the second Fourier coefficient

$$v_2 = \langle \cos[2(\phi - \psi_2)] \rangle . \tag{3.6}$$

This is the most intuitive component caused by the almond shape in non-central colliding nuclei (see Figure 3.7). Accordingly, the elliptic flow is dominant in peripheral and mid-central collisions and directly related to the reaction plane. In Pb–Pb collisions at $\sqrt{s} = 2.76\,\mathrm{TeV}$, it reaches its maximum of almost 10 % around $40-50$ centrality percentile [Aam+11b]. For central events, with impact parameter aproaching to zero, the spatial asymmetry becomes less and thus the elliptic flow vanishes. Therefore higher harmonics become relevant. The next important is the *triangular flow*,

$$v_3 = \langle \cos[3(\phi - \psi_3)] \rangle . \tag{3.7}$$

At the LHC it is in the order of 2 to 3 % and almost independent of the impact parameter, it only slighty increases from central to peripheral events [Aam+11b]. More details about recent measurements of anisotropic flow by ALICE are given in [Aam+10d; Aam+11b].

The experimental observable of the reaction plane is the so-called *event plane*, which is measured by a Fourier analysis of the particle's flow. In the presented studies the event plane is obtained from the charged tracks reconstructed in the TPC within $|\eta| < 0.8$ and $0.15\,\mathrm{GeV}/c < p_\mathrm{t} < 20\,\mathrm{GeV}/c$ by using the class `AliEPSelectionTask`. The tracks are weighted by their p_t (in GeV/c) or by 2 for tracks with $p_\mathrm{T} > 2.0\,\mathrm{GeV}/c$. The limitation of high p_t tracks reduces the impact of hard processes to the measurement, which are not correlated to the event plane in terms of an initial pressure gradient. However, the spatial anisotropies are of relevance for jet measurements in terms of jet quenching due to different path lengths of the partons within the quark-gluon plasma (QGP). Therefore, it is important to disentangle the estimation of the event plane from the jet contributions.

The previously introduced estimation of the event plane via TPC tracks is the main method which is used in this work. Alternative methods are the estimation with the VZERO or FMD. The decisive difference is the different probed rapidity range of the event, which is in case of VZERO $-3.7 < \eta < -1.7$ and $2.8 < \eta < 5.1$ and in case of FMD $-3.4 < \eta < -1.7$ and $1.7 < \eta < 5.0$. Therefore, the measurements are presumably less correlated with the measured

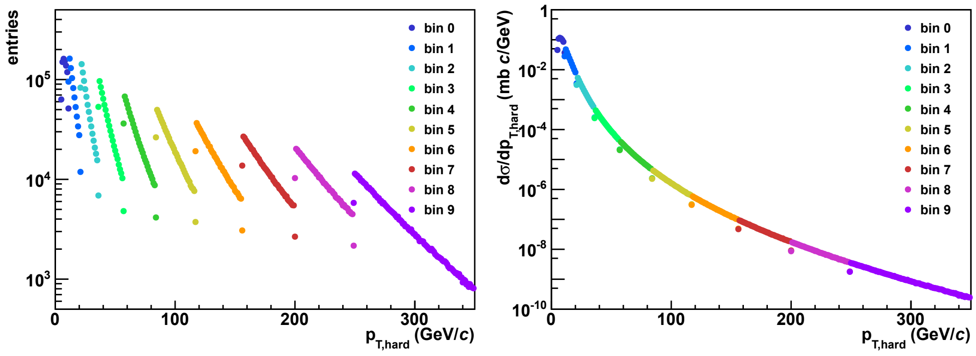

(a) Raw simulated p_t^{hard} distribution.

(b) Weighted p_t^{hard} distribution.

Figure 3.8: Raw and weighted p_t^{hard} distribution of jet simulation (pp at $\sqrt{s} = 2.76$ TeV) used for embedding.

---

jets in mid-rapidity ($|\eta| < 0.9$). However, there are still correlations, e.g. from the back-to-back jet, and a dedicated p_t cut on single tracks is not possible. Another restriction for the measurement with VZERO is a worse resolution of the event plane orientation compared to the event plane measured via TPC tracks [San11]. The event plane resolution of FMD is almost as good as those from TPC tracks [San11].

3.5.5 Event Simulation

On behalf of the ALICE jet analysis group, various event simulations were prepared. In this thesis, two simulations of pp collisions with $\sqrt{s} = 2.76$ TeV and $\sqrt{s} = 7$ TeV produced by PYTHIA 6.4.21 [SMS06] with full detector response by GEANT 3.21 [BCG94] were used. The simulated events are dedicated jet events since a hard parton interaction (2 → 2 process) was generated. In the final state, a jet is required within a specified acceptance interval. This is tested on simulation level by PYCELL, a PYTHIA integrated jet finder. Both simulated event samples are separated in ten p_t^{hard} bins, as can be seen in Figure 3.8 for 2.76 TeV and in Table 3.3. p_t^{hard} is the exchange of transverse momentum given by PYTHIA between the two scattered partons. In fact, p_t^{hard} can be slightly different from the actual momentum transfer due to occurrent initial-state radiation (ISR), which is in the generation process of PYTHIA radiated after

Table 3.2: Parameter of the jet-jet simulations.

MC generator	PYTHIA 6.4.21
beam	proton-proton
tune	Perugia-0
collision energy (cms)	7.00 TeV (LHC11a1a-j) 2.76 TeV (LHC11a2a-j)
anchor run	126 007 (LHC10d, pass2)
process	jet-jet
p_t hard bins	10 bins (→Table 3.3)
jet range	$\|\eta\| < 1.5$, full azimuth
jet E_t	$10 - 1000$ GeV
intrinsic k_t	5 GeV/c
initial gluon radiation	on
final gluon radiation	on
quenching	off
pycell parameters	
η max.	2.0
nb. of cells ($\eta \times \phi$)	274×432
cell threshold	0.0 GeV
E_t seed	4.0 GeV
min. jet E_t	5.0 GeV
cone radius	1.0

$p_\mathrm{t}^\mathrm{hard}$ is defined. The separation in ten $p_\mathrm{t}^\mathrm{hard}$ bins provides high statistics for a wide range of jet p_t over several orders of magnitudes in cross-section.

For each $p_\mathrm{t}^\mathrm{hard}$ bin the average cross-section, $\sigma_{\mathrm{p}_\mathrm{t}^\mathrm{hard}}$, and the number of events, N_events, are recorded. In this case, the number of events includes all trials during the simulation. This especially means those events are also count where no PYCELL jet within the required p_t or acceptance interval was found and the event was discarded (but counts for the cross-section of $p_\mathrm{t}^\mathrm{hard}$). The events from different $p_\mathrm{t}^\mathrm{hard}$ bins are weighted by scaling factor:

$$s_{\mathrm{p}_\mathrm{t}^\mathrm{hard}} = \frac{\sigma_{\mathrm{p}_\mathrm{t}^\mathrm{hard}}}{N_\mathrm{events}}, \tag{3.8}$$

Table 3.3: p_t hard bins of LHC11a1a-j (7 TeV) and LHC11a2a-j (2.76 TeV) productions.

bin	p_t hard (GeV/c)	simulated events	
		7 TeV	2.76 TeV
a	5 – 11	1 041 200	1 002 800
b	11 – 21	1 107 600	967 200
c	21 – 36	1 046 000	1 025 200
d	36 – 57	1 000 800	997 600
e	57 – 84	964 000	901 600
f	84 – 117	856 000	821 200
g	117 – 156	786 800	723 600
h	156 – 200	654 800	668 400
i	200 – 249	561 600	573 200
j	> 249	440 400	476 000

such that they describe a realistic p_t^{hard} and jet p_t spectrum, respectively. The weighted p_t^{hard} spectrum is shown in Figure 3.8b.

Details about both used jet simulations are listed in Table 3.2. An important item for the comparison with data is the selection of the anchor run. It defines the detector configuration and beam vertex condition, which is relevant for tracking efficiencies and track momentum resolution. A simulation for all runs is not possible due to computational cost and limited disk space. Therefore, a run needs to be chosen which represents as good as possible a larger data sample. The runs are divided in different run periods. Each run period is a period of data taking under similar detector conditions and reconstruction settings. Anchor run 126 007 from run period LHC10d has been selected because the run period and the run itself represent a large amount of the data from 2010. Furthermore, the second pass of reconstruction was already available for this run when the simulation was prepared. This ensures a good detector calibration.

Chapter 4

Jets in ALICE

One advantages of jet reconstruction in ALICE is the good tracking of charged tracks from very low to high p_t. This allows a detailed analysis of the jet structure. Furthermore, the tracking detectors at mid-rapidity cover the full azimuthal angle, which is important for any kind of track correlations or back-to-back di-jet studies.

For tracking detectors, the momentum of a particle is directly accessible from the deflection of the track in the magnetic field. The energy is only known with particle identification which gives the particle mass. For jet finding, the jets and its constituents are considered as massless, which is reasonable for high $p_\mathrm{t} \gg m_0 c$, where m_0 is the rest mass. So the energy and momentum can be equivalently used, $E = pc$. Nevertheless, the jet momentum is stated to emphasize that the mass is not measured. Also in the following description of the jet algorithms, track p_t and calorimeter cell E_t can be interchanged.

The tracking detectors allow only the reconstruction of charged tracks and charged jets, respectively. Therefore this thesis discusses only the reconstruction of charged jets and its analyses. The EMCAL in ALICE also allows full jet reconstruction, including the neutral part (mainly photons). Whereas the acceptance is limited to $|\eta| < 0.7$ and 107° in azimuth and the EMCAL is only completely installed since beginning of this year. In other, upcoming jet analysis of ALICE the EMCAL is used.

4.1 Jet Reconstruction

The aim of jet finder algorithms is to reconstruct the properties of the original parton from the spray of hadrons. It is reflected in the momentum and direction of the reconstructed jets. Two different principles of jet algorithms are commonly used: The cone algorithms and the recombination algorithms.

Cone jet finders define a jet as the energy flow in a cone of (mostly) fixed radius R in (η,ϕ) space. Typically, cone algorithms require a seed particle above a transverse momentum threshold, $p_{\mathrm{t}}^{\mathrm{seed}}$. All particles within the cone contribute to the jet p_{t} and define the jet direction, which is stated by the cone axis, according to the recombination scheme. The advantage of the cone algorithms is that they are quite intuitive to understand and have been used for 30 years in electron and proton collider experiments. However, without further improvements, the original cone jet finder algorithms are neither completely infrared nor collinear safe. Infrared and collinear safety of a jet algorithm is described in Section 4.1.2.

The original idea of recombination algorithms is to undo the parton branching. Nearby particles with similar transverse momentum are sequentially recombined to quasi-particles, so-called clusters, until finally all tracks of the event are clustered to *jet candidates*. The jet size, even though not obligatory conical and fixed, is characterized by a parameter similar to the radius R of cone algorithms. The clustering algorithms are inherently collinear and infrared safe.

4.1.1 Recombination Scheme

Whereas jet finding algorithms describe the rules which particles are integrated to jets, the recombination scheme defines, on a more fundamental level, in which way the momenta of particles are combined. The most common recombination scheme, especially at hadron colliders, is the Snowmass accord [Hut+90]. In this convention, the transverse jet-momentum, $p_{\mathrm{t}}^{\mathrm{jet}}$, is the sum of transverse momenta of all particles within the identified jet ($p_{\mathrm{t}}^{\mathrm{jet}} \equiv \sum p_{\mathrm{t},i}$). The jet direction $(\eta_{\mathrm{J}},\phi_{\mathrm{J}})$ is calculated from the p_{t}-weighted pseudo-rapidity η and azimuthal angle ϕ of the individual jet particles. A drawback of the Snowmass accord is that it is not Lorentz invariant.

Another practical recombination scheme is the E-scheme. According to this scheme, the jet variables are calculated by summing up the complete four-momenta of the included particles. This procedure is Lorentz invariant.

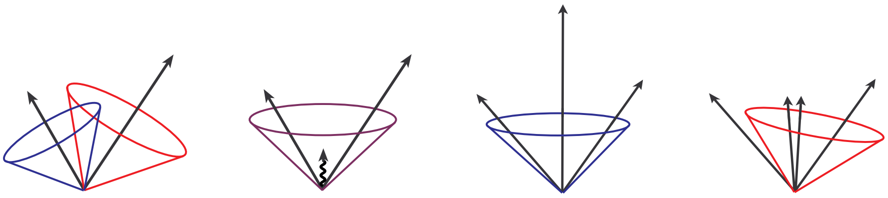

(a) Infrared Safety. **(b)** Collinear Safety.

Figure 4.1: Illustration of (a) merged jets caused by soft radiation (infrared unsafe) and (b) by collinear p_t splitting affected jet reconstruction (collinear unsafe). Taken from [Bla+00].

4.1.2 Infrared and Collinear Safety

An important property of jet algorithms is their collinear and infrared safety, which is illustrated in Figure 4.1 [Bla+00]. It is of relevance for the consistency between reconstructed jets and QCD predictions. An additional soft radiation between two jets may cause a merging of both jets. Jet finder which are infrared safe are insensitive against an additional soft particle. This is of particular relevance for heavy-ion collisions with a large amount of soft background, as is discussed in Chapter 7.

Jet reconstruction may also be affected if a high-p_t particle is replaced by two exactly collinear particles with $p_\mathrm{t}/2$. Collinear safe jet finders are insensitive to the p_t ordering of the particles that act as seeds.

4.1.3 Cone Algorithms

A historical cone algorithm is the UA1 jet finder from the experiment with the same name [Arn+82]. The Heavy-Ion Jet Algorithm (HIJA) [Bly05; Bly+07] is based on the UA1 algorithm. It contains several refinements to make it more suitable for the comparison with next-to-leading order (NLO) pQCD calculations. This algorithm is in general used in analyses of ALICE which refer to the UA1 algorithm.

A process chart of the HIJA is shown in Figure 4.2. The algorithm starts with a (η,ϕ) grid $(\Delta\eta \times \Delta\phi = 0.015 \times 0.015, |\eta| < 2)$, which is filled with the transverse momenta of all charged particles. If used, transverse energies of calorimeter cells can also be included. For a first background reduction, a track p_t cut is applied before the grid is filled. After each execution of the jet finder loop the difference between the background level $(p_\mathrm{t}^\mathrm{bg})$ is calculated.

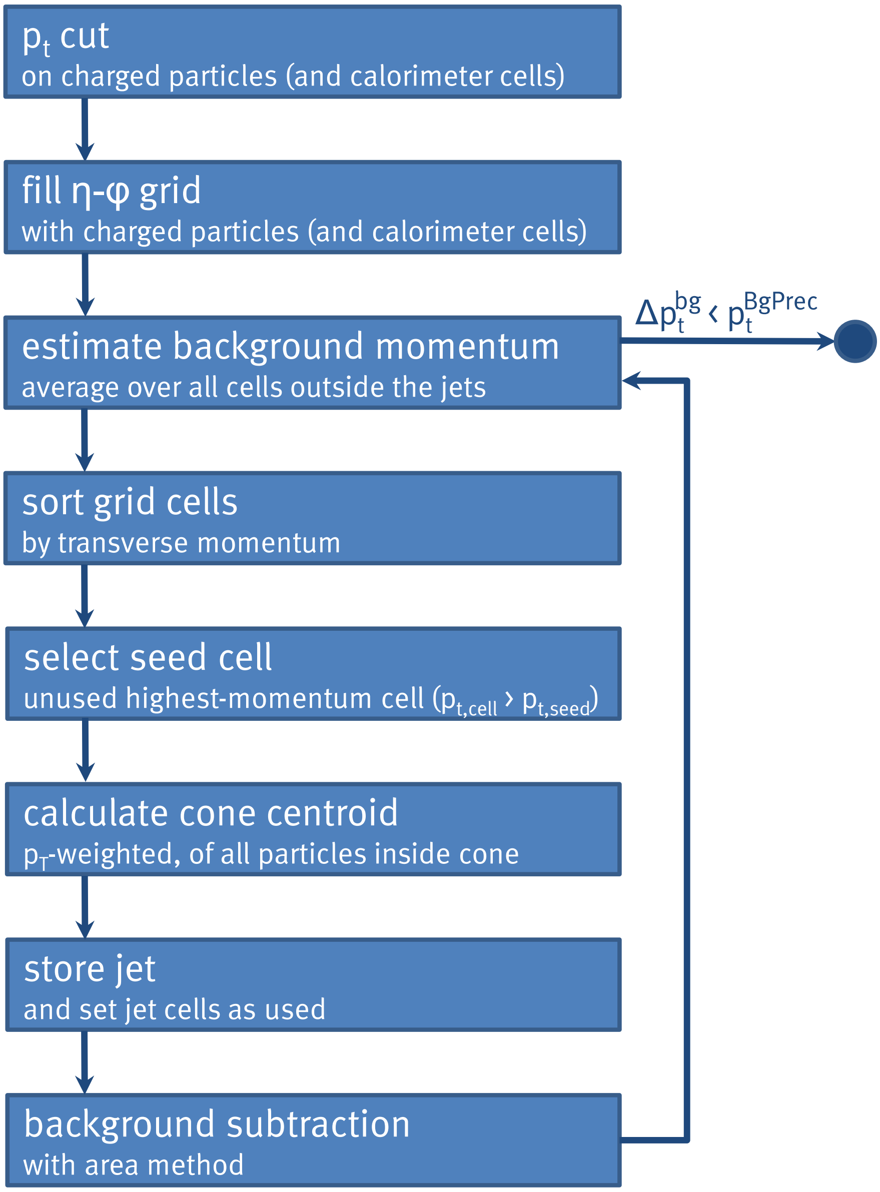

Figure 4.2: Process chart of the Heavy-Ion Jet Algorithm (based on UA1).

The background level is the average momentum of all cells which do not contribute to jets. The loop continues until the change in the background level is smaller than the background threshold $p_{\mathrm{t}}^{\mathrm{BgPrec}}$ [= 0.035], but at least two iterations are performed.

With each iteration of the loop, the cells are sorted by momentum in decreasing order. Cells with momentum above the seed threshold $p_{\mathrm{t}}^{\mathrm{seed}}$ [$= 4\,\mathrm{GeV}/c$] are taken as a seed of a jet. It starts with the cell of highest momentum. From all cells within the cone radius R_{C} [$= 0.4$] the p_{t}-weighted centroid is estimated. The calculation is protected with a maximum (δR_{max} [$= 0.15$]) and a minimum (δR_{min} [$= 0.05$]) displacement of the cone center. If the displacement exceeds one of these thresholds, the cone centroid is fixed. The jet candidate is stored if the jet momentum inside the cone is above the average background in the event plus one standard deviation of the background fluctuations. Finally, one of the background subtraction methods, preferentially the area method, is used for each jet. Only jets with a momentum above $p_{\mathrm{t}}^{\mathrm{min}}$ [$> 5\,\mathrm{GeV/c}$] and within the jet acceptance $|\eta_{\mathrm{jet}}|$ [< 1.5] are kept stored. The noted values of the parameters are commonly used in ALICE and in this work.

Another cone algorithm is SISCone [SS07], a Seedless Infrared Safe Cone jet algorithm. It was developed by G. Salam and G. Soyez. As the name suggests this algorithm manages the jet finding procedure without requiring a seed and is infrared safe. Another feature is that overlapped cones are split or merged following the procedure of Tevatron Run II [Bla+00]. Hence, the cones are not necessarily of fixed size and concentric.

4.1.4 Recombination Algorithms

Recombination algorithms are currently preferably used in hadron collider experiments. In ALICE and this thesis, the two related k_{t} and anti-k_{t} recombination algorithms are mostly used. Both are almost identical, only the p_{t} ordering of recombination is inverted. Therefore they show a different characteristic, especially within a large amount of soft background. The advantages of both algorithms are discussed later. They are used and described as implemented in the FastJet 2.4.2 package [CS06]:

1. For each particle i in the event, the geometrical closest particle $\mathcal{G}_i$ is estimated.

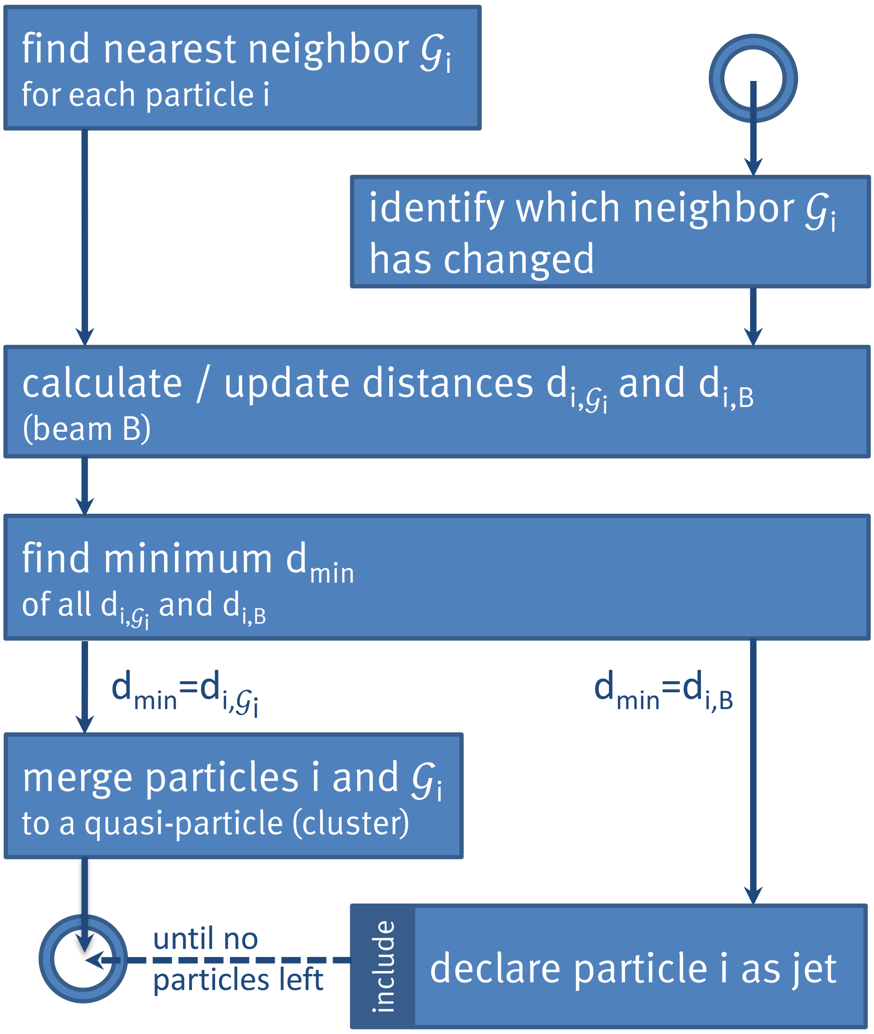

Figure 4.3: Process chart of the FastJet algorithm.

2. The particle i with the smallest distance $d_{i,\mathcal{G}_i}$ or $d_{i,B}$ is identified. Whereas the distance to the geometrical closest particle is defined as:

$$d_{i,\mathcal{G}_i} = \min(p_{\mathrm{t},i}^{2l}, p_{\mathrm{t},\mathcal{G}_i}^{2l}) \frac{\Delta R_{i,\mathcal{G}_i}^2}{R^2}. \tag{4.1}$$

   $\Delta R_{i,\mathcal{G}_i} = \sqrt{(\Delta\eta_{i,\mathcal{G}_i})^2 - (\Delta\phi_{i,\mathcal{G}_i})^2}$ is the distance in the (η,ϕ) plane. It is normalized to the pre-defined distance parameter R (similar to the cone radius of the cone algorithms) and weighted with the minimum of the particle's transverse momenta $p_{\mathrm{t},i}^{2l}$ and $p_{\mathrm{t},\mathcal{G}_i}^{2l}$. The exponent l depends on the algorithm and is 1 for the k_t algorithm or -1 for the anti-k_t algorithm. That defines the order of clustering.
   The distance to the beam B is defined by:

$$d_{i,B} = p_{\mathrm{t},i}^{2l}. \tag{4.2}$$

3. Depending on the result:
   a) $d_{\min} = d_{i,\mathcal{G}_i}$: Particle i and $\mathcal{G}_i$ are combined to a *pseudo-particle.*
   b) $d_{\min} = d_{i,B}$: (Pseudo-)Particle i is assigned as *jet candidate* and removed from the list.

4. The list of $d_{i,\mathcal{G}_i}$ and $d_{i,B}$ is updated. It is continued with step 2 if any particles are left.

This is done until all tracks of the event are related to a jet candidate. Basically, a (pseudo-)particle is assigned as a jet candidate once the distance to the next (pseudo-)particle is above the distance parameter R. Figure 4.3 illustrates the FastJet algorithms in a process chart.

The FastJet package provides different recombination schemes. The used scheme in this work is the boost-invariant p_t scheme. The rapidity y and azimuth angle ϕ of two (pseudo-)particles i and j are combined with a weight of p_t:

$$y_r = \frac{p_{\mathrm{t},i} y_i + p_{\mathrm{t},j} y_j}{p_{\mathrm{t},i} + p_{\mathrm{t},j}}, \tag{4.3}$$

$$\phi_r = \frac{p_{\mathrm{t},i} \phi_i + p_{\mathrm{t},j} \phi_j}{p_{\mathrm{t},i} + p_{\mathrm{t},j}}. \tag{4.4}$$

The transverse momenta just add up:

$$p_{\mathrm{t},r} = p_{\mathrm{t},i} + p_{\mathrm{t},j}. \tag{4.5}$$

For some time in the past, recombination algorithms required high computational costs of $\mathcal{O}(N^3)$ operations for an event with N tracks [CS06]. In the original k_t and anti-k_t algorithms the distance $d_{\mathrm{i,j}}$ has been calculated for all particle combinations in the event, not only for the geometrical closest particles. Therefore, those algorithms appeared to be impractical for high multiplicity heavy-ion events, as expected at the LHC. In 2005, Cacciari and Salam presented [CS06] (and implemented in the FastJet package) a possibility which requires only $\mathcal{O}(N \ln N)$ operations. They solved the issue by applying a geometrical ansatz based on the Voronoi diagram [Dir50; Aur91] to determine the geometrical closest neighbor. This makes the algorithms even faster than other common jet finders [CS06].

4.1.5 The Anti-$\mathrm{k_t}$ Algorithm and Signal Jets

For the anti-k_t algorithm [CSS08a] in Equation 4.1 and 4.2, the exponent l is -1, i.e. the distance parameter $d_{i,j}$ is small for tracks with high p_t. As a consequence, jets grow from the hardest to the softest constituents and are basically clustered around a high-p_t seed. That results usually in almost concentric areas with radius R. This algorithm is quite robust against the soft event and is therefore preferably used for the reconstruction of *signal jets* in heavy-ion collisions.

For the presented studies the used distance parameter is $R = 0.4$, even though the typical area into which the hadrons from an initial hard-scattered parton fragment is larger. In Figure 4.4, the charged-jet energy is shown as function of the cone radius R. The jet radius suggested in the Snowmass accord is $R = 0.7$ [Hut+90]. Also in experiments with $\mathrm{p\bar{p}}$ collisions at Tevatron, the common jet radius was $R = 0.7$ [Abu+06; Aba+12]. In heavy-ion collisions the situation is different. With a large jet area, the contribution from the underlying event is also enriched, while most of the momentum of the initial parton is in a more collimated core. Both are also visible in Figure 4.4. Therefore, a radius parameter around 0.4 is common for heavy-ion collisions. In addition it is appreciated in ALICE due to the quite small covered tracking acceptance in pseudo-rapidity and it is often used in pp collisions for comparison with heavy-ion collisions.

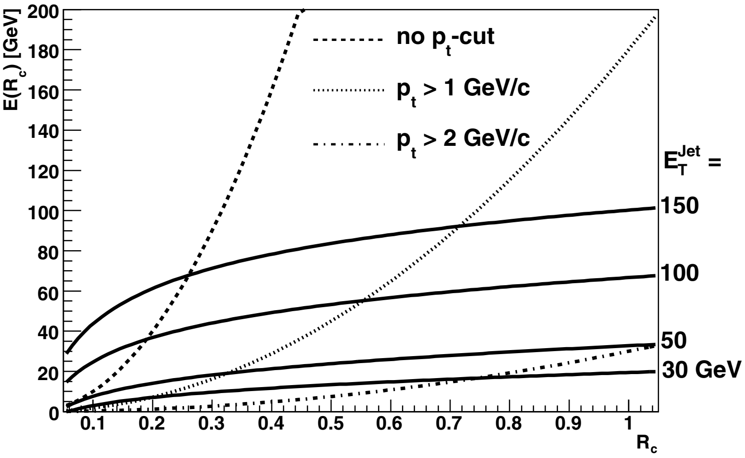

Figure 4.4: Charged-jet energy within a cone of radius R_c (full lines). And the contribution of the underlying event for different track-p_t thresholds (dashed lines) estimated by HIJING with $b < 5$ fm. Taken from [Ale+06].

According to the distance parameter $R = 0.4$ and the tracking acceptance of $|\eta| < 0.9$, the jet acceptance in ALICE is in pseudo-rapidity limited to $|\eta| < 0.5$. While the clustering process itself is not limited to this interval. This is important to avoid side-effects at the edges of the acceptance interval.

4.1.6 The k_t Algorithm and Background Clusters

The classical sequential-recombination algorithm is the k_t algorithm [Cat+91; Cat+93; ES93]. It works just like the anti-k_t algorithm, but with the exponent $l = 1$ in Equation 4.1 and 4.2 for the distance parameter $d_{i,j}$ and $d_{i,B}$. As a consequence, the clustering order is inverted to anti-k_t and the recombination process preferable starts with low-p_t tracks. This results to some extent in low-p_t clusters with irregular area. For events with minor soft contributions, e.g. from pp collisions, both algorithms, anti-k_t and k_t, produce comparable results. The variation becomes larger with larger contributions of soft background. While the anti-k_t algorithm is preferred for the reconstruction of signal jets, the k_t algorithm is convenient for the estimation of the background density in the event. It sums up the transverse momentum of the entire event with a dedicated estimation of the area. More details about the calculation of the average background in the event are given in Section 7.1 in context of the studies about background fluctuations in heavy-ion collisions. Due to its application, reconstructed clusters from the k_{t} algorithm are in this thesis called *clusters* or *background clusters* and not jet candidates.

4.1.7 Jet Area

To estimate the jet candidate or cluster area, the *active area* method [CSS08b] from the FastJet package is used. Over a defined phase space *ghost particles* of infinitesimal small momentum ($p_{\mathrm{t}}^{\mathrm{ghost}} \approx 10^{-100}\,\mathrm{GeV}/c$ [CSS08b]) are distributed. The number of ghost particles is defined by the ghost area which is allocated for each ghost particle. The size of the ghost area actually is important for the resolution of the estimated jet/cluster area. By default, a ghost area of 0.01 is set. For the background studies in Chapter 7 a smaller ghost area of 0.005 was used in order to get a better jet/cluster area resolution. The ghost area of 0.005 was chosen as compromise between good area resolution, computing time and memory consumption. The ghost particles have been distributed in the same acceptance as for track reconstruction ($|\eta| < 0.9$).

4.2 Track Selection

Jet analyses require ambitious track quality cuts, especially since homogeneous tracking efficiencies within the track acceptance are demanded. Otherwise easily artificial correlations would appear. The common tracking procedure of charged tracks in the central barrel of ALICE is mainly based on clusters in the TPC and the ITS. Especially hits in the two innermost layers close to the vertex, namely the SPD, are important for a good momentum resolution. Since some parts of the SPD were switched off during the used run periods in 2010, inefficient regions for common track reconstruction are apparent if high quality tracks are required with strict requirement on the SPD track points. This includes a successful reverse fit through the ITS in the last iteration of the tracking, the so-called refit, which defines the global track parameters [Aam+08]. To ensure flat distributions in the (η,ϕ) plane, an approach of hybrid tracks [KV11] of following types is used:

1. Global tracks with SPD hit(s) and an ITS refit.
2. Global tracks without SPD hit and no required ITS refit, constrained to the primary vertex.

As far as available, tracks of the first type with ITS information are used. In studied heavy-ion events, these are 78 % of all tracks [Aam+12a]. They give the best resolution in transverse momentum. Tracks of the second type without any track points in the SPD or without ITS refit are constrained to the primary vertex of the event, in order to improve the p_t resolution in spite of a missing tracking information from SPD. The primary vertex is estimated from other tracks in the event with SPD hits. An overall worse p_t resolution compared to stricter track-cuts needs to be accepted in favor of high and homogeneous tracking efficiency when both types of tracks are combined. Nevertheless, with this approach the p_t resolution is for all tracks $\sigma(p_\mathrm{t})/p_\mathrm{t} \approx 1\,\%$ at 1 GeV/c and for the majority of the tracks it is still $\sigma(p_\mathrm{t})/p_\mathrm{t} \approx 10\,\%$ at 50 GeV/c [Aam+12a]. Only 6 % of all tracks have a resolution of $\sigma(p_\mathrm{t})/p_\mathrm{t} \approx 20\,\%$ at 50 GeV/c. The tracking efficiency is 50 % at a track p_t of 0.15 GeV/c and increases to 90 % at 1 GeV/c and above [Aam+12a].

In a previous approach, only standalone TPC tracks constrained to the primary vertex have been used. These allow also a quite homogeneous tracking efficiency but produce tracks with unreasonable high reconstructed p_t in some cases. This is now avoided since the global central barrel information of all available detectors is used and an additional cut on the number of clusters in the TPC after first tracking iteration ($N_\mathrm{cls}^\mathrm{iter1}$) was introduced.

In the three presented parts of analysis in this thesis, two slightly different generations of these hybrid track cuts were used. The first generation, as implemented in AliRoot v5-02-04-AN [AliSVNa], has a fixed minimum number of TPC clusters (after first iteration) of $N_\mathrm{cls}^\mathrm{iter1} = 70$. This was applied for the background fluctuation studies in Chapter 7. The updated track cuts use a linear p_t dependence of $N_\mathrm{cls}^\mathrm{iter1}$. For track $p_\mathrm{t} < 20$ GeV/c is $N_\mathrm{cls}^\mathrm{iter1} > 70+(30/20)\,p_\mathrm{t}$ and above 20 GeV/c it is fixed at $N_\mathrm{cls}^\mathrm{iter1} = 100$. Also, an additional cut on the χ^2 between the global track and the TPC constrained track was applied. Both new cuts better reject fake tracks at high p_t. Therefore, the track p_t efficiency is a bit reduced compared to the first generation. These updated track cuts, as implemented in AliRoot v5-03-08-AN [AliSVNb], were used for the presented results of the momentum distribution in jets (Chapter 5) and the trigger studies (Chapter 6).

In addition, jets containing a track with $p_\mathrm{t} > 100$ GeV/c are tagged. They can be rejected afterwards in the user analysis. For the studies presented in this work, the rejection of those jets was only implemented for the background studies (Chapter 7). The approach of hybrid tracks allows with the current understanding the best compromise of homogeneous tracking efficiency and best achievable track p_t resolution [Ver11].

The track selection is realized with the ESD filter (class `AliAnalysisTaskESDfilter` configured by `AddTaskESDFilterPWG4Train.C`). This task assigns filter bits to each track according to its properties. In both noted AliRoot revisions, the first track type of the hybrid tracks corresponds to filter bit 16 ($1 << 4$), the second track type to filter bit 256 ($1 << 8$).

Chapter 5

Fractional Charged Particle Momentum Distribution in Jets

In this chapter, the fragmentation pattern of charged jets is presented as the first of three analysis parts in this thesis. The ultimate aim of such a study is the measurement of a medium-modified fragmentation pattern in Pb–Pb collisions. Here, preparative measurements of pp collisions as baseline are discussed. As introduced in Section 2.3.3, the fragmentation pattern is measured as fractional charged p_t distribution of tracks within charged jets:

$$F_\mathrm{ch}(z) = \frac{1}{N_\mathrm{jet}} \frac{\mathrm{d}N_\mathrm{trk}}{\mathrm{d}z_\mathrm{ch}} \qquad \text{with} \quad z_\mathrm{ch} = \frac{p_\mathrm{t}^\mathrm{trk(ch)}}{p_\mathrm{t}^\mathrm{jet(ch)}}. \tag{5.1}$$

Alternatively the fragmentation pattern is presented in form of the hump-backed plateau, as function of ξ_ch, which emphasizes the soft fragmentation:

$$\xi_\mathrm{ch} = \ln \frac{1}{z_\mathrm{ch}} = \ln \frac{p_\mathrm{t}^\mathrm{jet(ch)}}{p_\mathrm{t}^\mathrm{trk(ch)}}, \tag{5.2}$$

In the presented case of a jet p_t of 80 GeV/c and 150 MeV/c tracks, the hump-backed plateau reaches up to $\xi = 6.3$. More than half of the distribution ($\xi > 2.3$) corresponds to the very soft fragmentation region of $z < 0.1$, as was shown in Table 2.3.

As also discussed in Section 2.3.3, this measurement is closely related to the fragmentation function ($\mathscr{D}(z, Q^2)$ in Equation 2.9), which describes the

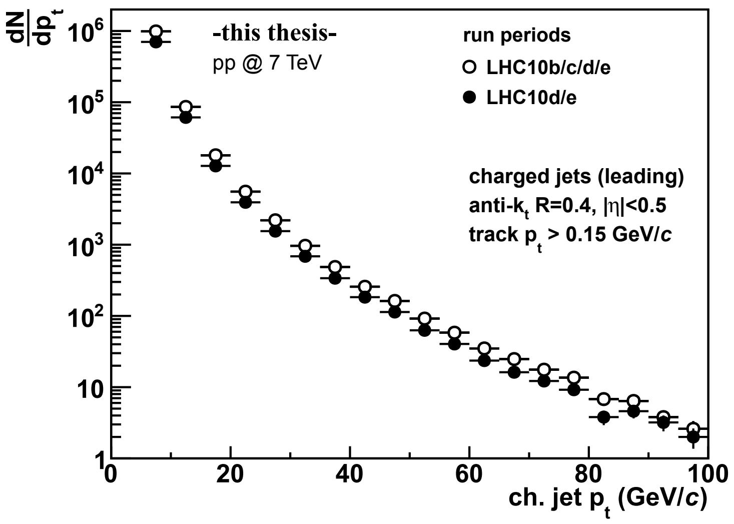

Figure 5.1: Number of reconstructed leading jets (uncorrected) in all analyzed run periods.

branching process of the hard-scattered parent parton into the final hadronic-state. A restriction in the measurement of charged particles only, is the impact on the jet p_t scale and its resolution.

5.1 Event Selection

The analyzed data was taken with the ALICE experiment in the first year of LHC operation in 2010 with a center-of-mass energy of $\sqrt{s} = 7\,\mathrm{TeV}$. This includes four run periods (namely LHC10b, LHC10c, LHC10d and LHC10e) with 242 good runs[1]. Only the last two run periods with 156 runs were used for the combined results, as will be discussed later. Each run period is a period of data taking under similar detector conditions and reconstruction settings. All runs were taken with the nominal solenoid magnetic field in the central barrel of $|B| = 0.5$ (with both possible polarizations). On the complete data sample of minimum-bias (MB) events, an offline event selection which rejects background events, like beam-gas collisions, was applied. Furthermore, only events with a reconstructed vertex and a vertex position of $|z| < 8\,\mathrm{cm}$ have

---

[1] Quality according to the ALICE Run Condition Table: `http://alimonitor.cern.ch/configuration/`

Table 5.1: Number of charged leading jets in slices of p_t in the different run periods LHC10b, LHC10c, LHC10d, LHC10e, written as b, c, d, e.

jet p_t (GeV/c)	b	c	d	e	b−e (all)	d+e
20 - 30	3 069	8 287	18 325	9 084	38 765	27 409
30 - 40	539	1 594	3 395	1 730	7 258	5 125
40 - 60	220	626	1 362	638	2 846	2 000
60 - 80	48	101	207	99	455	306

been accepted. Overall 277 million MB events passed all quality cuts and were analyzed, whereas 190 million events are from the later two run periods (see Table A.2). With an inelastic cross-section of $\sigma = (73.2^{+2.0}_{-4.6} \pm 2.6)\,\mathrm{mb}$ [AliEN], 190 million events correspond to an analyzed integrated luminosity of $\mathscr{L}_\mathrm{int} = (2.60^{+0.16}_{-0.07} \pm 0.09)\,\mathrm{nb}^{-1}$. More about the minimum-bias trigger in ALICE and the event selection is written in Section 3.5.2.

For comparison with simulations on detector level, PYTHIA jet-jet events of pp collisions at $\sqrt{s} = 7$ TeV, as introduced in Section 3.5.5, were used. The simulations were anchored to a run in the largest run period LHC10d. This means the simulation was done with corresponding detector configuration and beam vertex condition.

5.2 Jet Reconstruction

The analysis is based on leading jets, i. e. jets of largest p_t in the event. They were reconstructed with the anti-k_t or HIJA/UA1 algorithms with a radius parameter of $R = 0.4$ and track $p_\mathrm{t}^\mathrm{min}$ of 0.15 GeV/c. The covered pseudo-rapidity range is defined to $|\eta| < 0.5$ by the tracking acceptance ($|\eta| < 0.9$) and the jet size. Note that always the reconstructed jet axis is taken as jet direction in (η,ϕ). The latest generation of hybrid tracks with quality cuts as described in Section 4.2 was used in this studies.

The obtained charged leading jet spectrum reaches up to about 100 GeV/c, as can be seen from Figure 5.1, for all run periods and for LHC10d and LHC10e only. The momentum distribution in jets is analyzed in different jet p_t bins. The numbers of anti-k_t jets per bin are listed in Table 5.1. For the presented final results, from the run periods LHC10d and LHC10e, the yield is shown in the last column.

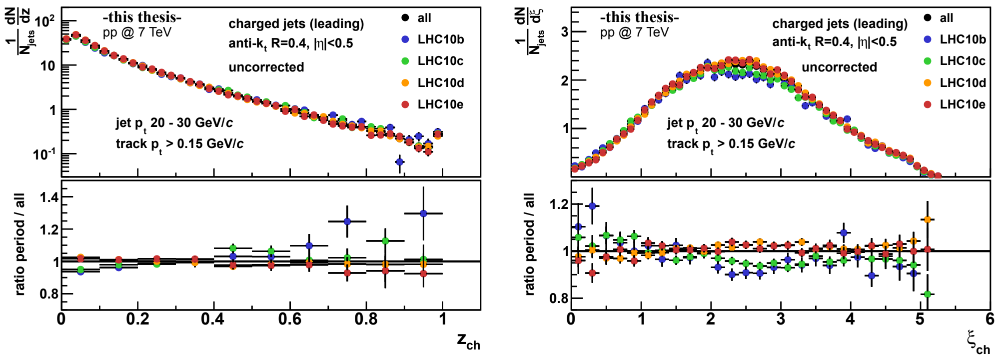

Figure 5.2: Momentum distribution in jets, z (left) and ξ (right), in different data taking periods. Error bars are purely statistical.

5.3 Measurement of the Charged Particle Momentum Distributions

The fractional particle momentum distribution is determined from all reconstructed tracks within the identified jets, whereas all tracks within a cone of radius R_{asc} around the jet axis (η,ϕ) are associated to the jet. This method is used for the presented results. Consider all tracks which are related to the jet during the finding process is another option. For a jet finder with fixed conical area of radius R_{jet}, like HIJA, both methods are equivalent if $R_{\mathrm{asc}} = R_{\mathrm{jet}}$ and jets do not overlap. For cluster algorithms, like anti-k_{t}, the jet area is only close to conical and not fixed. Therefore, not necessarily all associated tracks are part of the reconstructed jet, i. e. $\sum p_{\mathrm{t}}^{\mathrm{tracks}} \neq p_{\mathrm{t}}^{\mathrm{jet}}$ and even $p_{\mathrm{t}}^{\mathrm{track}} > p_{\mathrm{t}}^{\mathrm{jet}}$ with $z > 1$ is possible as consequence. However, in pp events the size of anti-k_{t} jets varies only little and the effect is negligible.

An advantage of the first method is the independence of the used jet finder. In addition, this method allows to change the radius of the associated tracks, R_{asc}, while the jet finding process is unchanged. This enables the possibility to study the jet structure as function of R_{asc}. In the context of this thesis the value was kept fixed to $R_{\mathrm{asc}} = 0.4$.

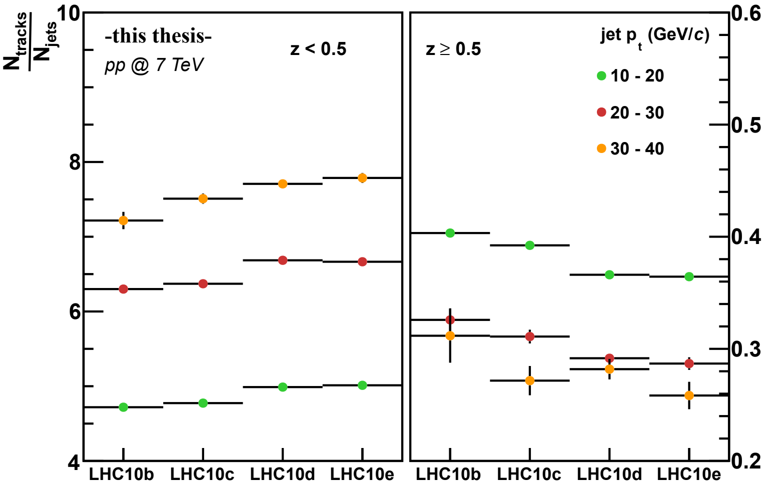

Figure 5.3: Comparison of soft-fragmented ($z < 0.5$, left) and hard-fragmented region ($z \geq 0.5$, right) in different data taking periods. Error bars are purely statistical.

5.3.1 Results from Run Periods

In this section, the different run periods are compared in order to ensure consistent results. Figure 5.2 shows the raw z- and ξ-distribution of one jet p_t bin for all four considered run periods. The presented ratios are related to the combined results from all run periods. The ratios of run period LHC10d and LHC10e are close to unity due to the larger statistical weight in these run periods. Of relevance is the apparent divergence between the different periods. In the later run periods (LHC10d, LHC10e), the measured fragmentation is softer. The z-distributions seems to be tilted relative to each other, with a fixed point around $z = 0.35$, though, the statistics at high z is quite low. The ξ-distribution illustrates that there is a large deviation close to the maximum of the hump-backed plateau around $\xi = 2.5$. This corresponds roughly to a track p_t of $1.5 - 2.5$ GeV/c. Indeed, in the track p_t spectra there is a deviation in these low p_t region.

In Figure 5.3, the numbers of tracks from soft ($z < 0.5$) and from hard ($z \geq 0.5$) fragmentation are shown for all four run periods and three jet p_t bins. The obvious softer fragmentation and larger number of tracks in high

p_t jets is discussed later. The trend from earlier (LHC10b) to later (LHC10e) run periods towards softer fragmentation in the measurement is apparent for all jet p_t. Since the momentum is conserved within a jet p_t bin, the trend in the number of tracks in the soft and in the hard fragmented region goes in opposite direction. Run-by-run the measured fragmentation is, besides some statistical fluctuations, rather the same within the run-periods (see Figure A.1 in Appendix A).

The explanation, for the discrepancy in the run periods, is a different tracking procedure which was applied for the later run periods beginning from LHC10d [Bus12]. That leads to an overall better tracking efficiency at low momenta and $\eta \approx 0$, close to the central electrode in the TPC. Due to the worse performance in the earlier run periods, LHC10b and LHC10c, and the fact that the simulations are based on period LHC10d, only the run periods LHC10d and LHC10e are used for the following results. Furthermore, these two run periods constitute 69 % of all available events. An improvement for the other run periods can be expected with a new reconstruction pass of the data.

5.3.2 Uncertainties and Background

An essential amount of background in jet measurements comes from the underlying event (UE) [Abe+11]. It occurs from

- beam remnants fragmentation,
- soft processes,
- initial-state radiation (ISR),
- final-state radiation (FSR), and
- multiple partonic interactions (MPI).

Strictly speaking, final-state radiation, as soft gluon radiation out of the jet cone, is no background in terms of jet measurements. Nevertheless, it is treated as background since it can experimentally not be distinguished from other underlying event which does not originate from hard processes.

Different approaches exist to estimate the contribution from the underlying event [Est11]. In Figure 5.4, for one jet p_t bin the reconstructed fractional momentum distribution in jets (signal + background) is shown, together with the underlying event estimated by two methods, and the resulting distribution

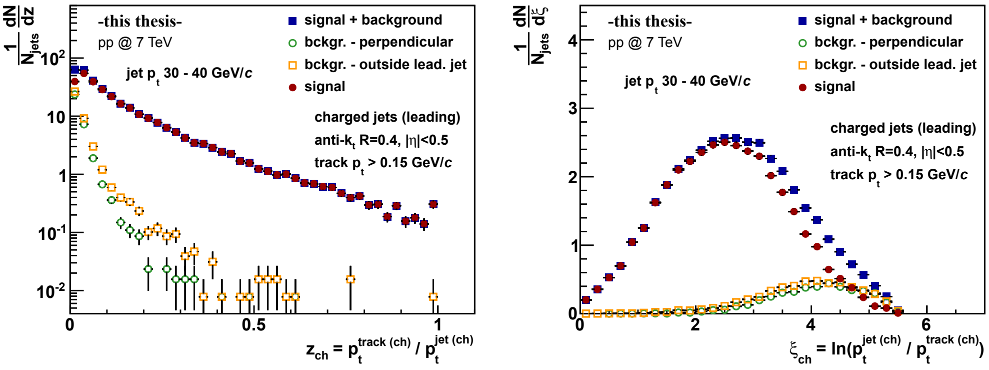

Figure 5.4: Momentum distribution in jets and the background from the underlying event in pp collisions. Shown is the background (open symbols) estimated by two different methods: 1) Perpendicular to the jet axis and 2) outside of the leading jet. The reconstructed distribution (signal+bckg.) is subtracted by the background estimated by method 1.

after underlying event subtraction (signal). The background was estimated by measuring the momentum flux in the event:

1. in a cone, perpendicular to the jet axis, and
2. in the region, outside of the leading jet.

The first method directly measures the momentum contribution of the underlying event in a cone with a radius equal to the nominal jet size ($R = 0.4$). The cone axis is rotated to the jet axis by $\pi/2$ in ϕ. This cone perpendicular to the jet axis probes the event in a region, also called "transverse region" [Abe+11], which should exhibit only little correlation to the jet fragmentation.

In the second method, all tracks outside of the leading jet are considered, whereas a minimum distance of the tracks to the jet axis of $R_{\mathrm{bckg}} = 0.7$ is required. To factor the jet size in, n tracks are randomly selected from those N tracks. The ratio of the selected tracks, n/N, is defined by $A_{\mathrm{jet}}/(A_{\mathrm{trk}}^{\mathrm{asc}} - A_{\mathrm{bckg}}^{\mathrm{jet}})$, where $A_{\mathrm{jet}} = \pi R_{\mathrm{jet}}^2 = \pi \cdot 0.4^2$ is the jet area, $A_{\mathrm{trk}}^{\mathrm{asc}} = 1.8 \times 2\pi = 11.3\,(\eta \times \phi)$ is the area of track acceptance and $A_{\mathrm{bckg}}^{\mathrm{jet}} = \pi R_{\mathrm{bckg}}^2 = \pi \cdot 0.7^2$ is the jet area with increased radius from which tracks are excluded. The underlying event, estimated by this method, has a larger tail in the z-distribution compared to the first method, as can be seen in Figure 5.4. The *away-side region*, with possible contributions from the jet recoiling from the leading jet, is also included by this method.

Table 5.2: Average number of reconstructed charged tracks (S+B) in jets, the estimated background (B), and the residual signal (S). The last column gives the signal to background ratio.

	$\langle N_{\text{tracks}} \rangle$			
jet p_t (GeV/c)	S+B	B	S	S/B
$20-30$	6.97 ± 0.04	0.86 ± 0.01	6.11 ± 0.04	7.1 ± 0.1
$30-40$	8.01 ± 0.11	0.86 ± 0.01	7.15 ± 0.11	8.3 ± 0.2
$40-60$	8.92 ± 0.20	0.88 ± 0.02	8.04 ± 0.20	9.1 ± 0.3
$60-80$	10.11 ± 0.57	0.81 ± 0.05	9.29 ± 0.58	11.5 ± 1.0

Since those jets are strongly correlated, this method does not estimate only the pure underlying event, but overestimates it on average. Optionally, one could exclude the two largest jets in the event to estimate the underlying event. However, on the other hand, that may underestimate the underlying event since only a small fraction of all events has the away-side jet within the acceptance.

The measurement of the underlying event perpendicular to the jet axis is more adequate. It probes the background directly in a cone size of a jet and reproduces best the $\mathrm{d}N/\mathrm{d}\eta$ distribution of background tracks in jets. Therefore, it was used for corrections in this thesis.

As seen in Figure 5.4, the underlying event naturally has the most impact on the soft part. In the z-distribution, it significantly effects only the lowest bins and is almost negligible; note the logarithmic scale. In the ξ-distribution, which is more sensitive to the soft region, the underlying event is much more apparent. In Table 5.2, the uncorrected average number of tracks are listed for the raw reconstructed jets (S+B), the underlying event as background (B), and the resulting signal (S). Even though the number of tracks in the reconstructed jets increases with increasing jet p_t, the estimated background is constant within its statistical uncertainties. This confirms the independence of the estimated underlying event, for the used method, from the hard process at high p_t. This is in line with the published underlying-event measurements from ALICE [Abe+11]. On average, the underlying event contributes with 0.86 ± 0.01 tracks to a jet. The signal to background ratio increases from 7.1 ± 0.1 for low jet p_t ($20-30$ GeV/c) to 11.5 ± 1.0 for $60-80$ GeV/c jets, see Table 5.2.

The following results are only partially corrected for the underlying event and indicate statistical uncertainties only. The momentum distributions are

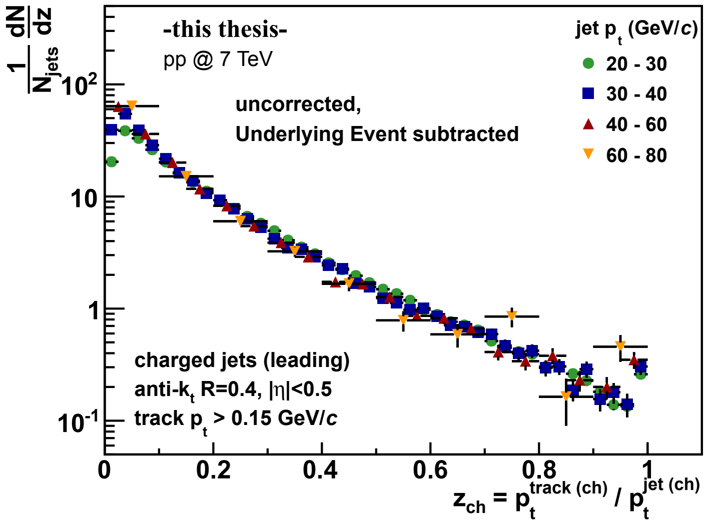

Figure 5.5: Charged momentum distribution in jets, $z_{\mathrm{ch}} = p_{\mathrm{t}}^{\mathrm{track}}/p_{\mathrm{t}}^{\mathrm{jet}}$, corrected for the underlying event. The shown uncertainties are statistical.

---

subtracted by the underlying event estimated from the perpendicular cone, whereas the jet scale is not corrected. Corrections for tracking inefficiencies and secondary contaminations are also necessary for a full correction. The correction is not only a common one-dimensional scaling, but as z and ξ are corrected, it has an influence on the jet scale, which results in an additional shift of z and ξ. Furthermore, the tracking efficiency is different in reconstructed jets than it is in an inclusive sample of minimum-bias events [Bus11]. Obviously, there is a larger number of high-p_{t} tracks in a more dense phase-space in jets. Hence, the tracking efficiency of high-p_{t} tracks in jets is reduced. On the other hand, a reconstructed jet already implies reconstructed tracks. This leads to an intrinsically better tracking efficiency towards tracks of high z since the jet reconstruction is biased accordingly (conditional probability), e. g. [Bus10]. These effects are expected to be well reproduced in simulations, so that the raw distributions corrected for the underlying event can be compared in Monte-Carlo simulations and data, in a later section. This allows a systematical view on the capabilities of ALICE and a validation of the simulations, which were also used in other analysis parts of this thesis.

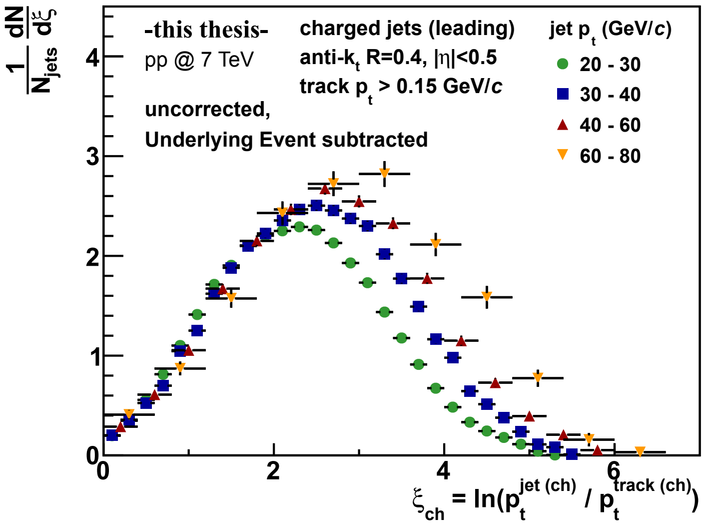

Figure 5.6: Hump-backed plateau of charged jets, $\xi_{\mathrm{ch}} = \ln(1/z)$, corrected for the underlying event. The shown uncertainties are statistical.

5.3.3 Measured Distributions

As already seen in Figure 5.3 and Table 5.2, jets with increasing p_{t} fragment softer, into a larger number of tracks. The average number of tracks in the jets increases from 6.11 ± 0.04 for $20 - 30$ GeV/c to 9.3 ± 0.6 for $60 - 80$ GeV/c. The corresponding full z-distributions are shown in Figure 5.5 for four jet p_{t} slices up to 80 GeV/c. The largest deviation between the distributions exists at the very soft part of $z < 0.1$. This is visible in more detail in the hump-backed plateau in Figure 5.6. As expected from pQCD, the maximum of the distribution is, with increasing jet p_{t}, shifted towards larger ξ, whereas the slope at low ξ (hard fragmentation) is similar for all jet p_{t}.

In the last bin of the z-distributions, a conspicuous step-up is visible. This comes from single track jets with $z = 1$. It is also present, even though a bit less pronounced, in the PYTHIA simulations, which are discussed in the next section.

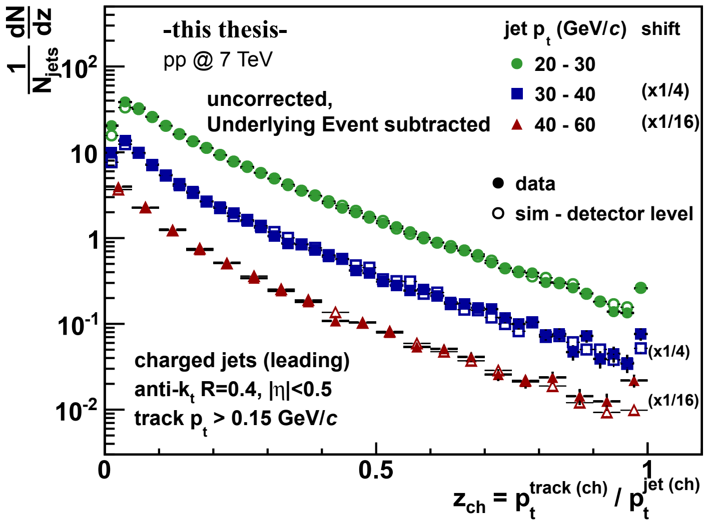

Figure 5.7: Charged momentum distribution in jets, $z_{\mathrm{ch}} = p_{\mathrm{t}}^{\mathrm{track}}/p_{\mathrm{t}}^{\mathrm{jet}}$, from data in comparison with PYTHIA simulations on detector level, both corrected for the underlying event. The distributions are scaled for clarity. The shown uncertainties are statistical.

5.3.4 Results in Comparison with Simulations

In Figure 5.7 and Figure 5.8, the distributions are presented in comparison to PYTHIA simulations on detector level. The z-distributions of the different jet p_{t} ranges are scaled for clarity. The softer fragmentation with increasing jet p_{t} seems to be generally reflected by the simulations. But in the lowest bins of the z-distribution ($z < 0.25$) and, with more detail and significance in the high ξ region ($\xi > 3$), a discrepancy is apparent between the measurement and Monte-Carlo simulations. For clarity, only two jet p_{t} ranges of the ξ-distributions are shown. The ratio of measurements over simulations is shown in Figure 5.9. The deviation starts at little lower ξ for lower jet p_{t}. This indicates that it is a deviation which depends mainly on track p_{t}. As seen before, the underlying event is a relevant background in the affected region. For the presented PYTHIA simulations, the Perugia-0 tune [Ska10] was applied. Already in underlying event studies [Abe+11] in ALICE it has been observed that PYTHIA Perugia-0 simulations do underestimate the low p_{t} region at the new regime of LHC energies by about 15 %. In general, the multiplicities at

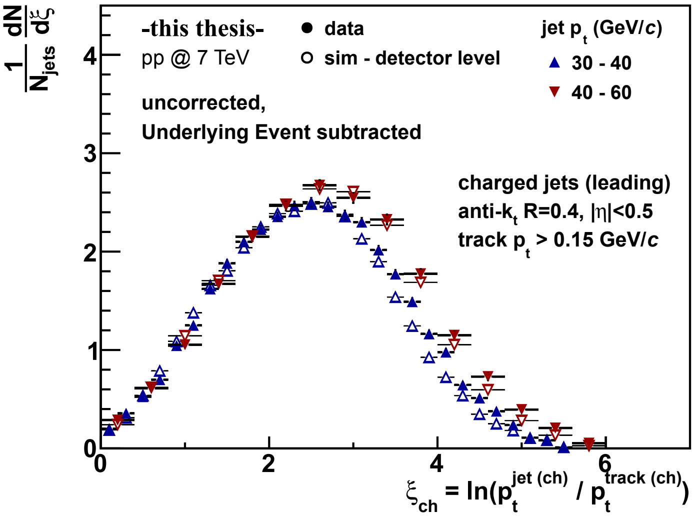

Figure 5.8: Hump-backed plateau of charged jets, $\xi_{ch} = \ln(1/z)$, from data in comparison with PYTHIA simulations on detector level, both corrected for the underlying event. The shown uncertainties are statistical. Ratios are shown in Figure 5.9.

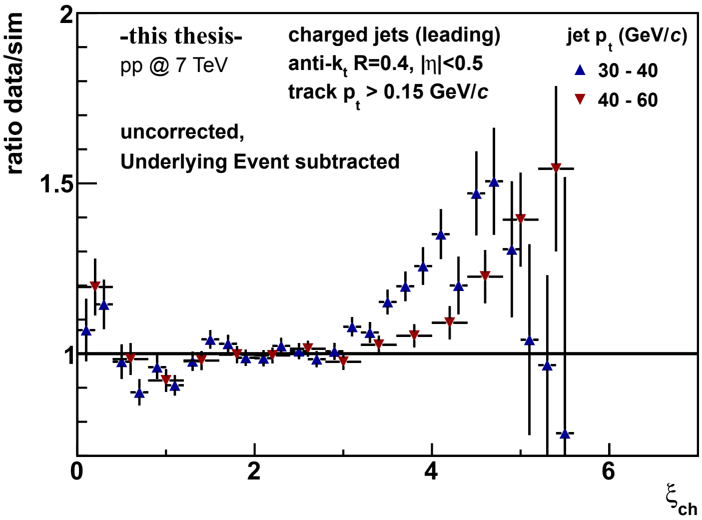

Figure 5.9: Ratio of measured hump-backed plateau to PYTHIA simulations at detector level, as shown in Figure 5.8.

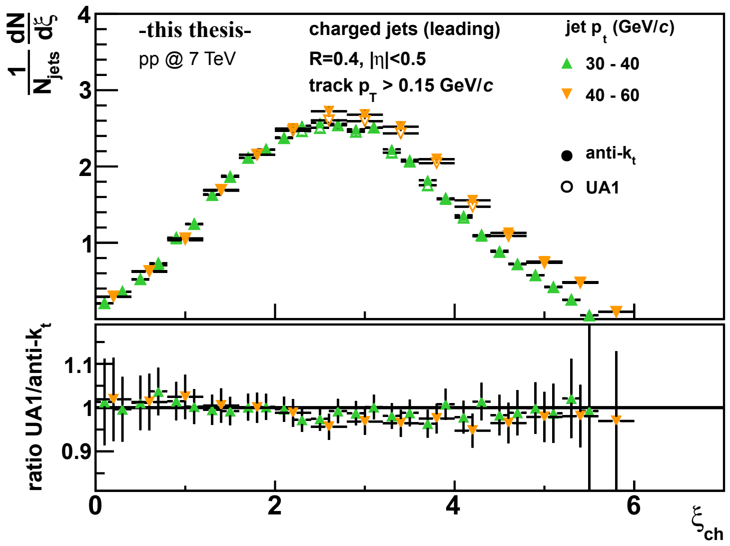

Figure 5.10: Comparison of the hump-backed plateau measured with anti-k_t (full) and UA1 (open) jet algorithms, for two jet-p_t bins.

$\sqrt{s} = 7$ TeV are underestimated by most of the models from the pre-LHC age. Nevertheless, this cannot explain the deviation which is seen in Figure 5.9 with distributions corrected for the underlying event.

At intermediate $\xi \approx 1.5 - 3$, the data agrees with the simulation with a maximum deviation of 3 %. Below this region, again discrepancies between measurement and simulation are visible. There, the statistical uncertainties also increase, but the divergence is still significant. A possible explanation is that in this region the track p_t resolution is crucial and may not be fully reproduced by the simulations, especially since the simulations are anchored to one run only. The apparent divergences fit in the picture of redistributed tracks from low to high p_t due to resolution and a steeply falling track spectrum.

5.3.5 Robustness Against Jet Finder Algorithms

The UA1 cone algorithm gives jets with comparable structure as those from anti-k_t jets, as can be seen in Figure 5.10, where results of both algorithms are compared for two jet p_t bins. The deviations are less than 5 %. It appears that the UA1 algorithm leads to slightly more hard-fragmented jets. This can

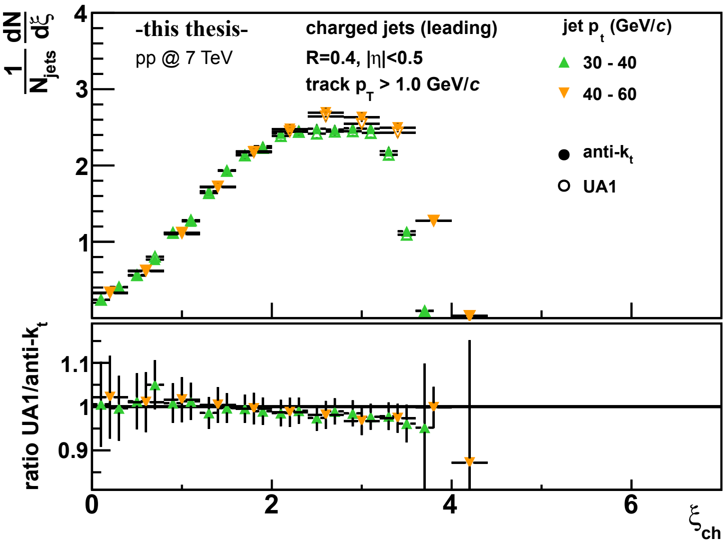

Figure 5.11: Hump-backed plateau for an increased track-p_t cut of 1 GeV/c. The distribution is shown for anti-k_t (full) and UA1 jets (open), for two jet-p_t bins.

be understood since the UA1 jets are biased by the required seed particles of 4 GeV/c. Therefore, this algorithm might miss some very soft-fragmented jets. For jet p_t far above this threshold the bias actually should be negligible, though. As introduced earlier, tracks associated to the jets are collected in a fixed cone around the jet axis for this fragmentation measurements. This is independen of the used jet finder, a larger or smaller jet size of the anti-k_t jet can only effect the jet p_t scale. However, within the statistical uncertainties, the ratio of both distributions are still consistent with unity.

At this point, the influence of a larger track-p_t cut shall be discussed. Figure 5.11 shows the measured hump-backed plateau with an increased minimum track-p_t cut-off of 1 GeV/c. It shall be noted, even though the same ranges of raw jet p_t as for the lower track-p_t cut are shown, the scale of the true jet p_t is different. While for a low track-p_t cut of 150 MeV/c the expected true charged-jet p_t is still close to the reconstructed jet p_t, the reconstructed jet p_t is significantly reduced by the larger track-p_t cut of 1 GeV/c. A larger track-p_t cut-off sometimes is considered to reduce the impact of the underlying event in heavy-ion jet reconstruction. As visible in Figure 5.11, the anti-k_t and UA1 algorithm give similar results concerning the fragmentation. But a larger track-

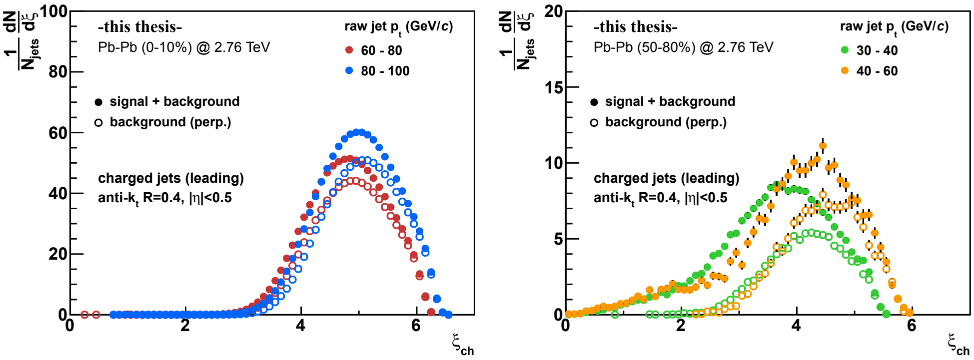

(a) Central events (0 – 10 %).

(b) Peripheral events (50 – 80 %).

Figure 5.12: Illustration of the underlying event in central and peripheral Pb–Pb collisions. Note the different scale at the ordinate.

p_t cut significantly cuts in the ξ-distribution, in a region which is sensitive to an expected jet-quenching. Here the ALICE experiment actually can profit from its good tracking capabilities from high p_t, which is indispensable for jet reconstruction, to very low p_t, which allows a detailed study of the soft fragmentation.

5.4 Outlook to Pb–Pb

As seen before, a contribution of the underlying event is apparent in pp collisions. Nevertheless, it is small compared to the signal ($S/B \approx 10$), and the uncertainties on the corrections are just as small. In Pb–Pb collisions the soft background is much larger. In Figure 5.12 the underlying event measured in the transverse region in Pb–Pb collisions at $\sqrt{s_{NN}} = 2.76\,\text{TeV}$ is shown for two centrality classes. Note the different scale at the ordinate. In the presented jet p_t region below 100 GeV/c, the underlying event is of the same order or even larger than the signal. For example, the estimated signal to background ratio in central collisions (0-10 %) for uncorrected $80 - 100$ GeV/c jets is 0.226, with an average of 91.8 background and 20.8 signal tracks, even though this is dominated by low p_t at high ξ. In the more peripheral collisions ($50 - 80$ %), the signal to background ratio is still 0.8 for $40 - 60$ GeV/c jets ($\langle N_{bkg} \rangle = 13.7 \pm 0.7$, $\langle N_{sgn} \rangle = 10.7 \pm 1.4$).

Furthermore, the underlying event fluctuates from event-to-event. A good understanding of the background is mandatory for the pure jet cross-section measurement already. A detailed study of the event background fluctuations in Pb–Pb collisions is presented and discussed in Chapter 7. If possible one can, in addition, look into higher jet energy regions in terms to increase the signal. The statistics of jets from pp events, which are used as baseline, reaches up to about 100 GeV/c after one year minimum-bias data-taking, as presented. For sufficient reference statistics at higher jet p_{t}, a jet trigger is necessary. Some studies about a possible jet trigger in ALICE with the TRD are presented in the next section.

Chapter 6

TRD Jet-Trigger in pp

In order to optimize the use of the delivered luminosity for jet reconstruction, an efficient online trigger is necessary. The read-out rate of ALICE is limited by the TPC to about 300 Hz in Pb–Pb and about 1.4 kHz in pp mode, respectively [Alm+10]. While the interaction rate in pp collisions is at nominal luminosity of $\mathscr{L} = 10^{30}\,\mathrm{cm}^{-2}\mathrm{s}^{-1}$ close to 100 kHz. The TRD is designed to identify charged high-p_t particles within the central barrel and provides a L1 trigger decision based on this before the TPC starts the read-out. In this chapter, studies of a jet trigger with the TRD are presented.

6.1 General Nomenclature

At first some basic variables like trigger efficiency and rejection factor shall be introduced, and it shall be explained how they are used in context of this thesis. Assuming a set of minimum-bias events, A (all MB), which consists of two disjoint sub-sets, $A = S \cup B$, with signal events S and background events B. The events are also uniquely classified by the trigger decision in two other sets of triggered events, T, and rejected events, R, hence it is $A = T \cup R$ (see Figure 6.1). The aim of an efficient trigger with large rejection factor and low contamination is to trigger preferably all signal events and reject all background events.

The efficiency ϵ_trg of the trigger is defined as triggered signal events over all signal events:

$$\epsilon_\mathrm{trg} = \frac{|S \cap T|}{|S|}. \tag{6.1}$$

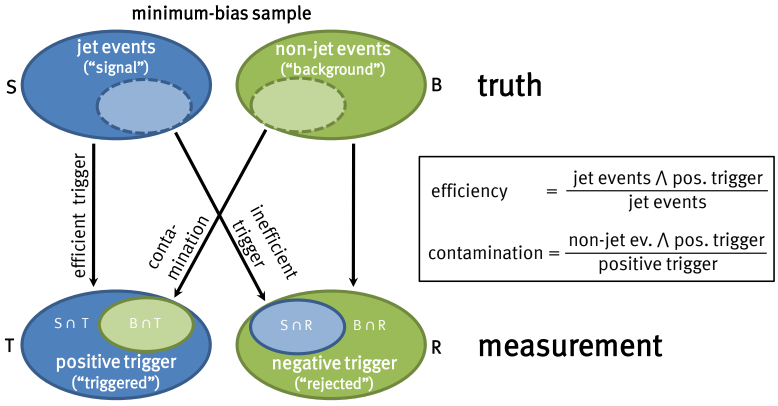

Figure 6.1: Scheme of a trigger selection of jet events as desired signal from a minimum-bias data sample.

Triggered background events contribute to the contamination of the trigger:

$$C = \frac{|B \cap T|}{|T|}. \tag{6.2}$$

Another important variable is the rejection factor RF, which describes the reduction of the recorded events in relation to all (minimum-bias) events. It is the inverse of all triggered events over all events:

$$RF = \frac{|A|}{|T|} = \frac{|T \cup R|}{|T|}. \tag{6.3}$$

The rejection factor is relevant for the bandwidth occupied by the trigger. Often it is necessary to find the best trigger condition, according to the efficiency and bias, for a given rejection factor.

A bias, in this term, is understood as any deviation in a distribution obtained from the triggered sample in comparison to the true distribution. The bias depends on the variable which is considered. A trigger which is not uniformly efficient in a variable introduces a bias for this variable. In fact, an efficiency which is not constant for the variable κ, $\epsilon(\kappa) \neq \text{const.}$, describes the bias in κ in the triggered data sample. Some inefficiencies and the related biases even are desired, e. g. the reduction of low-p_{t} jets in the recorded data sample in favor of high-p_{t} jets.

In case of a jet trigger, the signal events S are jet events and background events B are non-jet events, respectively. The jet trigger efficiency is in general determined as function of the jet transverse momentum. The question of what is a jet event and how large is the jet p_t in consequence needs a clear definition. The trigger efficiency is only well defined in context of the jet description (see Chapter 4). In the following studies, anti-k_t jets with radius parameter $R = 0.4$ within pseudo-rapidity $|\eta| < 0.5$ are used, as a preferable definition in jet analyses in ALICE.

Since for a meaningful trigger the desired signals, e. g. high-p_t jets, are rare in a minimum-bias sample A, a very large number of (simulated) events would be needed to study the trigger efficiency. It can be estimated from the set of signals S, as can be seen from Equation 6.1. In simulations, high p_t jets can be specifically produced, e. g. in PYTHIA simulations by requiring hard partonic scatter within a certain p_t-hard range, see Section 3.5.5. Hence, a specific sample of jet events, J, with $A \supseteq J \supseteq S$ can be generated and used for studies of the trigger efficiency. The trigger should be efficient down to low p_t, where the statistics of real minimum-bias data is sufficient high, in order to have some overlap with the triggered data. This is important for the data-driven verification of the trigger efficiency.

The sample of signal events does not allow to estimate the contamination or rejection factor. For this, a minimum-bias sample is required. However, in that case the number of contained signals, i. e. jets, can be low. The minimum-bias sample can be from simulations, but should also be verified with real data. In Chapter 5, it has been demonstrated that the fragmentation pattern between data and PYTHIA agrees well with the hard fragmentation, which is relevant for the trigger. A good agreement of the fragmentation is essential for the evaluation of trigger biases in these observables.

6.2 Trigger Concept

The short drift time of the TRD (described in Section 3.4) enables a fast read-out. Specialized read-out electronics directly mounted on top of the detector feature highly parallelized data acquisition for a trigger decision. The radial distance of the TRD to the beam pipe gives a good lever arm for the determination of high transverse-momenta. All that makes the TRD an ideal detector for triggering on high-p_t hadrons. In addition, the measurement of transition radiation, for electron identification and pion rejection, enables the implementation of an electron trigger [Wes13], which is crucial for heavy flavor analyses. In this thesis only the charged-jet trigger shall be discussed.

Due to the segmentation of the TRD in stacks, one stack of TRD chambers can be used as a (squared) "cone" for a potential jet. A stack has a dimension of about $0.35 \times 0.35\,(\eta \times \phi)$. That means, a cone of radius 0.18 fits in the stack and the area of a stack of 0.12 corresponds to a cone with radius 0.20. In pseudo-rapidity, η, the dimension of the stacks varies between roughly 0.33 at mid-rapidity and 0.38 at larger rapidities.

The implementation of a trigger closest to offline jet reconstruction would be the summation of the transverse momenta of all tracks within one stack, i. e. of one TMU. A summation, however, is not possible since at this stage only the displacement a of the linear fit of the TRD tracklets to the nominal interaction point is known from all tracks. For a description of the TRD and its data flow, see Section 3.4. An alternative option is to count the number of tracks above a dedicated threshold $p_{\mathrm{t}}^{\mathrm{min}}$, which can be defined as a threshold of parameter a. The threshold should be selected in a way that most of the tracks which belong to the underlying event are rejected. If a minimum number of tracks $N_{\mathrm{trk}}^{\mathrm{min}}$ with $p_{\mathrm{t}} > p_{\mathrm{t}}^{\mathrm{min}}$ is found, at least a jet momentum of $p_{\mathrm{t}}^{\mathrm{jet}} > N_{\mathrm{trk}}^{\mathrm{min}} \cdot p_{\mathrm{t}}^{\mathrm{min}}$ is reached, though from the small area of a stack only.

6.2.1 Challenges

Using the simple procedure with hard thresholds, like $N_{\mathrm{trk}}^{\mathrm{min}}$ tracks and minimum $p_{\mathrm{t}}^{\mathrm{min}}$, to identify online jets with the TRD, one easily introduces a bias on the triggered jets. For example, jets are discriminated which just miss one threshold ($N_{\mathrm{trk}}^{\mathrm{min}}$ or $p_{\mathrm{t}}^{\mathrm{min}}$) but greatly exceed the other one. That obviously has an influence on the fragmentation pattern of the triggered jets. Additional thresholds, e. g. $p_{\mathrm{t},2}^{\mathrm{min}} > p_{\mathrm{t}}^{\mathrm{min}}$ and $N_{\mathrm{trk},2}^{\mathrm{min}} < N_{\mathrm{trk}}^{\mathrm{min}}$, may be sufficient to reduce the bias. But needed resources (logic cells) of the GTU do limit the possible number of thresholds and conditions.

Another constraint for a trigger with this approach may be the fixed "cone" size and position due to the detector geometry. The detected jet area of an equivalent cone radius $R = 0.2$ is too small for full charged-jet reconstruction, even if the jet core hits the center of the stack. In any case the trigger shall only verify the existence of a jet, wherefore the stack size should be sufficient. The fixed position of the stacks causes problems with jets whose centroids are close to an edge of the stack. It can be expected that such jets are discriminated if only single stacks are taken into account. Including adjacent stacks, either

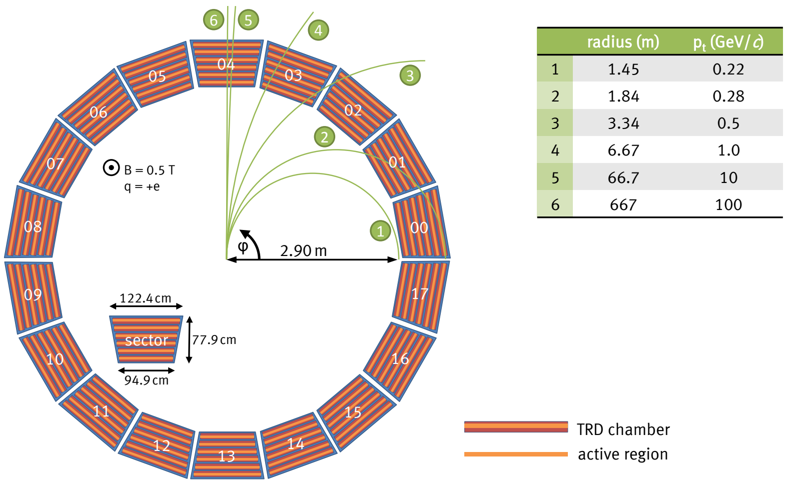

	radius (m)	p_t (GeV/c)
1	1.45	0.22
2	1.84	0.28
3	3.34	0.5
4	6.67	1.0
5	66.7	10
6	667	100

Figure 6.2: View of the 18 TRD super-modules in beam direction and the deflection of charged particles ($q = +e$) with different transverse momenta in the magnetic field $B = 0.5$ T.

generally or in special cases, may solve this challenge. Moreover, due to GTU design, only stacks within the same super-module can be considered together in the SMU before the L1 trigger decision.

Also the deflection of the particles caused by the magnetic field of (up to) $B = 0.5$ T has to be taken into consideration (see Figure 6.2). The particles, starting at the vertex, cover a distance of at least 2.90 m, traversing the ITS and the TPC, before they reach the TRD. For example, particles with $p_t > 2$ GeV/c undergo a deflection equivalent to a shift in azimuthal angle of $\Delta\phi < 0.11$ at the inner-side of the TRD. Consequently, up to 31 % of particles with a transverse momentum above a supposed p_t cut of 2 GeV/c may be shifted from one stack to another. This is an intrinsic limitation of meaningful p_t^{min} already.

The following studies illustrate the feasibility of a TRD jet trigger and find the most practical procedure with well defined thresholds. Since the trigger decision will be made on the basis of charged particles and will depend on the detector geometry, the trigger will, in any case, not be without any bias. Hence, it is crucial to know the trigger bias and consider it in the jet analysis if triggered data samples are used.

6.2.2 Approach

For the presented trigger studies, simulated offline TRD stand-alone tracks were used, while the real trigger decision relies on online tracklets and on tracks reconstructed by the TMU in the GTU. The only requirement to the offline TRD tracks is that they have at least four tracklets within the same stack. Then the track is assigned to this stack. The TMU cannot match online tracklets from different stacks and also requires at least four tracklets. No other quality cuts were applied to the offline tracks. From now on, the offline stand-alone tracks with these conditions are just called *TRD tracks*.

A different tracking efficiency and momentum resolution between online and offline may deter the accuracy of the obtained values. The online track reconstruction by the LTU is conceptually different from the offline tracking. For the online tracking the tracking efficiency drops for $p_t = \mathcal{O}(1-3)$ GeV/c [Kle11e] due to the strong curvature. Up to an offline track $p_t = \mathcal{O}(10)$ GeV/c the p_t resolution is about 20 % [Kle11d]. Above, the resolution does inrcrease and, in addition, the p_t is underestimated on average. Both values illustrate the lower and upper limit of possible trigger p_t thresholds. However, these are preliminary numbers and the settings of the TRD front-end electronics are not yet completely optimized, this study provides insights into the feasibility of a TRD jet-trigger without the detailed implementation of the online tracking and has been one of the first studies of this kind. It illustrates the introduced biases and presents solutions to minimize these. The verification with real data is not discussed.

As mentioned earlier, the studies in this thesis are done with jets as reference from the FastJet anti-k_t jet finder with radius parameter $R = 0.4$. They are reconstructed from global tracks, i. e. offline tracks with full detector information, and a minimum track-p_t of 0.15 GeV/c. The hybrid track approach is used as described in Section 4.2. Jets, referred to as “generated jets”, are reconstructed from Monte-Carlo particles which are physical primaries, charged, and $p_t > 0.15$ GeV/c.

6.3 Rejection Factor

From a simulated minimum-bias event sample the rejection factors are obtained. The variables are N_{trk} and p_t^{min}, the minimum number of tracks N_{trk} above a transverse momentum threshold p_t^{min} within one TRD stack. Figure 6.3

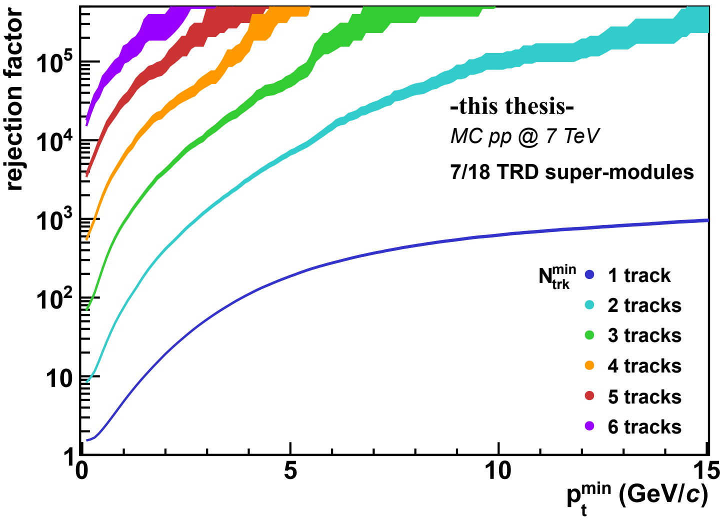

Figure 6.3: Rejection factor for the trigger condition of at least N_{trk} TRD tracks with a reconstructed track p_{t} above $p_{\text{t}}^{\text{min}}$ within one TRD stack. The used pp simulation of minimum-bias events is for 7 TeV collision energy and with 7 out of 18 TRD SMs. The widths of the bands indicate statistical uncertainties.

shows the rejection factor for different trigger thresholds. The used PYTHIA pp event production (LHC10f6a) was simulated for $\sqrt{s} = 7$ TeV, B=0.5 T, and anchor runs from the LHC10d run period. Data from 31 simulated runs[1] around the anchor run 126007 of the jet-jet production was used. Note that only 3 % of the full simulated statistics have TRD stand-alone tracker information and could be used. Hence, the study is limited to 2.2 million events out of the processed 70.4 million events.

The data is for 7 (out of 18) installed TRD super modules. For the fully installed TRD, the rejection factor would be lower by a factor of about 18/7. In fact, the factor of $18/7 \approx 2.6$ is an upper limit for the scaling factor. It approaches this limit under the condition that the rejection factor is dominated by trigger on real signals, i. e. the contamination approaches to zero, and the triggered signals are strongly focused compared to the dimension of a super

---

[1] anchor runs 125296, 125628, 125630, 125632, 125633, 125842, 125843, 125844, 125847, 125848, 125849, 125850, 125851, 126004, 126007, 126008, 126073, 126078, 126081, 126082, 126088, 126090, 126097, 126158, 126160, 126167, 126168, 126283, 126284, 126285, 125855

module. The second is not completely true for jets, but since the seven TRD super modules were installed in two groups of adjacent sectors (17–00–01: $-20° < \phi < 40°$ and 07–08–09–10: $120° < \phi < 200°$) this is of little relevance. It would be different if they were equally distributed in azimuth. With the discussed uncertainties a necessary scaling factor close to 2.6 can be assumed. In any case, this provides an upper limit and a demonstration of good rejection factors is also possible with the used simulation.

In order to study the impact trigger efficiency and the biases, two different trigger condition with the same rejection factors shall be identified:

(1) One condition with higher p_t^{min} and lower N_{trk}^{min}, and

(2) a second condition with lower p_t^{min} but larger N_{trk}^{min}.

Following trigger conditions with rejection factors above 10^5 were chosen from the simulations (see Figure 6.3):

	N_{trk}^{min}	p_t^{min} (GeV/c)	rejection ($\times 10^5$)
(1)	2	12.0	$1.48^{+0.42}_{-0.35}$
(2)	5	2.3	$1.39^{+0.38}_{-0.32}$

The rejection factors are listed as obtained from the simulations for 7 out of 18 super module, they were not scaled. For the fully installed TRD, they may be reduced up to a factor of 2.6, i. e. $RF \approx 0.5 \cdot 10^5$. The p_t thresholds are at the limit of the TRD trigger due to tracking efficiency (at lower threshold) and p_t resolution (at higher threshold). Nevertheless, they are chosen to illustrate the feasibility of the jet trigger, especially in consideration of the introduced bias, which is expected to be more pronounced under extreme conditions.

6.4 Jet Trigger Efficiency and Biases

The bias introduced by the different trigger conditions needs to be evaluated for various jet observables, like

- transverse momentum,
- (η,ϕ) position,
- collimation,

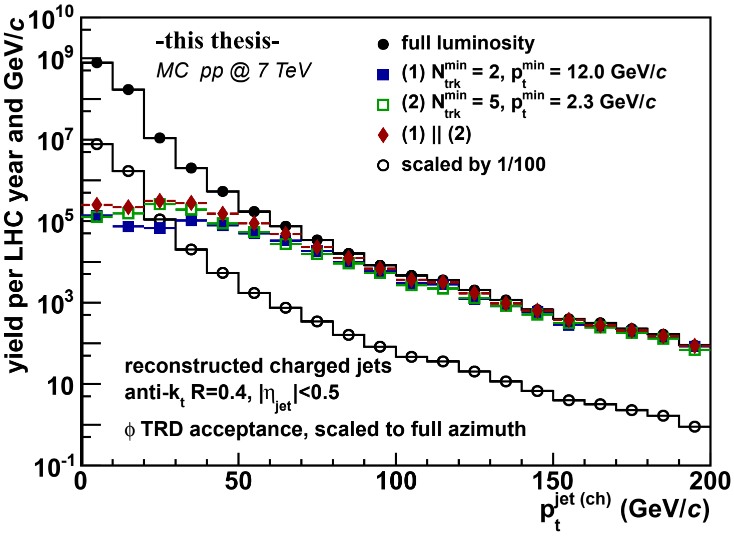

Figure 6.4: Charged-jet spectra for different trigger conditions. The indicated thresholds belong to TRD tracks within one stack. The down-scaled spectrum corresponds to the maximum L2 rate. The spectra are not corrected for tracking efficiencies and p_t resolution. Errors are only statistical. Resulting efficiencies are shown in Figure 6.5.

- fraction of charged particles, or
- momentum distribution within the jets.

The trigger efficiencies and biases are studied from the corresponding distributions which are obtained from jet simulations at $\sqrt{s} = 7$ TeV (see Section 3.5.5). The different p_t-hard bins of the simulation are scaled according to the cross-section and number of events which includes the events discarded during simulation ($s = \sigma(p_t^{hard})/N_{ev}$). Jets with $p_t^{jet} > 1.5\,p_t^{hard}$ are not taken into account. Reconstructed jets above this threshold are considered unphysical and create peaks in the distribution since only few entries at high jet p_t from low p_t^{hard} bins have a large weight.

Trigger Efficiency The obtained jet spectrum, as shown in Figure 6.4, is scaled to the yield of jets per year and 1 GeV/c. For this, a nominal luminosity of $\mathscr{L} = 10^{30}\,\text{cm}^{-2}\text{s}^{-1}$ (corresponding to an inelastic interaction rate of about 100 kHz) and effective LHC running time of 10^7 seconds per year

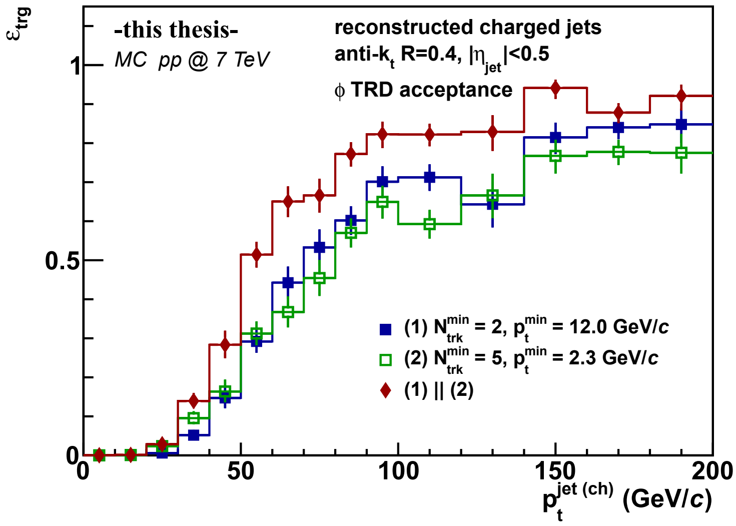

Figure 6.5: Trigger efficiencies of charged jets for different trigger conditions. The indicated thresholds belong to TRD tracks within one stack. The jet p_t is not corrected for tracking efficiencies and p_t resolution. Errors are only statistical. Associated jet spectra are shown in Figure 6.4.

(≈ 9.25 h per day over 10 months) is assumed. The spectra are estimated for the jet acceptance of $|\eta| < 0.5$. In azimuth, only the TRD acceptance with 7 installed SMs, as used in the simulation, was considered; this is $\phi < 2\pi/9$ (sector 00 − 01), $7\pi/9 < \phi < 11\pi/9$ (sec. 07 to 10), and $17\pi/9 < \phi$ (sec. 17). The spectra are scaled by 18/7 to obtain the expected yield with fully installed TRD. Also, the spectrum down-scaled by factor 100, corresponding to a realistic L2 rate of about 1 kHz, is shown. From the unbiased case ("full luminosity") and the estimated jet spectra for the chosen trigger conditions the trigger efficiency, ε_{jet}, as function of jet p_t is calculated (Figure 6.5). It illustrates the bias in jet p_t towards high-p_t jets. In general, biases have to be avoided. This bias in jet p_t is a special case, since a low trigger efficiency, $\epsilon_{jet}(p_t)$, at low jet-p_t is appreciated in favor of a good rejection factor. An ideal trigger would reject low-p_t jets ($\epsilon_{jet} = 0$) and would be full efficient at high p_t ($\epsilon_{jet} = 1$), with a sharp step at a jet p_t given by the trigger threshold, slightly below the maximum jet p_t which is reached with good statistics from minimum-bias data. That would provide the best available statistics up to high jet-p_t with the lowest required trigger rate. An overlap with the low-p_t jet spectrum from the minimum-bias data is necessary to ensure, in the final jet analysis, an sufficient transition from low p_t (from minimum-bias) to high p_t(from triggered data). This way, the scaling factor can be verified from the data.

If an efficiency of 1 is not possible at high p_t, it is important that the efficiency reaches a constant value. This indicates no bias in the observable and only a constant scaling factor is needed. Otherwise the correction of the bias complicates the measurement and introduces addition dependencies on modeling the bias with Monte-Carlo simulations.

From other trigger conditions, it was also seen that the trigger efficiency basically depends on the rejection factor and varies little for the exact trigger condition. For the two presented conditions with rejection factor about 10^5, the efficiency of triggered reconstructed jets reaches a plateau of $\epsilon_\mathrm{jet} \approx 0.8$ at around $p_\mathrm{t}^\mathrm{jet} = 150$ GeV/c(see Figure 6.5). The statistics of jets can be enriched sufficiently up to about jet $p_\mathrm{t}^\mathrm{jet} = 200$ GeV/c, with this conditions. The expected number of triggered jets with $p_\mathrm{t}^\mathrm{jet} = 190 - 200$ GeV/c for one year data taking is about 10^3. With a minimum-bias trigger that is downscaled by a factor of 100, such that a number of jets can be reached only up to $p_\mathrm{t}^\mathrm{jet} = 90 - 100$ GeV/c. The combination of both trigger conditions, as also shown in Figure 6.5, is discussed later together with the apparent biases.

The number of measured jets, N_meas, is the number of generated jets, N_gen, combined with the reconstruction efficiency, ϵ_rec, and the trigger efficiency, ϵ_trg:

$$N_\mathrm{meas} = N_\mathrm{gen} \cdot \epsilon_\mathrm{rec} \cdot \epsilon_\mathrm{trg}. \tag{6.4}$$

All elements in this equation depend on p_t, η, and ϕ ($N_\mathrm{meas} = N_\mathrm{meas}(p_\mathrm{t}; \eta, \phi)$). For the noted values, the considered geometrical acceptance in (η,ϕ) and the p_t interval are relevant. Furthermore, the number of generated jets, N_gen, is not fixed, but rather depends on the jet finder algorithm. The number of reconstructible jets N_rec is

$$N_\mathrm{rec} = N_\mathrm{gen} \cdot \epsilon_\mathrm{rec}. \tag{6.5}$$

The reconstruction efficiency, ϵ_rec, accounts for detector inefficiencies, for example at the sector boundaries. Then the trigger efficiency, ϵ_trg, is the fraction of measured jets (in the triggered data sample) in relation to all reconstructible jets:

$$\epsilon_\mathrm{trg} = \frac{N_\mathrm{meas}}{N_\mathrm{rec}}. \tag{6.6}$$

The trigger efficiency actually is the product of the trigger efficiencies from all trigger levels:

$$\epsilon_{\mathrm{trg}} = \epsilon_{\mathrm{L0}} \cdot \epsilon_{\mathrm{L1}} \cdot \epsilon_{\mathrm{L2}} \cdot \epsilon_{\mathrm{HLT}}. \tag{6.7}$$

While in this work, it is assumed that $\epsilon_{\mathrm{L0}} = \epsilon_{\mathrm{L2}} = \epsilon_{\mathrm{HLT}} = 1$ for jets where the L1 trigger is efficient, i. e.

$$\epsilon_{\mathrm{trg}} = \epsilon_{\mathrm{L1}}. \tag{6.8}$$

In the following section, further biases are discussed. Again, the variables are estimated first for each individual $p_{\mathrm{t}}^{\mathrm{hard}}$ bin and merged with the weighting factor s of each bin. Here only jets with $60 < p_{\mathrm{t}}^{\mathrm{jet}} < 100$ GeV/c are considered. This results in only few entries with very large statistical uncertainties, for the lower $p_{\mathrm{t}}^{\mathrm{hard}}$ bins. Hence, only bins with $p_{\mathrm{t}}^{\mathrm{hard}} > 57$ GeV/c are used (see Table 3.3), in order to avoid unreasonable large uncertainties in the results.

A jet-p_{t} range between 60 and 100 GeV/c was chosen since in this range the efficiency is still increasing and the bias is expected to be large. Thus the "worst case" in terms of the bias is studied. The trigger conditions were selected accordingly. In addition, jets from minimum-bias data as potential reference are available only up to 100 GeV/c.

η Distribution The jets are reconstructed in $|\eta| < 0.5$. In order to illustrate the geometrical acceptance of the TRD, including the end of the super modules at $\eta = 0.9$, generated jets are used, as can be seen in Figure 6.6. It shows the reconstruction efficiency times the trigger efficiency ($\epsilon_{\mathrm{rec}} \times \epsilon_{\mathrm{trg}}$). The reconstruction efficiency ϵ_{rec}, can be considered as constant within $|\eta| < 0.9$. For $|\eta| < 0.5$ it is estimated to $\epsilon_{\mathrm{rec}} = 0.76 \pm 0.02$.

In Figure 6.6, upper panel, a reduced trigger acceptance is visible for jets around the gaps of the TRD stacks. The behavior is similar for both trigger conditions. The bias is a bit less pronounced though for the trigger condition with less required tracks (1). This can be understood because it triggers on more collimated jets, as will be discussed later.

To reduce the trigger inefficiencies between stacks, two adjacent stacks within the same SM are combined for the trigger decision. This has almost no consequences if the trigger requires only two high-p_{t} tracks (1), neither in the observed bias in η nor in the overall trigger efficiency. In case of five required tracks (2), the trigger acceptance is more homogeneous between

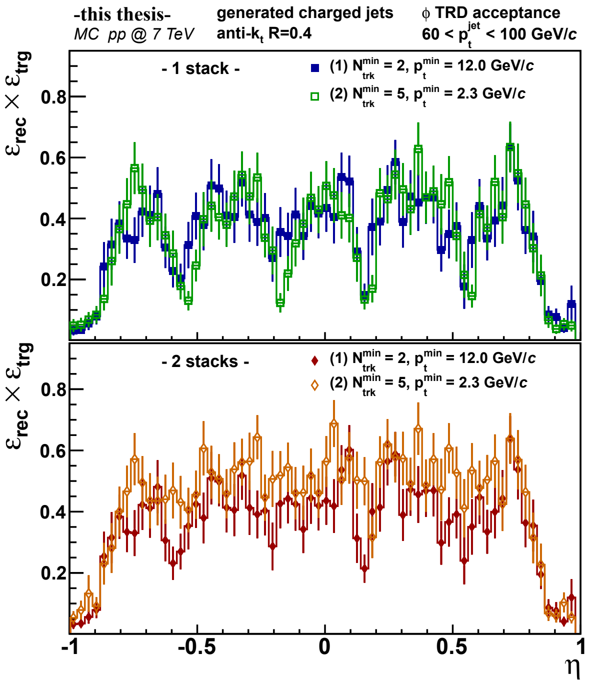

Figure 6.6: Fraction of the triggered, generated jets in relation to all generated jets at full luminosity between 60 and 100 GeV/c in the ϕ TRD acceptance as function of pseudo-rapidity η. It illustrates the bias caused by the TRD segmentation if one stack (top) or two adjacent stacks (bottom) are considered for the trigger decision.

---

the stacks within one super-module (Figure 6.6). It is reasonable that a larger active trigger area is more relevant for a trigger condition with larger number of required tracks.

ϕ Distribution The trigger efficiency in ϕ is presented in Figure 6.7. For clarity, only a range from sector 07 to 10 is shown. Here, the segmentation in sectors, physically in super modules, is visible. The consideration of two adjacent stacks (lower plot) does basically not effect this bias. This is expected since only adjacent stacks within the same SM are combined. Combined information of stacks in adjacent SMs can in the GTU only be incorporated at the stage beyond the SMU which is the TGU. This, however, would slow down the trigger decision.

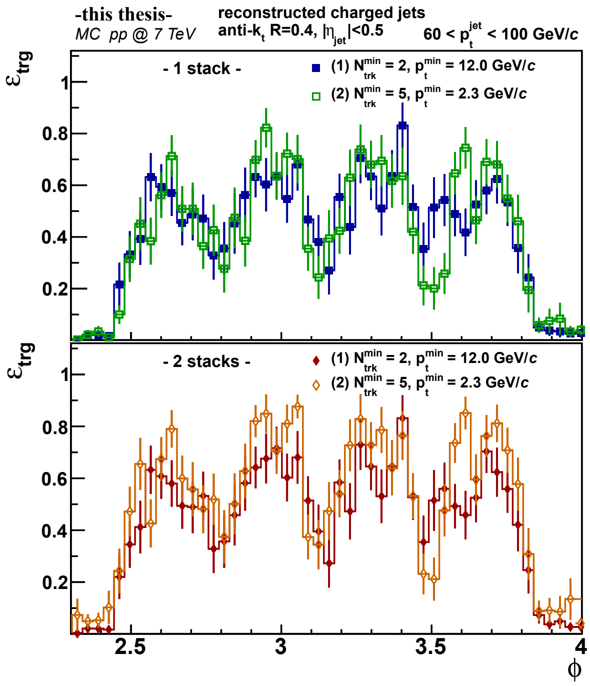

Figure 6.7: Fraction of triggered, reconstructed jets and all reconstructed jets between 60 and 100 GeV/c and $|\eta| < 0.5$ at full luminosity as function of azimuth ϕ. Only a ϕ range with sectors 07 to 10 is shown for clarity. It illustrates the bias caused by the segmentation in SMs if one stack (top) or two adjacent stacks (bottom) are considered for the trigger decision.

Jet Collimation The next studied bias is the collimation of the jets, as shown in Figure 6.8. From now on, only one stack as a segmentation of the trigger area is considered, again. The collimation is measured by the track density in the circular ring in distance ΔR to the jet axis. The number of tracks is binwise normalized to the area $A_i = \pi((\Delta R_i)^2 - (\Delta R_{i-1})^2)$ of the circular ring. A preference by the trigger of strongly collimated jets is visible. As expected, this bias is more pronounced if only few but very high-p_t particles (1) are required. Those jets have a track density which is about 10 % larger within $\Delta R < 0.05$ around the jet axis and a reduced track density for $0.05 < \Delta R < R_\mathrm{jet} = 0.4$. Condition (2) triggers on softer jets, but a bias probably caused by the stack dimension ($\Delta R < 0.2$) is still apparent.

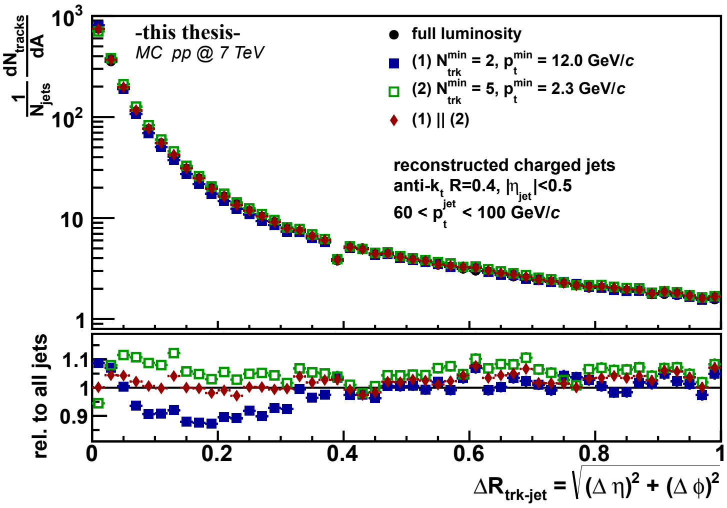

Figure 6.8: Collimation of jets. The track density in the circular ring in distance ΔR to the jet axis is shown. The distributions are bin-wise normalized by the area of the circular ring: $A_i = \pi((\Delta R_i)^2 - (\Delta R_{i-1})^2)$. The lower canvas shows the ratios of the triggered jets in relation to the unbiased jets at full luminosity.

The dip at $\Delta R = 0.4$ in Figure 6.8 is an example of a bias which is already introduced by the jet definition of the FastJet anti-k_t algorithm. The algorithm prefers low track density around the boundary $R_{jet} = 0.4$. Another natural bias of the jet finder algorithm follows from its purpose to enhance the momentum flow in the reconstructed jets. Consequently, the jet finder is itself biased towards collimated jets. The selection of the trigger can enhance or even reduce this effect. This also illustrates that the declaration of a bias is only meaningful in relation to a clearly defined signal, e. g. the bias can be stronger or weaker for another jet finder.

Momentum Distribution in Jets Most relevant of all studied biases for a physical analysis is the following view to the momentum distribution in jets. In Figure 6.9, a clear bias introduced by the trigger condition around the track p_t threshold of 2.3 GeV/c or 12.0 GeV/c can be seen, respectively. In the triggered jets the number of tracks above the respective threshold are enhanced on average, while they are reduced below. The latter is especially visible for the higher track p_t threshold.

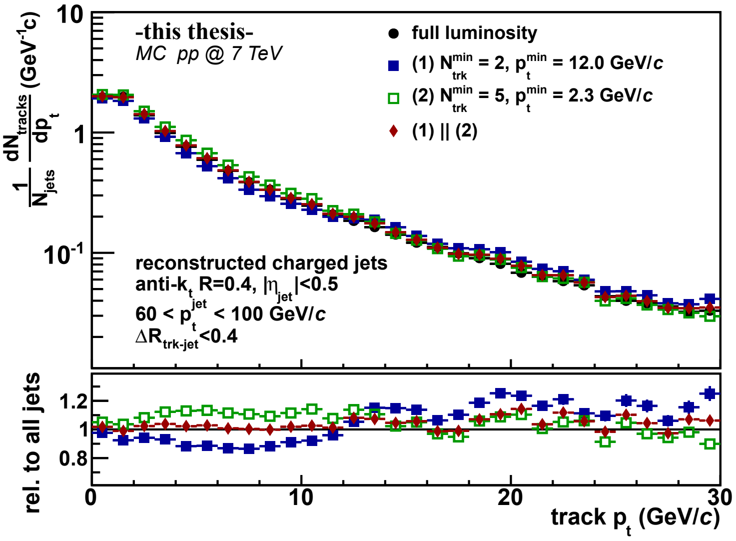

Figure 6.9: Track-p_t spectra within (triggered) jets, and in the lower canvas, the ratios in relation to the unbiased spectrum from jets at full luminosity. Reconstructed jets with $60 < p_\mathrm{t}^\mathrm{jet} < 100$ GeV/c and $|\eta_\mathrm{jet}| < 0.5$ are shown.

The bias is also apparent in the humped-backed plateau in Figure 6.10. The ranges in ξ which corresponds to the p_t thresholds for the considered jet p_t of 60-100 GeV/c are indicated by the ruled areas. Remember that low ξ correspond to high track p_t and high ξ correspond to low track p_t. Compared to the unbiased distribution of ξ, the hump-backed plateau in the region of $\xi \approx 2-4$ is over- or underestimated in the triggered dataset.

In addition, the shape is biased towards soft-fragmented jets. Hard fragmented jets (low ξ) are strongly suppressed, due to the required number of tracks. For a minimum of $N_\mathrm{trk}^\mathrm{min}$ tracks, the bias is at:

$$z > 1/N_\mathrm{trk}^\mathrm{min} \qquad \text{or} \qquad \xi < \log(N_\mathrm{trk}^\mathrm{min}), \tag{6.9}$$

respectively. For the presented trigger conditions that is at:

(1) $\xi < \log(2) = 0.69$ and

(2) $\xi < \log(5) = 1.61$.

In summary, caused by the two trigger thresholds $N_\mathrm{trk}^\mathrm{min}$ and $p_\mathrm{t}^\mathrm{min}$, the momentum distribution is:

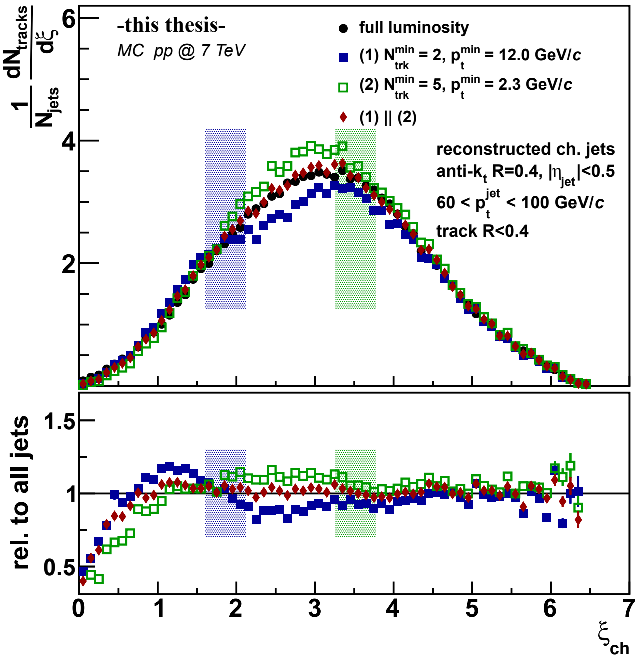

Figure 6.10: The hump-backed plateau, $\xi_{\mathrm{ch}} = \log\left(p_{\mathrm{t}}^{\mathrm{jet(ch)}}/p_{\mathrm{t}}^{\mathrm{track(ch)}}\right)$, of triggered jets in comparison to unbiased jets at full luminosity. The lower canvas shows the ratios in relation to the unbiased case. Reconstructed charged jets with $60 < p_{\mathrm{t}}^{\mathrm{jet}} < 100$ GeV/c and $|\eta_{\mathrm{jet}}| < 0.5$ are shown. The ruled areas illustrate the ranges of ξ which are equivalent to the p_{t} thresholds for the shown jet-p_{t} range.

- overestimated for $\log(N_{\mathrm{trk}}^{\mathrm{min}}) < \xi < \log(p_{\mathrm{t}}^{\mathrm{jet}}/p_{\mathrm{t}}^{\mathrm{track}})$ and
- underestimated outside this region, especially for $\xi < \log(N_{\mathrm{trk}}^{\mathrm{min}})$.

It is apparent that both trigger conditions, (1) and (2), often result in an opposite bias. Hence, it is expedient to combine (logical OR) the two trigger decisions of (1) with few tracks of high p_{t} and (2) with more tracks of lower p_{t}. That means the trigger decision (3) = (1) || (2) is positive if either one or both conditions is fulfilled. Therefore, the trigger bias of both conditions mostly compensate each other, as can be seen e. g. in Figure 6.8 or Figure 6.10. Only the bias at $\xi < \log(N_{\mathrm{trk}})$ towards soft-fragmented jets persists as long as the number of required tracks is $N_{\mathrm{trk}} > 1$. Naturally, the combination also results in a significant increase in jet trigger efficiency (Figure 6.5). A further advantage is the steeper turn-on of the efficiency with jet p_t. The triggered events of both trigger conditions appeared to be mostly disjoint. In the studied minimum-bias sample no event fulfilled both trigger conditions. Therefore, the reaction factor is reduced by a factor of two.

Several trigger set-ups for the TRD for triggering on jets, J/ψ, and single $\mathrm{e}^\pm$ are currently under validation with real data. A first jet trigger is planned with a condition of 3 tracks above 3 GeV/c in one TRD stack [Kle12]. Real triggering is foreseen within this year.

Chapter 7

Soft Background and Background Fluctuations in Pb–Pb

The study presented in this chapter is motivated by the impact of background on jet measurements in heavy-ion collisions. In previous sections the focus was on jet reconstruction in pp collisions, where also the contribution of the underlying event (UE) has been discussed in Chapter 5 in context of the momentum distribution in jets. In pp collisions in a typical jet cone of $R = 0.4$, the UE is in average less than 1 GeV/c and therefore almost negligible for jets of a few tens of GeV/c.

The situation is different in heavy-ion collisions. With a multiple number of participant nucleons in such collisions, the amount of soft background from the UE is much larger. This complicates jet reconstruction in many ways: The bulk of background limits the identification of jets at low jet energies. At higher jet energies, where reconstruction is possible, the jet energy resolution is constrained by the precision of the estimated contribution of the background. Even if the average background of an event is well measured, region-to-region fluctuations become relevant in heavy-ion collisions. Furthermore, possible side-effects on the jet reconstruction algorithms—like jet splitting, merging, spatial shifts, or an impact on the jet size—need to be considered. Not only since the first results of jet measurements at the LHC, which indicate by asymmetric jet events in central Pb–Pb collisions a strong jet quenching [Aad+10; Cha+11b], the impact of background and its fluctuations on jet reconstruction is widely discussed [CS08; Jac10; Cac+11; CSS11].

In ALICE, a detailed measurement of the event background fluctuations in Pb–Pb collisions at $\sqrt{s_{\mathrm{NN}}} = 2.76\,\mathrm{TeV}$ have been done [Aam+12a]. This chapter outlines the analysis methods and the results of these studies. The focus is on the embedding of single tracks and jets into the heavy-ion events in order to investigate the response of the jet algorithm. This part of the background fluctuation studies has been prepared mainly in the context of this thesis.

7.1 Event Background

The average background density in an event is $\rho_{\mathrm{UE}} = p_{\mathrm{t}}^{\mathrm{UE}}/A$, where $p_{\mathrm{t}}^{\mathrm{UE}}$ is the cumulated transverse momentum (excluding the signal) in acceptance area A. This can be calculated event-by-event, as will be seen later in this section. However, it is not exactly known what is the contribution of the background to a measured jet, since the background is not homogeneously distributed over the event but fluctuates from region-to-region. Those fluctuations can be described as the deviation, $\delta\rho$, between the locally present momentum density ρ_{local}, around (η, ϕ), which contributes to the measured signal, and the globally estimated momentum density ρ_{global} in the event:

$$\delta\rho(\eta,\phi) = \rho_{\mathrm{local}}(\eta,\phi) - \rho_{\mathrm{global}}. \tag{7.1}$$

In practice, this is quantified as a deviation of p_{t}, integrated over an area A^{rec}:

$$\begin{aligned} \delta p_{\mathrm{t}}(A^{\mathrm{rec}}) &= (\rho_{\mathrm{local}} - \rho_{\mathrm{global}}) \cdot A^{\mathrm{rec}} & (7.2)\\ &= p_{\mathrm{t}}^{\mathrm{rec}} - \rho_{\mathrm{global}} \cdot A^{\mathrm{rec}}, & (7.3) \end{aligned}$$

where $\rho_{\mathrm{local}} = p_{\mathrm{t}}^{\mathrm{rec}}/A^{\mathrm{rec}}$ is the reconstructed transverse momentum $p_{\mathrm{t}}^{\mathrm{rec}}$ over area A^{rec}. As quantitative value of the p_{t} fluctuations, the standard deviation of several measurements, $\sigma(\delta p_{\mathrm{t}})$, is generally specified, which is associated to the standard deviation of the local background p_{t}-density $\sigma(\rho_{\mathrm{local}})$ for a given area A.

As will be shown in this chapter, the sources of those fluctuations can be classified as

1. ***Poissonian fluctuations***—random, uncorrelated fluctuations of particle number and momentum, and
2. ***non-Poissonian fluctuations***—region-to-region correlated variations of the momentum density, induced by
   a) ***detector effects***—e. g. non-uniform efficiency, in particular due to detector segmentation, and

b) the ***heavy-ion collision***—e. g. due to irregularities in the geometrical overlap region of the colliding nucleons, resulting in collective flow of particles, and

c) ***hard partonic scatter***—i. e. jets, locally collimated particle flux with preferable high track-p_t.

In order to subtract the globally averaged background of the event, the background density is estimated by clustering the full event with the k_t-algorithm from the FastJet package (see Section 4.1). It provides a list of reconstructed clusters with transverse momentum $p_{\mathrm{t},i}^{\mathrm{rec}}$, area A_i^{rec} in (η,ϕ) plane, and consequently a momentum density $\rho_i^{\mathrm{rec}} = p_{\mathrm{t},i}^{\mathrm{rec}}/A_i^{\mathrm{rec}}$. The global background of the event, ρ, is defined as the median of these *background clusters*:

$$\rho \coloneqq \mathrm{median}\left(\rho_i^{\mathrm{rec}}\right) = \mathrm{median}\left(\frac{p_{\mathrm{t},i}^{\mathrm{rec}}}{A_i^{\mathrm{rec}}}\right). \tag{7.4}$$

The two hardest clusters, with highest p_t, were excluded beforehand from this calculation in order to make the estimation of the soft background as far as possible insensitive to contributions from hard partonic interactions. This is also the intention of using the median, which is less sensitive to outliers of background clusters than a simple averaging of the event. Both is only possible with the prior clustering of the event. The radius parameter R of the k_t-algorithm was set to 0.4, in reference to the nominal value for jet reconstruction. In addition, only background clusters within the common jet acceptance, $|\eta| < 0.5$, have been used, in order to minimize the influence of the track acceptance ($|\eta| < 0.9$) on the cluster area.

In Figure 7.1, the determined background p_t-density, ρ, with a low track-p_t cut of $p_\mathrm{t}^{\mathrm{min}} = 0.15$ GeV/c is shown as function of the uncorrected multiplicity of tracks within the track acceptance, $N_{\mathrm{input}}^{\mathrm{raw}}$. A linear correlation of ρ with the number of tracks is apparent. Accordingly, the average track p_t of the soft background is independent of the multiplicity and centrality, respectively. Corresponding to the linear fit and the track acceptance area ($A_{\mathrm{acc}} = 11.3$) it was estimated to $\langle p_\mathrm{t}\rangle \approx 0.70$ GeV/c. This is consistent with the mean p_t of the single particle p_t spectrum.

The insets of Figure 7.1 show the projected distributions of the raw multiplicity and the background p_t-density for the 10 % most central events. The multiplicity in these most central events is $\left\langle N_{\mathrm{input}}^{\mathrm{raw}}\right\rangle = 2272 \pm 278$ and the average background p_t-density:

$$\langle\rho\rangle = (138.32 \pm 0.02)\,\mathrm{GeV}/c. \tag{7.5}$$

Table 7.1: Average background p_{t}-density, $\langle\rho\rangle$, and the event-by-event standard deviation, $\sigma(\rho)$, for different centralities and minimum track-p_{t} cuts. The quoted uncertainties are purely statistical.

$p_{\mathrm{t}}^{\mathrm{min}}$	0.15 GeV/c		1.0 GeV/c		2.0 GeV/c	
Centrality Class	$\langle\rho\rangle$	$\sigma(\rho)$	$\langle\rho\rangle$	$\sigma(\rho)$	$\langle\rho\rangle$	$\sigma(\rho)$
0–10 %	138.33±0.02	18.50±0.01	59.30±0.01	9.27±0.01	12.29±0.01	3.29±0.01
10–20 %	92.73±0.01	13.05±0.01	39.66±0.01	7.05±0.01	8.54±0.01	2.56±0.01
20–30 %	61.13±0.01	9.81±0.01	25.71±0.01	5.45±0.01	6.45±0.01	1.87±0.01
30–40 %	38.46±0.01	7.24±0.01	15.68±0.01	4.06±0.01	5.36±0.01	1.40±0.01
40–50 %	22.58±0.01	5.12±0.01	8.77±0.01	2.87±0.01	4.77±0.01	1.12±0.01
50–60 %	12.05±0.01	3.41±0.01	4.82±0.01	1.77±0.01	4.41±0.05	0.92±0.03
60–70 %	5.62±0.01	2.12±0.01	3.26±0.01	1.04±0.01	4.81±0.53	1.49±0.37
70–80 %	2.30±0.01	1.16±0.01	2.67±0.01	0.74±0.01	0.00±0.01	0.00±0.01

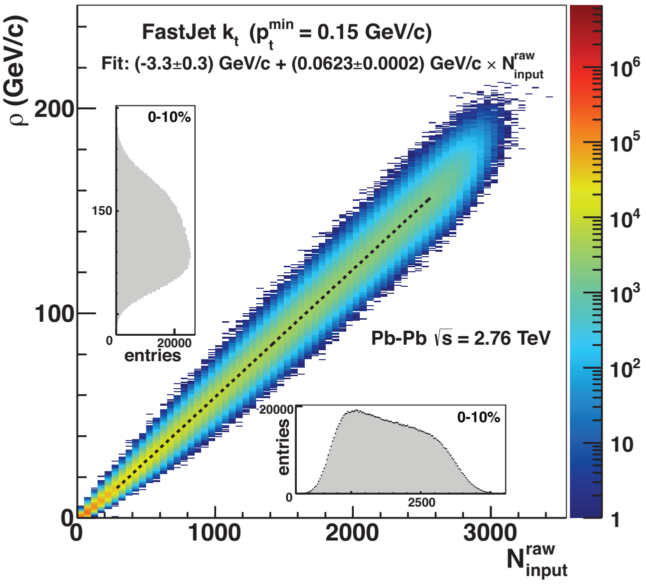

Figure 7.1: Charged-particle background p_t-density, ρ, as function of uncorrected multiplicity of tracks within $|\eta| < 0.9$, $N^\mathrm{raw}_\mathrm{input}$. The track p_t cut is $p^\mathrm{min}_\mathrm{t} = 0.15\,\mathrm{GeV}/c$. The dotted line is a linear fit to the centroids in each multiplicity bin. The insets show the projected distribution of ρ and $N^\mathrm{raw}_\mathrm{input}$ for the 10 % most central events. [Aam+12a]

The event-by-event standard deviation of the background p_t-density is:

$$\sigma(\rho) = (15.51 \pm 0.01)\,\mathrm{GeV}/c. \tag{7.6}$$

For other centralities and minimum track-p_t, $p^\mathrm{min}_\mathrm{t}$, the values of $\langle\rho\rangle$ and $\sigma(\rho)$ are listed in Table 7.1.

The expected amount of background p_t which contributes to the jet momentum is $\rho \cdot A_\mathrm{jet}$. In central events for a jet radius of $R = 0.4$ and corresponding jet area of $A_\mathrm{jet} \approx 0.5$, this is:

$$\left\langle \rho \cdot A_\mathrm{jet} \right\rangle \approx 69\,\mathrm{GeV}/c \tag{7.7}$$

with a spread of

$$\sigma(\rho \cdot A_\mathrm{jet}) \approx 7.8\ \mathrm{GeV}/c. \tag{7.8}$$

The strong event-by-event deviation of the background density, $\sigma(\rho)$, illustrates the importance of the event-wise calculation of ρ. Then any reconstructed jet-p_t can be corrected for ρ by subtraction:

$$p_\mathrm{t} = p_\mathrm{t}^\mathrm{rec} - \rho \cdot A_\mathrm{jet}. \tag{7.9}$$

The impact of the region-to-region background p_t fluctuation still persists, and is one of the largest uncertainties in the measurement of jets in heavy-ion collisions. The estimation and characterization of the background fluctuations is subject of the following sections.

7.2 Event and Track Selection

7.2.1 Event Selection

The background fluctuation studies are based on Pb–Pb collisions from the first run period at the LHC recorded with ALICE in November of 2010. The center-of-mass energy per nucleon pair was $\sqrt{s_\mathrm{NN}} = 2.76$ TeV. From all recorded runs, 91 runs of good quality[1] were chosen to be analyzed. A complete list of the selected runs is in the appendix Table B.1.

About 15 million Pb–Pb minimum-bias events have been accepted. The numbers slightly vary for different analyses due to processing efficiencies:

Random Cones	13.3 M
Track Embedding	15.5 M
Jet Embedding	15.8 M

More information about the event selection is given in Section 3.5.2. A detailed list with the number of events in the different steps of event selection can be found in Table B.2 in the appendix. From those data samples of accepted events, only the 80 % most central events have been processed in the complete chain of analysis tasks. More details about the centrality estimation can be found in Section 3.5.3. Most of the studies are presented for the 10 % most central events. Here the energy density is largest and the medium effects should be most pronounced. Furthermore, the amount of soft background is largest and the jet reconstruction should be most affected. The 10 % most central events cover a large range in multiplicity, which becomes important for the description of the background fluctuations, as it is shown later.

---

[1] Quality according to the ALICE Run Condition Table:
`http://alimonitor.cern.ch/configuration/index.jsp?partition=LHC10h`

7.2.2 Track Selection

As discussed in Section 4.2, jet analyses do require ambitious track quality cuts with homogeneous tracking efficiency. A uniform tracking distribution in η and ϕ is equally important for the background studies, even when it does not utilize jet finding algorithms, since any non-homogeneous efficiencies result in additional region-to-region variations of the local momentum density. In these studies global hybrid tracks as described in Section 4.2 were used.

In the following studies on jet response, jets that contain a track with $p_{\mathrm{t}} > 100\,\mathrm{GeV}/c$ were rejected. However, this is of little relevance since only probe jets with p_{t} between 60 and $100\,\mathrm{GeV}/c$ have been embedded. The few jets, which were rejected after embedding due to this condition (see Table B.2), by implication contain an additional track with p_{t} above $100\,\mathrm{GeV}/c$ from the heavy-ion event and result in a reconstructed jet p_{t} of more than $160\,\mathrm{GeV}/c$ and $\delta p_{\mathrm{t}} > 100\,\mathrm{GeV}/c$.

7.3 Analysis Methods

Next the basics of the applied methods to probe the heavy-ion event background, random cones and probe embedding are discussed, before results of the studies are presented in Section 7.4.

7.3.1 Random Cones

One method which was used to determine the event background p_{t} fluctuations are random cones (RC). Cones with radius R were placed at random position (η,ϕ) in the fully reconstructed Pb–Pb event, see Figure 7.2. The residuals δp_{t} of the scalar sum of all track p_{t} within the cones and the subtracted average background, $\rho \cdot A_{\mathrm{cone}}$, measure the background p_{t} fluctuations (see Equation 7.3):

$$\delta p_{\mathrm{t}} = \sum_i p_{\mathrm{t,i}} - \rho \cdot A_{\mathrm{cone}}, \tag{7.10}$$

where $A_{\mathrm{cone}} = \pi R^2$ is the area of the RC in (η,ϕ) plane, fixed by radius parameter R. The estimation of the background fluctuations by RCs is an unbiased measurement since they are placed randomly, do not react to the probed event, and are independent of any jet finder. However, the result strongly

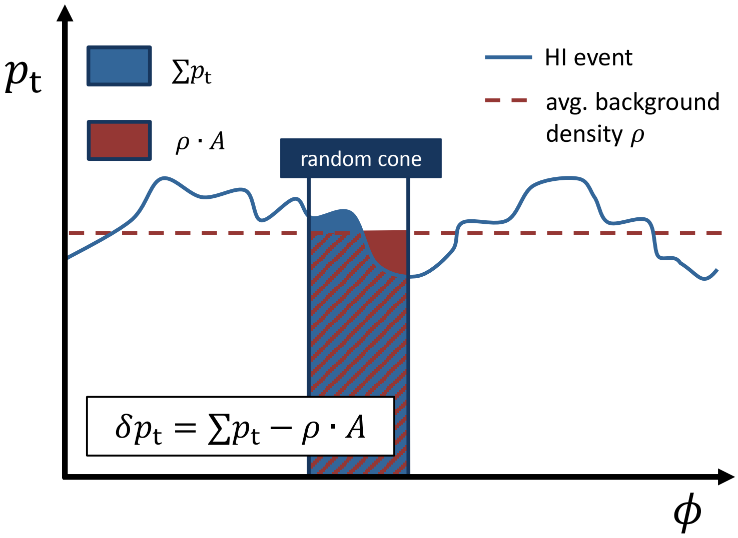

Figure 7.2: Sketch of a random cone, placed in a heavy-ion event, probing the background p_t fluctuation, δp_t.

depends on the chosen radius parameter R and the consequently probed area A since the measured δp_t is the integrated background p_t fluctuation over A. For all measurement δp_t-distributions the nominal radius $R = 0.4$, probing the dimension of a typical jet area, was used in this work. That corresponds to 1/22.5 of the full area of track acceptance. For this cone size and the track acceptance of $|\eta| < 0.9$, the cone center is randomly placed within pseudo-rapidity $|\eta| < 0.5$ and full azimuthal angle ϕ.

Due to the unbiased measurement and its flexibility the method of random cones is ideally suited to classify the various sources of the background p_t fluctuations. Two **additional, optional conditions** for the random cones were utilized:

1. A ***minimum distance D*** $\boldsymbol{> 1.0}$ of the random cone (center) to the leading (highest p_t) background cluster, determined by k_t clusterizer, has been ensured. That reduces the probability to probe correlated upward fluctuations in the heavy-ion event, probably from (mini-)jets. However, some of these upward fluctuations can also be caused by collective flow or just by random fluctuations. It cannot be distinguished between those.

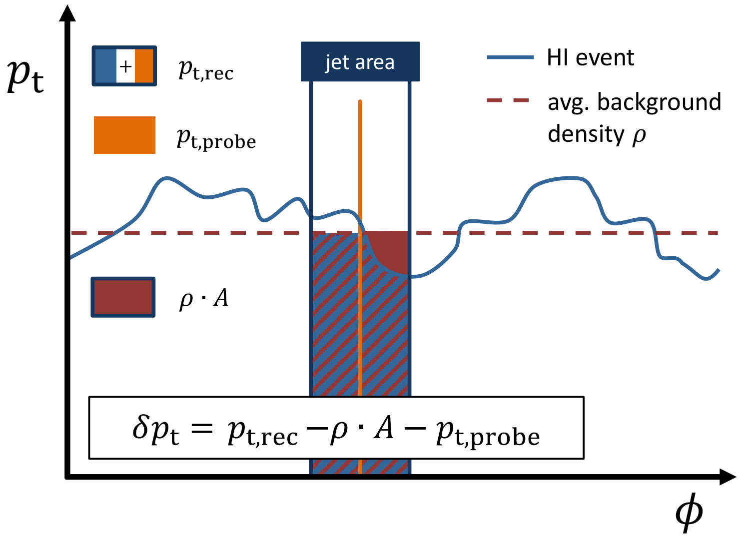

Figure 7.3: Sketch of a high-p_t track embedded in a heavy-ion event.

2. All tracks of the heavy-ion event have been ***randomized in (η,ϕ) direction*** (within the track acceptance) while the total number of tracks and their individual p_t, were conserved. That destroys all correlated contributions of the background fluctuations. Hence, purely uncorrelated fluctuations are expected approaching the Poissonian limit. However, it should to be noted that the randomized events still are populated by high p_t tracks from potential hard-fragmented jets in the event.

The major results of the random cone method with more insights to the sources of the measured fluctuations are presented in Section 7.4.1.

7.3.2 Probe Embedding

Another method to investigate the background is the embedding of known probes into heavy-ion events and its reconstruction with the same jet finder also used in the jet analysis. The used probes are single high-p_t toy tracks or fully simulated pp jet events. The embedded events are PYTHIA jet events at $\sqrt{s} = 2.76\,\text{TeV}$ as described in Section 3.5.5. In the following, the observables of the raw probe, as reconstructed before the embedding, are called *probe observables* (e. g. p_t^{probe}) and reconstructed observables after embedding

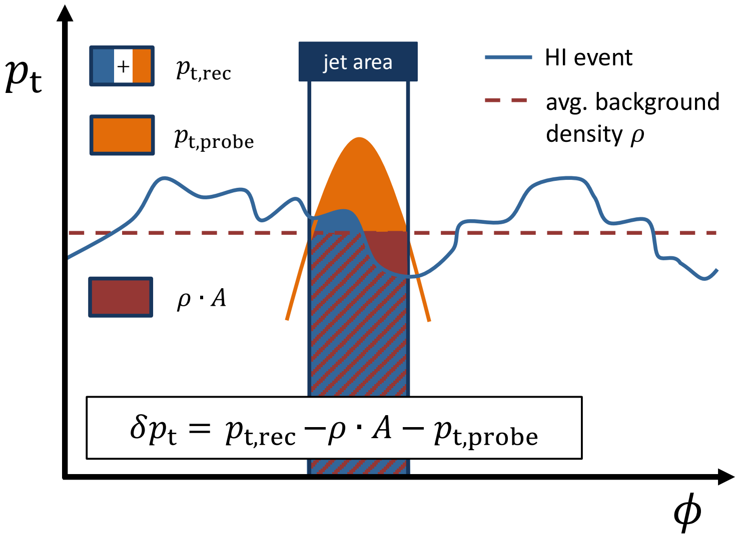

Figure 7.4: Sketch of a jet embedded in a heavy-ion event.

into the heavy-ion event are called *reconstructed observables* (e. g. p_t^{rec}). The background fluctuations are measured as the residual of the in the heavy-ion event reconstructed jet p_t (p_t^{rec}), the subtracted average event background p_t ($\rho \cdot A_{rec}$), and the subtracted embedded probe p_t (p_t^{probe}):

$$\delta p_t = p_t^{rec} - \rho \cdot A_{rec} - p_t^{probe}. \tag{7.11}$$

While random cones allow an unbiased measurement of the heavy-ion event, the reconstruction of the embedded probe among the soft background introduces systematic effects of jet reconstruction to the measurement. So the measured δp_t represent not only pure background fluctuations in this case. However, the embedded single high-p_t tracks (Figure 7.3) are still delta probes for the jet finder, as long as the embedded track p_t is well above the typical track p_t of the heavy-ion event. It is a seed and anchor for the jet finding process. Since the anti-k_t algorithm generates close to concentric jet areas with radius R [CSS08a] and the shift of the reconstructed jet in comparison to the embedded jet, caused by the background, is low for a high-p_t seed well above the background; the measurement is similar to random cones. This discussion is continued with the results in Section 7.4.2.

When full pp jet events are embedded (Figure 7.4), in addition the fragmentation pattern of the jets which appear as probes becomes important. The constituents of the embedded probe are not necessarily part of the reconstructed jet in the heavy-ion event in this case. Thus a well-defined matching condition is needed, so that the reconstructed jets in the heavy-ion event can be related to the embedded probe. The matching condition is described in Section 7.3.4.

The embedding methods have been developed and implemented in an user task `AliAnalysisTaskFastEmbedding`. It is available in AliRoot [AliSVN] in the subfolder `JETAN`. The task allows the embedding of

1.) full events from AODs,
2.) tracks related to jets from AOD events,
3.) jet momentum and direction from AODs as single track, and
4.) toy tracks.

As described in Section 3.5.1, AODs are Analysis Object Data files containing filtered data obtained from Event Summary Data (ESD) files or other AODs. In general they are composed for a dedicated analysis.The toy tracks can be generated randomly in a defined p_t, η, and ϕ range. From AODs all events can be used or only events which contain a jet with a minimum p_t. The choice to embed full events, contrary to embed only those tracks related to jets from the event, is motivated by the real dimension of a typical jet, which is larger than the cone radius $R = 0.4$. Tracks outside this cone would be missing but might be relevant once the event is embedded.

7.3.3 Subtraction of Underlying Event from pp

In case of fully embedded pp events, the background is estimated only from the heavy-ion event, even though additional soft background from the pp event is included. This background from the pp event is not taken into account in ρ because it is part of the probe p_t and already subtracted with it (see Figure 7.5). Otherwise it would be incorporated twice. A side effect is that a shift of the reconstructed jet in the heavy-ion event with respect to the embedded probe can introduce another contribution to the measured δp_t from spatial fluctuations in the underlying event of the embedded event. This is small though, since the shift in general[2], is small. Even the absolute

---

[2] Rare exceptions are the cases of jet splitting and merging, as discussed in Section 7.4.2.

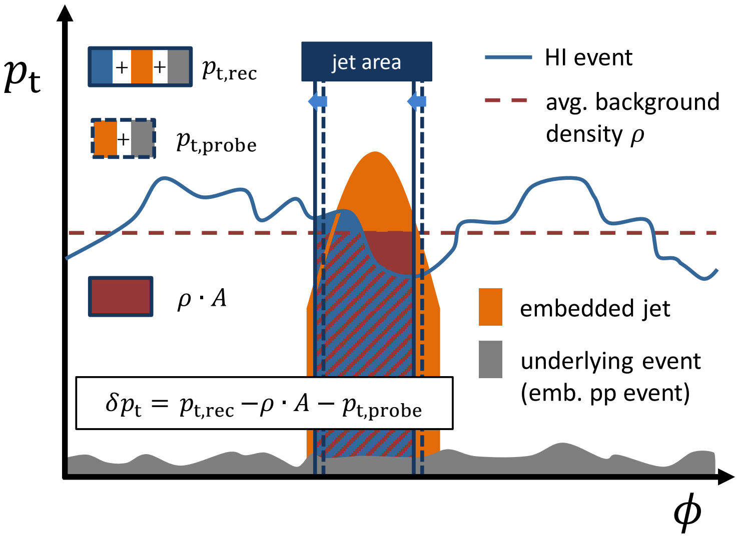

Figure 7.5: Sketch of an pp event, consisting of a jet and underlying event, embedded in an heavy-ion event.

---

contribution from the underlying event in the jet area is only of the order of one GeV/c.

7.3.4 Probe Matching

In order to match the jets from the embedded pp event with the reconstructed jets after embedding in the heavy-ion event, track references are used. From all tracks in the probe jet, a minimum sum of their p_t of 50 % is required to be constituent of the reconstructed jet in the heavy-ion event. Requiring the majority fraction of the momentum of the probe in the reconstructed jet ensures an unique matching condition of probe jets to the reconstructed jets. For a bijective association it is for reconstructed jets only allowed to match with one probe jet. In case it consists of more than one probe jet it is linked only to the probe jet with largest transverse momentum, the other probe jet is then taken as lost. Not all jets of the embedded event and the heavy-ion event are taken into account in the matching procedure. Only the N jets with highest transverse momentum are employed. In the presented studies a list of the four leading reconstructed jets and probe jets, respectively, was used.

With this condition a good matching efficiency has been reached as is shown later in Section 7.4.4. In fact, the embedded pp events unlikely contain more than four jets. In addition the probe jets need to be within the required jet p_t range, which is in this work 60 to 100 GeV/c.

The same matching routine is used for embedded single toy tracks. Even though it is much more trivial in this case: Either the embedded track is part of the reconstructed jet in the heavy-ion event or it is not. The matching routine has been implemented as function `GetJetMatching` in class `AliAnalysisHelperJetTasks` (in AliRoot [AliSVN] subfolder `PWG/Tools`, originally in `PWG4/JetTasks`).

7.4 Results

7.4.1 Sources of Background Fluctuations

From the random cone probes [Aam+12a; Men] of the Pb–Pb events, an unbiased measurement of the event background p_t fluctuations for charged tracks has been obtained. In Figure 7.6 the δp_t distribution in the 10 % most central events with $p_\mathrm{t}^\mathrm{min}$ of 0.15 GeV/c is plotted. Also the two additional types of random cones are shown, where

1. random cones with distance $D < 1.0$ to the leading jet are neglected, or
2. all tracks in the event were randomized in (η,ϕ).

The observation that the δp_t distribution is peaked at zero demonstrates that the average background subtraction works well. The standard deviation of the remaining charged background p_t fluctuations in central events was measured to:

$$\sigma(\delta p_\mathrm{t}) = 11.0\,\mathrm{GeV}/c. \tag{7.12}$$

Furthermore, a Gaussian fit at the left-hand side (LHS) of the δp_t distribution was applied. It is iteratively fitted in a range of $[\mu^\mathrm{LHS} - 3\sigma^\mathrm{LHS}, \mu^\mathrm{LHS} + 0.5\sigma^\mathrm{LHS}]$, while μ^LHS is the mean and σ^LHS the standard deviation of the fit. More details about the fitting procedure can be found in Section 7.4.3. In Figure 7.6 the Gaussian fit is extrapolated over the full range, so the asymmetry of the δp_t distribution is apparent. It is not expected that the distribution follows exactly a Gaussian shape, since already the shapes of the underlying single particle p_t

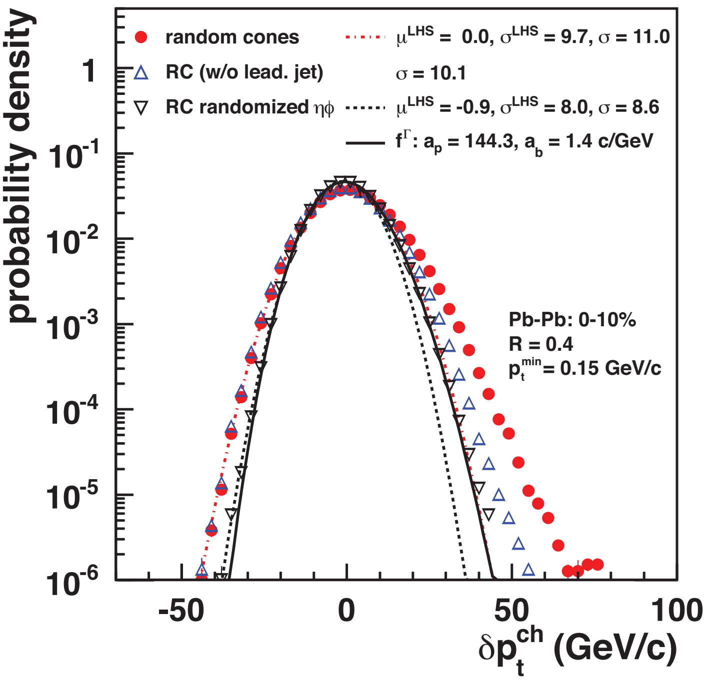

Figure 7.6: Background p_t fluctuations, δp_t, in the 10 % most central events with track $p_\mathrm{t}^\mathrm{min} = 0.15\,\mathrm{GeV}/c$ estimated by the common random cones (RC) and two additional types. The dashed lines represent Gaussian fits of the left-hand side and its extrapolation to positive δp_t. The solid line is a fit with a Γ function shifted to zero. [Aam+12a]

---

and multiplicity distribution are non-Gaussian. A more precise description of event-by-event average p_t fluctuations actually is given by a Γ function [Tan01; Tan04]. In events with a large number of tracks, i. e. in central events as discussed here, this causes only a small part of the tail at the right-hand side (RHS). Most of the tail is expected to be from true jets. They contribute to the background fluctuations as correlated upward fluctuations with positive δp_t.

The impact of inherent jets to the measured background fluctuations has been reduced for illustration by removing random cones which overlay the leading jet in the event. Then the tail at the right-hand side is much less pronounced, while the left-hand side is basically unaffected. The slight enhancement at the left-hand side can be explained by the normalization due to less contributions to the right-hand side. The standard deviation of this distribution without leading jets, $\sigma(\delta p_{\mathrm{t}}) = 10.1\,\mathrm{GeV}/c$, is close to the standard deviation of the Gaussian fit from the standard random cones, $\sigma^{LHS} = 9.7\,\mathrm{GeV}/c$. The comparison is only for illustration since on the one hand only contributions from leading jets have been removed, and there might still be upward fluctuations from sub-leading jets. On the other hand, it cannot be distinguished to what extent the removed "leading jets" are true jets or uncorrelated upwards fluctuations. And, even more importantly, the expected shape of the δp_{t} distribution is more like a Γ distribution than a Gaussian distribution, as mentioned already. This is further discussed in the next paragraph.

For the third plotted δp_{t} distribution, all reconstructed tracks within one event have been randomized in their (η,ϕ) orientation within the acceptance ($|\eta| < 0.9$). At the same time, the transverse momentum p_{t} of the tracks was conserved. That destroys all correlations in the event. It can be seen in Figure 7.6 that in this case also the left-hand side of the δp_{t} distribution is affected, as well as the right-hand side is more reduced. The impact on the left-hand side reveals that there contribute also correlated fluctuations to negative δp_{t}. Those later will be (partially) explained by collective flow (see Section 3.5.4). The left-hand side Gaussian fit shows a standard deviation of $\sigma^{LHS} = 8.0\,\mathrm{GeV}/c$, while the distribution has a standard deviation of $\sigma(\delta p_{\mathrm{t}}) = 8.6\,\mathrm{GeV}/c$. This deviation demonstrates the non-Gaussian distribution of the uncorrelated background fluctuations. Even though the high p_{t} tracks from hard-fragmented jets are now randomized they still contribute to a tail at the right-hand side. But even without those tracks, a similar tail would be present because the track p_{t} and multiplicity distributions themselves are asymmetric. The measurement of δp_{t} is a measurement of $\langle p_{\mathrm{t}} \rangle$ fluctuations in a limited phase space, with an additional subtraction of the average background. Hence, a Γ function is supposed to be a better description of the δp_{t} for uncorrelated particle emission. The δp_{t} distribution obtained from random cones in randomized events, in Figure 7.6, is fitted with [Jac10; Kle; Pop11]

$$f^{\Gamma}(\delta p_{\mathrm{t}}) = A \cdot a_b / \Gamma(a_p) \cdot (a_b \delta p_{\mathrm{t}} + a_p)^{a_p - 1} \cdot e^{-(a_b \delta p_{\mathrm{t}} + a_p)}, \tag{7.13}$$

a Γ function shifted by $-a_p/a_b$ in such a way that the mean is set to zero and the standard deviation is $\sigma^{\Gamma} = \sqrt{a_p}/a_b$. With $a_p = 144.3$ and $a_b = 1.4\,(\mathrm{GeV}/c)^{-1}$, resulting in $\sigma^{\Gamma} = 8.6\,\mathrm{GeV}/c$ is the Γ distribution in a good agreement with the measured δp_{t} distribution [Kle]. The slight divergences at both

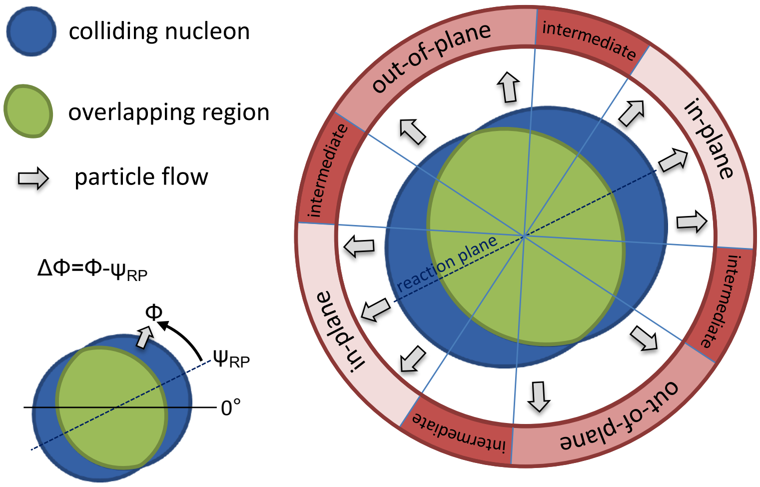

Figure 7.7: View of colliding nuclei along the beam axis. The three bins of the orientation of the probe center to the reaction/event plane, $\Delta\phi$, are shown.

---

sides can be explained by a limited description of the average p_t and multiplicity fluctuations due to the low p_t cut-off and the power law at high p_t.

Impact of the Event Plane

Collective flow, as introduced in Section 3.5.4, appears as an azimuth dependent variation of the particle yield. Therefore it is a natural contribution to correlated region-to-region fluctuations. The background p_t fluctuations are studied in bins of different orientation to the event plane. Three bins of $\Delta\phi = \phi - \psi_{RP}$ were defined, where ϕ is the azimuthal angle of the probed region (center of random cones or reconstructed jets), and ψ_{RP} is the orientation of the event plane with respect to the azimuth:

- $\Delta\phi < 30^\circ$ – in-plane,
- $30^\circ < \Delta\phi < 60^\circ$ – intermediate,
- $\Delta\phi > 60^\circ$ – out-of-plane.

The segmentation is also shown in Figure 7.7. Note that the bins are defined for the center of the probe, whereas the probed area can partially overlap

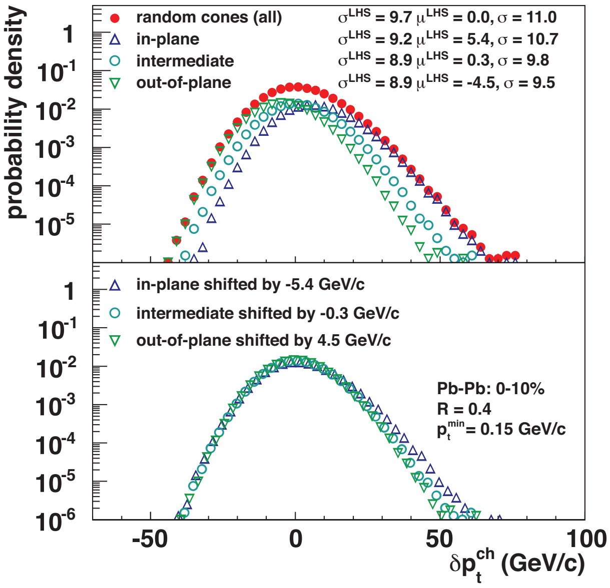

Figure 7.8: δp_t in the 10 % most central events with track $p_\mathrm{t}^\mathrm{min} = 0.15\,\mathrm{GeV}/c$ estimated by random cones depending on the orientation to the event plane. For the bottom panel the distributions have been shifted by the negative mean of the left-hand-side Gaussian fit, $-\mu^\mathrm{LHS}$. [Aam+12a]

---

the boundaries. Thus the boundaries of the bins are practically blurred in perspective of the contributing flow. A radius of 0.4 corresponds to almost 23° in azimuth direction as maximal overlap. The regions which are mostly compared, in-plane and out-of-plane, do not overlap in any sense.

In Figure 7.8, the δp_t distributions are shown for the three different orientations of the probed region to the event plane. In addition, the inclusive δp_t distribution is shown. In relation to the different orientations to the event plane a shift of the δp_t distribution is visible. A deviation from zero of the mean of the distribution is equivalent to an over- or underestimation of the background. Taking the mean of the LHS Gaussian fit as reference, the charged event background is in-plane underestimated by 5.4 GeV/c, in average, and out-of-plane overestimated by 4.5 GeV/c, while the mean is with 0.3 GeV/c close to zero for the intermediate region.

The width of the δp_t distribution for the three different bins varies from $\sigma = 9.5\,\mathrm{GeV}/c$ (out-of-plane) to $\sigma = 10.7\,\mathrm{GeV}/c$ (in-plane). Whereas they are represented by almost the same Gaussian shape at the left-hand side ($\sigma^{\mathrm{LHS}} = 8.9-9.2\,\mathrm{GeV}/c$). Hence, the difference is due to differently pronounced tails at the right-hand side. That also can be seen in the bottom panel of Figure 7.8 where the δp_{t} distributions for the three different orientations to the event plane are shifted by the mean of the Gaussian fit, in such ways that they are centered at zero afterwards.

The stronger pronounced tail at the RHS in orientation with the event plane can indicate an auto-correlation between the estimated event plane and jets or upward-fluctuations in the event. Especially since back-to-back jets also have a 180° symmetry they can appear similar to collective flow. On the other hand, the orientation to the event plane is important with respect to the average path length through the quark-gluon plasma of a hard-scattered parton and the resulting quenching effect. According to an irregular overlapping region of the colliding ions, the size of the medium is less in-plane than out of the reaction plane. Hence, it can be expected that jets with orientation to the event plane are less quenched than jets orthogonal to the event plane. To distinguish the auto-correlation from quenching effects it is important to minimize the correlation between jets and the measured event plane.

A potential bias of high p_{t} contributions is already reduced in the event plane (EP) calculation with TPC tracks as it is done with tracks up to 2 GeV/c and tracks above this threshold contribute only with a constant weight. Nevertheless, it cannot be distinguished from this measurement if the auto-correlation or quenching dominates. Measurements with the VZERO detectors promise a smaller bias toward upward fluctuations or jets but have the disadvantage of a poor resolution. Both result in a less pronounced event plane dependence of the δp_{t} distributions. Hence, an interpretation of a reduction of the shift in δp_{t} is difficult. The observations were not conclusive [Kle+11]. A future measurement with the FMD which provide better event plane resolution could clarify the situation.

Multiplicity Dependence

So far the background fluctuations have been discussed only for the 10 % most central events. Assuming the uncorrelated, statistical fluctuations are the dominant part, the background fluctuations are strongly dependent on the centrality, or more precisely on the number of reconstructed particles N, since the Poissonian fluctuation is proportional to $\sqrt{N}$. Therefore in Figure 7.9 the standard deviation $\sigma(\delta p_{\mathrm{t}})$ in dependence of the raw number of reconstructed

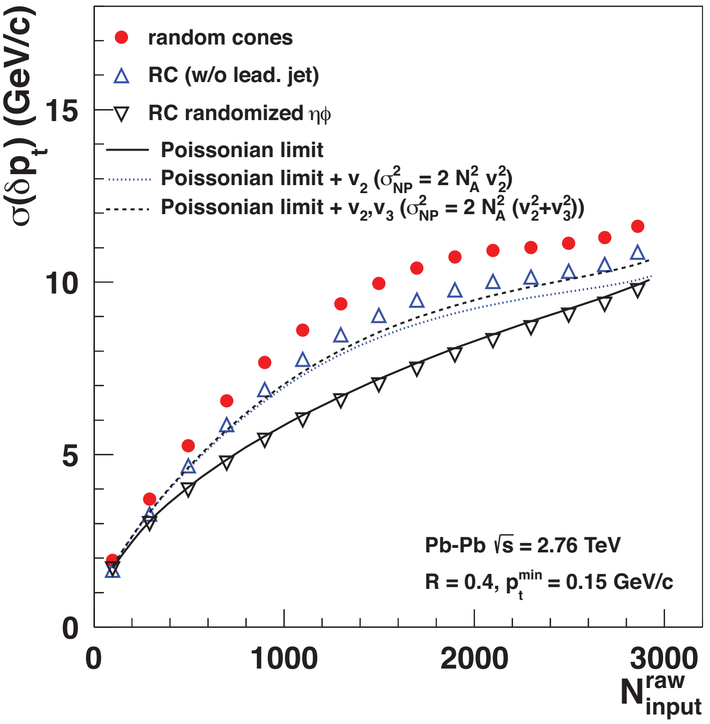

Figure 7.9: Standard deviation of the δp_{t} distribution, $\sigma(\delta p_{\mathrm{t}})$, vs. the uncorrected multiplicity of charged tracks within $\eta < 0.9$, $N^{\mathrm{raw}}_{\mathrm{input}}$, for the three types of random cones. The lines represent the Poissonian limit derived alone from the measured track p_{t} spectrum, and with additional contributions from elliptic (v_2) and triangular flow (v_3). [Aam+12a]

tracks $N^{\mathrm{raw}}_{\mathrm{input}}$ is shown. $N^{\mathrm{raw}}_{\mathrm{input}}$ is based on the same tracks that are used as input for the background estimation, or later for jet reconstruction, respectivly. From Figure 7.1 it can be seen that the 10 % most central events cover a wide range of $N^{\mathrm{raw}}_{\mathrm{input}}$ from about 2000 to 3000 tracks if the minimum track p_{t} is 0.15 GeV/c. For an investigation of the different sources of the background fluctuations, again, the three different types of random cones were used. First, the random cones from randomized events can be compared to the expected Poissonian limit. It represents the width of the δp_{t} distribution which results from purely random fluctuations according to the expected number of tracks N_A in the cone area A and the measured single particle p_t spectrum [Ale+06]:

$$\sigma(\delta p_\mathrm{t}) = \sqrt{N_A \cdot \sigma^2(p_\mathrm{t}) + N_A \cdot \langle p_\mathrm{t} \rangle^2}. \tag{7.14}$$

N_A results from the geometrical relation of the cone area $A = 2\pi R^2$ with $R = 0.4$ and the tracking acceptance $2\pi \times 2 \cdot 0.9$ ($\phi \times \eta$), i. e. $N_A = 0.0\bar{8} \cdot N_\mathrm{input}^\mathrm{raw}$. $\langle p_\mathrm{t} \rangle$ is the average p_t and $\sigma(p_\mathrm{t})$ the standard deviation of the measured track p_t spectrum. Those were used in order to calculate the Poissonian limit as shown in Figure 7.9 [Kle11c]. Local variations of N_A, $\langle p_\mathrm{t} \rangle$, and $\sigma(p_\mathrm{t})$ are not taken into account and result in additional fluctuations which are not represented by this model. The fluctuations from randomized events agree well with the Poissonian limit which is proportional to $\sqrt{N_\mathrm{input}^\mathrm{raw}}$.

In addition, non-Poissonian (NP) fluctuations from collective flow have been taken into account, in terms of additional region-to-region variation of the average multiplicity [Kle11b]:

$$\sigma(\delta p_\mathrm{t}) = \sqrt{N_A \cdot \sigma^2(p_\mathrm{t}) + (N_A + \sigma_{NP}^2(N_A)) \cdot \langle p_\mathrm{t} \rangle^2}. \tag{7.15}$$

In case of elliptic flow it holds:

$$\sigma_{NP}^2(N_A) \approx 2 v_2^2 N_A^2, \tag{7.16}$$

where v_2 is p_t-integrated over the p_t range $0.2 < p_\mathrm{t} < 5.0\,\mathrm{GeV}/c$ measured by ALICE for different centralities [Aam+10d]. Also triangular flow, v_3, was considered. Since v_2 and v_3 are not correlated via a common plane of symmetry [Aam+11b] v_3 can be added in quadrature to

$$\sigma_{NP}^2(N_A) \approx 2 N_A^2 (v_2^2 + v_3^2). \tag{7.17}$$

v_3 is almost constant over all centralities. Here, an approximate value of $v_3 = 2.4\,\%$ was used. Already, this rough parametrisation of the collective flow is a good characterization for the deviation from $\sqrt{N_\mathrm{input}^\mathrm{raw}}$ of the measured background p_t fluctuations with the anti-bias to jet contributions.

7.4.2 Impact on Jet Reconstruction

Heretofore, background fluctuations were characterized with random cones as unbiased probe. In following embedded single high-p_t toy tracks and full

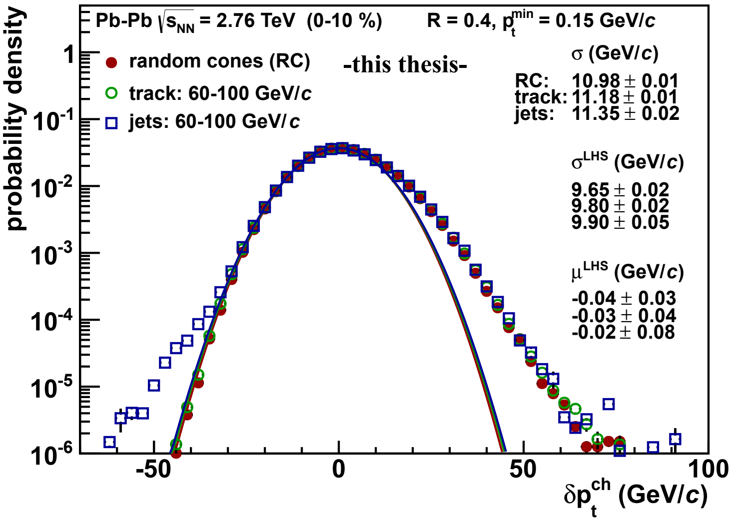

Figure 7.10: Background p_t fluctuations, δp_t, estimated with the three methods, random cones, track embedding, and jet embedding, for minimum track p_t of 0.15 GeV/c and centrality $0-10\,\%$.

(simulated) pp jet events were used as probes. They are reconstructed with a jet finder algorithm which responds to the combined structure of the probe and the underlying event. The measurement depends on the reconstruction algorithm including its settings and the structure of the embedded probe. This is not an unbiased measurement of the pure background fluctuations anymore, but provides relevant results about the impact of the soft background in heavy-ion collision on jet reconstruction. This is important for the interpretation of the reconstructed jets within heavy-ion collisions and its corrections.

Embedded single high-p_t tracks are still a delta probe and simply a seed for the jet finder (as long as the embedded track p_t is well above the background track p_t). With such probes, the sensitivity of the subsequent clustering of the jet finder is measured. For example, a spatial shift of the reconstructed jet or the formation of an irregular jet area can bias the measured δp_t.

For embedded jets, the fragmentation pattern in addition becomes relevant, especially when a part of the embedded jet carries a similar momentum as the bulk of background. Therefore, the jet embedding enables a much more realistic response of the jet finder to the soft background for a given jet signal.

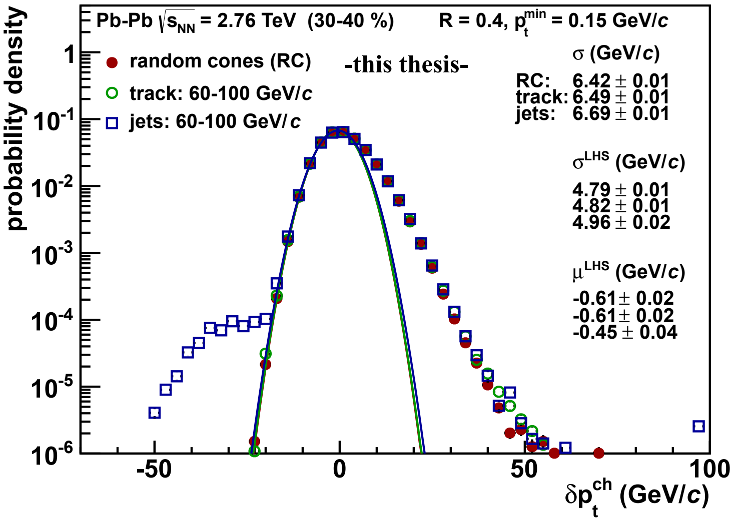

Figure 7.11: Background p_{t} fluctuations, δp_{t}, estimated with the three methods, random cones, track embedding, and jet embedding, for minimum track p_{t} of 0.15 GeV/c and centrality $30-40$ %.

In Figure 7.10, the δp_{t} distributions of all three different methods (random cones, track embedding, and jet embedding) are shown for the 10 % most central events and $p_{\mathrm{t}}^{\mathrm{min}} = 0.15\,\mathrm{GeV}/c$. The intrisic standard deviations of the distributions for different centralities are listed in Table 7.2. They are similar for all three methods, but an overal bit wider δp_{t} distribution from track embedding compared to random cones and from jet embedding compared to the other two methods is apparent. $\sigma(\delta p_{\mathrm{t}})$ obtained from track embedding is for centrality class $0-10\%$:

$$\sigma(\delta p_{\mathrm{t}}) = 11.2\,\mathrm{GeV}/c, \tag{7.18}$$

compared to the previously discussed $\sigma(\delta p_{\mathrm{t}})$ of 11.0 GeV/c from random cones. The difference is basically an effect of the jet area resolution of the sequential-recombination jet finder algorithms. In the presented case a ghost area size of 0.005 was used. For smaller ghost areas, the δp_{t} distribution from track embedding approaches those from random cones. The utilized ghost area size provides a compromise between area resolution and computing time plus memory consumption.

Table 7.2: Standard deviation of the δp_{t} distributions for the three different methods and different centrality bins, using the track embedding probe and $p_{\mathrm{t}}^{\mathrm{min}} = 0.15$ GeV/c.

	$\sigma(\delta p_{\mathrm{t}})$ (GeV/c)		
Centrality Class	RC	track emb.	jet emb.
0–10 %	10.98 ± 0.01	11.18 ± 0.01	11.35 ± 0.02
10–20 %	10.02 ± 0.01	10.18 ± 0.01	10.31 ± 0.02
20–30 %	8.34 ± 0.01	8.44 ± 0.01	8.62 ± 0.01
30–40 %	6.42 ± 0.01	6.49 ± 0.01	6.69 ± 0.01
40–50 %	4.65 ± 0.01	4.69 ± 0.01	4.89 ± 0.01
50–60 %	3.22 ± 0.01	3.24 ± 0.01	3.42 ± 0.01
60–70 %	2.15 ± 0.01	2.16 ± 0.01	2.32 ± 0.01
70–80 %	1.40 ± 0.01	1.40 ± 0.01	1.54 ± 0.01

The additional broadening of the δp_{t} distribution with the embedding of pp jet events, can be explained with stronger pronounced (but still slight) shifts of jet direction and changes in the jet area, comparing the embedded probe with the reconstructed jet in the heavy-ion event. Furthermore, with the embedding of jets, outliers of the common δp_{t} distribution are apparent at the left-hand side (-20 GeV/$c \lesssim \delta p_{\mathrm{t}} \lesssim$ -50 GeV/c). For the most central events and the low-p_{t} track cut of 0.15 GeV/c, these outliers are mostly hidden by the overall distribution, they are better visible for more peripheral events, like 30-40 % in Figure 7.11, where the δp_{t} distributions are smaller. Those outliers result from splitting of the embedded jets when they are reconstructed beneath the background. More about jet splitting and jet merging is discussed in Section 7.4.2. Prior to that, the more general impact of the fluctuations on the jet spectrum is discussed.

Impact on the Jet Spectrum

The δp_{t} distribution represents the probability that a jet with transverse momentum $p_{\mathrm{t}}^{\mathrm{jet}}$ is over- or underestimated by δp_{t} if it is reconstructed in an environment of soft background from heavy-ion events. Therefore it is also directly a contribution to the reconstructed jet p_{t} resolution in heavy-ion collisions. It cannot be corrected event-by-event as it is done for the median event background. The δp_{t} distribution can be used as input to unfold the original

Table 7.3: Standard deviation of the δp_{t} distributions for different centrality bins and $p_{\mathrm{t}}^{\mathrm{min}}$ cuts, using the track embedding probe. All values have a statistical uncertainty of 0.01 GeV/c.

		$\sigma(\delta p_{\mathrm{t}})$ (GeV/c)		
Centrality Class	$p_{\mathrm{t}}^{\mathrm{min}} =$	0.15 GeV/c	1.0 GeV/c	2.0 GeV/c
0–10 %		11.18	8.60	4.85
10–20 %		10.18	7.65	4.27
20–30 %		8.44	6.33	3.61
30–40 %		6.49	4.90	2.82
40–50 %		4.69	3.59	2.13
50–60 %		3.24	2.59	1.56
60–70 %		2.16	1.75	1.07
70–80 %		1.40	1.12	0.70

jet p_{t} spectrum from the reconstructed jet p_{t} spectrum, though. Since the jet p_{t} spectrum is steeply falling with p_{t} (power law), the upward fluctuations are the most relevant part, i. e. especially the tail at positive δp_{t}.

In order to get a first approximation of the impact of the background fluctuations (δp_{t}) to the jet p_{t} spectrum the power law spectrum $f(p_{\mathrm{t}}) = 0.7/(0.7 + p_{\mathrm{t}}^5)$ with $p_{\mathrm{t}} > 4\,\mathrm{GeV}/c$ has been folded with the δp_{t} distributions from the employed methods for $0-10\,\%$ centrality and with different Gaussian distributions [Ver]. Those studies indicate that the background fluctuations are relevant in the $0-10\,\%$ centrality for jet reconstruction up to about $p_{\mathrm{t}}^{\mathrm{jet}} \approx (100 \pm 15)\,\mathrm{GeV}/c$ for $p_{\mathrm{t}}^{\mathrm{min}} = 0.15\,\mathrm{GeV}/c$ and up to about $p_{\mathrm{t}}^{\mathrm{jet}} \approx (60 \pm 10)\,\mathrm{GeV}/c$ for the larger $p_{\mathrm{t}}^{\mathrm{min}} = 2.0\,\mathrm{GeV}/c$. At these values, the increase of yield due to background fluctuations falls below 50 % [Ver]. The same studies with the Gaussian distribuation illustrate the relevance of the jet tail of the δp_{t} distribution. The standard deviations of the fluctuations for different $p_{\mathrm{t}}^{\mathrm{min}}$ are listed in Table 7.3.

Strictly speaking, the tail of the measured δp_{t} distribution does not exactly correspond to the jet p_{t} resolution of an inclusive jet of the heavy-ion event. With the δp_{t} measurement, most demonstrative with the jet embedding, an additional binary collision is added to the event. Therefore, actually the δp_{t} distribution of $N_{\mathrm{coll}} + 1$ binary collisions is measured. The probability that a jet is overlaid by another jet, which then contributes to the jet tail, is overestimated by $1/(N_{\mathrm{coll}}-1)$, compared to an event with N_{coll} binary collisions[3]. For central events where the number of binary collisions is $\mathcal{O}(10^3)$, this is not significant and the measured δp_{t} distribution can be used for corrections of the jet spectrum.

With the tools, which were developed for the studies of the background fluctuations, an improvement of the event-wise subtraction of the median background can also be considered. A correction of the subtracted background in dependence of the orientation of the jet to the event plane could be applied. The correction factor can be estimated from the mean of the background density in the probe over the globally estimated background density: $\kappa_{\rho}(\Delta\phi) = \left\langle \rho_{\mathrm{local}}/\rho_{\mathrm{global}} \right\rangle$, where $\Delta\phi = \phi_{\mathrm{EP}} - \phi_{\mathrm{jet}}$. This correction especially improves the resolution of the jet p_{t} scale in event-by-event studies of jets where no unfolding can by used. Though, it is necessary to ensured that the event plane estimation is not correlated with the measured jets. This requires further studies.

Jet Splitting and Merging

In special cases, it can happen that an embedded jet in the environment of a heavy-ion event is reconstructed as two jets (jet splitting) or it is merged with a neighboring jet. The splitting, as illustrated in Figure 7.12, preferably happens for jets which consist of two hard cores of similar p_{t} with a distance d of less than the radius parameter ($d < R$) [CSS08a]. This results, without the heavy-ion background, in jets with atypical large jet area (*probe area*) where both hard cores are included, i. e. $A_{\mathrm{probe}} \approx 0.6-0.8$ for $R = 0.4$ (nominal $A = \pi R^2 \approx 0.5$). Those jets are located in Figure 7.13a at large negative δp_{t} (-20 GeV/$c \lesssim \delta p_{\mathrm{t}} \lesssim$ -50 GeV/c). Once they are reconstructed in the heavy-ion event, the radius is reduced to nominal jet area or less ($A_{\mathrm{rec}} \approx 0.3-0.5$) due to the split-up, as can be seen in Figure 7.13b for the leading jet of both split jets. The split-up results in a negative δp_{t}, whereas the second jet, which is not matched with the reconstructed jet, carries the missing p_{t}. The shift of the jet axis of $\delta d \approx 0.2$ in this δp_{t} region (Figure 7.13d) also indicates that it is a real split-up of two similar jets and not only a reduction in the jet area. This is not the case for the region around $\delta p_{\mathrm{t}} \approx 0$ GeV/c where one also sees some irregular jet area.

---

[3] If $p = q \cdot (N_{\mathrm{coll}}-1)$ is the probability, for a measured jet in an event with N_{coll} binary collision, to overlap with a jet of specified p_{t}, then the probability is $q \cdot N_{\mathrm{coll}}$ in an event with an additional binary collision. Hence, the overestimation is: $\frac{N_{\mathrm{coll}}}{N_{\mathrm{coll}}-1} - 1 = \frac{1}{N_{\mathrm{coll}}-1}$.

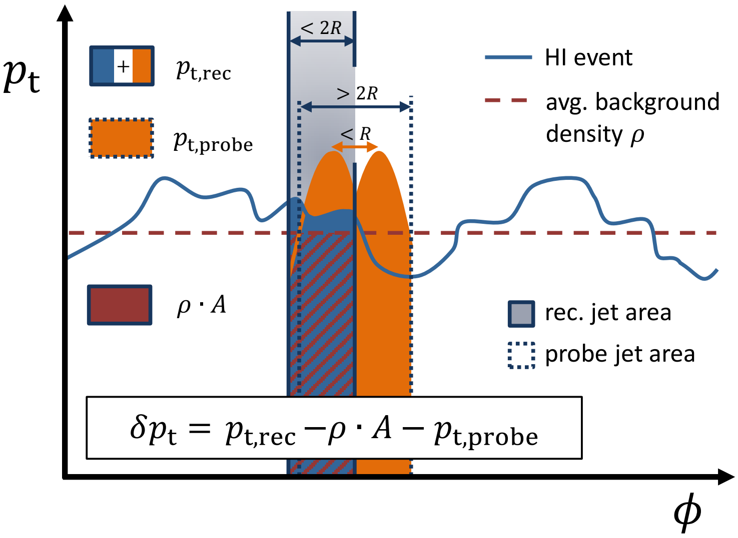

Figure 7.12: Sketch of an embedded jet with two hard cores in distance of less than R, which is split-up after embedding in a heavy-ion event. The size of the reconstructed jet is smaller than nominal and spatial shifted compared to the embedded jet. The momentum of the lost jet is contribution to negative δp_t.

With a rough δp_t dependent approximation of:

$$\delta A = A_{\text{rec}} - A_{\text{probe}} < -0.31 - (9.31 \times 10^{-3})\delta p_t \tag{7.19}$$

for jet splitting (see Figure 7.13c) the incidence rate for embedded jets above 60 GeV/c has been estimated to $\mathcal{O}(10^{-3})$. Figure 7.13 is presented for the intermediate centrality 30 − 40 % because, on the one hand, the $\delta A(\delta p_t)$ region where jet splitting is expected is not overlayed by the common background fluctuations as it is the case for the most central events, and, on the other hand, the incidence rate of jet splitting should be still of the same order as for the most central events since it depends on the rate of large area jets in the embedded probe. Plots for all centrality classes and for single track embedding, as reference of a delta probe, are available in the appendix, Section B.2.2. The estimated ratio of split-up jets reaches from $1.8 \cdot 10^{-3}$ in 0 − 10 % centrality to $2.8 \cdot 10^{-4}$ in 70 − 80 % centrality (for jets above 60 GeV/c).

From track embedding, where jet splitting does not happen by construction, the accuracy of the estimate of split-up jets by the rough definintion of

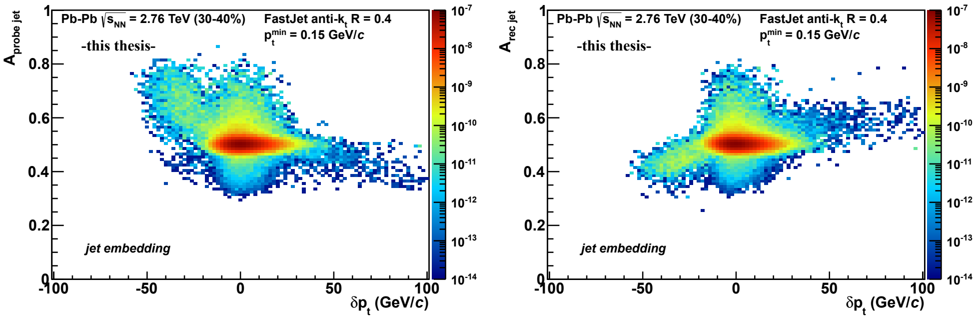

(a) Probe jet area.

(b) Reconstructed jet area.

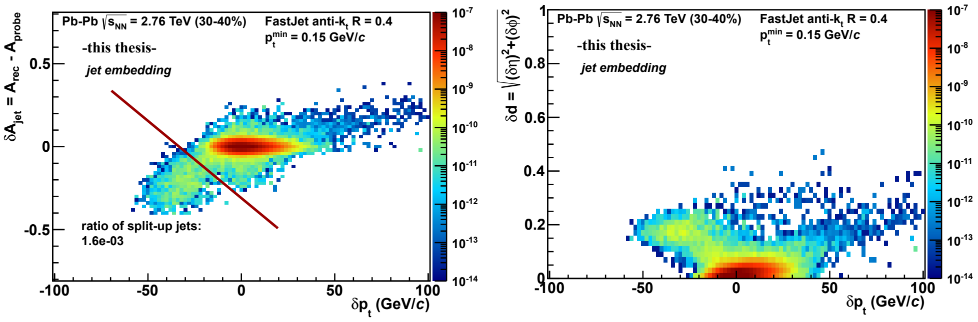

(c) Change of jet area, δA.

(d) Shift of jet axis, $\delta d = \sqrt{(\delta\eta)^2 + (\delta\phi)^2}$.

Figure 7.13: Jet areas before and after embedding in a heavy-ion event and the shift of the jet in the (η,ϕ) plane as function of δp_{t}, for centrality $30-40\,\%$.

Equation 7.19 can be deduced. Accordingly, for the most central events, a ratio of $2.7 \cdot 10^{-4}$ have been misidentified as split-up jets. The value above is already corrected for this. For centralities above 20 % the number of misidentified split-up jets is zero.

Also the opposite effect occurs: Two jets individually reconstructed in pp events are reconstructed as one jet in the presence of heavy-ion background (jet merging). This happens if two hard radiated cores exist in a distance $R < d < 2R$ [CSS08a]. This is only little evident in the δp_{t} distributions because of the jet tail, and it is distributed over a wider δp_{t} range between about 30 GeV/c and 100 GeV/c, as seen in Figure 7.13. The change of the jet area is also a bit less pronounced. In this case the jets are reconstructed in pp with a not perfectly conical area about $A_{\mathrm{probe}} \approx 0.50 - 0.35 < \pi R^2$ and in heavy-ion roughly with $A_{\mathrm{rec}} \approx 0.5 - 0.7 > \pi R^2$.

In the appendix, Section B.2.2, the corresponding plots for single track embedding are also presented. In the case of track embedding basically all jet areas are nominal ($A \approx 0.5$) and do not change much in the heavy-ion background. Only for positive δp_{t} some entries with a larger spatial shift, δd, are apparent. Those embedded tracks are merged with a true jet from the heavy-ion event. In the case of embedded jets (from pp events) both can happen: the merging with another jet from the heavy-ion event or another jet embedded with the pp event. The fraction can be estimated from the merging of embedded tracks.

Embedded jet p_{t} spectrum

For the jet embedding, simulated pp events as described in Section 3.5.5 were used. In particular for this purpose pp collisions with energy of $\sqrt{s} = 2.76$ TeV were generated. As described, the simulations were done in ten separated $p_{\mathrm{t}}^{\mathrm{hard}}$ bins. Therefore, the studies are done separately for all $p_{\mathrm{t}}^{\mathrm{hard}}$ bins and the results are merged according to the scaling factor $s_{\mathrm{p}_{\mathrm{t}}^{\mathrm{hard}}} = \sigma_{\mathrm{p}_{\mathrm{t}}^{\mathrm{hard}}}/N_{\mathrm{events}}$, whereas N_{events} includes the events discarded during simulation. Figure 7.14 compares the bin-wise weighted spectra of the embedded jets with the simulated spectrum. Besides the embedded jets which are actually used as probes (jet p_{t} 60−100 GeV/c, $p_{\mathrm{t}}^{\mathrm{hard}}$ bin >3), those without restricted jet p_{t} and from all p_{t} hard bins are also shown. The spectrum of the embedded jets should agree with the simulated spectrum, but they are not naturally identical since the embedded events were selected (semi-)randomly and (potentially) several times. Furthermore, a bias to higher jet p_{t} can be expected according to the jet matching efficiency. This only becomes relevant for jet p_{t} below 60 GeV/c, though (see Section 7.4.4). The good agreement between the spectrum confirms a sufficient event selection by the embedding task.

Since only probes with $p_{\mathrm{t}} > 60$ GeV/c are embedded, events with $p_{\mathrm{t}}^{\mathrm{hard}} < p_{\mathrm{t}}^{\mathrm{probe}}$ only contribute in exceptional cases. The probe is by definition affected by other (semi-)hard processes. Of course, this also can happen in real data. The problem is that those fluctuations in the simulation have a large weight due to the large cross-section of lower $p_{\mathrm{t}}^{\mathrm{hard}}$. In the jet spectrum this leads to peaks in the spectrum caused by single or few entries. Therefore, an upper limit for jet p_{t} of $p_{\mathrm{t}}^{\mathrm{rec}} < 2p_{\mathrm{t}}^{\mathrm{hard}}$ is applied.

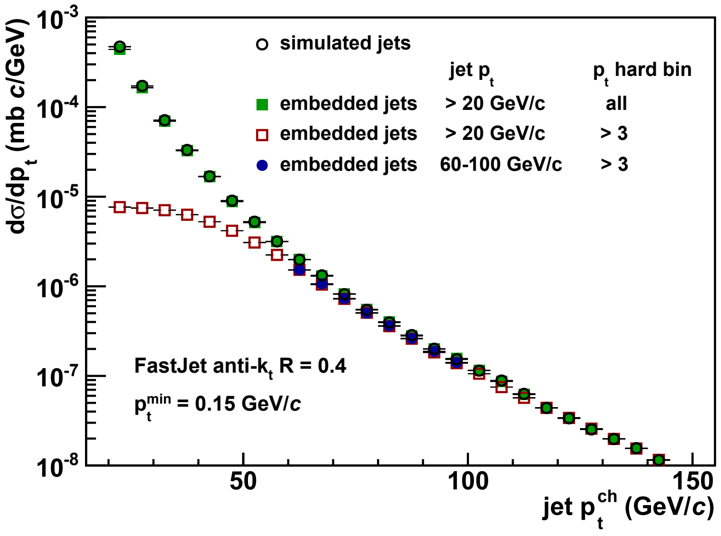

Figure 7.14: Simulated jet spectrum (black, open circles) in comparison with the effective embedded probe jet spectrum (blue). Also shown is an embedded jet spectrum for probe p_{t} above 20 GeV/c with all $p_{\mathrm{t}}^{\mathrm{hard}}$ bins (green) and bins with $p_{\mathrm{t}}^{\mathrm{hard}} > 57$ GeV/c (red).

Due to the requirement of probe $p_{\mathrm{t}} > 60$ GeV/c, only few events remain before this threshold in the corresponding $p_{\mathrm{t}}^{\mathrm{hard}}$ bins. Just by chance they basically all contribute to $\delta p_{\mathrm{t}} \approx 0$ GeV/c, hence the δp_{t} distributions of those $p_{\mathrm{t}}^{\mathrm{hard}}$ bins are lacking any tails. On the other hand they contribute with a large weighting factor to the inclusive δp_{t} distribution, which distorts its shape unreasonable, as seen from Figure B.15 in Appendix. That is the reason why the lowest four $p_{\mathrm{t}}^{\mathrm{hard}}$ bins with $p_{\mathrm{t}}^{\mathrm{hard}} < 57$ GeV/c (bin<4) have not been used for the final studies. As a side effect, skipping the $p_{\mathrm{t}}^{\mathrm{hard}}$ bins speeds up the analysis. As visible in Figure 7.14 this leads to a small deviation from the simulated jet spectrum. This is not significant for the results of the presented studies.

7.4.3 Iterative Gaussian Fit (and the Intrinsic Standard Deviation)

A left-hand side (LHS) Gaussian fit of the background p_{t} fluctuation distribution, δp_{t}, is a convenient method for an intuitive measurement of the background fluctuations ignoring the apparent tail from jets at the right-hand side. Even though already from pure random fluctuations we know that the distribution is asymmetric and can be better described by a Γ function [Tan01; Tan04; Pop11]. Nevertheless, the LHS is almost Gaussian in high multiplicity, i. e. central events, and the extrapolation to the right-hand side (RHS) can illustrate the divergence.

The standard deviation of the full distribution, σ, and the fit parameters, σ^{LHS} and μ^{LHS}, are obtained from the distribution with the binning of highest available granularity. For the embedding and random cones it is $1\,\mathrm{GeV}/c$. The presented distributions have been re-binned with the aim of clarity. This is more relevant for strongly falling distributions. Hence, the obtained standard deviations, σ, from re-binned distributions would increase more in peripheral events than in central events. As an example, in case of re-binning by factor three in central events and $p_{\mathrm{t}}^{\mathrm{min}} = 0.15\,\mathrm{GeV}/c$ the difference is in order of $0.03\,\mathrm{GeV}/c$, whereas it reaches in peripheral events more than $0.1\,\mathrm{GeV}/c$.

To ensure that the peak of the distribution is correctly found by the fit, it is unavoidable that also a small part of the right-hand side is taken into account. In addition it cannot be a priori expected that the peak of the distribution is at $\delta p_{\mathrm{t}} = 0$. In fact, this is a test of the background subtraction. For that reason variable fitting ranges and an iterative fitting procedure were chosen. The range was chosen to $[\mu^{\mathrm{LHS}} - 3\sigma^{\mathrm{LHS}}, \mu^{\mathrm{LHS}} + 0.5\sigma^{\mathrm{LHS}}]$, with the mean μ^{LHS} and standard deviation σ^{LHS} from the previous iteration. For the initial step, the fit range is set to $[-60.0\,\mathrm{GeV}/c, 5.0\,\mathrm{GeV}/c]$ and $\mu^{\mathrm{LHS}} = 0.0\,\mathrm{GeV}/c$. The terminate condition is a change in μ^{LHS} of less than $0.01\,\mathrm{GeV}/c$, while the minimum number of iterations is two and the maximum number of iterations is 20. The results published in [Aam+12a] have been obtained with a minimum number of one iteration. Thus, it could happen, if $|\mu^{\mathrm{LHS}}| < 0.01$, that the final fit range is the unchanged, initial range of $[-60.0\,\mathrm{GeV}/c, 5.0\,\mathrm{GeV}/c]$. Therefore, values in this thesis may slightly vary compared to the published results.

In studies with modified fit ranges, the chosen values were confirmed as suitable. Some results are listed in the appendix, Section B.2.3. Most crucial is the upper limit of the fitting interval. Although, even an upper bound of the fitting range at μ^{LHS} works reliably with high statistics, contrary to first studies with lower statistics. Obviously the Gaussian fit becomes difficult and less meaningful for narrower δp_{t} distributions of peripheral events and/or higher track p_{t} cuts, at the latest when the width of the Gaussian is of the order of the bin width, namely $1\,\mathrm{GeV}/c$, it cannot produce reasonable results. In the case of $p_{\mathrm{t}}^{\mathrm{min}} = 2\,\mathrm{GeV}/c$, in addition, the track p_{t} cut causes a depletion in the δp_{t} distribution between $0 - 2\ \mathrm{GeV}/c$, which cannot be accounted for by the fit. The fit is not considered if the fit failed, e. g. due to no data in the fit range because the peak was not found correctly, if the number of degrees of freedom (NDF) is less than 1, or $\chi^2/\mathrm{NDF} > 5000$ (see e. g. Section B.2.1 in the appendix).

In some cases, the fitting iterations does terminate only after 20 iterations. This is in general the case if the fitting procedure oscillates between (mostly two) different results. The outcome of those unstable fits, which is accidentally chosen from the possible results, is marked with an asterisk.

7.4.4 Systematic Studies

Probe Matching

With the matching condition described in Section 7.3.4, a very high matching efficiency of the embedded probe has been reached. A detailed list about the statistics can be found in the appendix in Table B.2. Only eight out of more than 12 million embedded singles tracks could not be related to jets in the heavy-ion event anymore. All of them had quite low p_t between 60 and 70 GeV/c and have been embedded in central events ($< 20\,\%$).

For embedded jets, the matching is more crucial since their p_t is distributed over several tracks. The momentum density, p_t/A, of some embedded jets is only of the order of or even less than the median event background density, ρ, in central events. Nevertheless, from the more than 9.5 million embedded jets between 60 and 100 GeV/c only 437 jets, i. e. a ratio of $4.6 \cdot 10^{-5}$, could not be matched in the heavy-ion event. Most of them carry quite low p_t again ($<$ 70 GeV/c: 308 jets, $<$ 80 GeV/c: 414 jets). A centrality dependence is visible, even though only weakly pronounced. Another 485 jets could only be matched with a fraction of the embedded jets of less than 50 %, hence they were rejected. This happens over a wider range of probe p_t but is still dominated by low p_t.

Most of the loss of embedded probes actually is due to the acceptance cut. Of the embedded single tracks about 1 %, roughly 120 000, have been rejected afterwards, since the corresponding jet in the heavy-ion were reconstructed with $|\eta| > 0.5$. A centrality dependence is also apparent here. In peripheral events, that happens only in about 0.2 % of all cases, while almost 1.9 % were rejected in central events. This agrees well with the expectation due to the resolution of jet axis in pseudo-rapidity η in those centrality classes. For centrality $0-10\,\%$ the standard deviation of the smearing is $\sigma(\delta\eta) = 2.6 \cdot 10^{-2}$, while it is only $\sigma(\delta\eta) = 1.3 \cdot 10^{-3}$ in centrality $70-80\,\%$. According to the

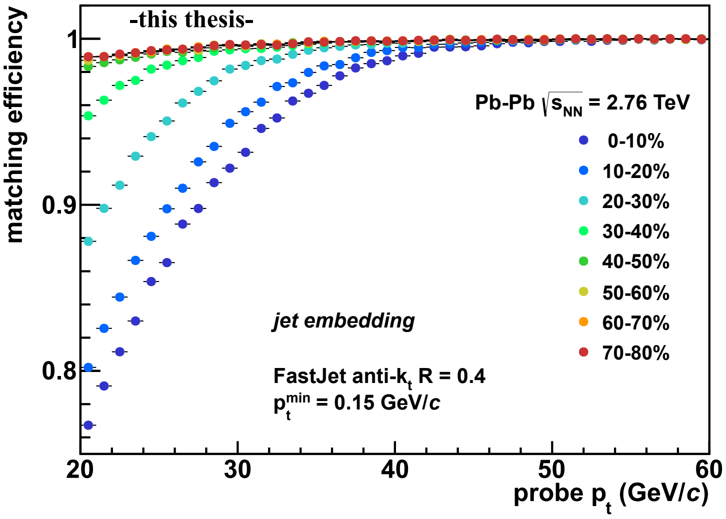

Figure 7.15: Matching efficiency of embedded jets as function of probe p_t for different centralities.

---

cummulative distribution function for the standard normal distribution and with our pseudo-rapidity window of $|\eta| < 0.5$, for those standard deviations the expected ratio of reconstructed jets with $|\eta| > 0.5$ is for peripheral events 0.11 % and for central events 2.1 %.

As seen in Figure 7.15, the matching efficiency drops for probe p_t below 50 GeV/c, depending on the centrality. Identifying jets of those p_t (and the simulated fragmentation) beneath the background is difficult, and they probably are biased towards hard fragmentation. Uncertainties from this have been avoided since only probes above 60 GeV/c have been taken into account for the background fluctuation studies.

Run Trending of $\delta \mathbf{p}_t$

For the final results, the stability of the fluctuations over the run period is essential. Figure 7.16 shows the standard deviation of the background p_t fluctuations, $\sigma(\delta p_t)$, as function of the run number. The number of entries

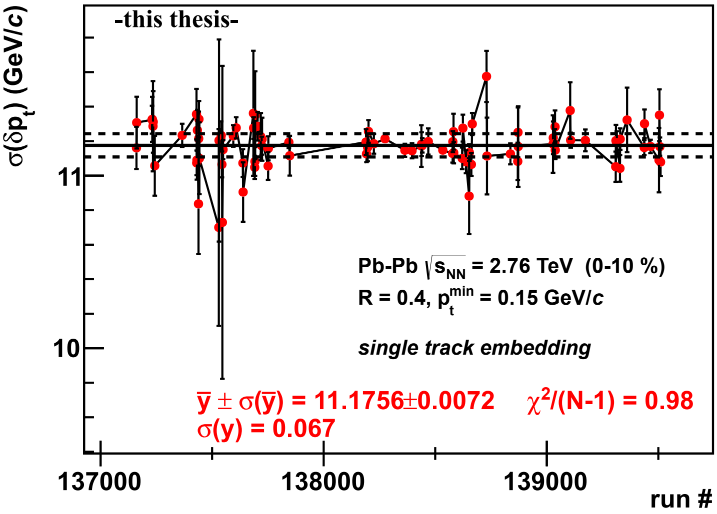

Figure 7.16: Standard deviation of the background p_{t} fluctuations, $\sigma(\delta p_{\mathrm{t}}) =: y$, as function of run number for centrality $0-10\,\%$. The solid line shows the average $\sigma(\delta p_{\mathrm{t}})$, the dashed lines represent the 1σ band.

---

per run for this centrality class reaches from $\mathcal{O}(10^2)$ to $\mathcal{O}(10^5)$, which results in different statistical uncertainties. The weighted average of $\sigma(\delta p_{\mathrm{t}}) =: y$,

$$\overline{y} = \frac{\sum_i w_i y_i}{\sum_i w_i}, \tag{7.20}$$

has been estimated to $\overline{y} = \overline{\sigma(\delta p_{\mathrm{t}})} = 11.18 \pm 0.01\,\mathrm{GeV}/c$, where the weighting factor is $w_i = 1/\sigma(y)$, with $\sigma(y)$ as the run-by-run standard deviation, and the combined uncertainty is $\sigma(\overline{y}) = 1/\sqrt{\sum_i w_i}$. The solid line shows the weighted average $\overline{y}$, while the dashed lines represents the run-by-run 1σ interval of y ($\sigma(y) = 0.07\,\mathrm{GeV}/c$). The combined standard deviation $\sigma(\overline{y}) = 0.01\,\mathrm{GeV}/c$ is much smaller. The weighted average $\sigma(\delta p_{\mathrm{t}})$ is consistent with the inclusive results of all runs (see Table 7.2). A χ^2/NDF of 0.98 for the run-by-run fluctuations indicates that they are in good agreement with the pure statistical uncertainties. Therefore, the run-by-run systematic errors can be considered as negligible. Considering the uncertainties from the statistics in the individual runs, no strong outliers, which would necessitate to exclude those runs from the analysis, are present.

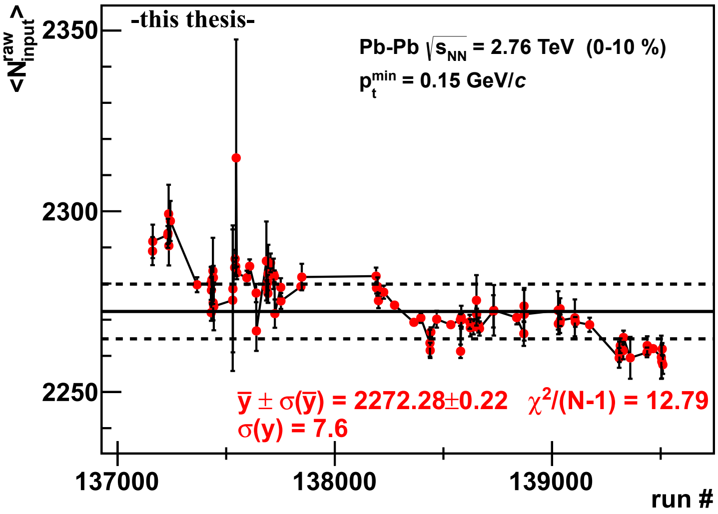

Figure 7.17: Average raw multiplicity, $\left\langle N_{\text{input}}^{\text{raw}} \right\rangle =: y$, as function of run number for centrality $0-10\,\%$. The solid line shows the average raw multiplicity over all runs, the dashed lines represent the 1σ band.

The average raw multiplicity, $\left\langle N_{\text{input}}^{\text{raw}} \right\rangle$, in centrality class $0-10\,\%$ is shown in Figure 7.17 as function of run number. With progressing run period a slight decrease of multiplicity is visible. The decrease is of the order of the standard deviation $\sigma(\left\langle N_{\text{input}}^{\text{raw}} \right\rangle) = 7.6$, though. For the first five runs the average multipicity is $\left\langle N_{\text{input}}^{\text{raw}} \right\rangle = 2292.7 \pm 1.7$, while it is reduced for the last five runs to $\left\langle N_{\text{input}}^{\text{raw}} \right\rangle = 2261.3 \pm 0.9$. That indicates a decrease in the tracking efficiency of about 1.4 % during the run period. For the pure statistical fluctuation which is proportianal to square root of multiplicity, $\sqrt{N_{\text{input}}^{\text{raw}}}$, that means an expected decrease of the background p_{t} fluctuations, $\sigma(\delta p_{\text{t}})$, by 0.7 %. The decrease of the fluctuations caused by flow, which is roughly linear proportinal to the multiplicity, $N_{\text{input}}^{\text{raw}}$, is accordingly expected to be about 1.4 %. However, the statistical fluctuations are the dominant contribution in central events (see Figure 7.9). Such a trend in δp_{t} is not obvious in Figure 7.16. The effect is too small compared to the run-by-run fluctuations of $\sigma(\delta p_{\text{t}})$. The difference between the first five runs with $\sigma(\delta p_{\text{t}}) = (11.29 \pm 0.05)\,\text{GeV}/c$ and the last

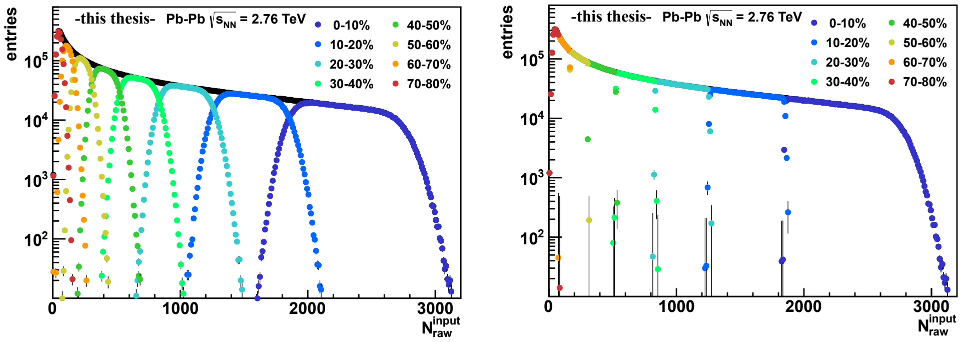

(a) Centrality estimated by VZERO.

(b) Centrality from the track multiplicity.

Figure 7.18: Comparison of the centrality classes obtained from VZERO (left) and from the number of reconstructed tracks (right).

five runs with $\sigma(\delta p_{\mathrm{t}}) = (11.16 \pm 0.03)\,\mathrm{GeV}/c$ is of the order of 1 %, but not significant.

Centrality Estimation

A further systematic uncertainty in the measured δp_{t} distributions is the centrality estimation. The most common detectors in ALICE which are used to determine the centrality of an event are the VZERO detectors ($-3.7 < \eta < -1.7$, $2.8 < \eta < 5.1$). They provide the best centrality percentile resolution [Toi11]. Hence, this was also the choice for the studies of the background fluctuations as discussed in Section 3.5.2. Nevertheless, for these measurements the closest related method is the centrality obtained from the number of tracks, $N_{\mathrm{input}}^{\mathrm{raw}}$, in the central barreln $|\eta| < 0.9$. In the previous section, it was discussed how different contributions to the background p_{t} fluctuations are either proportional to $\sqrt{N_{\mathrm{input}}^{\mathrm{raw}}}$ (Poissonian) or $N_{\mathrm{input}}^{\mathrm{raw}}$ (collective flow).

The estimation of the centrality percentile by the number of tracks in the central barrel is independent, but principally equivalent to those by VZERO signals. It is only estimated from a different pseudo-rapidity region. In fact, the SPD and TPC (among others) are also used for the validation of the centrality measurement by VZERO [Toi11]. Fluctuations and detector inefficiencies induce for both measurements its own finite resolution. The centrality classes estimated by tracks have (in simplest case) intrinsically a sharp threshold in

Table 7.4: Standard deviation of δp_t obtained from track embedding for centrality classes estimated by VZERO, the track multiplicity, and weighted with the number of binary collisions, N_coll. The statistical uncertainties are 0.01 GeV/c for all values.

	$\sigma(\delta p_\mathrm{t})$ (GeV/c)		
Centrality	VZERO	Muliplicity (un-weighted)	Muliplicity (N_coll weighted)
0–10 %	11.18	11.21	11.24
10–20 %	10.18	10.18	10.24
20–30 %	8.44	8.43	8.51
30–40 %	6.49	6.47	6.56
40–50 %	4.69	4.67	4.76
50–60 %	3.24	3.23	3.31
60–70 %	2.16	2.15	2.21
70–80 %	1.40	1.35	1.41
0–20 %	10.69	10.71	10.87
20–40 %	7.53	7.51	7.86
40–60 %	4.03	4.01	4.33
60–80 %	1.82	1.79	2.01

the number of these reconstructed tracks. While the VZERO centrality classes are smeared out in the number of tracks, as can be seen in Figure 7.18a.

Whereas the VZERO centrality has been estimated with the standard centrality class of ALICE, the thresholds for the centrality classes from the number of tracks were estimated run-by-run based on the same track cuts which were used in the analysis, since the tracking efficiencies may be different. Actually, a slight trend in the average number of tracks during the run period has been observed, as was discussed before. Therefore, the centrality classes over all runs do not have sharp thresholds in the number of tracks, even though still close to it. The resulting distributions are presented in Figure 7.18b.

By comparing both centrality classifications it is important to understand the difference between the corresponding δp_t distributions. Since the VZERO centrality classes are smeared-out in the number of tracks, one could expect that these δp_t distributions differ less with centrality than those in centrality classes from the multiplicity. Even though the effect is almost evanescent, it is still apparent in the peripheral bins as can be seen in Table 7.4. The result

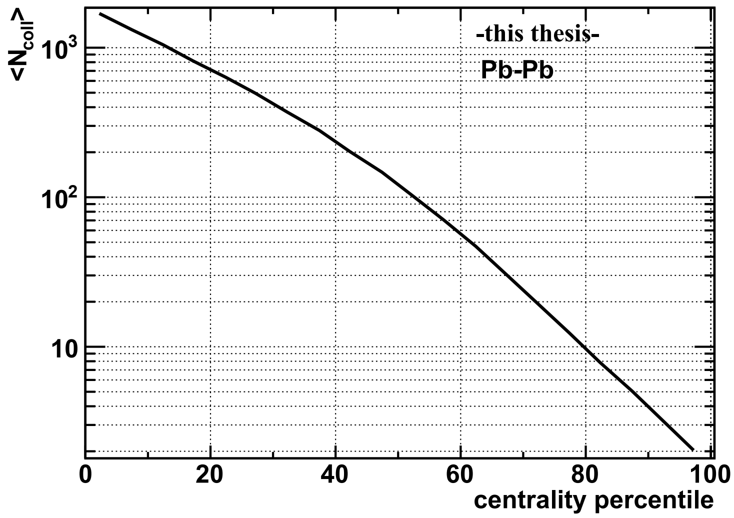

Figure 7.19: Average number of binary collisions as function of centrality from Glauber calculations.

weighted with the number of binary collisions, N_{coll}, is also shown. This is discussed in the following section.

Weighting with Number of Binary Collisions

The heavy-ion events are by definition distributed flatly over the centrality percentile. The embedding of one pp jet event corresponds to an apposition of one additional binary collision in such an event. Consequently, the probes are also uniformly distributed in centrality. The inclusive distribution of a high p_{t} probe, like the jet distribution, is on the other hand not homogeneously distributed over the events in all centralities. The expected jet production scales with the number of binary collisions N_{coll} which increases stronger than linearly with the centrality percentile (see Figure 7.19). Since the background fluctuations are measured in a finite centrality percentile interval (or multiplicity interval, respectively), the centroid of the events is for realistic inclusive distributions shifted to more central events (or events with higher multiplicity) than it is for the probed flat distributions where it is in the bin center.

The impact of this on the measured background p_t fluctuations is studied by weighting the measurement with the average number of binary collisions of a heavy-ion event at the given centrality. The number of binary collisions, N_coll, is calculated from the centrality and the resulting impact parameter based on studies done by Alberica Toia [AliCS] using the Glauber model [Mil+07]. As shown in Figure 7.19, it reaches from single collisions in peripheral events up to $\mathcal{O}(10^3)$ in central collisions.

The centrality percentile of the event is estimated from the number of accepted tracks since those were available in finer binning than the VZERO centrality. The difference between both methods was discussed in the previous section. The determined standard deviations of the δp_t distributions are listed in Table 7.4. The weighted δp_t distributions show a bit larger standard deviations since they satisfy the larger contributions from more central events within the specified centrality bin. For 10 % centrality bins, the discrepancy is less than 0.1 GeV/c. Thus, it is a small systematic uncertainty on the presented results. It is obvious that the variation strongly depends on the width of centrality bin, so it larger for the shown 20 % bins.

Chapter 8

Summary

In this thesis, jet measurements with the ALICE experiment at the LHC (CERN) have been presented. Jets are studied with the intention of probing the quark-gluon plasma (QGP), which is generated in heavy-ion collisions, at an early stage. Of special interest is the fragmentation pattern of jets which is expected to be modified in the hot and dense medium. As a baseline for the measurements in heavy-ion collisions, the analysis of proton-proton (pp) collisions is essential. First results have been presented in this thesis for the charged particle momentum distribution in jets in pp collisions. It was measured with ALICE at a center-of-mass energy of $\sqrt{s} = 7\,\text{TeV}$. The outlined measurements reach up to a charged-jet p_t of 80 GeV. The measured fragmentation shows the behavior of softening with increasing jet p_t, as expected from pQCD. In comparison with PYTHIA simulations (Perugia-0 tune), a deviation of the soft fragmentation ($\xi = \ln\left(p_\text{t}^\text{jet}/p_\text{t}^\text{trk}\right) > 3$) up to a factor of about 1.5 at $\xi \approx 5.5$ (for jet $p_\text{t} \approx 50$ GeV/c) has been observed. The hard fragmentation is better described by the simulations. The results are robust against different types of jet finders, as has been shown for UA1 cone and anti-k_t recombination algorithms.

In order to compensate for the higher yield of hard processes per event in Pb–Pb collisions, a trigger for jets in pp is needed, which enhances the statistics above 100 GeV/c. In this thesis, the possible performance of the Transition Radiation Detector (TRD) of ALICE as a jet trigger has been investigated. Results have been obtained based on PYTHIA simulations from offline TRD stand-alone tracks, under the assumption that the online tracking of the TRD fulfills a similar performance. It has been demonstrated that the TRD can provide a high rejection factor of the order of the required 10^4 to 10^5 in coincidence with high jet-trigger efficiencies. At jet p_{t} above 100 GeV/c, the trigger efficiency reaches more than 80 %. As a result, the TRD can enlarge the reach of reconstructed charged jets in ALICE to roughly 200 GeV/c. The expected yield is, compared to recordable minimum-bias data, increased by a factor of about 100. This means about 10^3 reconstructed charged jets with $p_{\mathrm{t}} = 190 - 200$ GeV/c after one year of data taking. A pure minimum-bias trigger can sample such a statistic only for jets up to 100 GeV/c.

The bias on the jet sample introduced by the trigger has been evaluated. As a baseline for a medium-modified fragmentation function in heavy-ion collisions, a potentially introduced bias on the momentum distribution in jets from pp collisions is critical. According to the chosen trigger thresholds in number of required tracks and minimum track p_{t}, a respective bias has been observed. Moreover, it has been shown that it can be reduced by careful selection of the trigger condition, without essential loss of rejection factor. Especially the combination of two trigger conditions, one which triggers on hard-fragmented jets (high track p_{t} threshold with low number of required tracks) and another which triggers on more soft-fragmented jets (larger number of required tracks with lower track p_{t} threshold) has shown an improved performance with respect to fragmentation bias and trigger turn-on.

In the last part of analysis presented in this thesis, it has been shown that the soft underlying-event in heavy-ion collisions and its fluctuations have a large impact on jet reconstruction. A good understanding of the background is important for the interpretation of jet measurements and their correction. Therefore, charged background p_{t}-fluctuations in Pb–Pb collisions at LHC energies ($\sqrt{s_{\mathrm{NN}}} = 2.76\,\mathrm{TeV}$) have been studied and characterized. The events were probed under conditions, e. g. with track quality cuts and probe area, as they are typically used for reconstruction of charged jets in ALICE.

The average charged background p_{t}-density in the 10 % most central events has been estimated to $\langle\rho\rangle = (138.32 \pm 0.02)\,\mathrm{GeV}/c$ with an event-by-event spread of $\sigma(\rho) = (15.51 \pm 0.01)\,\mathrm{GeV}/c$. This globally estimated background is event-wise subtracted from the reconstructed jets, whereas the background is overlaid by remaining region-to-region fluctuations. The fluctuations in the events of central collisions have been measured (by random cones) to $\sigma(\delta p_{\mathrm{t}}) = (10.98 \pm 0.01)\,\mathrm{GeV}/c$. With the measured δp_{t} distribution, peaked at zero, the methods of the average background subtraction also could be verified.

For the region-to-region fluctuations, different sources have been characterized. Some of the fluctuations are caused by purely random, statistical fluctuations of the particle number and momenta in a defined region. These Poissonian fluctuations show a strong centrality dependence, since they are roughly proportional to $\sqrt{N}$, where N is the number of tracks. In addition several source of non-Poissonian fluctuations contribute. One is the presence of jets, apparent as a correlated flux of (high-p_t) tracks in the event. Even though they are not considered as an underlying event in common definition from pp collisions, there is, especially in heavy-ion collisions, a finite chance for jets to overlap and one jet needs to be counted as background modification to the other. In the δp_t distribution, they appear as tails at the high-p_t side.

Further region-to-region variations of the background have been explained by collective flow of particles caused by geometrical anisotropy of the overlap region of the colliding nuclei. As an additional variation in the number of tracks, the flow basically causes a shift in δp_t, depending on the orientation to the reaction plane. All the mentioned Poissonian and non-Poissonian fluctuations can describe most of the observed background p_t fluctuations. Further possible sources of non-Poissonian fluctuations, e. g. introduced by inefficient detector regions, were not considered in the presented studies.

The background fluctuations cause an essential contribution to the resolution of the reconstructed charged jet-p_t scale in heavy-ion collisions. This is further increased by an impact of the soft bulk in heavy-ion collisions on the jet finding process. Due to this, the width of the δp_t distribution is increased if it is measured using embedded tracks or jets as probes, which utilizes jet reconstruction. For embedded jets from simulated pp events and using the anti-k_t jet finder, it has been measured to $\sigma(\delta p_\mathrm{t}) = (11.34 \pm 0.02)\,\mathrm{GeV}/c$. This result strongly depends on the used jet finder and its settings. A notable relevance of the applied ghost area size and the consequent jet area resolution has been identified. Furthermore, jet splitting and merging, introduced by the soft background, has been observed. However, it occurs so rarely ($\mathcal{O}(10^{-3})$ for jets above 60 GeV/c) that it is not reflected in the measured $\sigma(\delta p_\mathrm{t})$.

In summary, the studies in this thesis form a basis to determine the medium-modified jet fragmentation, using a jet-trigger for the baseline measurements in pp collisions. The measurements of the background fluctuation are an essential contribution for the unfolding of the measured jet spectrum in Pb–Pb collisions.

Zusammenfassung

Im Rahmen dieser Arbeit wurden Jet-Messungen mit dem ALICE-Experiment des LHC (CERN) vorgestellt. Die Motivation, sich mit Jets zu befassen, ist die Erforschung des in Schwerionen-Kollisionen erzeugten Quark-Gluon-Plasmas (QGP). Jets sind das Endprodukt von harten Sonden, die das QGP in einem frühen Stadium testen. Von besonderem Interesse ist die Fragmentierung der Jets, welche durch das heiße und dichte Medium beeinflusst werden sollte. Als Referenz für die Modifikation in Schwerionen-Kollisionen ist die Messung von Jets in Proton-Proton-Kollisionen (pp) notwendig. In dieser Arbeit wurden erste Ergebnisse der Impulsverteilung geladener Teilchen in Jets, welche die Jet-Fragmentierung repräsentiert, aus pp-Kollisionen präsentiert. Die Messungen wurden mit dem ALICE Experiment bei einer Schwerpunktsenergie von $\sqrt{s} = 7\,\text{TeV}$ durchgeführt. Die gezeigten Ergebnisse reichen bis zu einem geladenen Jet-p_t von 80 GeV/c. Die untersuchten Jets zeigen mit zunehmendem Jet-p_t eine weichere Fragmentierung, wie aus pQCD erwartet. Im Vergleich zu PYTHIA-Simulationen (mit Perugia-0 Tune) wird in der weichen Fragmentierung ($\xi = \ln\left(p_\text{t}^\text{jet}/p_\text{t}^\text{trk}\right) > 3$) eine Abweichung von bis zu einem Faktor 1,5 bei $\xi \approx 5.5$ (bei einem Jet $p_\text{t} \approx 50$ GeV/c) beobachtet. Die harte Fragmentierung wird durch die Simulation besser beschrieben. Die Ergebnisse sind stabil für verschiedene Typen von Jet-Findern, wie mit dem UA1 Cone- und anti-k_t Rekombinationsalgorithmus gezeigt wurde.

Um die in Pb–Pb-Kollisionen gegenüber pp-Kollisionen vermehrte Produktion an harten Prozessen pro Ereignis auszugleichen, wird für letztere ein Trigger für Jets benötigt, welcher die Statistik oberhalb von 100 GeV/c erhöht. In dieser Arbeit werden die zu erwartenden Eigenschaften des Übergangsstrahlungsdetektors (transition radiation detector, TRD) von ALICE im Einsatz als Jet-Trigger untersucht. Die Ergebnisse wurden aus PYTHIA-Simulationen gewonnen, basierend auf (offline) rekonstruierten Teilchenspuren im TRD, in der Annahme, dass die Ad-hoc-Spurrekonstruktion des TRD im Zuge der

Messung (online) ähnliche Eigenschaften aufweist. Es wurde gezeigt, dass ein TRD Jet-Trigger einen hohen Unterdrückungsfaktor der Ereignisrate in der Größenordnung der erforderlichen 10^4 bis 10^5 bei gleichzeitig hoher Jet-Trigger-Effizienz bereitstellen kann. Bei einem Jet-p_t oberhalb von 100 GeV/c erreicht die Trigger-Effizienz mehr als 80 %. So kann der TRD-Jet-Trigger prinzipiell den Impulsbereich rekonstruierter geladener Jets in ALICE auf bis etwa 200 GeV/c erweitern. Bei diesen Jet-p_t ist die Ausbeute im Vergleich zu den aufzeichenbaren Minimum-Bias-Daten um etwa einen Faktor 100 erhöht. Dies resultiert in etwa 10^3 rekonstruierte geladene Jets mit $p_\mathrm{t} = 190 - 200$ GeV/c nach einem Jahr Datennahme. Ein einfacher Minimum-Bias-Trigger kann eine solche Statistik nur für Jets bis 100 GeV/c erreichen.

Es wurde die durch den Trigger verursachte Voreingenommenheit (Bias) auf die Jet-Auswahl ermittelt. Besonders der Einfluss eines möglichen Bias auf die gemessene Impulsverteilung in Jets von pp-Kollisionen, als Basismessung für eine vom Medium modifizierte Jet-Fragmentation in Schwerionenkollisionen, ist kritisch. Entsprechend der gewählten Trigger-Schwellen, in der Anzahl der geforderten Teilchenspuren und einem minimalen Teilchenimpuls, wurde ein Bias in der Jet-Auswahl festgestellt. Zudem konnte gezeigt werden, dass mit einer sorgsamen Wahl der Trigger-Bedingungen dieser Bias erheblich reduziert werden kann, ohne eine wesentliche Verminderung des Unterdrückungsfaktors der Ereignisrate. Insbesondere die Kombination zweier Trigger-Bedingungen, wobei eine Bedingung auf hart fragmentierte Jets und eine andere Bedingung auf weicher fragmentierte Jets abzielt, zeigt eine Verminderung des Bias und eine Verbesserung des Ansprechverhaltens vom Trigger.

In der letzten vorgestellten Analyse dieser Arbeit wurde gezeigt, dass der weiche Ereignisuntergrund in Schwerionenkollisionen und dessen Fluktuationen eine große Auswirkung auf die Jet-Rekonstruktion haben. Ein gutes Verständnis des Untergrundes ist wichtig für die Auswertung von Jet-Messungen und dessen Korrekturen. Deswegen wurden p_t-Fluktuationen im geladenen Anteil des Untergrunds in Pb–Pb-Kollisionen bei LHC-Energien ($\sqrt{s_\mathrm{NN}} = 2.76\,\mathrm{TeV}$) untersucht und beschrieben. Dazu wurden die Ereignisse unter Bedingungen sondiert, wie sie üblicherweise bei der Rekonstruktion geladener Jets in ALICE angewandt werden. Darunter fallen z. B. die Qualitätsbedingungen an die Teilchenspuren und die Größe der sondierten Fläche.

Die durchschnittliche p_t-Dichte des geladenen Untergrunds wurde in den 10 % zentralsten Ereignissen zu $\langle\rho\rangle = (138.32 \pm 0.02)\,\mathrm{GeV}/c$ bestimmt, mit einer Streuung von $\sigma(\rho) = (15.51 \pm 0.01)\,\mathrm{GeV}/c$ von Ereignis zu Ereignis. Jeder rekonstruierte Jet wird einzeln für den durchschnittlichen, global ermittelten Untergrund des jeweiligen Ereignisses korrigiert. Es verbleiben noch der Einfluss von Region-zu-Region-Fluktuationen der Untergrunddichte. In den Ereignissen zentraler Kollisionen wurden die p_{t}-Fluktuationen (mit Random Cones, zufällig platzierten Sonden) zu $\sigma(\delta p_{\mathrm{t}}) = (10.98 \pm 0.01)\,\mathrm{GeV}/c$ gemessen. Mit den gemessenen, um Null verteilten δp_{t}-Verteilungen konnte auch die Jet-p_{t}-Korrektur für den globalen Untergrund im Ereignis verifiziert werden.

Die Region-zu-Region-Fluktuationen konnten durch die Kombination mehrerer Quellen beschrieben werden. Ein Teil wird durch zufällige, statistische Fluktuationen in der Anzahl der Teilchen und deren Impulse innerhalb eines definierten Raumbereichs hervorgerufen. Diese Poisson-Fluktuationen weisen eine starke Zentralitätsabhängigkeit auf, da sie annähernd proportional zu $\sqrt{N}$ sind, wobei N die Anzahl der rekonstruierten Teilchen ist. Darüber hinaus tragen verschiedene nicht statistische Effekte zu den Fluktuationen bei. Zum einen sind dies vorhandene Jets, die als korrelierte Teilchenproduktion (mit hohem p_{t}) in Ereignissen auftreten. Obwohl sie in der gebräuchlichen Charakterisierung aus pp-Kollisionen nicht als Ereignisuntergrund betrachtet werden, besteht insbesondere in Schwerionenkollisionen eine gewisse Wahrscheinlichkeit für Jets sich zu überlagern. In diesem Fall muss einer der Jets als erhöhter Untergrund des anderen betrachtet werden. In der δp_{t}-Verteilung führt dies zu vermehrten Einträgen bei hohen Transversalimpulsen.

Weitere Region-zu-Region-Schwankungen des Untergrunds wurden durch den kollektiven Teilchenfluss (Collective Flow) erklärt, welcher durch die geometrische Anisotropie im Überlappungsbereich der kollidierenden Atomkerne auftritt. Mit einer zusätzlichen lokalen Schwankung in der Anzahl der Teilchen verursacht der kollektive Teilchenfluss im Wesentlichen eine Verschiebung in δp_{t}, abhängig von der Orientierung der Probe zur Reaktionsebene der Atomkerne. Mit den genannten Poisson- und Nicht-Poisson-Fluktuationen können die beobachteten p_{t}-Fluktuationen im Untergrund fast vollständig beschrieben werden. Weitere mögliche Ursachen von Fluktuationen, wie zum Beispiel ineffiziente Detektorbereiche, wurden in den gezeigten Studien nicht betrachtet.

Die Untergrundfluktuationen tragen mit einem wesentlichen Anteil zur Auflösung der p_{t}-Skala der rekonstruierten geladenen Jets in Schwerionenkollisionen bei. Dies wird durch den zusätzlichen Einfluss auf den Jet-Findungsprozess weiter verstärkt. Aus diesem Grund ist die δp_{t}-Verteilung verbreitert, wenn sie von Proben (einzelnen Teilchen oder Jets), die in das Ereignis eingebettet werden, unter Verwendung von Jet-Rekonstruktion bestimmt wird. Die Standardabweichung wurde mit eingebetteten Jets von simulierten pp-Ereignissen und dem anti-k_t Jet-Finder zu $\sigma(\delta p_\mathrm{t}) = (11.34 \pm 0.02)\,\mathrm{GeV}/c$ gemessen. Dieses Ergebnis hängt stark vom verwendeten Jet-Finder und dessen Einstellungen ab. So konnte ein relevanter Einfluss von der Zellgröße (Ghost Area) zur Bestimmung des Jet-Ausmaßes und der damit verbundenen Auflösung der Jet-Größe festgestellt werden. Verursacht durch den weichen Untergrund, wurde des Weiteren die Aufspaltung und Vereinigung von Jets beobachtet. Allerdings tritt dies nur seltenen auf ($\mathcal{O}(10^{-3})$, für Jets oberhalb von 60 GeV/c), so dass es im gemessenen $\sigma(\delta p_\mathrm{t})$ nicht widergespiegelt wird.

Zusammenfassend bilden die Studien dieser Arbeit die Grundlage zur Bestimmung der medium-modifizierten Jet-Fragmentation unter Verwendung eines Jet-Triggers für die Referenzmessung in pp-Kollisionen. Die Messungen der Untergrundfluktuationen sind ein notwendiger Beitrag zur Korrektur des gemessenen Jet-Spektrums in Pb–Pb-Kollisionen.

Appendix A

Momentum Distribution in Jets

A.1 Analyzed Runs and Statistics

Table A.1: List of pp runs at $\sqrt{s} = 7$ TeV used for analysis of the momentum distribution in jets. Quoted number of events are accepted minimum-bias events.

LHC10b (pass2)		52 runs (24.3 M events)					
114931	115318	115335	115414	116288	116559	116574	116643
117050	117059	117077	117099	117118	115186	115322	115345
115514	116401	116561	116609	116644	117052	117060	117082
117109	117120	115193	115325	115393	116102	116402	116562
116610	116645	117053	117063	117086	117112	117220	115310
115328	115401	116112	116403	116571	116611	117048	117054
117065	117092	117116	117222				
LHC10c (pass2)		34 runs (62.5 M events)					
119159	119161	119163	119841	119844	119845	119846	119849
119853	119856	119859	119862	120067	120069	120072	120073
120076	120079	120244	120503	120505	120616	120617	120671
120741	120750	120758	120820	120821	120822	120823	120824
120825	120829						

Table A.1: (continued)
List of pp runs at $\sqrt{s} = 7$ TeV used for analysis of the momentum distribution in jets. Quoted number of events are accepted minimum-bias events.

LHC10d (pass2)	54 runs (127.5 M events)						
122374	125023	125085	125097	125100	125101	125133	125134
125139	125140	125156	125186	125296	125630	125632	125633
125842	125843	125844	125847	125848	125849	125850	125851
125855	126004	126007	126008	126073	126078	126081	126082
126088	126090	126097	126158	126283	126284	126285	126351
126352	126359	126403	126404	126405	126406	126407	126408
126409	126422	126424	126425	126432	126437		
LHC10e (pass2)	102 runs (62.5 M events)						
127712	127714	127718	127723	128495	128503	128504	128507
128582	128589	128605	128610	128615	128677	128678	128777
128778	128814	128817	128820	128823	128824	128835	128836
128843	128849	128853	128855	128913	129508	129510	129512
129513	129514	129520	129522	129523	129526	129527	129528
129529	129540	129541	129586	129587	129597	129598	129599
129639	129641	129647	129648	129649	129650	129651	129652
129653	129654	129655	129659	129665	129666	129667	129723
129725	129726	129729	129731	129734	129735	129736	129738
129742	129744	129745	129747	129748	129750	129760	129763
129959	129960	129961	129983	130156	130157	130158	130168
130170	130172	130179	130519	130627	130640	130696	130704
130793	130798	130799	130833	130834	130840		

Table A.2: List of event statistics for run periods (pp, $\sqrt{s} = 7\,\mathrm{TeV}$) used for analysis of the momentum distribution in jets. Quoted percentile is in relation to all processed events.

	LHC10b		LHC10c	
all events	33,909,742		73,370,013	
event selection	7,006,210	(20.6 %)	4,407,400	(6.0 %)
vertex cut (N contr)	2,490,183	(7.3 %)	5,833,799	(8.0 %)
vertex cut (z<8)	118,675	(0.3 %)	648,414	(0.9 %)
accepted events	**24,294,674**	**(71.6 %)**	**62,480,400**	**(85.2 %)**
	LHC10d		LHC10e	
all events	167,984,714		102,149,516	
event selection	9,446,090	(5.6 %)	24,499,950	(24.0 %)
vertex cut (N contr)	14,575,009	(8.7 %)	6,287,297	(6.2 %)
vertex cut (z<8)	16,510,327	(9.8 %)	8,817,189	(8.6 %)
accepted events	**127,453,288**	**(75.9 %)**	**62,545,080**	**(61.2 %)**

A.2 Run-by-Run Trend

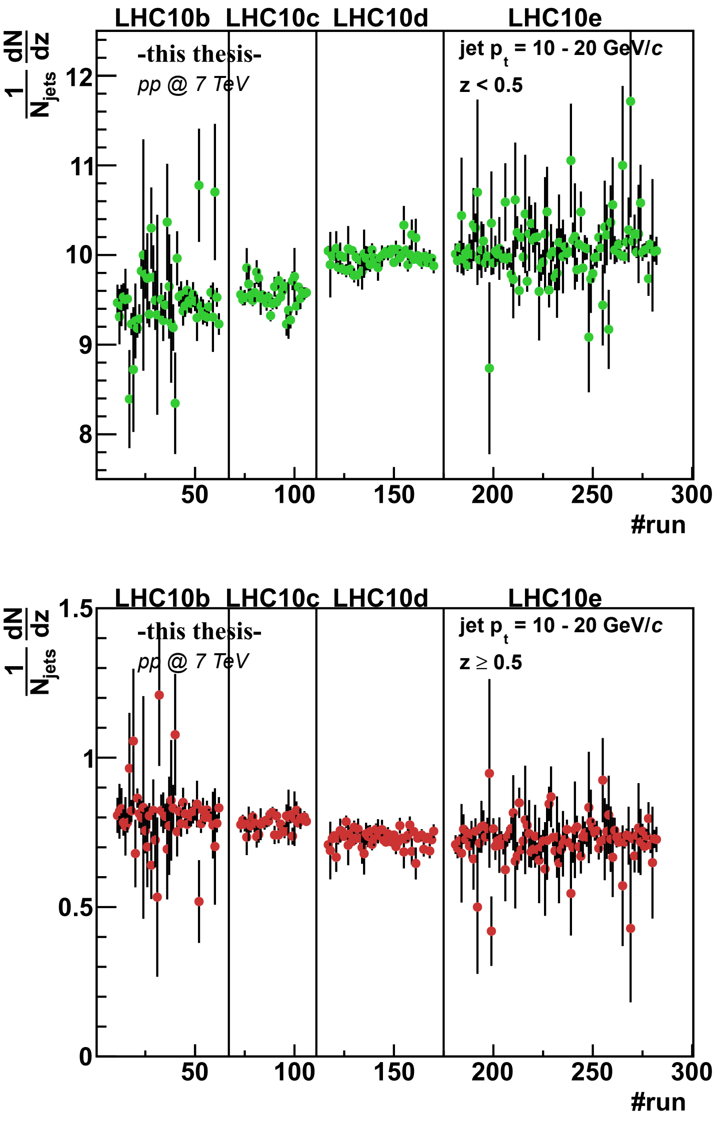

Figure A.1: Run-by-run trend of soft-fragmented ($z < 0.5$, top) and hard-fragmented region ($z \geq 0.5$, bottom).

Appendix B

Background Fluctuation Studies

B.1 Analyzed Runs and Statistics

Table B.1: List of Pb–Pb runs used for embedding tasks. All runs are from period LHC10h.

137161	137162	137231	137232	137235	137236	137243	137366
137430	137431	137432	137434	137439	137440	137441	137443
137530	137531	137539	137541	137544	137546	137549	137595
137608	137638	137639	137685	137686	137691	137692	137693
137704	137718	137722	137724	137751	137752	137844	137848
138190	138192	138197	138201	138225	138275	138364	138396
138438	138439	138442	138469	138534	138578	138579	138582
138583	138621	138624	138638	138652	138653	138662	138666
138730	138732	138837	138870	138871	138872	139028	139029
139036	139037	139038	139105	139107	139173	139309	139310
139314	139328	139329	139360	139437	139438	139465	139503
139505	139507	139510					

Table B.2: Event and probe statistics for applied cuts.

	emb. tracks		emb. jets	
input events	47,258,365		47,920,755	
offline event selection	- 27,343,609		- 27,666,507	
after offline selection	19,914,756	(100 %)	20,254,248	(100 %)
vertex cut ($z < 8\,\mathrm{cm}$)	- 4,557,022	(-22.9 %)	-4,634,393	(-22.9 %)
centrality cut (0-80 %)	- 2,964,166	(-14.9 %)	-3,014,575	(-14.9 %)
accepted events (0-80 %)	**12,393,568**	**(62.2 %)**	**12,605,528**	**(62.2 %)**
(100 % cent. equivalent	15,491,960		15,756,910	)
input probes	12,393,391	(100 %)	9,566,632	(100 %)
no matching	- 8	(-0.00 ‰)	-437	(-0.05 ‰)
fraction cut	- 0	(-0.00 ‰)	-485	(-0.05 ‰)
acceptance cut	- 121,054	(-1.0 %)	-1,210,770	(-12.7 %)
trigger excluded	- 8	(-0.00 ‰)	- 47	(-0.00 ‰)
accepted probes	**12,272,321**	**(99.0 %)**	**8,354,893**	**(87.3 %)**

B.2 Additional Analysis Plots

B.2.1 Background p_t Fluctuation

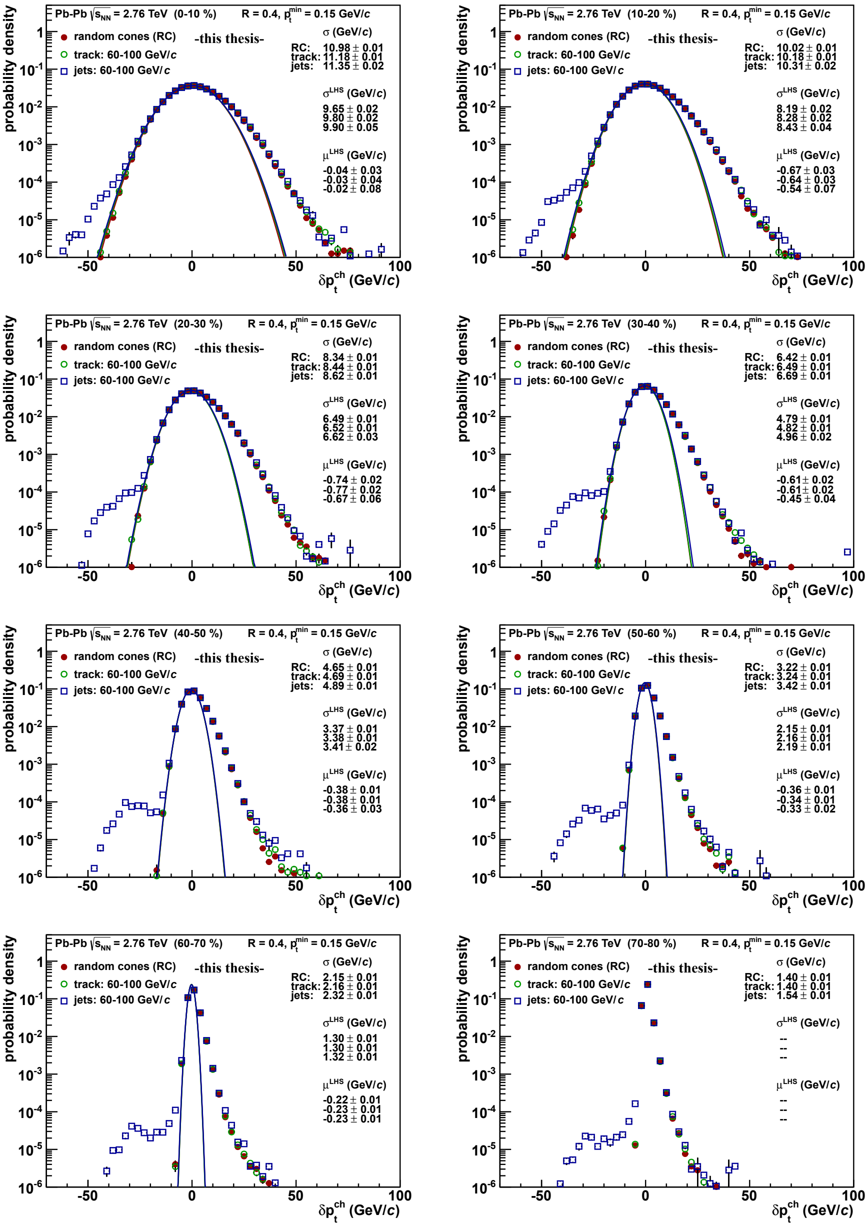

Figure B.1: Background p_t fluctuation, δp_t, for the three different methods and $p_t^{min} = 0.15\,\mathrm{GeV}/c$, for different centralities.

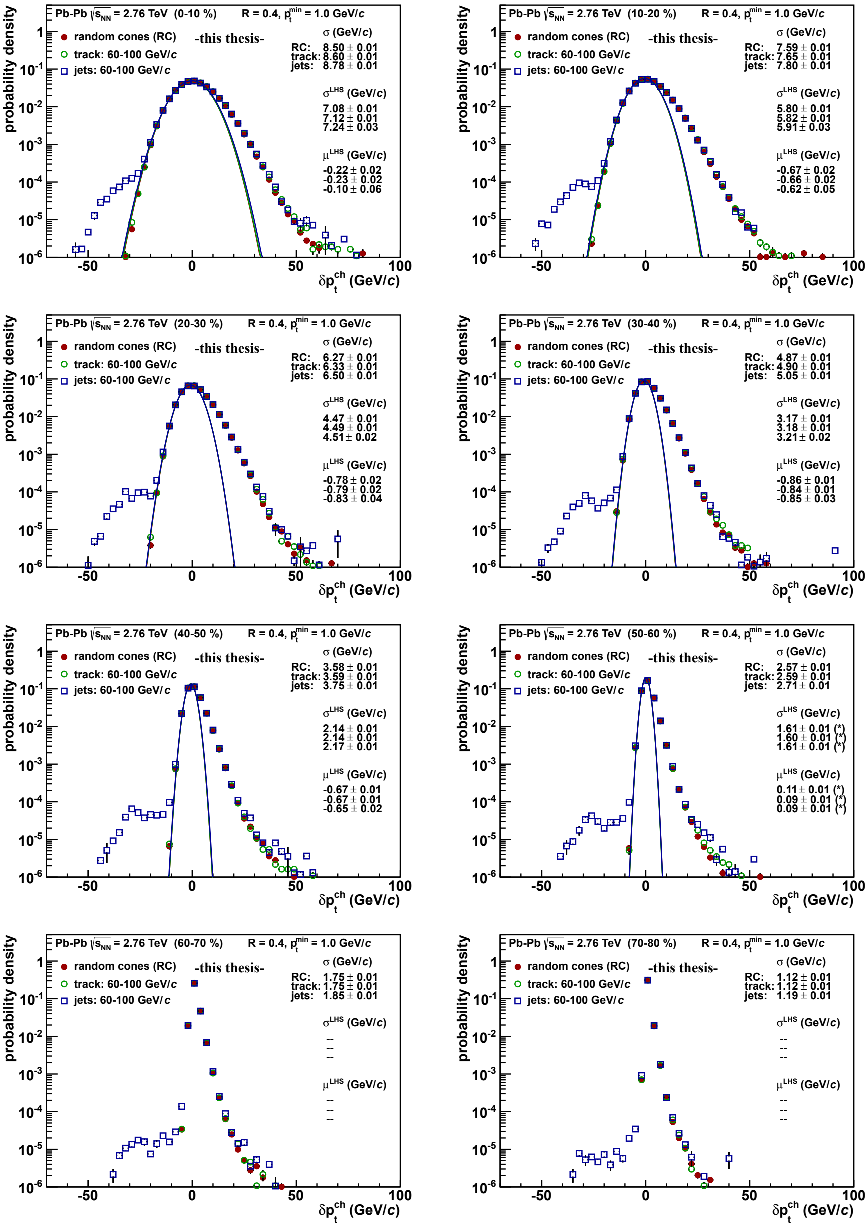

Figure B.2: Background p_t fluctuation, δp_t, for the three different methods and $p_t^{min} = 1.0\,\text{GeV}/c$, for different centralities.

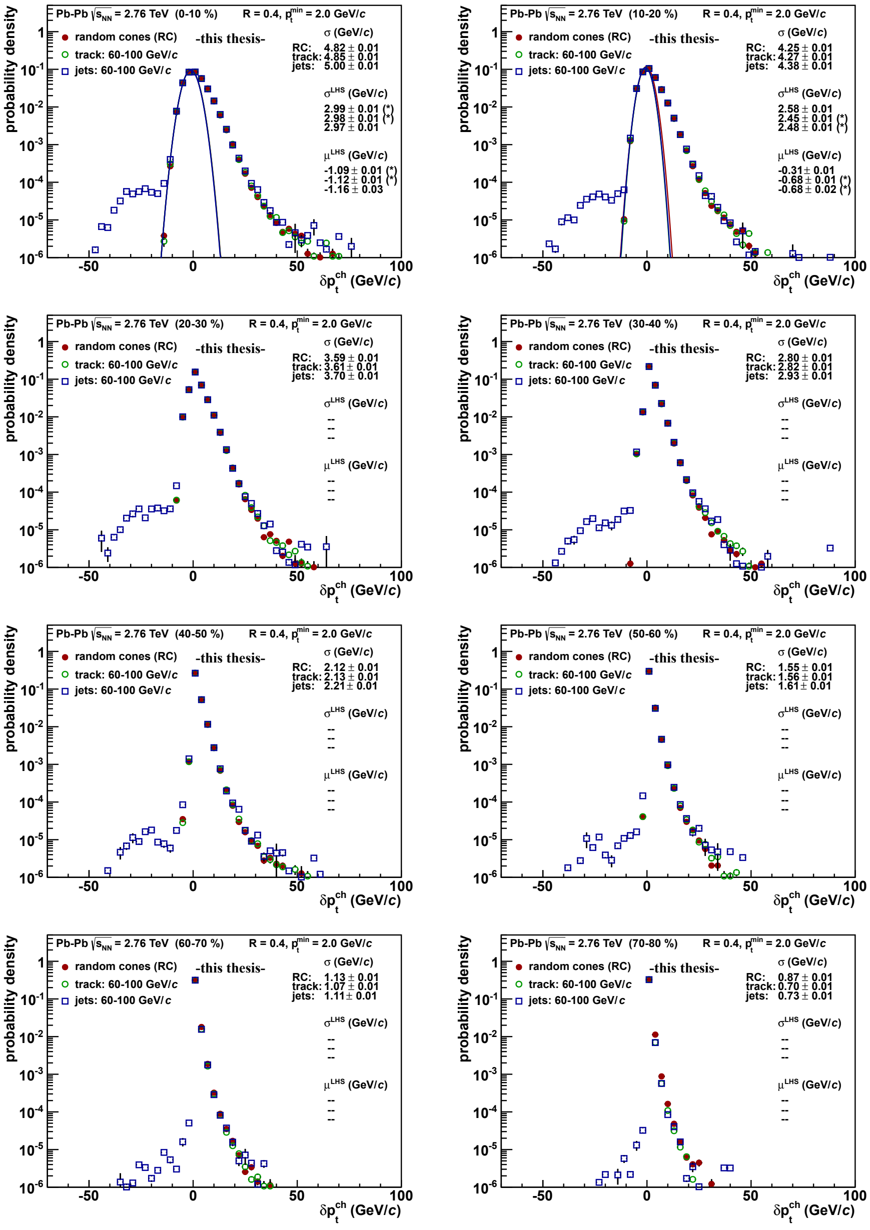

Figure B.3: Background p_{t} fluctuation, δp_{t}, for the three different methods and $p_{\mathrm{t}}^{\mathrm{min}} = 2.0\,\mathrm{GeV}/c$, for different centralities.

B.2.2 Jet Splitting and Jet Merging

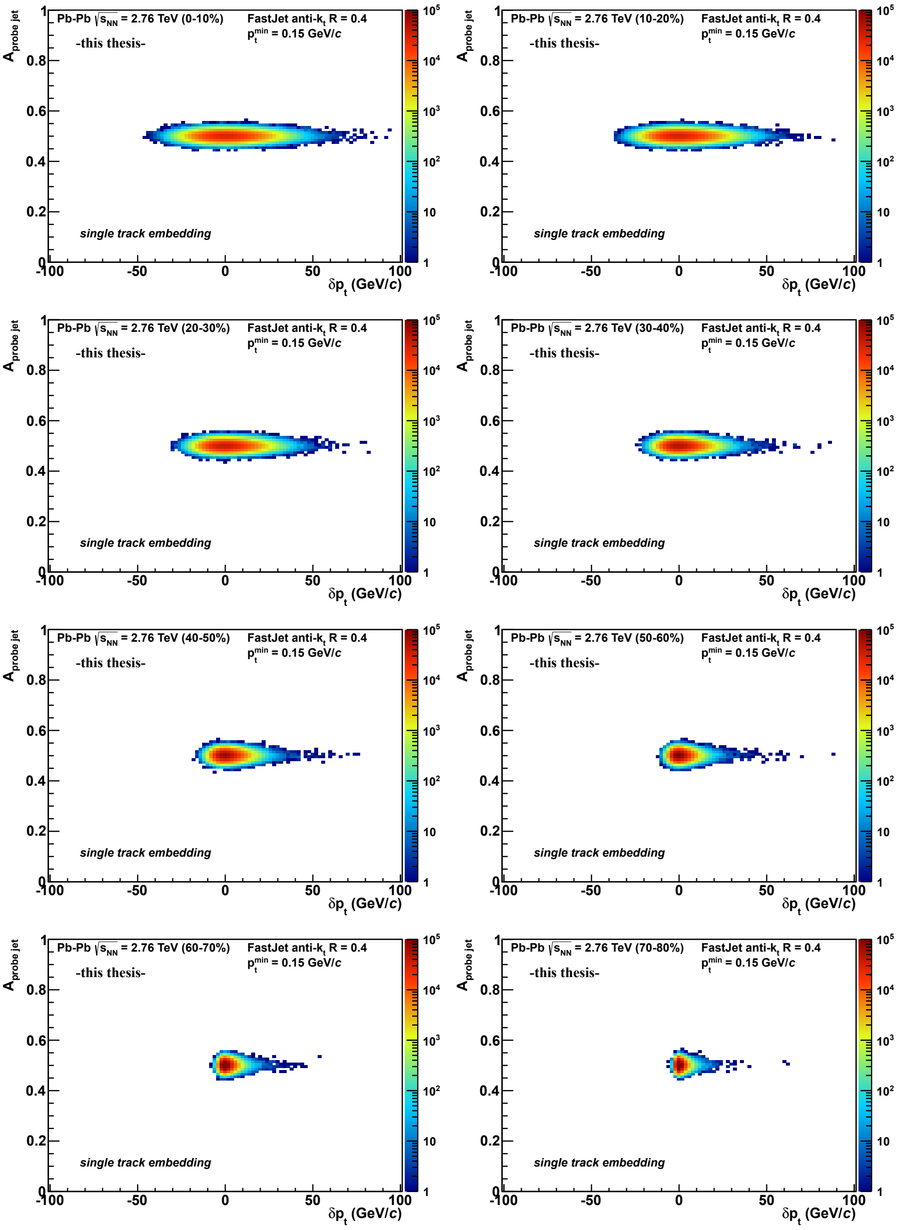

Figure B.4: Probe jet area, $A_{\text{probe,jet}}$, for embedded tracks and different centralities.

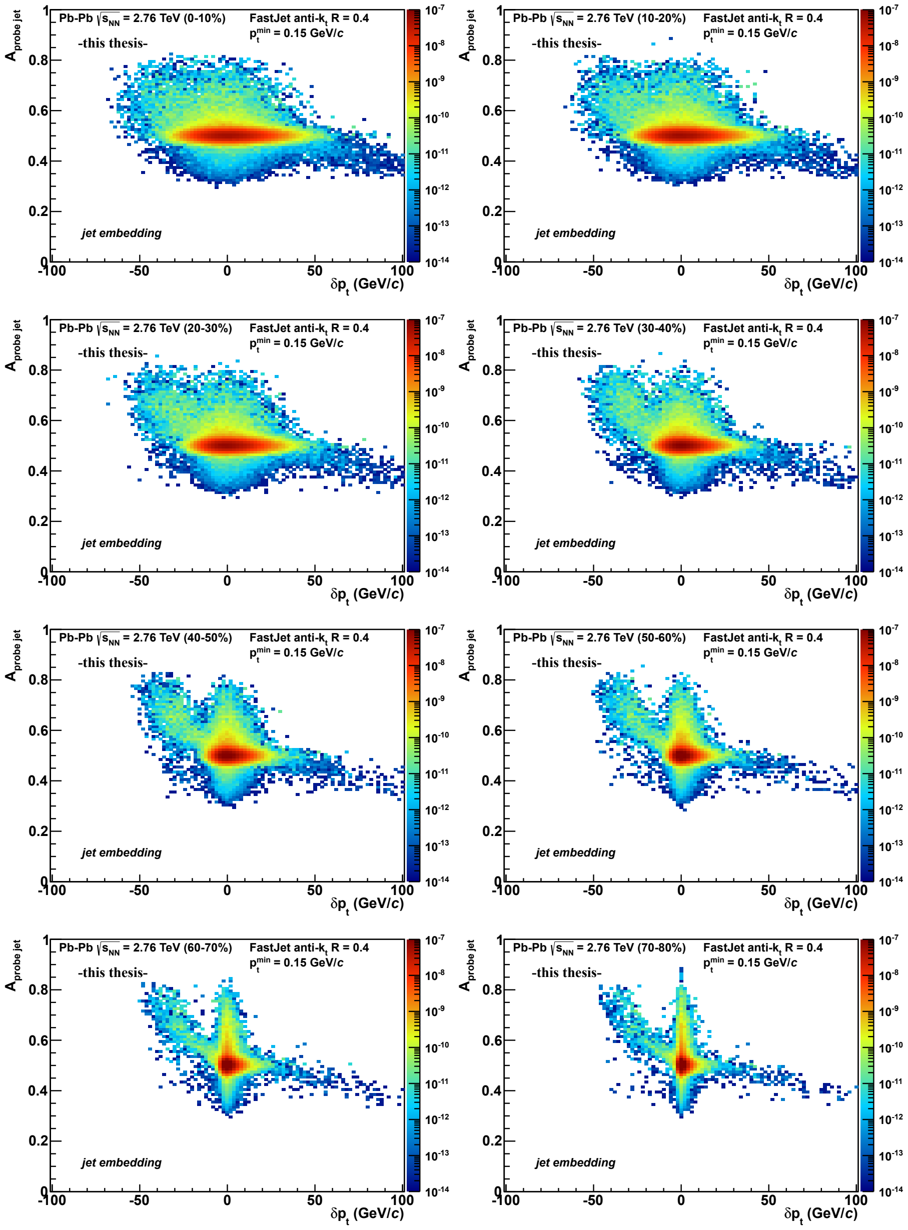

Figure B.5: Probe jet area, $A_{\text{probe,jet}}$, for embedded jets and different centralities.

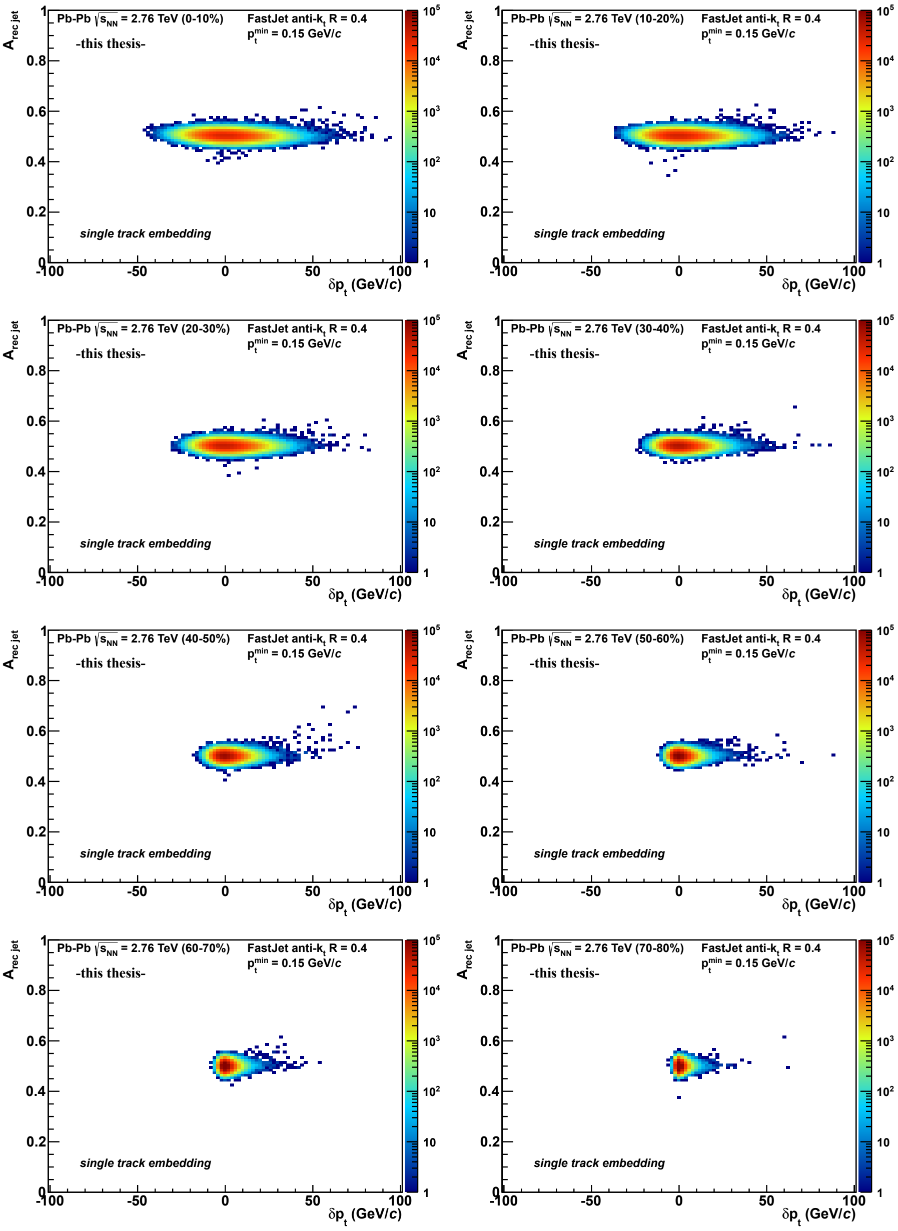

Figure B.6: Reconstructed jet area, $A_{\text{rec,jet}}$, for embedded tracks and different centralities.

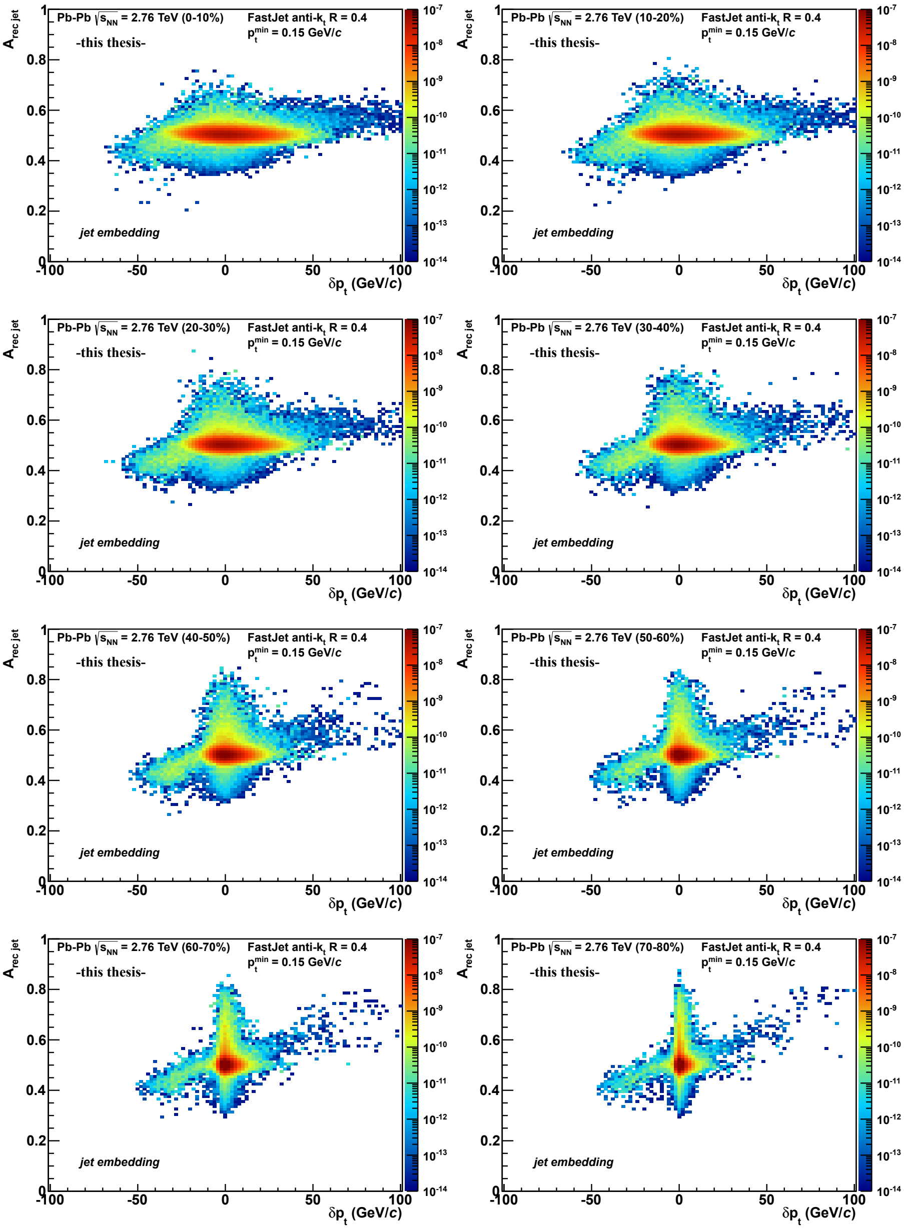

Figure B.7: Reconstructed jet area, $A_{\mathrm{rec,jet}}$, for embedded jets and different centralities.

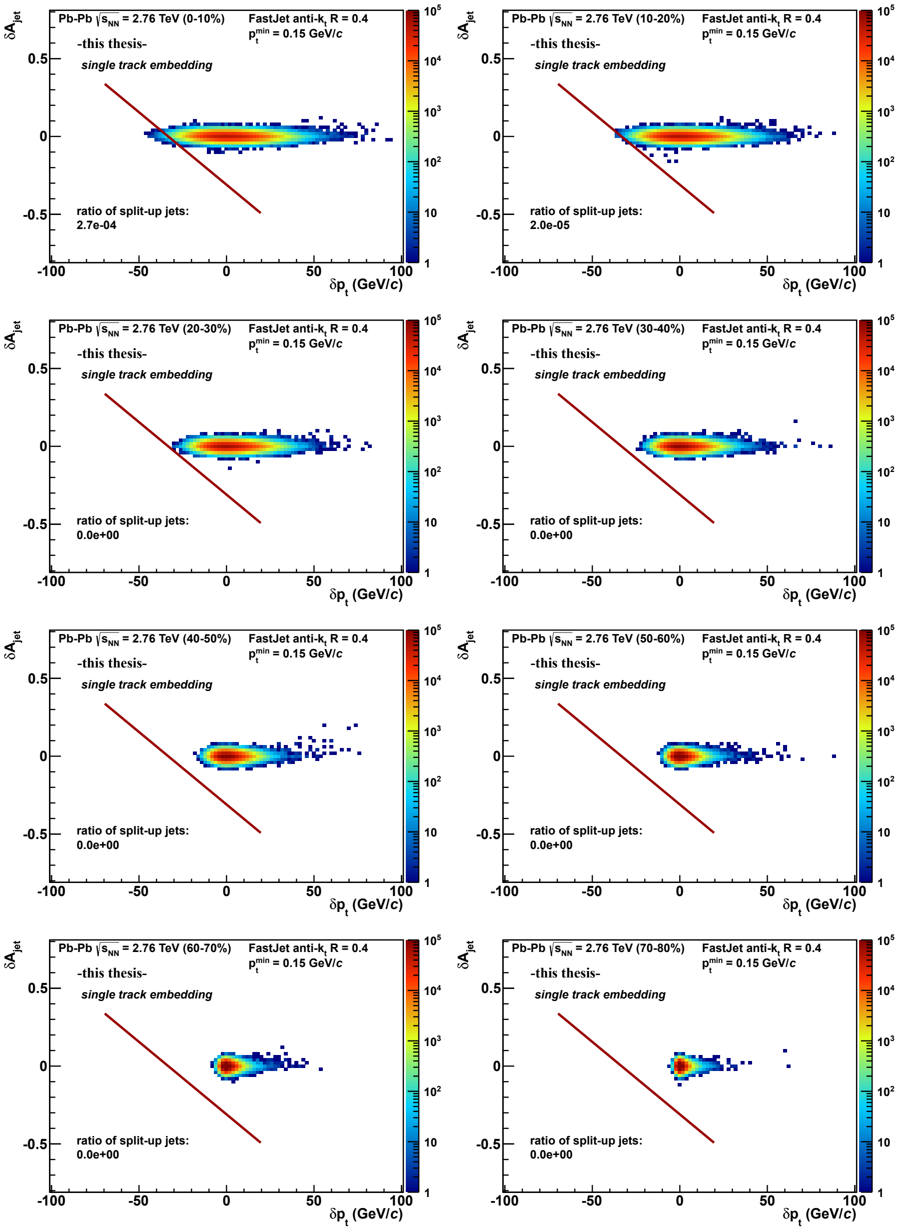

Figure B.8: Change in jet area, $\delta A = A_{\mathrm{rec}} - A_{\mathrm{probe}}$, for embedded tracks and different centralities. The red line ($\delta A = A_{\mathrm{rec}} - A_{\mathrm{probe}} < -0.31 - (9.31 \times 10^{-3})\delta p_{\mathrm{t}}$) indicates a limit as rough estimate of split-up jets. In case of track embedding, jet splitting does not happen by construction, see Section 7.4.2.

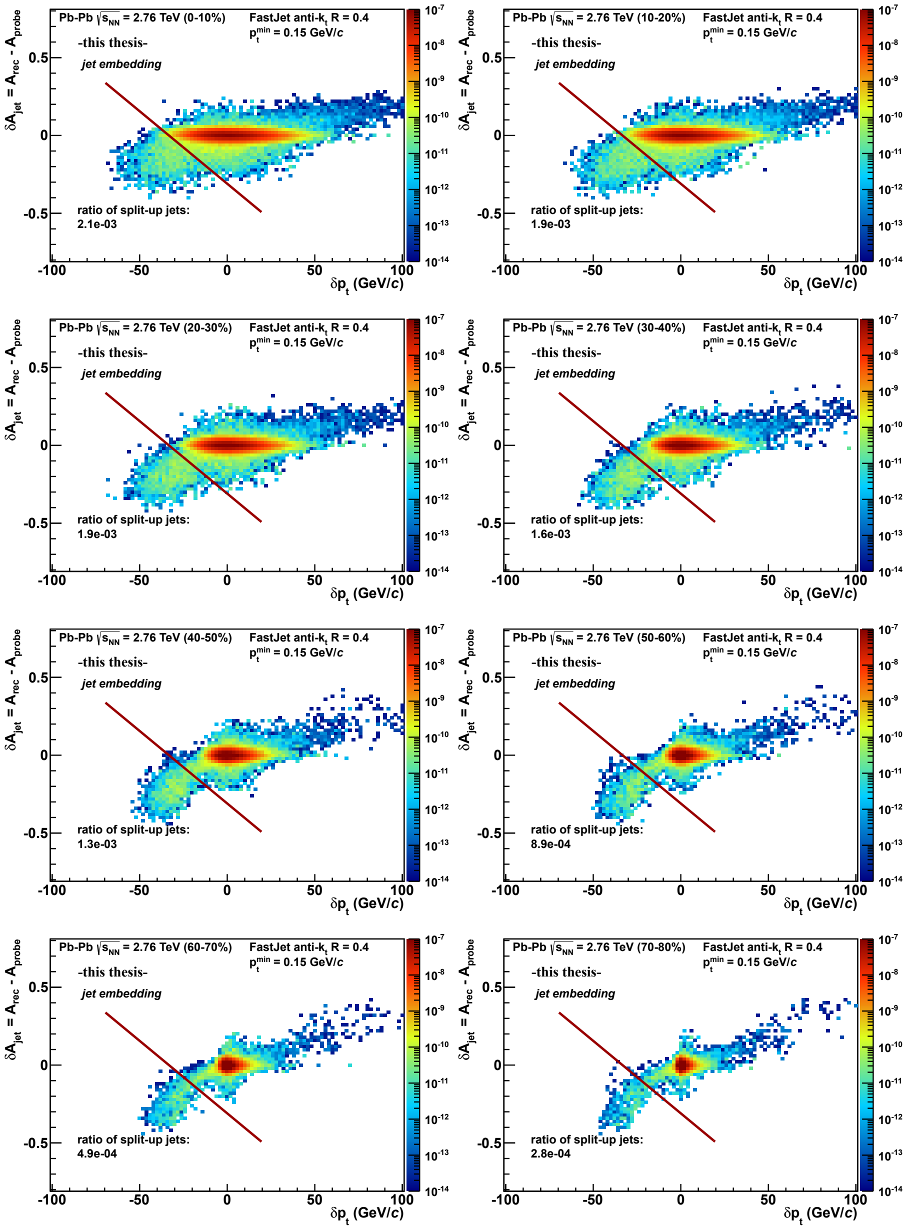

Figure B.9: Change in jet area, $\delta A = A_{\text{rec}} - A_{\text{probe}}$, for embedded jets and different centralities. The red line ($\delta A = A_{\text{rec}} - A_{\text{probe}} < -0.31 - (9.31 \times 10^{-3})\delta p_{\text{t}}$) indicates a limit as rough estimate of split-up jets, see Section 7.4.2.

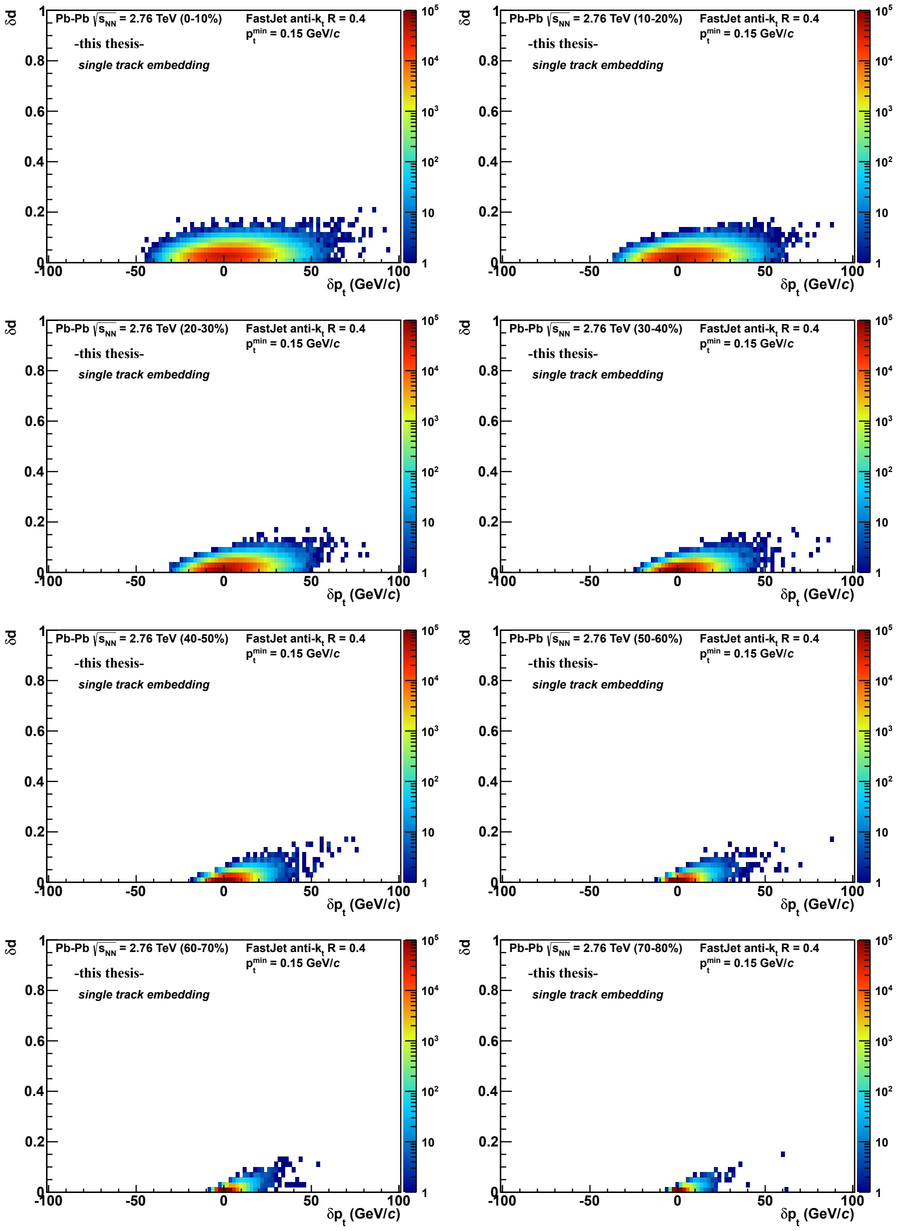

Figure B.10: Shift of jet axis, $\delta d = \sqrt{(\delta\eta)^2 + (\delta\phi)^2}$, for embedded tracks and different centralities.

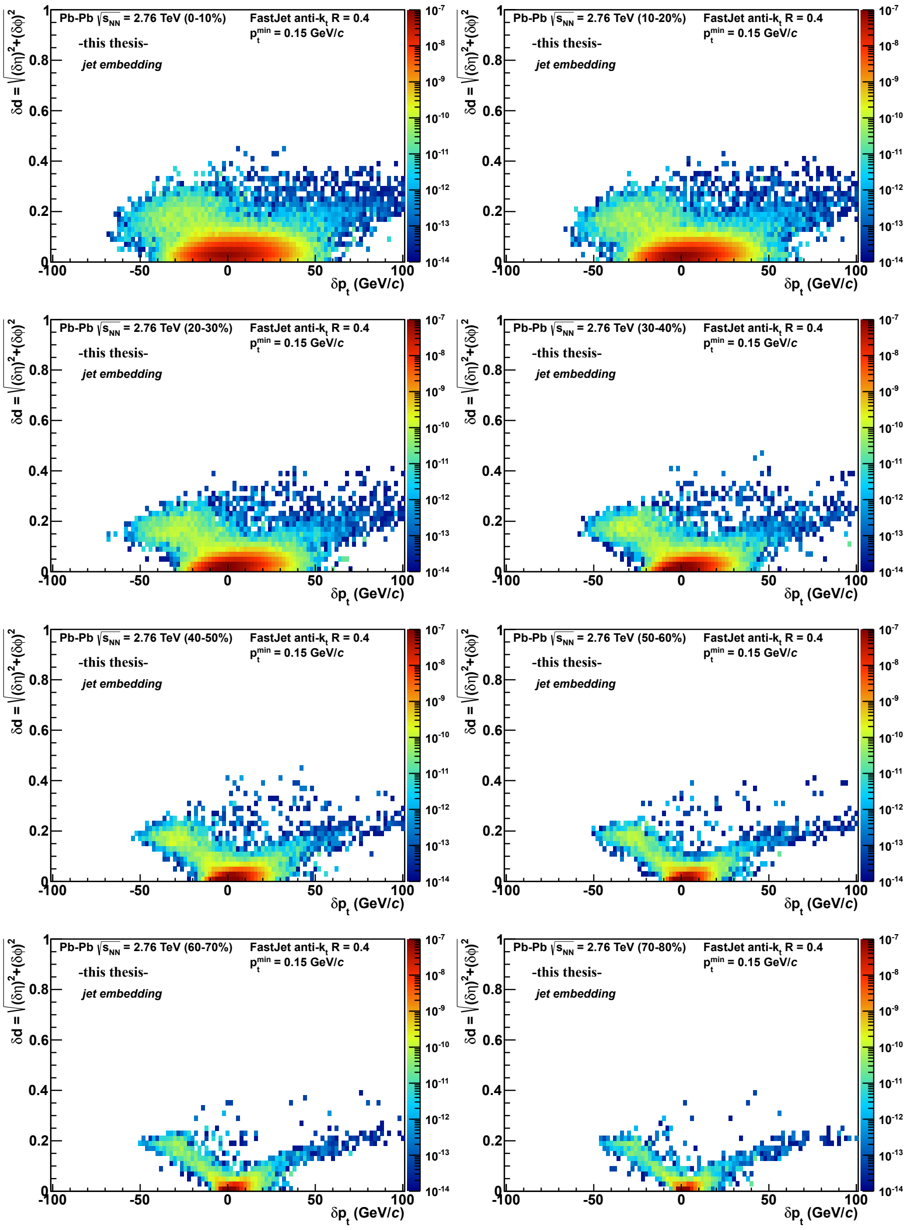

Figure B.11: Shift of jet axis, $\delta d = \sqrt{(\delta\eta)^2+(\delta\phi)^2}$, for embedded jets and different centralities.

B.2.3 Gaussian Fit Tests

Table B.3: Gaussian fit of the δp_{t} distribution from track embedding with different fitting ranges. The minimum track p_{t} is 0.15 GeV/c.

fit lower bound	fit upper bound	mean μ	σ	χ^2 / NDF	iterations
centrality 0-10 %					
-60. (fix)	5. (fix)	0.00 ± 0.03	9.80 ± 0.02	98.34 / 48	1
-999. (fix)	5. (fix)	0.00 ± 0.03	9.80 ± 0.02	98.34 / 48	1
-60. (fix)	$\mu + 5$	-0.07 ± 0.03	9.77 ± 0.02	77.22 / 47	3
$\mu - (3\sigma)$	$\mu + (0.0\sigma)$	-0.17 ± 0.07	9.75 ± 0.03	38.33 / 26	3
$\mu - (3\sigma)$	$\mu + (0.2\sigma)$	-0.13 ± 0.05	9.76 ± 0.03	39.75 / 28	3
$\mu - (3\sigma)$	$\mu + (0.5\sigma)$	-0.03 ± 0.04	9.80 ± 0.02	47.93 / 31	3
$\mu - (3\sigma)$	$\mu + (1.\sigma)$	0.04 ± 0.02	10.02 ± 0.01	287.22 / 37	4
$\mu - (5\sigma)$	$\mu + (0.5\sigma)$	-0.07 ± 0.03	9.77 ± 0.02	77.22 / 47	3
centrality 40-50 %					
-60.0 (fix)	5.0 (fix)	0.15 ± 0.01	3.65 ± 0.00	3871.87 / 20	1
-999.0 (fix)	5.0 (fix)	0.15 ± 0.01	3.65 ± 0.00	3871.87 / 20	1
-60.0 (fix)	$\mu + 5.0$	0.15 ± 0.01	3.65 ± 0.00	3871.87 / 20	2
$\mu - (3.0\sigma)$	$\mu + (0.0\sigma)$	-0.55 ± 0.02	3.31 ± 0.01	10.14 / 7	4
$\mu - (3.0\sigma)$	$\mu + (0.2\sigma)$	-0.47 ± 0.02	3.34 ± 0.01	31.37 / 8	3
$\mu - (3.0\sigma)$	$\mu + (0.5\sigma)$	-0.38 ± 0.01	3.38 ± 0.01	80.04 / 9	3
$\mu - (3.0\sigma)$	$\mu + (1.0\sigma)$	-0.12 ± 0.01	3.51 ± 0.00	807.84 / 11	3
$\mu - (5.0\sigma)$	$\mu + (0.5\sigma)$	-0.38 ± 0.01	3.38 ± 0.01	87.10 / 16	3
centrality 70-80 %					
-60.0 (fix)	5.0 (fix)	0.28 ± 0.00	0.97 ± 0.00	98727.48 / 8	1
-999.0 (fix)	5.0 (fix)	0.28 ± 0.00	0.97 ± 0.00	98727.48 / 8	1
-60.0 (fix)	$\mu + 5.0$	0.28 ± 0.00	0.97 ± 0.00	98727.48 / 8	2
$\mu - (3.0\sigma)$	$\mu + (0.0\sigma)$	0.10 ± 0.00	0.80 ± 0.00	0.00 / 0	3
$\mu - (3.0\sigma)$	$\mu + (0.2\sigma)$	0.10 ± 0.00	0.80 ± 0.00	0.00 / 0	3
$\mu - (3.0\sigma)$	$\mu + (0.5\sigma)$	0.10 ± 0.00	0.80 ± 0.00	0.00 / 0	3
$\mu - (3.0\sigma)$	$\mu + (1.0\sigma)$	0.10 ± 0.00	0.80 ± 0.00	0.00 / 0	4
$\mu - (5.0\sigma)$	$\mu + (0.5\sigma)$	0.13 ± 0.00	0.81 ± 0.00	286.19 / 1	3

B.2.4 Run Trending

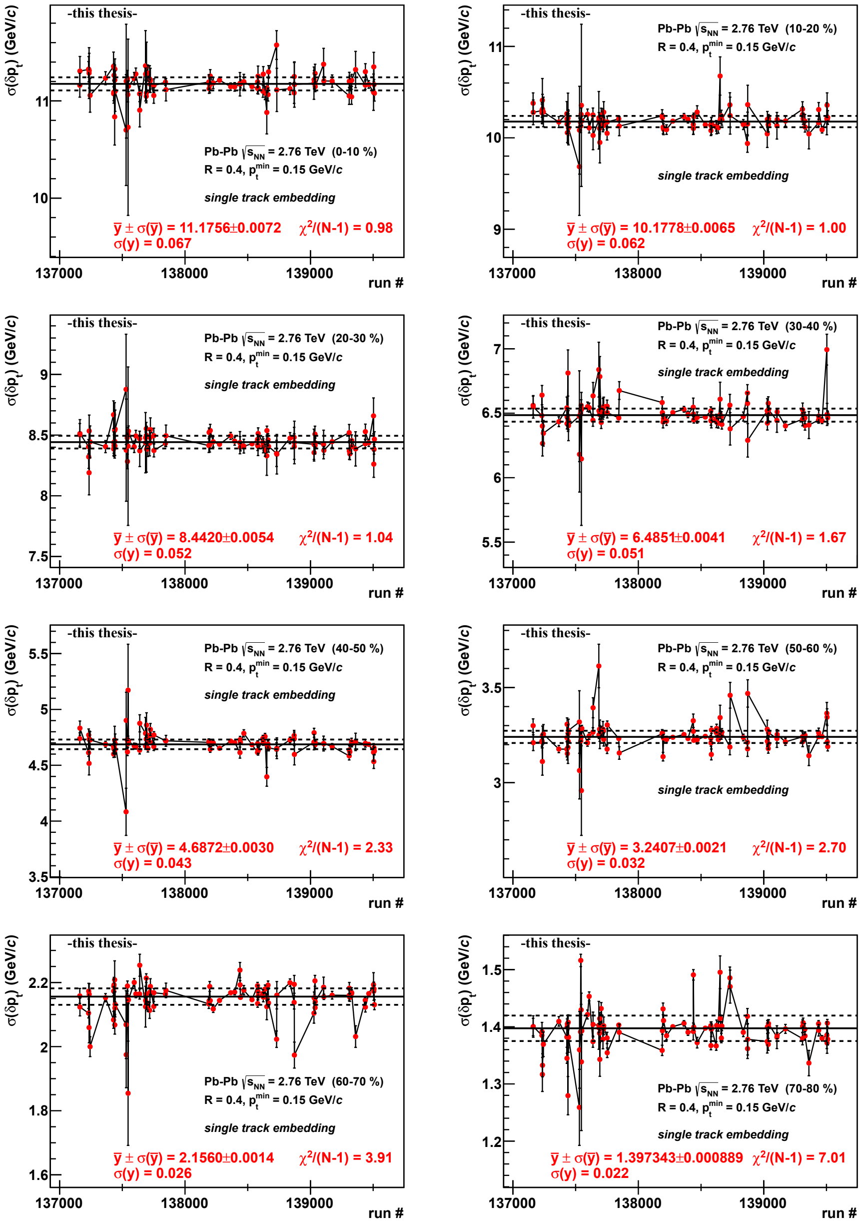

Figure B.12: Background p_t fluctuations, δp_t, from track embedding for different centrality classes.

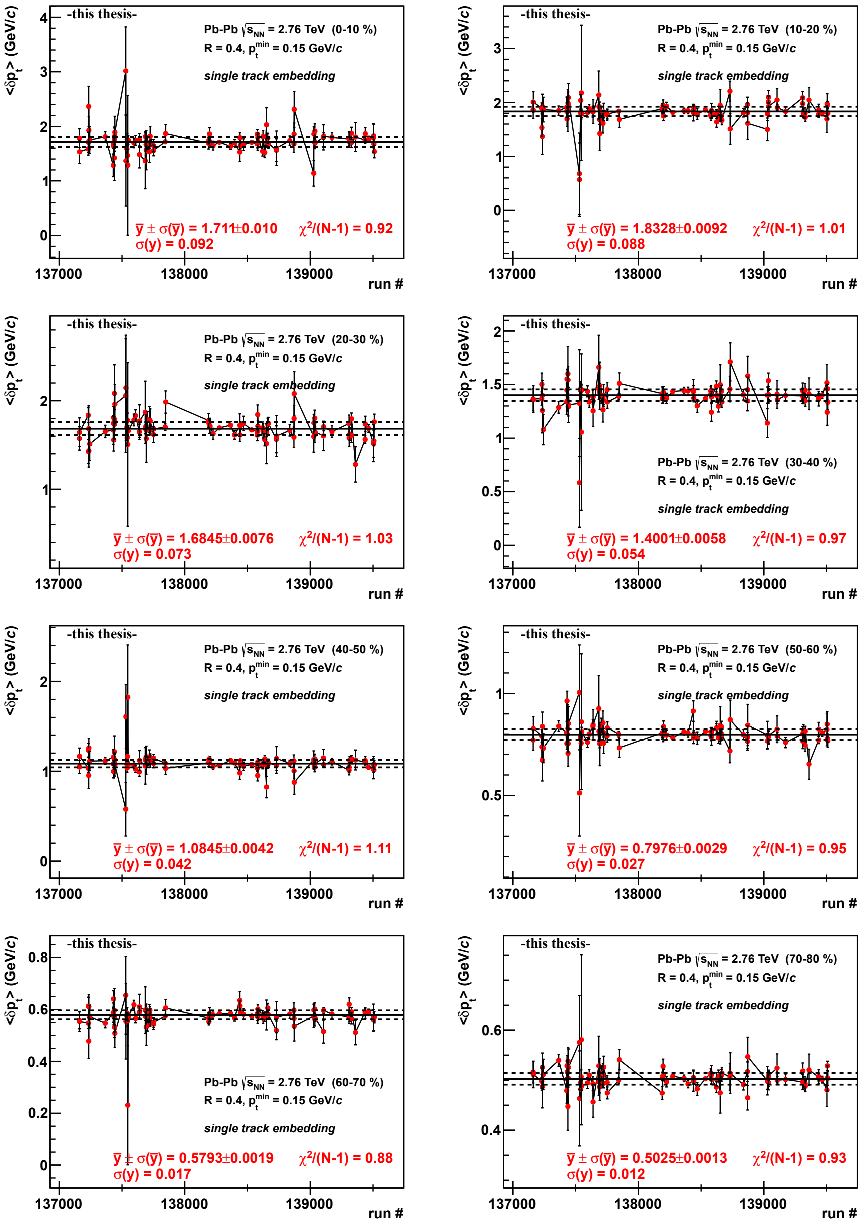

Figure B.13: Average background p_t fluctuations, $\langle \delta p_t \rangle$, from track embedding for different centrality classes.

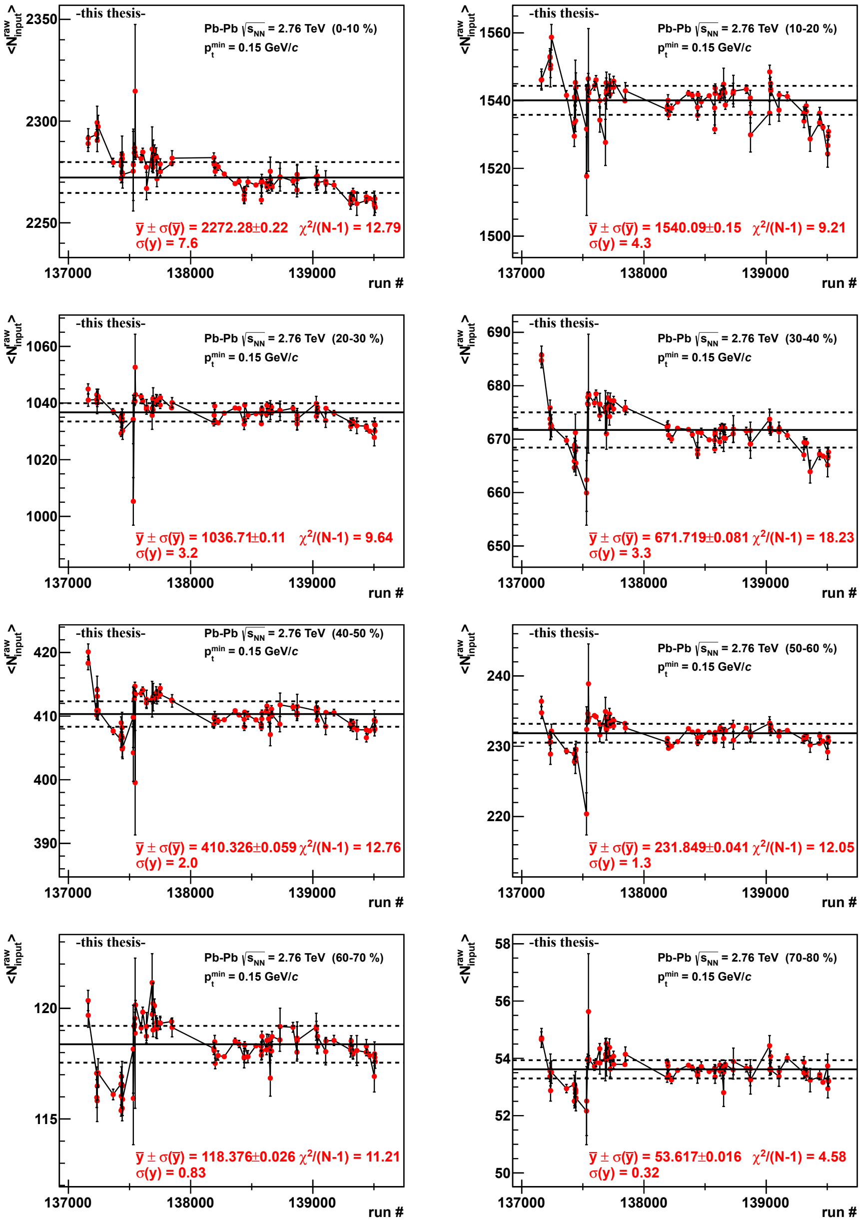

Figure B.14: Average track multiplicity, $\left\langle N_{\mathrm{input}}^{\mathrm{raw}} \right\rangle$, for different centrality classes.

B.2.5 Weighting of p_t^{hard} Bins

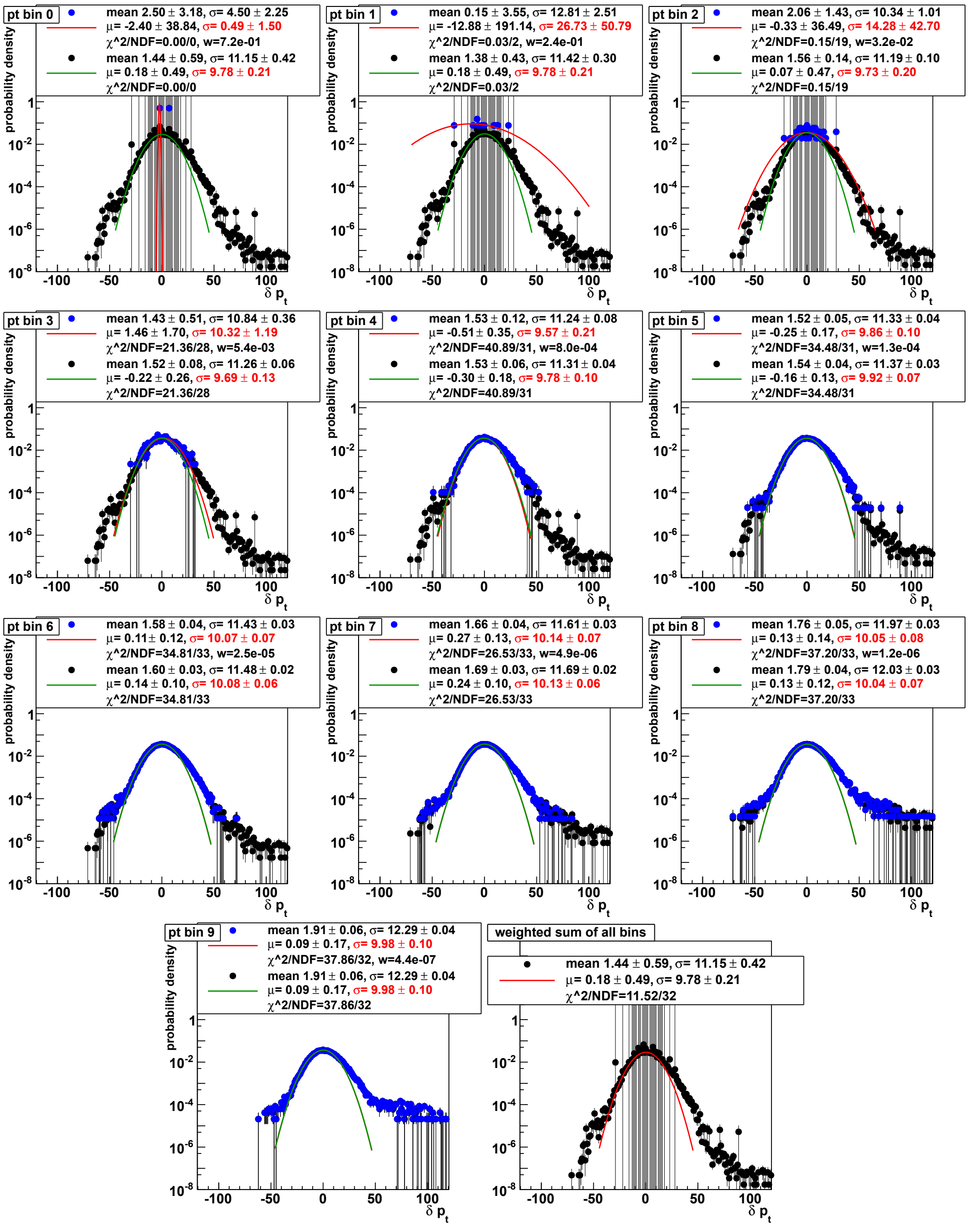

Figure B.15: δp_t distribution of simulated p_t^{hard} bins (blue) together with its left-hand side Gaussian fit (red line). The black symbols are the cumulative weighted sum of those distributions, beginning with the highest p_t^{hard} bin, and its LHS Gaussian fit (green line).

Appendix C

Acronyms

ACORDE	ALICE Cosmic Ray Detector
ALICE	A Large Ion Collider Experiment
AOD	Analysis Object Data
ASW	Armesto Salgado Wiedemann
ATLAS	A Toroidal LHC ApparatuS
BC	bunch-crossing
BDMPS	Baier Dokshitzer Mueller Peigné Schiff
BNL	Brookhaven National Laboratory
CERN	European Organization for Nuclear Research
CMS	Compact Muon Solenoid experiment
CTP	Central Trigger Processor
DAQ	data acquisition
DIS	deep inelastic scattering
ESD	Event Summary Data
EMCAL	electromagnetic calorimeter
EP	event plane

ISR	initial-state radiation
FF	fragmentation function
FMD	Forward Multiplicity Detector
FSR	final-state radiation
GTU	Global Tracking Unit
HIJA	Heavy-Ion Jet Algorithm
HLT	High-Level Trigger
HMPID	High-Momentum Particle Identification Detector
ITS	Inner Tracking System
IROC	inner read-out chamber
L0	Level-0
L1	Level-1
L2	Level-2
LHC	Large Hadron Collider
LHS	left-hand side
LHCb	Large Hadron Collider beauty experiment
LTU	Local Trigger Unit
LTU	Local Tracking Unit
LO	leading order
MB	minimum-bias
MCM	Multi Chip Module
MLLA	modified leading logarithmic approximation
MRPC	Multi-gap Resistive-Plate Chamber

MPI	multiple partonic interactions
NLO	next-to-leading order
ORI	Optical Readout Interface
OROC	outer read-out chamber
PASA	preamplifier shaper
Pb–Pb	lead-lead
PHOS	photon spectrometer
PMD	Photon Multiplicity Detector
pp	proton-proton
PS	Proton Synchrotron
PT	pre-trigger
pQCD	perturbative QCD
RC	random cones
RoI	region of interest
RHIC	Relativistic Heavy-Ion Collider
RHS	right-hand side
RP	reaction plane
PDF	parton distribution function
PWG	physics working group
SDD	Silicon Drift Detectors
SM	super module
SM	Standard Model
SMU	Super Module Unit

SSD	Silicon Strip Detectors
SPD	Silicon Pixel Detectors
SPS	Super Proton Synchrotron
SUSY	supersymmetric
TGU	Trigger Unit
TMU	Track Matching Unit
TOF	Time-Of-Flight
TPC	Time Projection Chamber
TRAP	Tracklet Processor
TRD	Transition Radiation Detector
UE	underlying event
QCD	quantum chromodynamics
QED	quantum electrodynamics
QFT	Quantum Field Theory
QGP	quark-gluon plasma
ZDC	Zero Degree Calorimeter

Bibliography

[Aad+08] G. Aad et al. “The ATLAS Experiment at the CERN Large Hadron Collider”. In: *JINST* 3 (2008), S08003. DOI: `10.1088/1748-0221/3/08/S08003`.

[Aad+10] Georges Aad et al. “Observation of a Centrality-Dependent Dijet Asymmetry in Lead-Lead Collisions at $\sqrt{s_{NN}} = 2.76$ TeV with the ATLAS Detector at the LHC”. In: *Phys. Rev. Lett.* 105 (2010), p. 252303. DOI: `10.1103/PhysRevLett.105.252303`. arXiv:`1011.6182 [hep-ex]`.

[Aam+08] K. Aamodt et al. “The ALICE experiment at the CERN LHC”. In: *JINST* 3 (2008), S08002. DOI: `10.1088/1748-0221/3/08/S08002`.

[Aam+10a] K. Aamodt et al. “Alignment of the ALICE Inner Tracking System with cosmic-ray tracks”. In: *JINST* 5 (Jan. 2010), P03003. DOI: `10.1088/1748-0221/5/03/P03003`. arXiv:`1001.0502 [physics.ins-det]`.

[Aam+10b] K. Aamodt et al. “Charged-particle multiplicity density at mid-rapidity in central Pb-Pb collisions at $\sqrt{s_{NN}} = 2.76$ TeV”. In: *Phys. Rev. Lett.* 105 (Nov. 2010), p. 252301. DOI: `10.1103/PhysRevLett.105.252301`. arXiv:`1011.3916 [nucl-ex]`.

[Aam+10c] K. Aamodt et al. “Charged-particle multiplicity measurement in proton-proton collisions at $\sqrt{s} = 7$ TeV with ALICE at LHC”. In: *Eur. Phys. J.* C68 (2010), pp. 345–354. DOI: `10.1140/epjc/s10052-010-1350-2`. arXiv:`1004.3514 [hep-ex]`.

[Aam+10d] K Aamodt et al. “Elliptic flow of charged particles in Pb-Pb collisions at 2.76 TeV”. In: *Phys. Rev. Lett.* 105 (2010), p. 252302. DOI: `10.1103/PhysRevLett.105.252302`. arXiv:`1011.3914 [nucl-ex]`.

[Aam+11a] K. Aamodt et al. “Centrality dependence of the charged-particle multiplicity density at mid-rapidity in Pb-Pb collisions at $\sqrt{s_{NN}} = 2.76$ TeV”. In: *Phys. Rev. Lett.* 106 (2011), p. 032301. DOI: `10.1103/PhysRevLett.106.032301`. arXiv:`1012.1657 [nucl-ex]`.

[Aam+11b] K. Aamodt et al. “Higher harmonic anisotropic flow measurements of charged particles in Pb-Pb collisions at 2.76 TeV”. In: *Phys. Rev. Lett.* 107 (May 2011), p. 032301. arXiv:`1105.3865 [nucl-ex]`.

[Aam+11c] K. Aamodt et al. “Suppression of Charged Particle Production at Large Transverse Momentum in Central Pb–Pb Collisions at $\sqrt{s_{_{NN}}} = 2.76$ TeV”. In: *Phys. Lett.* B696 (2011), pp. 30–39. DOI: `10.1016/j.physletb.2010.12.020`. arXiv:`1012.1004 [nucl-ex]`.

[Aam+12a] K. Aamodt et al. “Measurement of Event Background Fluctuations for Charged Particle Jet Reconstruction in Pb-Pb collisions at $\sqrt{s_{NN}} = 2.76$ TeV”. In: *JHEP* 03 (2012), p. 053. DOI: `10.1007/JHEP03(2012)053`. arXiv:`1201.2423 [hep-ex]`.

[Aam+12b] K. Aamodt et al. “Particle-yield modification in jet-like azimuthal dihadron correlations in Pb-Pb collisions at $\sqrt{s_{NN}} = 2.76$ TeV”. In: *Phys. Rev. Lett.* 108 (2012), p. 092301. DOI: `10.1103/PhysRevLett.108.092301`. arXiv:`1110.0121 [nucl-ex]`.

[Aba+12] Victor Mukhamedovich Abazov et al. “Measurement of the inclusive jet cross section in p pbar collisions at $\sqrt{s}$ =1.96 TeV”. In: *Phys. Rev.* D85 (2012), p. 052006. DOI: `10.1103/PhysRevD.85.052006`. arXiv:`1110.3771 [hep-ex]`.

[Abe+11] B. Abelev et al. “Underlying Event measurements in pp collisions at $\sqrt{s} = 0.9$ and 7 TeV with the ALICE experiment at the LHC”. Dec. 2011. arXiv:`1112.2082 [hep-ex]`.

[Abu+06] A. Abulencia et al. “Measurement of the Inclusive Jet Cross Section using the Kt algorithm in pp-bar Collisions at $\sqrt{s} = 1.96$ TeV”. In: *Phys. Rev. Lett.* 96 (2006), p. 122001. DOI: `10.1103/PhysRevLett.96.122001`. arXiv:`hep-ex/0512062`.

[Acc+03] A. Accardi et al. “Hard Probes in Heavy Ion Collisions at the LHC: Jet Physics”. 2003. arXiv:`hep-ph/0310274`.

[Ada+03] J. Adams et al. “Transverse momentum and collision energy dependence of high p_T hadron suppression in Au+Au collisions at ultrarelativistic energies”. In: *Phys. Rev. Lett.* 91 (2003), p. 172302. DOI: `10.1103/PhysRevLett.91.172302`. arXiv:`nucl-ex/0305015 [nucl-ex]`.

[Ada+05] John Adams et al. “Experimental and theoretical challenges in the search for the quark gluon plasma: The STAR collaboration’s critical assessment of the evidence from RHIC collisions”. In: *Nucl. Phys.* A757 (2005), pp. 102–183. DOI: `10.1016/j.nuclphysa.2005.03.085`. arXiv:`nucl-ex/0501009`.

[Adc+05] K. Adcox et al. “Formation of dense partonic matter in relativistic nucleus nucleus collisions at RHIC: Experimental evaluation by the PHENIX collaboration”. In: *Nucl. Phys.* A757 (2005), pp. 184–283. DOI: `10.1016/j.nuclphysa.2005.03.086`. arXiv:`nucl-ex/0410003`.

[Adl+04] S.S. Adler et al. “High p_T charged hadron suppression in Au + Au collisions at $\sqrt{s}_{NN} = 200$ GeV”. In: *Phys. Rev.* C69 (2004), p. 034910. DOI: `10.1103/PhysRevC.69.034910`. arXiv:`nucl-ex/0308006 [nucl-ex]`.

[Ale+06] B. Alessandro et al. “ALICE: Physics Performance Report, Volume II”. In: *J. Phys.* G32 (2006), pp. 1295–2040. DOI: `10.1088/0954-3899/32/10/001`.

[AliCS] *Centrality Studies.* ALICE Wiki (internal). URL: `https://twiki.cern.ch/twiki/bin/viewauth/ALICE/CentStudies` (visited on 08/07/2011).

[AliEN] *Event Normalization.* ALICE Wiki (internal). URL: `https://twiki.cern.ch/twiki/bin/viewauth/ALICE/EventNormalization` (visited on 06/11/2012).

[AliOff] ALICE Off-line Project. URL: `http://aliweb.cern.ch/Offline/`.

[AliSVN] AliRoot SVN repository. URL: `http://alisoft.cern.ch/viewvc/?root=AliRoot`.

[AliSVNa] AliRoot tag v5-02-04-AN. URL: `http://alisoft.cern.ch/viewvc/tags/v5-02-04-AN/?root=AliRoot`.

[AliSVNb] AliRoot tag v5-03-08-AN. URL: `http://alisoft.cern.ch/viewvc/tags/v5-03-08-AN/?root=AliRoot`.

[Alm+10] J. Alme et al. “The ALICE TPC, a large 3-dimensional tracking device with fast readout for ultra-high multiplicity events”. In: *Nucl. Instrum. Meth.* A622 (Jan. 2010), pp. 316–367. DOI: `10.1016/j.nima.2010.04.042`. arXiv:`1001.1950 [physics.ins-det]`.

[Alv+08] Jr. Alves A. Augusto et al. “The LHCb Detector at the LHC”. In: *JINST* 3 (2008), S08005. DOI: `10.1088/1748-0221/3/08/S08005`.

[Ang06] V. Angelov. “Design and performance of the ALICE TRD front-end electronics”. In: *Nucl. Instrum. Meth.* A563 (2006), pp. 317–320. DOI: `10.1016/j.nima.2006.02.169`.

[Aok+06] Y. Aoki et al. “The Order of the quantum chromodynamics transition predicted by the standard model of particle physics”. In: *Nature* 443 (2006), pp. 675–678. DOI: `10.1038/nature05120`. arXiv:`hep-lat/0611014 [hep-lat]`.

[App11] Harald Appelshauser. “Particle Production at Large Transverse Momentum with ALICE”. In: *J. Phys.* G38 (2011), p. 124014. DOI: `10.1088/0954-3899/38/12/124014`. arXiv:`1110.0638 [nucl-ex]`.

[Arn+82] G. Arnison et al. “First observation of correlations between high transverse momentum charged particles in events from the CERN proton-antiproton collider”. In: *Phys. Lett.* B118 (1982), pp. 173–177. DOI: `10.1016/0370-2693(82)90624-4`.

[Ars+05] I. Arsene et al. “Quark Gluon Plasma and Color Glass Condensate at RHIC? The perspective from the BRAHMS experiment”. In: *Nucl. Phys.* A757 (2005), pp. 1–27. DOI: `10.1016/j.nuclphysa.2005.02.130`. arXiv:`nucl-ex/0410020`.

[ATL12] ATLAS collaboration. “An update to the combined search for the Standard Model Higgs boson with the ATLAS detector at the LHC using up to 4.9 fb^{-1} of pp collision data at $\sqrt{s} = 7$ TeV”. ATLAS–CONF–2012–019. Mar. 2012. URL: `http://cdsweb.cern.ch/record/1430033`.

[Aur91] Franz Aurenhammer. “Voronoi Diagrams – A Survey of a Fundamental Geometric Data Structure”. In: *ACM Computing Surveys* 23 (1991), pp. 345–405. DOI: `10.1145/116873.116880`.

[Azi+86] Yakov I. Azimov et al. “Humpbacked QCD Plateau in Hadron Spectra”. In: *Z. Phys.* C31 (1986), p. 213. DOI: `10.1007/BF01479529`.

[Bac+05] B. B. Back et al. “The PHOBOS perspective on discoveries at RHIC”. In: *Nucl. Phys.* A757 (2005), pp. 28–101. DOI: `10.1016/j.nuclphysa.2005.03.084`. arXiv:`nucl-ex/0410022`.

[Bai03] R. Baier. “Jet quenching”. In: *Nucl. Phys.* A715 (2003), pp. 209–218. DOI: `10.1016/S0375-9474(02)01429-X`. arXiv:`hep-ph/0209038 [hep-ph]`.

[Bai+97a] R. Baier et al. “Radiative energy loss and $p_\perp$-broadening of high energy partons in nuclei”. In: *Nucl. Phys.* B484 (1997), pp. 265–282. DOI: `10.1016/S0550-3213(96)00581-0`. arXiv:`hep-ph/9608322`.

[Bai+97b] R. Baier et al. “Radiative energy loss of high energy quarks and gluons in a finite volume quark-gluon plasma”. In: *Nucl. Phys.* B483 (1997), pp. 291–320. DOI: `10.1016/S0550-3213(96)00553-6`. arXiv:`hep-ph/9607355`.

[Bar77] Bertrand C. Barrois. “Superconducting Quark Matter”. In: *Nucl. Phys.* B129 (1977), p. 390. DOI: `10.1016/0550-3213(77)90123-7`.

[BCG94] Rene Brun, Federico Carminati, and Simone Giani. *GEANT Detector Description and Simulation Tool.* CERN Program Library Long Writeup. W5013. Mar. 1994. URL: `http://wwwasd.web.cern.ch/wwwasd/geant/`.

[Bet09] Siegfried Bethke. “The 2009 World Average of alpha(s)”. In: *Eur. Phys. J.* C64 (2009), pp. 689–703. DOI: `10.1140/epjc/s10052-009-1173-1`. arXiv:`0908.1135 [hep-ph]`.

[Bha+07] A Bhasin et al. “Implementation of the ALICE Trigger System”. In: Real-Time Conference, 15th IEEE-NPSS. Apr. 2007, pp. 1–8. DOI: `10.1109/RTC.2007.4382861`.

[Bjo82] J. D. Bjorken. “Energy Loss of Energetic Partons in Quark-Gluon Plasma: Possible Extinction of High p_t Jets in Hadron-Hadron Collisions”. FERMILAB-PUB-82-059-THY. 1982.

[Bla+00] Gerald C. Blazey et al. “Run II Jet Physics: Proceedings of the Run II QCD and Weak Boson Physics Workshop”. 2000. arXiv:`hep-ex/0005012`.

[Bly05] Sarah-Louise Blyth. “Jet Study in Ultra-Relativistic Heavy-Ion Collisions with the ALICE Detectors at the LHC”. MA thesis. 2005. arXiv:`nucl-ex/0510065`.

[Bly+07] S-L Blyth et al. “A Cone Jet-Finding Algorithm for Heavy-Ion Collisions at LHC Energies”. In: *J. Phys.* G34 (2007), pp. 271–281. DOI: `10.1088/0954-3899/34/2/008`. arXiv:`nucl-ex/0609023`.

[Bor+10] Szabolcs Borsanyi et al. “The QCD equation of state with dynamical quarks”. In: *JHEP* 1011 (2010), p. 077. DOI: `10.1007/JHEP11(2010)077`. arXiv:`1007.2580 [hep-lat]`.

[Bro78] Laurie M. Brown. “The idea of the neutrino”. In: *Phys. Today* 31N9 (1978), pp. 23–28. DOI: `10.1063/1.2995181`; W. Pauli. “Dear radioactive ladies and gentlemen”. In: *Phys. Today* 31N9 (1978), p. 27.

[Bus10] Oliver Busch. *Update Efficiency.* Internal presentation in ALICE jet meeting 11-17-2010. Nov. 2010. URL: `https://indico.cern.ch/conferenceDisplay.py?confId=113801`.

[Bus11] Oliver Busch. *Two-Track Resolution in Jets*. Internal presentation in ALICE jet meeting 10-26-2011. Oct. 2011. URL: `https://indico.cern.ch/conferenceDisplay.py?confId=160523`.

[Bus12] Oliver Busch. *Fragmentation functions in pp*. Internal presentation in the ALICE jet meeting 05-01-2012. May 2012. URL: `https://indico.cern.ch/conferenceDisplay.py?confId=188906`.

[BW05] Nicolas Borghini and Urs Achim Wiedemann. "Distorting the hump-backed plateau of jets with dense QCD matter". 2005. arXiv:`hep-ph/0506218 [hep-ph]`.

[BW09] P. Braun-Munzinger and J. Wambach. "Colloquium: Phase diagram of strongly interacting matter". In: *Rev. Mod. Phys.* 81 (2009), pp. 1031–1050. DOI: `10.1103/RevModPhys.81.1031`.

[Cac+11] Matteo Cacciari et al. "Jet Reconstruction in Heavy Ion Collisions". In: *Eur. Phys. J.* C71 (Oct. 2011), p. 1539. DOI: `10.1140/epjc/s10052-011-1539-z`. arXiv:`1010.1759 [hep-ph]`.

[Cat+91] S. Catani et al. "New clustering algorithm for multi - jet cross-sections in e+ e- annihilation". In: *Phys. Lett.* B269 (1991), pp. 432–438. DOI: `10.1016/0370-2693(91)90196-W`.

[Cat+93] S. Catani et al. "Longitudinally-invariant $k_\perp$-clustering algorithm for hadron-hadron collisions". In: *Nucl. Phys.* B406 (1993), pp. 187–224. DOI: `10.1016/0550-3213(93)90166-M`.

[CDS] CERN Document Server. CERN-DI-0812015. URL: `http://cdsweb.cern.ch/record/1260465`.

[Cha+08] S. Chatrchyan et al. "The CMS experiment at the CERN LHC". In: *JINST* 3 (2008), S08004. DOI: `10.1088/1748-0221/3/08/S08004`.

[Cha+11a] Serguei Chatrchyan et al. "Dependence on pseudorapidity and centrality of charged hadron production in PbPb collisions at a nucleon-nucleon centre-of-mass energy of 2.76 TeV". In: *JHEP* 08 (2011), p. 141. DOI: `10.1007/JHEP08(2011)141`. arXiv:`1107.4800 [nucl-ex]`.

[Cha+11b] Serguei Chatrchyan et al. "Observation and studies of jet quenching in PbPb collisions at nucleon-nucleon center-of-mass energy = 2.76 TeV". In: *Phys. Rev.* C84 (2011), p. 024906. DOI: `10.1103/PhysRevC.84.024906`. arXiv:`1102.1957 [nucl-ex]`.

[Cha+12a] Serguei Chatrchyan et al. "Combined results of searches for the standard model Higgs boson in pp collisions at $\sqrt{s} = 7$ TeV". In: *Phys. Lett.* B710 (2012), pp. 26–48. arXiv:`1202.1488 [hep-ex]`.

[Cha+12b] Serguei Chatrchyan et al. “Study of high-pT charged particle suppression in PbPb compared to pp collisions at $\sqrt{s_{NN}} = 2.76$ TeV”. In: *Eur. Phys. J.* C72 (2012), p. 1945. DOI: `10.1140/epjc/s10052-012-1945-x`. arXiv:`1202.2554 [nucl-ex]`.

[Cor01] P Cortese. “ALICE transition-radiation detector: Technical Design Report”. CERN-LHCC-2001-021. 2001. URL: `http://cdsweb.cern.ch/record/519145`.

[CP75a] N. Cabibbo and G. Parisi. “Exponential Hadronic Spectrum and Quark Liberation”. In: *Phys. Lett.* B59 (1975), pp. 67–69. DOI: `10.1016/0370-2693(75)90158-6`.

[CP75b] John C. Collins and M. J. Perry. “Superdense Matter: Neutrons Or Asymptotically Free Quarks?” In: *Phys. Rev. Lett.* 34 (1975), p. 1353. DOI: `10.1103/PhysRevLett.34.1353`.

[CS06] Matteo Cacciari and Gavin P. Salam. “Dispelling the N^3 myth for the Kt jet-finder”. In: *Phys. Lett.* B641 (2006), pp. 57–61. DOI: `10.1016/j.physletb.2006.08.037`. arXiv:`hep-ph/0512210`.

[CS08] Matteo Cacciari and Gavin P. Salam. “Pileup subtraction using jet areas”. In: *Phys. Lett.* B659 (2008), pp. 119–126. DOI: `10.1016/j.physletb.2007.09.077`. arXiv:`0707.1378 [hep-ph]`.

[CSS08a] Matteo Cacciari, Gavin P. Salam, and Gregory Soyez. “The anti-k_{t} jet clustering algorithm”. In: *JHEP* 0804 (2008), p. 063. DOI: `10.1088/1126-6708/2008/04/063`. arXiv:`0802.1189 [hep-ph]`.

[CSS08b] Matteo Cacciari, Gavin P. Salam, and Gregory Soyez. “The Catchment Area of Jets”. In: *JHEP* 04 (Feb. 2008), p. 005. DOI: `10.1088/1126-6708/2008/04/005`. arXiv:`0802.1188 [hep-ph]`.

[CSS11] Matteo Cacciari, Gavin P. Salam, and Gregory Soyez. “Fluctuations and asymmetric jet events in PbPb collisions at the LHC”. In: *Eur. Phys. J.* C71 (2011), p. 1692. DOI: `10.1140/epjc/s10052-011-1692-4`. arXiv:`1101.2878 [hep-ph]`.

[Cuv09] Jan de Cuveland. “A track reconstructing low-latency trigger processor for high-energy physics”. PhD thesis. University of Heidelberg, 2009.

[Del+00] G. Dellacasa et al. “ALICE technical design report of the time of flight system (TOF)”. CERN-LHCC-2000-012. 2000. URL: `http://cdsweb.cern.ch/record/430132`; P. Cortese et al. “ALICE: Addendum to the technical design report of the time of flight system (TOF)”. CERN-

LHCC-2002-016. 2002. URL: `http://cdsweb.cern.ch/record/545834`.

[dEn09] David d'Enterria. "Jet quenching". 2009. arXiv:`0902.2011 [nucl-ex]`.

[DFK82] Yuri L. Dokshitzer, Victor S. Fadin, and Valery A. Khoze. "Coherent Effects in the Perturbative QCD Parton Jets". In: *Phys. Lett.* B115 (1982), pp. 242–246. DOI: `10.1016/0370-2693(82)90654-2`.

[Dir50] G. L. Dirichlet. "Über die Reduction der positiven quadratischen Formen mit drei unbestimmten ganzen Zahlen". In: *J. Reine und Ang. Math.* 40 (1850), p. 209.

[Dok+88] Yu. L. Dokshitzer et al. "QCD coherence in high-energy reactions". In: *Rev. Mod. Phys.* 60 (2 Apr. 1988), pp. 373–388. DOI: `10.1103/RevModPhys.60.373`.

[Dok+91] Yuri L. Dokshitzer et al. *Basics of perturbative QCD.* 1991. URL: `http://www.lpthe.jussieu.fr/~yuri/`.

[EB08] Lyndon Evans and Philip Bryant. "LHC Machine". In: *JINST* 3 (2008), S08001. DOI: `10.1088/1748-0221/3/08/S08001`.

[ES93] Stephen D. Ellis and Davision E. Soper. "Successive Combination Jet Algorithm For Hadron Collisions". In: *Phys. Rev.* D48 (1993), pp. 3160–3166. DOI: `10.1103/PhysRevD.48.3160`. arXiv:`hep-ph/9305266`.

[Esk+05] K.J. Eskola et al. "The Fragility of high-p(T) hadron spectra as a hard probe". In: *Nucl. Phys.* A747 (2005), pp. 511–529. DOI: `10.1016/j.nuclphysa.2004.09.070`. arXiv:`hep-ph/0406319 [hep-ph]`.

[Est11] M. Estienne. "Jet fragmentation Monte Carlo study in vacuum and in medium in the ALICE experiment at the LHC". In: *Nuovo Cimento C* 034 (2011), pp. 49–55. DOI: `10.1393/ncc/i2011-10844-7`.

[Fab+04] Christian Wolfgang Fabjan et al. "ALICE trigger data-acquisition high-level trigger and control system: Technical Design Report". CERN-LHCC-2003-062. 2004. URL: `http://cdsweb.cern.ch/record/684651`.

[FG72] Harald Fritzsch and Murray Gell-Mann. "Current Algebra: Quarks and What Else?" In: *eConf* 720906V2 (1972), pp. 135–165. arXiv:`hep-ph/0208010`.

[FGL73] H. Fritzsch, M. Gell-Mann, and H. Leutwyler. "Advantages of the color octet gluon picture". In: *Phys. Lett.* B47 (1973), pp. 365–368. DOI: `10.1016/0370-2693(73)90625-4`.

[Gel64] M. Gell-Mann. “A schematic model of baryons and mesons”. In: *Phys. Lett.* 8 (1964), pp. 214–215. DOI: `10.1016/S0031-9163(64)92001-3`.

[Gla61] S.L. Glashow. “Partial Symmetries of Weak Interactions”. In: *Nucl. Phys.* 22 (1961), pp. 579–588. DOI: `10.1016/0029-5582(61)90469-2`.

[Gro10] Jan Fiete Grosse-Oetringhaus. “Minimum-Bias and Early QCD Physics in ALICE”. 2010. arXiv:`1010.2448 [hep-ex]`.

[GW73] D.J. Gross and Frank Wilczek. “Ultraviolet Behavior of Nonabelian Gauge Theories”. In: *Phys. Rev. Lett.* 30 (1973), pp. 1343–1346. DOI: `10.1103/PhysRevLett.30.1343`.

[HJ00] Ulrich W. Heinz and Maurice Jacob. “Evidence for a new state of matter: An Assessment of the results from the CERN lead beam program”. 2000. arXiv:`nucl-th/0002042 [nucl-th]`.

[Hut+90] J. E. Huth et al. “Toward a Standardization of Jet Definitions”. In: *Fermilab-Conf-90-249-E* (1990). Presented at Summer Study on High Energy Physics, Reasearch Directions for the Decade, Snowmass, CO, Jun 25 - Jul 13, 1990.

[Jac10] Peter Jacobs. “Background Fluctuations in Heavy Ion Jet Reconstruction”. Dec. 2010. arXiv:`1012.2406 [nucl-ex]`.

[Kir+10] Stefan Kirsch et al. “An FPGA-based High-Speed, Low-Latency Processing System for High-Energy Physics”. In: *Proceedings of the 2010 International Conference on Field Programmable Logic and Applications.* FPL ’10. Washington, DC, USA: IEEE Computer Society, 2010, pp. 562–567. ISBN: 978-0-7695-4179-2. DOI: `10.1109/FPL.2010.110`.

[KL03] F. Karsch and E. Laermann. *Thermodynamics and in-medium hadron properties from lattice QCD.* prepared for "Quark-Gluon Plasma III". World Scientific, 2003. arXiv:`hep-lat/0305025`.

[Kle] C. Klein-Bösing. *private communication.*

[Kle+11] Christian Klein-Boesing et al. *Fluctuations with VZERO.* Internal presentation in the ALICE jet meeting 10-19-2011. Oct. 2011. URL: `https://indico.cern.ch/conferenceDisplay.py?confId=159516`.

[Kle11a] Christian Klein-Boesing. “Reconstruction of Jet Properties in Pb-Pb Collisions with the ALICE-Experiment”. 2011. arXiv:`1110.1195 [nucl-ex]`.

[Kle11b] Christian Klein-Bösing. *Fluctuations Paper.* Internal presentation in the ALICE jet meeting 08-12-2011. Aug. 2011. URL: `https://indico.cern.ch/conferenceDisplay.py?confId=151094`.

[Kle11c] Christian Klein-Bösing. *Poissonian Limits.* Internal presentation in the ALICE jet meeting 04-18-2011. Apr. 2011. URL: `https://indico.cern.ch/conferenceDisplay.py?confId=135965`; Christian Klein-Bösing. *Poissonian Limit revisited, VZERO Event Plane.* Internal presentation in the ALICE jet meeting 08-17-2011. Aug. 2011. URL: `https://indico.cern.ch/conferenceDisplay.py?confId=151652`.

[Kle11d] Jochen Klein. "Triggering with the ALICE TRD". Dec. 2011. arXiv:`1112.5110 [nucl-ex]`.

[Kle11e] Jochen Klein. *Triggering with the ALICE TRD.* Presentation at the 4th Workshop on Advanced Transition Radiation Detectors for Accelerator and Space Applications, Bari, Italy. Sept. 2011. URL: `http://agenda.infn.it/contributionDisplay.py?contribId=7&confId=3468`.

[Kle12] Jochen Klein. *TRD jet trigger.* Internal presentation in the ALICE jet meeting 05-15-2012. May 2012.

[KV11] C. Klein-Bösing and M. Verweij. *Hybrid Tracks.* Internal presentation in the ALICE jet meeting 06-15-2011. June 2011. URL: `https://indico.cern.ch/conferenceDisplay.py?confId=143605`.

[MBD07] A. Moraes, C. Buttar, and I. Dawson. "Prediction for minimum bias and the underlying event at LHC energies". In: *Eur. Phys. J.* C50 (2007), pp. 435–466. DOI: `10.1140/epjc/s10052-007-0239-1`.

[Men] Leticia Cunqueiro Mendez. *private communication.*

[Mil+07] M. L. Miller et al. "Glauber Modeling in High-Energy Nuclear Collisions". In: *Annu. Rev. Nucl. Part. Sci.* 57 (2007), pp. 205–243. DOI: `10.1146/annurev.nucl.57.090506.123020`. arXiv:`nucl-ex/0701025`.

[MS01] R. Machleidt and I. Slaus. "The Nucleon-nucleon interaction: Topical review". In: *J. Phys.* G27 (2001), R69–R108. DOI: `10.1088/0954-3899/27/5/201`. arXiv:`nucl-th/0101056 [nucl-th]`.

[Nak+10] K. Nakamura et al. "Review of Particle Physics". In: *J. Phys.* G37 (2010). And 2011 partial update (online web edition) for the 2012 edition. Cut-off date was January 15, 2011., p. 075021. URL: `http://pdg.lbl.gov/`.

[Per00] D. H. Perkins. *Introduction to high energy physics.* 4th ed. ISBN 0-521-62196-8. Cambridge University Press, 2000.

[Phi11] Owe Philipsen. "Status of the QCD phase diagram from lattice calculations". 2011. arXiv:`1111.5370 [hep-ph]`.

[Pol73] H. David Politzer. "Reliable Perturbative Results for Strong Interactions?" In: *Phys. Rev. Lett.* 30 (1973), pp. 1346–1349. DOI: `10.1103/PhysRevLett.30.1346`.

[Pop11] Hendrik Poppenborg. "Characterization of Heavy-Ion-Background in Jet-Reconstruction". Bachelor's Thesis. Westfälische Wilhelms-Universität Münster, Sept. 2011.

[PV98] A. M. Poskanzer and S. A. Voloshin. "Methods for analyzing anisotropic flow in relativistic nuclear collisions". In: *Phys. Rev.* C58 (1998), pp. 1671–1678. DOI: `10.1103/PhysRevC.58.1671`. arXiv:`nucl-ex/9805001`.

[RC53] F. Reines and C.L. Cowan. "Detection of the free neutrino". In: *Phys. Rev.* 92 (1953), pp. 830–831. DOI: `10.1103/PhysRev.92.830`; C.L. Cowan et al. "Detection of the free neutrino: A Confirmation". In: *Science* 124 (1956), pp. 103–104. DOI: `10.1126/science.124.3212.103`.

[RC56] Frederick Reines and Clyde L. Cowan. "The neutrino". In: *Nature* 178 (1956), pp. 446–449. DOI: `10.1038/178446a0`.

[Ren+11] Thorsten Renk et al. "Systematics of the charged-hadron P_T spectrum and the nuclear suppression factor in heavy-ion collisions from $\sqrt{s} =$ 200 GeV to $\sqrt{s} = 2.76$ TeV". In: *Phys. Rev.* C84 (2011), p. 014906. DOI: `10.1103/PhysRevC.84.014906`. arXiv:`1103.5308 [hep-ph]`.

[Root] ROOT website. URL: `http://root.cern.ch/drupal/`.

[Sal80] Abdus Salam. "Gauge Unification of Fundamental Forces". In: *Rev. Mod. Phys.* 52 (1980). Nobel lecture 1979, pp. 525–538. DOI: `10.1103/RevModPhys.52.525`.

[San11] Masato Sano. *Pi,K,anti-p flow with EP method using VZERO and FMD.* Internal presentation in the ALICE flow meeting 2011-26-08. Aug. 2011.

[Shu78] Edward V. Shuryak. "Quark-Gluon Plasma and Hadronic Production of Leptons, Photons and Psions". In: *Phys. Lett.* B78 (1978), p. 150. DOI: `10.1016/0370-2693(78)90370-2`.

[Ska10] Peter Zeiler Skands. "Tuning Monte Carlo Generators: The Perugia Tunes". In: *Phys. Rev.* D82 (2010), p. 074018. DOI: `10.1103/PhysRevD.82.074018`. arXiv:`1005.3457 [hep-ph]`.

[SMS06] Torbjorn Sjostrand, Stephen Mrenna, and Peter Skands. "PYTHIA 6.4 Physics and Manual". In: *JHEP* 05 (2006), p. 026. DOI: `10.1088/1126-6708/2006/05/026`. arXiv:`hep-ph/0603175`.

[Sne11] Raimond Snellings. “Elliptic Flow: A Brief Review”. In: *New J. Phys.* 13 (2011), p. 055008. DOI: `10.1088/1367-2630/13/5/055008`. arXiv:`1102.3010 [nucl-ex]`.

[SS07] Gavin P. Salam and Gregory Soyez. “A practical Seedless Infrared-Safe Cone jet algorithm”. In: *JHEP* 0705 (Apr. 2007), p. 086. DOI: `10.1088/1126-6708/2007/05/086`. arXiv:`0704.0292 [hep-ph]`.

[STA10] STAR Collaboration. “An Experimental Exploration of the QCD Phase Diagram: The Search for the Critical Point and the Onset of De-confinement”. July 2010. arXiv:`1007.2613 [nucl-ex]`.

[Tan01] M. J. Tannenbaum. “The distribution function of the event-by-event average p_T for statistically independent emission”. In: *Phys. Lett.* B498 (2001), pp. 29–34. DOI: `10.1016/S0370-2693(00)01325-3`.

[Tan04] M. J. Tannenbaum. “Event-by-event average p_T fluctuations in $\sqrt{s_{NN}} = 200$ GeV Au + Au and p + p collisions in PHENIX: Measurements and jet contribution simulations”. In: *J. Phys.* G30 (2004), S1367–S1370. DOI: `10.1088/0954-3899/30/8/129`. arXiv:`nucl-ex/0403048`.

[Toi11] Alberica Toia. “Bulk properties of Pb-Pb collisions at $\sqrt{s_{NN}} = 2.76$ TeV measured by ALICE”. In: *J. Phys.* G38 (2011), p. 124007. DOI: `10.1088/0954-3899/38/12/124007`. arXiv:`1107.1973 [nucl-ex]`.

[Ver] M. Verweij. *private communication.*

[Ver11] Marta Verweij. *Track QA and Cuts.* Internal presentation in the ALICE jet meeting 10-11-2011. Oct. 2011. URL: `https://indico.cern.ch/conferenceDisplay.py?confId=159516`.

[Vil+07] O Villalobos Baillie et al. “Recent developments on the ALICE central Trigger processor”. Prepared for 12th Workshop on Electronics for LHC and Future Experiments (LECC 2006), Valencia, Spain, 25-29 Sep 2006. 2007. URL: `http://cdsweb.cern.ch/record/1027489`.

[VZ96] S. Voloshin and Y. Zhang. “Flow Study in Relativistic Nuclear Collisions by Fourier Expansion of Azimuthal Particle Distributions”. In: *Z. Phys.* C70 (1996), pp. 665–672. DOI: `10.1007/s002880050141`. arXiv:`hep-ph/9407282`.

[Wei67] Steven Weinberg. “A Model of Leptons”. In: *Phys. Rev. Lett.* 19 (1967), pp. 1264–1266. DOI: `10.1103/PhysRevLett.19.1264`.

[Wes13] Uwe Westerhoff. Thesis in preparation. PhD thesis. Westfälische Wilhelms-Universität Münster, 2013.

[WG92] X.-N. Wang and M. Gyulassy. "Gluon Shadowing and Jet Quenching in A + A Collisions at $\sqrt{(s)} = 200$ AGeV". In: *Phys. Rev. Lett.* 68 (1992), pp. 1480–1483. DOI: `10.1103/PhysRevLett.68.1480`.

[Wie09] Urs Achim Wiedemann. "Jet Quenching in Heavy Ion Collisions". 2009. arXiv:`0908.2306 [hep-ph]`.

[Wil74] Kenneth G. Wilson. "Confinement of quarks". In: *Phys. Rev.* D10 (1974), pp. 2445–2459. DOI: `10.1103/PhysRevD.10.2445`.

[YHM08] Kohsuke Yagi, Tetsuo Hatsuda, and Yasuo Miake. *Quark-Gluon Plasma.* Cambridge University Press, 2008.

[Zwe64] G. Zweig. "An SU_3 model for strong interaction symmetry and its breaking - part I". CERN preprint CERN-TH-401. 1964. URL: `http://cdsweb.cern.ch/record/352337`; G. Zweig. "An SU_3 model for strong interaction symmetry and its breaking - part II". CERN preprint CERN-TH-412. 1964. URL: `http://cdsweb.cern.ch/record/570209`.

Acknowledgments / Danksagung

I would like to express my gratitude and thanks to all people who made their individual contributions to the success of this thesis.

Herrn Prof. Dr. Johannes P. Wessels danke ich für die Möglichkeit, in einem so interessanten Forschungsfeld mitgewirkt haben zu können. Ich möchte mich für die guten Arbeitsbedingungen am Institut für Kernphysik in Münster bedanken, sowie für die zahlreichen Konferenzen und Workshops, an denen ich teilnehmen konnte. Außerdem danke ich für die einmaligen Erfahrungen, die ich während meiner Zeit am CERN machen durfte.

Dr. Christian Klein-Bösing danke ich für die Betreuung meiner Arbeit. Ich bin sehr dankbar für seine ständige Bereitschaft zur kritischen Diskussion, vielen technischen Hilfestellungen und physikalischen Erklärungen. Darüber hinaus hat Christian Klein-Bösing mit vielen neuen Ideen und entscheidenden Hinweisen in ganz besonderem Maße zum Gelingen der Arbeit beigetragen.

A special thanks goes out to the ALICE collaboration and the jet analysis group. Especially, I thank Dr. Leticia Cunqueiro, Marta Verweij, and Dr. Christian Klein-Bösing for the very cooperative and productive work on the background fluctuations. I also sincerely thank Dr. Oliver Busch, Dr. Magali Estienne, and Swensy Jangal for a lot of support and helpful discussions concerning the jet structure analysis.

Der gesamten TRD-Trigger-Gruppe, insbesondere Dr. Tom Dietel, Stefan Kirsch, Jochen Klein und Felix Rettig danke ich für die tolle Zusammenarbeit und Unterstützung. Tom Dietel genießt meinen besonderen Dank für die zahlreichen Diskussionen und Hilfestellungen gerade, aber nicht nur, zu Beginn meiner Arbeit.

For the exciting time during my stay at CERN, I gratefully thank Dr. Yvonne Pachmayer, Dr. Jörg Lehnert, Dr. Ken Oyama, and Nora Pitz as representatives of the TRD P2 crew. I would also like to thank Dr. Oliver Busch for his great assistance with the PVSS work.

Für die kritische Durchsicht dieser Arbeit und die sehr hilfreichen Anmerkungen danke ich Dr. Oliver Busch, Dr. Tom Dietel, Markus Heide und Dr. Christian Klein-Bösing.

Ich danke der gesamten Arbeitsgruppe von Prof. Wessels, inklusive ehemaliger Mitglieder, für die freundliche Zusammenarbeit und Unterstützung: Björn Albrecht, Jonas Anielski, Dr. Christoph Baumann, Cyrano Bergmann, Jennifer Bersch, Dr. Katharina Büscher, Annika Busch, Dr. Tom Dietel, Stephan Dyba, Dr. David Emschermann, Linus Feldkamp, Henriette Gatz, Dr. Richard Glasow, Dr. Holger Gottschlag, Helge Grimm, Dr. Matus Kalisky, Thomas Keuter, Markus Heide, Norbert Heine, Dr. Christian Klein-Bösing, Dr. Melanie Klein-Bösing, Martin Kohn, Annika Passfeld, Jan-Frederik Pietschmann, Friederike Poppenborg, Henrik Poppenborg, Markus Rammler, Markus Tegeder, Prof. em. Dr. Rainer Santo, Dr. Klaus Reygers, Dr. Baldo Sahlmüller, Eva Sicking, Wolfgang Verhoeven, Don Vernekohl, Matthias Walter, Dr. Alexander Wilk, Prof. Dr. Johannes P. Wessels, Uwe Westerhoff, Svenja Wulff, Martin Wilde und Markus Zimmermann.
Darüber hinaus danke ich allen weiteren Kollegen am Institut für Kernphysik, der AG Prof. Frekers, AG Prof. Khoukaz, AG Prof. Weihneimer und den Werkstätten.

Nicht zuletzt danke ich meiner gesamten Familie, insbesondere meinen Eltern Marion Bathen-Reicher und Rainer Bathen, für ihre Unterstützung.